Tunable Mechanical Damping in Fast Perturbed Locomotion: Biomechanical Simulations and Biorobotic Applications

DISSERTATION

der Mathematisch-Naturwissenschaftlichen Fakultät
der Eberhard Karls Universität Tübingen
zur Erlangung des Grades eines
Doktors der Naturwissenschaften
(Dr. rer. nat.)

vorgelegt von
FABIO IZZI
aus Caserta/Italien

Tübingen
2023

Gedruckt mit Genehmigung der Mathematisch-Naturwissenschaftlichen Fakultät der Eberhard Karls Universität Tübingen.

Tag der mündlichen Qualifikation: 26.01.2024

Dekan: Prof. Dr. Thilo Stehle
1. Berichterstatter: Prof. Dr. Martin Giese
2. Berichterstatter: Prof. Dr. Daniel Haeufle

Abstract

Legged animals show extraordinary versatility in navigating complex environments and overcoming unexpected obstacles. This agility appears promoted by mechanical compliance intrinsic to their limbs. Extensive research has been conducted on the importance of elastic compliance for legged locomotion, demonstrating numerous benefits such as improved energy efficiency, enhanced shock absorption, and facilitated power generation. However, elastic compliance can also produce unwanted vibrations, reduce control bandwidth, and cannot counter energy disturbances. Although rarely implemented in legged robotics, mechanical damping is a promising solution to these limitations. Interestingly, muscle fibers exhibit viscous-like damping behavior when suddenly stretched. This capacity seems dependent on muscle excitation level, indicating that tunable mechanical damping plays a functional role in biological locomotion. In particular, tunable mechanical damping could facilitate a quick response to sudden perturbations, mitigating errors and delays in sensorimotor information.

This doctoral dissertation investigates principles of tunable mechanical damping in fast perturbed legged-locomotion. Through quantitative methodologies, it expands previous knowledge of how muscle fibers exploit tunable mechanical damping around touchdown. Central to this research was the force-velocity relation, a phenomenological function describing viscous-like capacities within muscle contraction dynamics. Additionally, this thesis explores technical solutions to achieve tunable mechanical damping in legged robotics, combining numerical analysis and hardware experiments. The content of this dissertation relies on five manuscripts (four peer-reviewed journal articles and a pre-print), the fruit of collaborative research during my doctoral project.

In two computational studies, we could confirm that the force-velocity relation grants muscle fibers tunable mechanical damping during the earliest response to step perturbations (i.e., the preflex phase). However, we found that current interpretations of this phenomenon require revision. Without feedforward neuronal modulation, muscle-produced mechanical damping played a minor contribution in regulating the preflex response. Large impact velocities during reference hopping could further compromise such contribution. In contrast, tunable mechanical damping produced by the force-velocity relation became a dominant regulating factor when feedforward stimulation was allowed. In particular, we observed more adjustment of touchdown force and preflex work in response to step perturbations and a simultaneous increase in hopping stability.

Since our computational studies relied on Hill-type muscle models, which are ansatz approximations of real muscle contraction, we conducted an in vitro investigation with realistic boundary conditions to validate our simulations. This study confirmed activity-dependent damping-like properties in biological muscle fibers. However, the results showed an initial short-range stiffness phase, which Hill-type models should include for better predictions. In vitro, the muscle fibers' viscous-like response developed more smoothly and later than what was observed in our simulations, suggesting the need for a better characterization of the force-velocity relation's eccentric side.

Inspired by the biological observations of viscous-like properties within the muscle fibers, we investigated the advantages of incorporating viscous dampers to provide tunable mechanical damping in

legged robots. Using numerical simulations of a robotic leg, we found that viscous damping consistently outperforms Coulomb friction damping in rejecting potential energy disturbances caused by step perturbations. In contrast, our empirical hardware experiments revealed that damping rate control of a viscous damper that is directly connected to the knee joint fails to generate mechanical damping that can be fine-tuned.

In a follow-up study, we overcame this limitation with a slack-damper mechanism. This device uses a cable with adjustable slackness to connect the viscous damper to the knee rotation. Using hopping experiments with various terrain disturbances, we demonstrate that slackness control could effectively and intuitively adjust energy dissipation in a leg prototype, indicating that tunable mechanical damping was achieved. These experiments also confirmed that embedded mechanical damping causes a trade-off between locomotion energy efficiency and robustness. We argue that the tunability of our slack-damper mechanism and its perturbation-triggered nature make this trade-off more favorable.

The findings of this dissertation support previous evidence that tunable mechanical damping is beneficial for legged locomotion. We demonstrate that tunable mechanical damping can naturally occur in biological systems due to an intricate interaction between neuromodulation, inner muscle mechanics, and environmental conditions. In legged robotics, our slack-damper mechanism shows that simple technical solutions are sufficient to implement tunable mechanical damping effectively.

Kurzfassung

Tiere mit Beinen zeigen eine außerordentliche Flexibilität bei der Navigation in komplexen Umgebungen und der Überwindung unerwarteter Hindernisse. Diese Beweglichkeit wird offenbar durch die mechanische Nachgiebigkeit der Gliedmaßen gefördert. Die Bedeutung der elastischen Nachgiebigkeit für die Fortbewegung von Beinen wurde bereits ausgiebig erforscht, wobei zahlreiche Vorteile wie verbesserte Energieeffizienz, verbesserte Stoßdämpfung und erleichterte Energieerzeugung nachgewiesen wurden. Allerdings kann die elastische Nachgiebigkeit auch unerwünschte Vibrationen erzeugen, die Kontrollbandbreite verringern und Energiestörungen nicht ausgleichen. Obwohl sie in der Beinrobotertechnik nur selten eingesetzt wird, ist die mechanische Dämpfung eine vielversprechende Lösung für diese Einschränkungen. Interessanterweise zeigen Muskelfasern ein viskoses, dämpfendes Verhalten, wenn sie plötzlich gedehnt werden. Diese Fähigkeit scheint vom Grad der Muskelanregung abhängig zu sein, was darauf hindeutet, dass eine einstellbare mechanische Dämpfung eine funktionelle Rolle bei der biologischen Fortbewegung spielt. Insbesondere könnte eine abstimmbare mechanische Dämpfung eine schnelle Reaktion auf plötzliche Störungen ermöglichen und so Fehler und Verzögerungen bei der sensomotorischen Information abmildern.

Diese Dissertation untersucht die Prinzipien der abstimmbaren mechanischen Dämpfung bei der schnellen, gestörten Fortbewegung mit den Beinen. Mit Hilfe quantitativer Methoden erweitert sie das bisherige Wissen darüber, wie Muskelfasern die abstimmbare mechanische Dämpfung beim Aufsetzen ausnutzen. Im Mittelpunkt dieser Forschung steht die Kraft-Geschwindigkeits-Relation, eine phänomenologische Funktion, die viskose Kapazitäten innerhalb der Muskelkontraktionsdynamik beschreibt. Darüber hinaus werden in dieser Arbeit technische Lösungen zur Erzielung einer abstimmbaren mechanischen Dämpfung in der Beinrobotertechnik untersucht, wobei numerische Analysen und Hardwareexperimente kombiniert werden. Der Inhalt dieser Dissertation stützt sich auf fünf Manuskripte (vier begutachtete Zeitschriftenartikel und ein Pre-Print), die das Ergebnis der gemeinschaftlichen Forschung während meines Promotionsprojekts sind.

In zwei Berechnungsstudien konnten wir bestätigen, dass die Kraft-Geschwindigkeits-Relation den Muskelfasern eine abstimmbare mechanische Dämpfung während der frühesten Reaktion auf Schrittstörungen (d. h. der Präflexphase) gewährt. Wir haben jedoch festgestellt, dass die derzeitigen Interpretationen dieses Phänomens einer Überarbeitung bedürfen. Ohne neuronale Feedforward-Modulation spielte die muskelerzeugte mechanische Dämpfung bei der Regulierung der präflexiven Reaktion eine untergeordnete Rolle. Große Aufprallgeschwindigkeiten beim Referenzhüpfen könnten diesen Beitrag weiter beeinträchtigen. Im Gegensatz dazu wurde die abstimmbare mechanische Dämpfung, die durch die Kraft-Geschwindigkeits-Relation erzeugt wird, zu einem dominanten regulierenden Faktor, wenn eine Feedforward-Stimulation erlaubt war. Insbesondere beobachteten wir eine stärkere Anpassung der Aufsetzkraft und der Präflexarbeit als Reaktion auf Schritt-Störungen und eine gleichzeitige Erhöhung der Sprungstabilität.

Da unsere Berechnungsstudien auf Hill-Muskelmodellen beruhten, die eine Annäherung an die reale Muskelkontraktion darstellen, führten wir eine In-vitro-Untersuchung mit realistischen Randbe-

dingungen durch, um unsere Simulationen zu validieren. Diese Studie bestätigte aktivitätsabhängige dämpfungsähnliche Eigenschaften in biologischen Muskelfasern. Die Ergebnisse zeigten jedoch eine anfängliche Kurzzeit-Steifigkeitsphase, die Hill-Modelle für bessere Vorhersagen berücksichtigen sollten. In vitro entwickelte sich die viskose Reaktion der Muskelfasern sanfter und später als in unseren Simulationen beobachtet, was auf die Notwendigkeit einer besseren Charakterisierung der exzentrischen Seite der Kraft-Geschwindigkeits-Beziehung hinweist.

Inspiriert von den biologischen Beobachtungen viskositätsähnlicher Eigenschaften in den Muskelfasern untersuchten wir die Vorteile der Einbeziehung viskoser Dämpfer, um eine abstimmbare mechanische Dämpfung in Beinrobotern zu ermöglichen. Anhand numerischer Simulationen eines Roboterbeins konnten wir feststellen, dass die viskose Dämpfung die Coulombsche Reibungsdämpfung bei der Unterdrückung von Störungen der potentiellen Energie, die durch Schrittstörungen verursacht werden, konsequent übertrifft. Im Gegensatz dazu haben unsere empirischen Hardware-Experimente gezeigt, dass die Steuerung der Dämpfungsrate eines viskosen Dämpfers, der direkt mit dem Kniegelenk verbunden ist, keine mechanische Dämpfung erzeugt, die sich fein abstimmen lässt.

In einer Folgestudie haben wir diese Einschränkung mit einem Slack-Damper-Mechanismus überwunden. Diese Vorrichtung verwendet ein Kabel mit einstellbarem Spiel, um den viskosen Dämpfer mit der Kniedrehung zu verbinden. Anhand von Hüpfexperimenten mit verschiedenen Geländestörungen konnten wir nachweisen, dass die Schlaffheitssteuerung die Energiedissipation in einem Beinprototyp effektiv und intuitiv anpassen konnte, was darauf hindeutet, dass eine abstimmbare mechanische Dämpfung erreicht wurde. Diese Experimente bestätigen auch, dass die eingebettete mechanische Dämpfung einen Kompromiss zwischen der Energieeffizienz der Fortbewegung und der Robustheit darstellt. Wir argumentieren, dass die Abstimmbarkeit unseres Slack-Damper-Mechanismus und seine störungsausgelöste Natur diesen Kompromiss begünstigen.

Die Ergebnisse dieser Dissertation unterstützen frühere Belege dafür, dass eine abstimmbare mechanische Dämpfung für die Fortbewegung von Beinen von Vorteil ist. Wir zeigen, dass abstimmbare mechanische Dämpfung in biologischen Systemen aufgrund einer komplizierten Interaktion zwischen Neuromodulation, innerer Muskelmechanik und Umweltbedingungen natürlich vorkommen kann. In der Beinrobotertechnik zeigt unser Slack-Damper-Mechanismus, dass einfache technische Lösungen ausreichen, um eine abstimmbare mechanische Dämpfung effektiv umzusetzen.

Acknowledgements

English version

I love joking about my Ph.D. being cursed. After all, it began with a massive wildfire in Australia, a global pandemic took place during my first conferences, and some major international crisis broke out every time I completed a project (please accept my apologies should my thesis defense trigger an alien invasion). However, Nature loves to find a stable equilibrium, a balance. At least, this occurred during my Ph.D., as I was also blessed with meeting wonderful people. This chapter is dedicated to them, without whom my Ph.D. period would have felt empty.

I want to start by thanking everyone who worked with me: my supervisors (Daniel Haeufle and Alexander Badri-Spröwitz), my co-authors, and the thesis committee. This dissertation would not exist without your support and expertise. In particular, I want to thank Daniel for being such an outstanding mentor throughout these years. Replacing every word of this dissertation with “Thank you, Daniel" will not be enough to express my gratitude. It will also cause this thesis to fail the peer-review process and me never to graduate. Therefore, I’ll just say this: receiving my academic training from you has been an honor and a pleasure.

I want to thank An for being the best research partner. Unveiling the mysteries of tunable mechanical damping with you was a great adventure, and I hope our paths will meet again. Expressing all my gratitude to Matthew is impossible (literally: it would require some inappropriate jokes, leaving this thesis unpublishable). You have been the best office buddy and gym bro I could have asked for. I am also grateful for Maria and Valerie, who have been such great partners in crime. Without you, the time spent writing this thesis would have felt way less joyful. Finally, I also thank all the MoCoM members (Pierre, Junya, Christian, Katrin, Isabell, John, Julius), DLG members (Steve, Bernadett, Alborz, Felix, Viktoriia), and IMPRS-IS coordinators (Leila and Sara) for your incredible support, great discussions, and nice coffee breaks together.

My Ph.D. also introduced me to wonderful people outside work. I am incredibly grateful for Agnese and Cristina, my two adopted sisters and personal therapists. Our chats, time together, and jokes made Tübingen feel like a second home to me. In this sense, I also want to express my gratitude to Andrea Cacioppo, who sadly is no longer among us... he lives in Rome now. Finally, I want to thank all the wonderful people I have met during these years, such as Olya, Roberta, Ran Sing, Stefania, Domenica, Ina, and David; each of you has made my Ph.D. journey memorable.

There is also a group of people already in my life before my Ph.D. for whom I am really thankful. Alessandro Sbaraglia, Mattia Poinelli, Gabriele Boncoraglio, Salil Apte, Abhinav Dahiya, and Stefano Carisi: you are the finest friends a person could have. Even in the darkest times, a conversation with you was all I needed to remember how to smile. Last but most important is my family, to whom I am eternally grateful. Matre, Papo, Taina, and Andrew: no words can describe how much I love you. You are both my pillars and my greatest treasure. Every success and achievement in my life would not have been possible without you (note: please edit this sentence should I become an evil tyrant in the future).

A huge thanks also to all my relatives, Zii, Cugini, and Rosanna, who make my life more colorful. Ultimately, I want to express my gratitude to my Nonna, the only person in the world who can make love become a physical entity: the most delicious food. Every time I return home, the accumulated belly fat from my stay makes me feel loved for months.

Traduzione in italiano

Mi piace molto scherzare sul fatto che il mio dottorato sia maledetto. Dopo tutto, è iniziato con un enorme incendio in Australia, una pandemia globale è scoppiata durante le mie prime conferenze e ogni volta che completavo un progetto si scatenava una qualche crisi internazionale (vi prego di accettare le mie scuse qualora la difesa della mia tesi dovesse provocare un'invasione aliena). Tuttavia, la realtà fisica in cui viviamo ama trovare un equilibrio. Così, accanto a queste bizzarre disavventure, il mio dottorato mi ha anche reso estremamente fortunato nel farmi incontrare persone meravigliose. Questo capitolo è dedicato a loro, senza i quali questi anni di ricerca sarebbero stati un periodo vuoto.

Vorrei iniziare ringraziando tutti coloro con cui ho avuto la fortuna di lavorare: i miei supervisori (Daniel Haeufle e Alexander Badri-Spröwitz), i miei coautori e la commissione di tesi. Questa disserzione non esisterebbe senza il vostro sostegno e la vostra competenza. In particolare, desidero ringraziare Daniel per essere stato un mentore eccezionale nel corso di questi anni. Sostituire ogni parola di questa tesi con "Grazie, Daniel" non sarebbe sufficiente ad esprimere tutta la mia gratitudine... inoltre, non farebbe superare alla tesi il processo di peer-review e io non mi laureerei mai. Pertanto, mi limiterò a dire che è stato un onore e una gioia ricevere la mia formazione accademica da te.

Voglio ringraziare An per essere stato il miglior partner di ricerca. Esplorare insieme i segreti del tunable mechanical damping è stata una grande avventura, e spero che le nostre strade si incontrino nuovamente in futuro. Esprimere la mia gratitudine a Matthew è impossibile (letteralmente: richiederebbe una qualche battuta inappropriata che renderebbe questa tesi impubblicabile). Sei stato il miglior compagno di ufficio e Gym Bro che potessi desiderare. Sono grato anche a Maria e Valerie, che sono state le migliori partner in crime. Senza di voi, il tempo trascorso a scrivere questa tesi sarebbe stato molto meno gioioso. Infine, ringrazio anche tutti i membri del MoCoM (Pierre, Junya, Christian, Katrin, Isabell, John, Julius), i membri del DLG (Steve, Bernadett, Alborz, Felix, Viktoriia) e i coordinatori dell'IMPRS-IS (Leila e Sara) per l'incredibile sostegno, le discussioni arricchenti e le piacevoli pause caffè.

Il mio dottorato mi ha anche fatto conoscere persone meravigliose al di fuori del lavoro. Sono incredibilmente grato ad Agnese e Cristina, le mie due sorelle adottive e psico-terapeute personali. Le nostre chiacchierate, il tempo trascorso insieme e l'atmosfera giocosa hanno fatto sì che Tubinga diventasse per me una seconda casa. In questo senso, voglio anche esprimere la mia gratitudine ad Andrea Cacioppo, che purtroppo non è più tra noi... ora vive a Roma. Infine, voglio ringraziare tutte le persone meravigliose che ho incontrato in questi anni, come Olya, Roberta, Ran Sing, Stefania, Domenica, Ina e David; ognuno di voi ha reso il mio percorso di dottorato memorabile.

C'è anche un gruppo di persone che faceva già parte della mia vita prima del dottorato e per il quale sono davvero grato. Alessandro Sbaraglia, Mattia Poinelli, Gabriele Boncoraglio, Salil Apte, Abhinav Dahiya e Stefano Carisi: siete i migliori amici che una persona possa avere. Anche nei momenti più bui, una conversazione con voi era tutto ciò di cui avevo bisogno per ricordare come sorridere. Infine, ma non per importanza, c'è la mia famiglia, alla quale sono eternamente grato. Matre, Papo, Taina e Andrew: nessuna parola può descrivere quanto vi amo. Siete i miei pilastri e il mio tesoro più grande. Ogni successo e realizzazione nella mia vita non sarebbe stato possibile senza di voi (nota: vi prego

di modificare quest'ultima frase qualora in futuro dovessi diventare un tiranno malvagio). Un enorme grazie anche a tutti i miei parenti, Zii, Cugini e Rosanna, che hanno contribuito a rendere la mia vita più colorata. Infine, voglio esprimere tutta la mia gratitudine verso mia Nonna, l'unica persona al mondo capace di trasformare l'amore in una realtà tangibile: il cibo più delizioso di sempre. Ogni volta che torno a casa, la panza che metto prima di ripartire continua a farmi sentire amato per mesi.

Table of contents

List of important symbols, mathematical notations and abbreviations

Symbols

F	muscle force (in N)
F^i	force contribution of the i-th entity to the muscle force (in N)
E_p	potential energy (in J)
W	muscle work (in J)
W^i	work contribution of the i-th entity to the muscle work (in J)
m	mass (in kg)
a	muscle activity
t	time (in s)
u	muscle stimulation
T	torque (in Nm)
r	lever arm (in m)
l	length (in m)
h_{ref}	reference apex height (in m)
Δh	step perturbation (in m)
v	velocity (in m/s)
δ	time delay (in s)
t_{TD}	touchdown time (in s)
t^*_{TD}	expected touchdown time (in s)
g	gravitational acceleration (in m/s^2)
S	hopping stability

Mathematical notation

x	scalar
$\frac{df}{dx}$	total derivative of f with respect to x
$\frac{\partial f}{\partial x}$	partial derivative of f with respect to x
$\dot{x}$	first time derivation of x
$\ddot{x}$	second time derivation of x
Δx	finite change in x
$\{x,y\}$	pair of x and y variables
$x \in [a,b]$	x can range between a and b values
$g(x)$	generic function of x
$\int_a^b y\,dx$	definite integral of y with respect to x from a to b values

List of abbreviations

CNS Central Nervous System

PNS Peripheral Nervous System

DoF Degree of Freedom

MTU Muscle-tendon unit

CE Contractile element

PEE Parallel elastic element

SEE Serial elastic element

SDE Serial damper element

AD Activation Dynamics

TD Touchdown

TO Take-off/toe-off

SRS Short-range stiffness

EDL Extensor digitorum longus

SLIP Spring-loaded Inverted Pendulum

PLA Polylactic Acid

GRF Ground reaction force

CPG Central pattern generator

CoH Cost of Hopping

CoT Cost of Transport

LL Leg length

ACT Activation solution

MS Mid-stance

1 Introduction

1.1 Motivation

Legged locomotion is a highly versatile solution to terrestrial mobility. Walking, sprinting and hopping are just a few of the many gaits legged animals can use to transverse broadly diverse terrains and obstacles. Legged locomotion has long captured the biorobotics community's attention, resulting in several bio-inspired robots (Kim and Wensing, 2017). Nevertheless, the functional mechanisms behind legged locomotion's agility remain elusive. A significant breakthrough in this regard was realizing the importance of mechanical compliance (Alexander, 1990; Blickhan, 1989; Chen et al., 2019; Geyer et al., 2006; Roberts and Azizi, 2011). Unlike rigid robots, systems with embedded mechanical compliance can instantly react to external disturbances, without requiring high bandwidth actuation and excellent sensing (Ashtiani et al., 2021). Moreover, mechanical compliance reduces the need for direct control when producing forces, which can save computing resources (Haeufle et al., 2020b).

Mechanical compliance in legged robotics has been predominately studied in the sense of mechanical elasticity (Chen et al., 2019). Numerous investigations have demonstrated how integrated elasticity offers several advantages to terrestrial locomotion, such as increased energy efficiency (Alexander et al., 1982; Geyer et al., 2006), improved shock tolerance (Roberts and Azizi, 2010) and enhanced gait self-stabilization (Iida et al., 2008). Thanks to this knowledge, numerous robots have shown improved locomotion performance by incorporating serial and parallel springs in their design (Grizzle et al., 2009; Hubicki et al., 2016; Spröwitz et al., 2013; Zhao et al., 2022). Nevertheless, elasticity alone cannot completely capture the complex compliant behavior observed in biological legged locomotion. A leg structure composed solely of elastic elements would result in harmful oscillations and decreased responsiveness (Monteleone et al., 2022). In addition, its energy-conservative nature would make it impossible to reject perturbations that modify the system's energy, such as a sudden shift in ground height. Therefore, it is reasonable to expect that mechanical damping plays a significant role in the compliance of biological legged locomotion (Garcia et al., 2011).

In a mechanical system, damping occurs when nonconservative forces reduce oscillations by dissipating energy. A classic example is viscous damping, which resists motion through damping forces proportional to the system's speed. Mechanical dampers are widely and successfully used in wheeled locomotion (Narwade et al., 2022). In contrast, relatively little is known about their benefits in legged locomotion (Shen and Seipel, 2012). Fundamental research suggests that mechanical damping improves the dynamic stability of legged systems (Abraham et al., 2015; Seipel and Holmes, 2007; Shen and Seipel, 2012), which is the ability to maintain motion trajectories after a disturbance. Specifically, mechanical damping helps stabilize changes in touchdown velocity (Shen and Seipel, 2012) and avoid falls following unexpected ground perturbations (Heim et al., 2020). However, the amount of mechanical damping beneficial for legged locomotion requires careful calibration. Too little damping can reduce dynamic stability (Shen and Seipel, 2012), while excessive damping can decrease locomotion energy efficiency without providing significant improvement in locomotion robustness (Heim et al., 2020).

Finding the right balance for optimal performance is not trivial due to the hybrid and nonlinear dynamics characterizing legged locomotion.

Vertebrate animals rely on their muscles to move. Muscle fibers possess unique viscoelastic properties that allow an instant mechanical response to external perturbations. The capacity of exploiting these mechanical properties to regulate motion takes the name of preflex (from preflex = pre-reflex) (Brown and Loeb, 2000). Preflexes promote motion robustness amid noise and delays in the transmission of sensorimotor information throughout the nervous system. It is argued that individual mechanical properties of the muscle fibers specialize the preflex response to external perturbations (Gerritsen et al., 1998). Specifically, simulation studies suggest that muscle fibers' force-velocity relation allows preflexes to counter perturbations such as impulses (Gerritsen et al., 1998) and step perturbations (Haeufle et al., 2010).

The force-velocity relation is a phenomenological function describing muscle fiber force's dependence on muscle fiber contraction velocity (Hill, 1938). Faster shortening velocities reduce muscle fibers' force production; faster lengthening velocities increase it. Therefore, the force-velocity relation resembles a source of biological viscous damping intrinsic to muscle fibers' material mechanics. In support of this hypothesis, research has demonstrated that removing or simplifying the force-velocity relation leads to effects similar to insufficient mechanical damping, such as decreased locomotion stability and increased risk of falling (Gerritsen et al., 1998; Haeufle et al., 2010).

The damper-like behavior of the force-velocity relation might be especially crucial to regulate fast locomotion. During fast locomotion, an unexpected step perturbation poses a severe risk of falling as the short stance duration (i.e., the ground-foot contact phase) limits the time the central nervous system has to react. In addition, even the fastest reflexes are subject to neurotransmission delays, and during fast locomotion, they can require up to about half the stance duration before affecting motion (More and Donelan, 2018). Therefore, the central nervous system would struggle to stabilize movement alone. However, when a sudden step perturbation occurs, the velocity at which the foot hits the ground differs from unperturbed conditions. This change propagates within the leg, causing the muscle fibers to contract at altered velocities. The force-velocity relation would resist this by instantly adjusting the muscle fiber force to the perturbed contraction velocity, mitigating the delayed response of the nervous system. Furthermore, such a damping-like response would help dissipate the change in the system's potential energy caused by the step perturbation, thereby reducing the need for active control.

Unfortunately, few studies (Gerritsen et al., 1998; Haeufle et al., 2010) have explicitly tested the ability of the force-velocity relation to act as a mechanical damper during fast perturbed locomotion. Most of the evidence supporting this hypothesis is qualitative, based on analyzing the shape of the force-velocity relation without considering the complex nonlinear dynamics of muscle contraction as a whole. When testing unexpected changes in ground stiffness, it was found that the force-velocity relation alone cannot explain measured muscle-driven regulation (van der Krogt et al., 2009). Instead, it was observed that feedforward neuronal stimulation tunes the force-velocity relation's response to the given perturbation, making preflexes more effective. This suggests that biological locomotion may take advantage of tunable mechanical damping, which could help maximize motion robustness in the face of uncertainties while minimizing energy dissipation on even terrains. Therefore, investigating tunable mechanical damping in legged locomotion is a crucial step for understanding legged locomotion's versatility.

1.2 Research objectives

The overall research objective of this dissertation was to investigate principles of tunable mechanical damping in fast, perturbed legged locomotion. Our central hypothesis was that tunable mechanical damping enhances robustness to unexpected step perturbations, i.e., ground height changes. We focused on the "preflex phase", the early stance duration when sensory feedback is unavailable due to neurotransmission delays. We hypothesized that by embedding tunable mechanical damping, a legged system could instantly generate forces to resist changes in impact velocity without requiring closed-loop control. These forces would adjust the energy dissipated during preflex, regulating the change in potential energy caused by any step perturbation. As a result, we predicted that a tunable mechanical damper would embed sensor-free regulation of the system's energy, promoting increased locomotion robustness. We also predicted that tunable mechanical damping could improve the trade-off between locomotion robustness and the cost of transportation. During steady locomotion, constant mechanical damping would result in unnecessary energy loss, which actuators must restore to maintain periodic locomotion. In contrast, tunable mechanical damping could impact locomotion energy efficiency less by minimizing damping forces and energy dissipation on unperturbed ground.

This doctoral dissertation combines mainly two research methodologies. The first approach relies on computational models to understand tunable mechanical damping in muscle fibers. As mentioned in Section 1.1, contraction experiments with muscle fibers have revealed a force-velocity relation that resembles mechanical viscous damping. Hill-type muscle models capture this property via a phenomenological function that describes the force-velocity relation mathematically. Therefore, we implemented neuro-musculoskeletal simulations incorporating Hill-type muscle models to explore principles of biological tunable damping. A significant benefit of this computational approach is that it permits measuring quantities otherwise difficult to trace in vivo. In addition, it facilitates the detection of muscle preflexes. In simulations, removing the concealing effect of other phenomena, such as reflexes and centrally-driven neuronal strategies, is simple and less resource-intensive than in vivo studies. Notice that the dynamics of muscle fiber contraction are highly nonlinear. This complexity is reflected in the mathematical formulation of Hill-type models, in which the effect of the force-velocity relation is coupled with other mechanisms, such as the force-length relation and fiber stimulation level. Accordingly, a primary objective of our computational research was the design of an algorithm to isolate and quantify the specific contribution of the force-velocity relation to muscle preflexes in simulated fast perturbed locomotion.

The second methodology in this doctoral research involves testing tunable mechanical damping in biorobotic leg prototypes. Analysis of such physical models is an invaluable complementary tool to the computational study of complex biomechanical systems. Hardware tests allow for verifying the numerous assumptions behind the design of computational models. At the same time, they keep the tested physical system more intuitive and tractable than analogous biological organisms. Within this methodology, and focusing on fast perturbed locomotion, our main research objectives were: (1) understanding how to produce effective mechanical damping in a robotic leg and (2) identifying an intuitive strategy for tuning such a mechanical damper.

The combined use of computer simulations and hardware experiments to understand tunable mechanical damping in perturbed legged locomotion could advance research in multiple disciplines. Computational analysis of biological damping could lead to a greater understanding of motion control on a biological level, potentially resulting in predictive models of locomotion impairments caused by muscle disorders. In addition to validating the results of biological simulations, hardware experiments allow extrapolating and optimizing functional principles of tunable mechanical damping for fast perturbed

locomotion. Together, these two methodologies can advance research on motor control and engineering design of legged robotics, potentially leading to new guidelines for motion rehabilitation and wearable assistive technology.

1.3 Doctoral thesis overview

The content of this doctoral thesis is organized as follows. Chapter 2 briefly overviews the five manuscripts (four journal articles and one pre-print) that comprise the research conducted during my doctoral project. Since these manuscripts result from collaborative research with multiple co-authors, my contribution to each investigation is explicitly highlighted in Chapter 2.

Chapter 3 provides a methodological background. The chapter briefly describes the neuro-musculoskeletal system and how its elements cooperate to generate motion. This summary is intended to help understand the complexity of investigating biological motion. It also provides justifications for some of our modeling choices. Following this summary is an explanation of how computational studies and bio-inspired robotics can assist biological investigations. The next section of Chapter 3 describes the specific neuro-musculoskeletal model that was the foundation for our computational research. It follows a description of the specific muscle model implemented. A particular emphasis is given to the force-velocity relation, as this property is hypothesized to generate muscle mechanical damping. Chapter 3 ends by presenting my main methodological contribution to this doctoral project: the decomposition algorithm.

Chapter 4 presents my core computational study on tunable mechanical damping in muscle-driven locomotion. Using a simplified hopping model and the decomposition algorithm, my co-authors and I explored whether the force-velocity relation can produce mechanical damping during the preflex response to step perturbations. We discovered that, without neuronal modulation, the force-velocity relation has a minor effect on the preflex response. In contrast, feedforward stimulation “activates" the damping capacity of the force-velocity relation, indicating that biological mechanical damping exists and is tunable.

Results in Chapter 4 suggest that the flattening profile for large eccentric velocities of the force-velocity relation reduces the force-velocity relation’s capacity to produce mechanical damping during preflexes. For this reason, Chapter 5 presents a study where we extended the experiments of Chapter 4 by testing different initial operative conditions of the force-velocity relation at touchdown. This analysis confirms that hitting the ground with the force-velocity relation operating along its flattening side can reduce the muscle’s damping response to step perturbations.

The computational studies in Chapters 4 and 5 rely on Hill-type muscle models, which are ansatz approximations of the natural muscle contraction dynamics. Chapter 6 presents a study where we tested the limitations introduced by the Hill-type model in our analyses. In this study, we extracted muscle trajectories from simulated hopping under different step perturbations and applied them to real muscle fibers in vitro. Afterward, we compared the response of biological muscle fibers to that predicted by our Hill-type model. We found that biological muscle fibers can generate an activity-dependent damping response to perturbed hopping trajectories. However, our in vitro results suggest that the short-range stiffness, typically neglected in Hill-type models, may be crucial to preflex production. Furthermore, more accurate modeling of the force-velocity relation at high eccentric velocities is needed.

Chapters 7 and 8 describe two projects in which we investigated strategies for achieving tunable mechanical damping in legged robotics. In the first study, we implemented a computer simulation of a

two-segment robotic leg with a spring-damper knee joint and simulated vertical hopping under various step perturbations. With this model, we found that viscous damping outperforms Coulomb friction damping in regulating the mechanical work to the perturbation level. However, when we implemented viscous dampers in a physical prototype and repeated the experiments with a hardware setup, we found that controlling the damping rate was ineffective and unintuitive for producing tunable mechanical damping.

In the second study (Chapter 8) , we overcome this limitation by coupling the viscous damper to the knee joint by a slack-tendon mechanism. The slack-damper mechanism allowed us to produce tunable mechanical damping intuitively, as the slackness level correlated to the amount of damped energy. In this study, we also confirmed the hypothesis that a trade-off between the cost of transport and locomotion robustness occurs when implementing tunable mechanical damping in a robotic leg. In this regard, the tunability of our slack-damper mechanism and its perturbation-triggered nature could promote a more favorable trade-off.

This thesis dissertation concludes with Chapter 9, which provides a detailed summary of the presented studies and a general discussion. Here, I discuss our key findings on tunable mechanical damping in fast perturbed locomotion from the perspective of muscle-driven locomotion and biorobotic implementation. The chapter ends with a list of take-home messages.

2 List of publications

During my doctoral research, I had the privilege of collaborating with multiple colleagues. Our collective effort resulted in a collection of manuscripts, the majority of which published in peer-reviewed scientific journals. As much of this thesis draws from previously published material, this chapter highlights my contribution to each work. All co-authors have agreed to the following list.

2.1 Accepted publications

2.1.1 Manuscript 1 - Izzi et al. (2023), Chapter 4

Title:	Muscle prestimulation tunes velocity preflex in simulated perturbed hopping
Authors:	Fabio Izzi, An Mo, Syn Schmitt, Alexander Badri-Spröwitz , and Daniel F.B. Haeufle
Journal:	Scientific Reports
Year:	2023
Link:	https://doi.org/10.1038/s41598-023-31179-6
Summary:	We isolated and quantified the preflex force produced by the force-velocity relation in neuro-musculoskeletal simulations of perturbed vertical hopping. We compared two stimulation protocols and tested whether muscle fibers' mechanical damping requires neuronal modulation. Preflex-Const prevented neuronal modulation, while Preflex-Rising allowed feedforward stimulation of the muscle fibers during preflexes. Using our decomposition algorithm (see section 3.5), we found that the force-velocity relation can generate a "velocity preflex" to regulate unexpected changes in ground height. However, this regulatory capacity is minimal without neuronal modulation. Simple feedforward stimulation was sufficient for scaling the force-velocity relation's contribution and producing a more effective velocity preflex.
Contribution:	I conceptualized the project under the supervision of Daniel Haeufle and Alexander Badri-Spröwitz. I designed and implemented the computer simulation. Along with Daniel Haeufle, I developed the decomposition algorithm. I conducted all simulations, data analysis, and interpretation. I prepared the figures with the help of An Mo. I wrote most of the manuscript and all of the supplementary electronic material. I organized manuscript submission and answers to reviews' feedback, as well as regular project meetings, discussions with co-authors, and project planning.

2.1.2 Manuscript 2 - Araz et al. (2023), Chapter 6

Title:	Muscle preflex response to perturbations in locomotion: In vitro experiments and simulations with realistic boundary conditions
Authors:	Matthew Araz, Sven Weidner, Fabio Izzi, Alexander Badri-Spröwitz, Tobias Siebert and Daniel F.B. Haeufle
Journal:	Frontiers in Bioengineering and Biotechnology, section Biomechanics
Year:	2023
Link:	https://doi.org/10.3389/fbioe.2023.1150170
Summary:	We measured the mechanical work and force modulation generated by muscle fibers during the preflex phase of in vitro contraction experiments. Our experiments used physiologically plausible stretching trajectories derived from simulated vertical hopping under different ground perturbations. We also compared muscle fiber contraction response in vitro to predictions from a Hill-type muscle model. Our findings confirm activity-dependent stiffness and damping in biological muscle fibers. The activity-dependent damping could regulate muscle fiber force to perturbed stretching velocity. However, the amount of fiber elongation was responsible for most of the energy regulation during preflexes. We also conclude that Hill-type models require short-range stifness and better modelling of the force-velocity relation's eccentric side for more accurate predictions.
Contribution:	I helped conceptualize the study and provided feedback on the methodology. I helped Matthew Araz conduct the simulations. I contributed to the data interpretation and discussion. I wrote the introduction with Matthew Araz, and I helped edit the rest of the manuscript. I wrote the table of model parameters in the electronic supplementary material. I participated in project meetings, discussions with co-authors, and project planning.

2.1.3 Manuscript 3 - Mo et al. (2020), Chapter 7

Title:	Effective viscous damping enables morphological computation in legged locomotion
Authors:	An Mo, Fabio Izzi, Daniel F.B. Haeufle and Alexander Badri-Spröwitz
Journal:	Frontiers in Robotics and AI, section Soft Robotics
Year:	2020
Link:	https://doi.org/10.3389/frobt.2020.00110

Summary:	We investigated tunable mechanical damping in legged robotics. We implemented numerical simulations and hardware experiments involving drop tests of a two-segment leg with a knee spring-damper device. We studied the system's response to step perturbations of various intensities. The numerical analysis revealed that viscous damping regulates the dissipated energy to the perturbation level more effectively than Coulomb friction damping. However, our hardware experiments demonstrated that damping rate control of viscous dampers directly coupled to the knee joint has negligible and unintuitive effects on energy regulation. We conclude that this is an ineffective strategy for implementing tunable mechanical damping in legged robotics.
Contribution:	Along with Daniel Haeufle, I conceptualized the simulation part of the project. I helped code and implement the computer model. I conducted the simulations, associated data analysis, and interpretation. I provided feedback on the hardware part of the study and helped interpret/validate results from hardware experiments. I prepared the figures related to the numerical simulations. I wrote the simulation part of the manuscript and helped write/edit the rest. I contributed to answering reviewers' feedback. I participated in regular project meetings, discussions with co-authors, and project planning.

2.1.4 Manuscript 4 - Mo et al. (2023), Chapter 8

Title:	Slack-based tunable damping leads to a trade-off between robustness and efficiency in legged locomotion
Authors:	An Mo, Fabio Izzi, Emre Cemal Gönen, Daniel F.B. Haeufle and Alexander Badri-Spröwitz
Journal:	Scientific Reports
Year:	2023
Link:	https://doi.org/10.1038/s41598-023-30318-3
Summary:	We designed a slack-damper mechanism to generate tunable viscous damping in a robotic leg that can hop vertically and forward over various terrains and ground obstacles. The slack-damper mechanism consists of a mechanical damper connected to the knee joint by a cable with adjustable slackness. We found that controlling the slackness level permits modulating the damping force, onset time, effective stroke, and energy dissipation of the slack-damper. Furthermore, our hardware experiments confirm that mechanical damping enhances locomotion robustness at the expense of energy efficiency. We conclude that the perturbation-triggered nature of our slack-damper could promote a more favorable trade-off.
Contribution:	I contributed to conceptualizing and conducting the analysis and interpretation of data. I helped code the scripts for data analysis and provided feedback on the methodology. I helped with data validation and curation. I contributed to writing/editing the original draft. I participated in regular project meetings, discussions with co-authors, and project planning.

2.2 Pre-print

2.2.1 Manuscript 5 - Izzi et al. (2022), Chapter 5

Title:	Muscle pre-stimulation tunes viscous-like perturbation rejection in legged hopping
Authors:	Fabio Izzi, An Mo, Syn Schmitt, Alexander Badri-Spröwitz , and Daniel F.B. Haeufle
Archive:	ArXiv
Year:	2022
Link:	https://doi.org/10.48550/arXiv.2202.02114
Summary:	This study extends the work done in Izzi et al. (2023). Using the same neuro-musculoskeletal hopping model and Preflex-Const stimulation, we tested the influence of the force-velocity relation's operative side in producing preflex regulation. We hypothesized that the force-velocity relation contributes less to preflex regulation when its touchdown state is on the plateau-side during reference hopping. Our analysis confirms our hypothesis for touchdown force and preflex work but not for hopping stability. We conclude that mechanical damping in muscle fibers is sensitive to reference hopping conditions.
Contribution:	I conceptualized the project under the supervision of Daniel Haeufle and Alexander Badri-Spröwitz. I designed and implemented the computer model. I conducted all simulations, data analysis, and interpretation. I prepared the figures with the help of An Mo. I wrote most of the manuscript. I organized manuscript submission, regular project meetings, discussions with co-authors, and project planning.

3 Methodological background

This chapter provides background knowledge. The chapter begins by describing the neuro-musculoskeletal system and how motion results from the coordinated activity of its many components. This description is intended to illustrate the complexity of studying the neuro-musculoskeletal system and to justify some of our modeling assumptions. It follows a concise explanation of how computational studies and bio-inspired robotics can facilitate biological investigations. The chapter continues by describing the neuro-musculoskeletal model that was the foundation for this thesis's computational research. The following section describes the muscle model used in our simulations. A detailed overview of the force-velocity relation is provided, as well as an intuitive explanation of how it may benefit fast perturbed locomotion. The chapter concludes by presenting the decomposition algorithm, the primary methodological contribution of this doctoral dissertation.

3.1 The neuro-musculoskeletal system

The biological entity that enables movement in vertebrate animals is known as the neuro-musculoskeletal system. Conceptually, it contains four main elements: the skeletal system, muscles, sensors, and the central nervous system. The following summaries are based on the reader by van der Kooij et al. (2008).

3.1.1 The skeletal system

The skeletal system, which forms the passive anatomical structure of a vertebrate organism, consists of a network of interconnected bones linked together through connective tissues and ligaments, forming joints. Joints constrain bones' relative motion. Fibrous joints tend to be immovable, cartilaginous joints exhibit a certain degree of mobility, and synovial joints tend to be freely movable along specific directions.

Technically, joints limit without fully constraining bones' relative displacement. This is because soft connective tissue and a certain degree of bone deformation during joint loading allow slight displacement along the restrained directions. In synovial joints, however, such movement is generally insignificant in relation to the joint's functional range of motion. Hence, it is standard to describe the skeletal system as a network of interconnected rigid bodies, with synovial joints forming mechanical connections that fully constrain bones' displacement along specific directions.

The neuro-musculoskeletal models in this dissertation focus on the knee joint, a synovial joint that allows angular movement between the upper (femur) and lower leg (tibia and fibula). As such, the knee joint is usually modeled as a hinge joint, as also done in this dissertation.

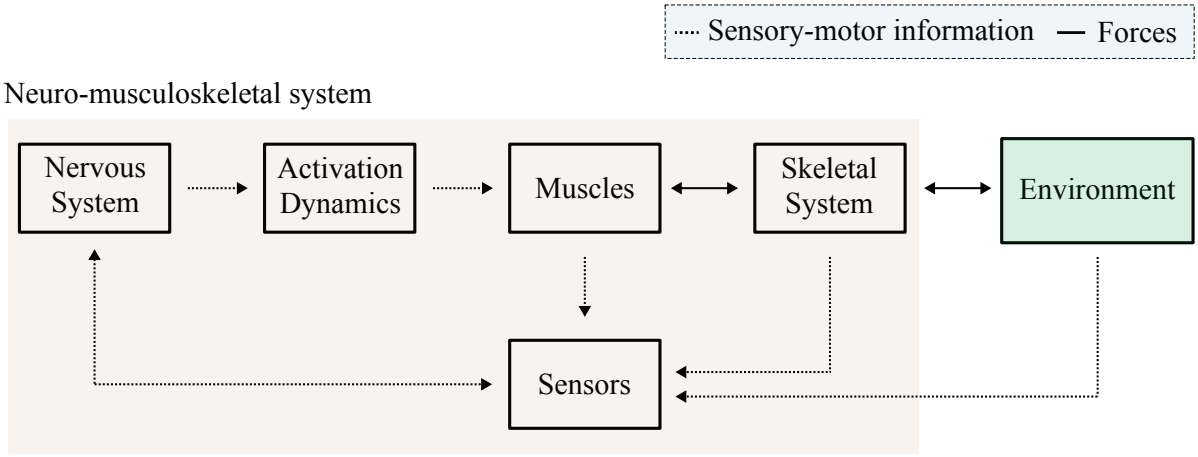

Figure 3.1: Simplified illustration of the interplay between the neuro-musculoskeletal system's elements. The nervous system sends motor command to muscles, filtered by the activation dynamics. Muscles exchange forces with the skeletal system, which in turn exchanges forces with the environment. Sensory organs collect information from the environment and body. This information is sent to the nervous system and used to update the command signals to the muscles. The double-sided arrow between the nervous system and the sensory organs indicates the nervous system's capacity to control these organs' sensitivity. Note that noise and time delays affect sensory-motor information transmission.

3.1.2 Muscles

There are three types of muscles. Cardiac muscles are found in the heart and are responsible for the blood circulation. Smooth muscles enable the flow of substances in hollow organs and are not consciously controlled. Skeletal muscles, the only type considered in this dissertation research, span across bones and are the actuators of the neuro-musculoskeletal system. They convert neural signals from the nerves into contraction forces. These forces exert motion on the bones via tendons. Thus, it is typical to refer to "muscle-tendon units" when describing skeletal muscles. For the sake of clarity, I will refer to skeletal muscles as "muscles" or "muscle-tendon units" in the following of this thesis.

Muscle architecture is complex. The smallest functional unit is the sarcomere, consisting of a bundle of threadlike structures called myofilaments. Myofilaments are of two types: thin filaments (actin) and thick filaments (myosin). The sliding of the myosin past the actin generates the sarcomere contraction, contributing to the net muscle contraction. A muscle fiber consists of a series of multiple sarcomeres. Several muscle fibers wrapped in bundles by layers of connective tissue form the entire muscle. This complex architecture grants muscles nonlinear viscoelastic properties and complex contraction dynamics.

There are three main approaches for modeling muscle contraction dynamics (Winters and Stark, 1987). The first approach employs second-order systems to approximate muscle-joint dynamics in a black-box manner, which offers a simple yet very approximated solution to muscle modeling. The second approach implements structural models based on phenomenological studies of isolated muscle tissues, known as Hill-type models, after the pioneering research of Archibald Hill (1938). Despite well-known approximations, Hill-type models offer a good compromise between prediction accuracy and computational cost. This characteristic makes them often preferred for neuro-musculoskeletal models, which are already computationally expensive due to the large number of subsystems they include. The third approach describes muscle dynamics by modeling the contractile sliding mechanism between

actin and myosin on a biophysical level. These biophysical models, known as Huxley models from the work of Andrew Huxley (1957), result in complex mathematical formulations that are computationally expensive and require numerous parameters. For this reason and in agreement with previous studies (Gerritsen et al., 1998; Haeufle et al., 2010; van der Krogt et al., 2009), the computational biomechanics research in this dissertation relied on a Hill-type formulation, described in section 3.4.

3.1.3 Sensors

Sensors are all those organs providing information to the central nervous system via nerve connections. Sensors can be classified into three main functional categories: homeostatic sensors, interoreceptors, and exteroreceptors. Homeostatic sensors provide information about the body's internal state, helping control internal body functions. Interoreceptors and exteroreceptors are more explicitly involved in locomotion. Interoreceptors provide information about the body's posture and movement. Examples of interoreceptors are the vestibular organ (sensing head orientation), joint receptors (sensing when joint motion reaches its boundaries), muscle spindles (sensing the length and velocity of the muscle fibers), and Golgi tendon organs (sensing the force transmitted via the muscle tendon). Exteroreceptors provide information about the environment (vision, hearing, tactile sense, taste, and smell).

Transmission of sensory information is not instantaneous and is subject to noise and delays (More and Donelan, 2018). This feature is a crucial rationale for this dissertation, which aims to understand the stabilizing role of tunable mechanical damping in fast perturbed legged locomotion prior to sensory-based corrections. This interest in a mechanical response to ground perturbations motivates the lack of sensor dynamics and sensor-based control in the biomechanical models and hardware implementations discussed in this thesis.

3.1.4 The nervous system

The nervous system consists of two main parts: the central and the peripheral nervous systems. The central nervous system (CNS) comprises the brain and the spinal cord, responsible for elaborating and coordinating neuronal information. The peripheral nervous system (PNS) is the network of neurons that connect the central nervous system to muscles and sensors.

Despite this division, the neuron serves as the functional unit of the entire nervous system. A neuron consists of dendrites, axons, and synapses. Dendrites are the sites where neurons receive information from other neurons or sensors. Axons are the shafts along which neuron information propagates. Synapses are the sites where electrical nerve impulses are exchanged.

A neuron that propagates information between two or more neurons is known as an interneuron. Interneurons' function is to elaborate information and generate command signals. Thus, interneourons form the central nervous system. On the contrary, the peripheral nervous system consists of efferent and afferent neurons. Efferent neurons send information from the central nervous system to muscles, while afferent neurons send information from sensors to the central nervous system.

The nervous system can control locomotion through feedback and feedforward control. Feedback control relies on sensory information to correct desired movement trajectories online. Feedforward control relies on internal models of the body-environment interaction to make predictions and plan motion commands in advance. Given the emphasis on sensor-free locomotion regulation, the research in this dissertation excludes feedback control, allowing only feedforward control to influence leg dynamics.

3.2 Motion control by neuro-musculoskeletal system

How the different elements in the neuro-musculoskeletal system collaborate to produce motion is complex, but it can be conceptually summarized as follows. The central nervous system selects target joint trajectories when planning a desired movement. Joint coordination occurs because the central nervous system converts these target trajectories into stimulation signals for the muscles. Once stimulated, muscles move the body by exerting forces on the skeletal system. Meanwhile, the central nervous system processes sensory information to update muscle stimulation (or target trajectories) based on the body's current state and environmental conditions. Figure 3.1 provides a visual intuition of such complex interplay.

The neuro-musculoskeletal system operates using a combination of feedforward and feedback control. The conversion of joint trajectories into muscle stimulation uses feedforward control, which also helps compensate for time delays and noise affecting neuro-transmission. Correction of feedforward signals based on the current state of the body-environment dynamics uses feedback control.

From an engineering perspective, the neuro-musculoskeletal system is a multi-input-multi-output system with time-dependent nonlinear dynamics. This type of system is very challenging to investigate. Furthermore, we can make limited direct measurements when the neuro-musculoskeletal system operates in vivo. We can mainly record outside-body variables, such as body kinematics and forces exchanged with the environment, and a few internal variables, such as brain or muscle electrical signals. This limitation in sensing technology makes it even more challenging to unveil the mechanisms behind the functionality of the neuro-musculoskeletal system. Among the methodologies to overcome these problems and study the neuro-musculoskeletal system are the use of computational models and bio-inspired robots.

3.2.1 Computational motor control

Computational motor control employs mathematical models and computer simulations of the neuro-musculoskeletal system to test hypotheses about biological motion. These digital models provide an experimental framework where unlimited variables can be measured and manipulated to assess their influence on motion control. Similar access and control over the system's variables are unattainable with in vivo experiments due to technological constraints and ethical implications. Notice, however, that computer simulations only approximate reality; validation of the simulated results is crucial.

Computer models of the neuro-musculoskeletal system also permit predictive analyses. Conceptually, one could use simulations to predict and optimize the performance of a rehabilitation protocol in restoring mobility. Similarly, one could simulate the interaction between an assistive device and the neuro-musculoskeletal system to determine an optimal design. Although these simulations would include inherent approximations, their outcomes could provide a valuable starting point for the prototyping of these technologies.

An example of these concepts is the research of Stollenmaier et al. (2020b), to which I contributed during my doctoral project. Notice that, despite my contribution, this manuscript is not part of this dissertation due to its significantly different research objective. In this study, we used a biomechanical model to simulate goal-directed arm movements in individuals with ataxia, a neurological disorder causing overshooting in motion trajectories. The arm model was initially developed in Stollenmaier et al. (2020a). We hypothesized that ataxia occurs when abnormal co-contraction levels affect the patient's initial arm posture. We simulated this hypothesis in the arm model and found it was sufficient

to replicate the joint trajectories of ataxia patients (see Figure 3 in Stollenmaier et al. (2020b)). After successfully replicating ataxia-like overshooting, we simulated the interaction between the arm model and a wearable device to correct the motion impairment using minimalistic assistive strategies. We found different approaches possible; however, our results underscore the importance of including muscle dynamics for correctly prototyping the assistive device. Therefore, the neuro-musculoskeletal simulations in Stollenmaier et al. (2020b) provided not only initial evidence for mechanisms explaining ataxia overshooting, but also guidelines for prototyping potential corrective technology.

In the literature, other studies exist that use neuro-musculoskeletal models to explain impaired movement generation (e.g., Bhanpuri et al. (2014), Mugge et al. (2012), Lassmann et al. (2023) and Song and Geyer (2018)) and predict the response to wearable assistive devices (e.g., Petrič et al. (2019) and Zhang et al. (2021)). These investigations, together with simulation studies on the neuro-biomechanics of healthy motion (e.g., Geyer and Herr (2010), Bunz et al. (2023), Haeufle et al. (2018), Schreff et al. (2022) and Dzeladini et al. (2014)), offer a digital environment to form initial hypotheses about how the neuro-musculoskeletal system operates.

3.2.2 Bio-inspired robotics

Bio-inspired robotics uses robots as physical models to investigate biological hypotheses (Iida and Ijspeert, 2016). As it should be evident from section 3.2, studying the neuro-musculoskeletal system demands both system-level analysis and exploring the individual functionality of its components. This practice is typical of robotic research, which requires individual design and system-level integration of numerous mechatronics components. Therefore, building bio-inspired robots offers a natural approach to investigating biological locomotion (Ijspeert, 2014).

As physical models, robots offer a good compromise between experimental accessibility and validity. Measuring, controlling, and reproducing tests with a robot is more accessible than during animal experiments. Furthermore, robotic components can be designed and replaced individually, permitting systematic analysis and even experimentations with hazardous conditions (Ijspeert, 2014). Simultaneously, robots are physical entities and thus obey the laws of physics (Nishikawa et al., 2007). Consequently, physical phenomena that are difficult to simulate, such as friction, hydrodynamics, and collisions, occur naturally and without approximations during robot experiments.

Designing bio-inspired robots to use as physical models requires accurately targeting the biological mechanisms to test. This task is challenging as the neuro-musculoskeletal system is complex, highly redundant, and performs multiple tasks simultaneously. An overly complicated robot design would conceal the fundamental physics driving biological motion, thus compromising the investigation. Strategies such as "templates and anchors modeling" have been proposed to facilitate targeting the proper robot design (Full and Koditschek, 1999). However, the proper level of abstraction in bio-inspired robotic research is still a matter of debate and requires accurate contextualization (Webb, 2001).

Several bio-inspired robots have been designed to understand legged locomotion. For example, Spröwitz et al. (2013) developed a cheetah cub robot to investigate the benefits of pantographic-compliant limbs in quadrupedal locomotion. Their design could produce robust dynamic gaits without sensory feedback, indicating that body morphology plays an important role in motion robustness. Similar studies have investigated the importance of passive dynamics (Collins et al., 2001; McGeer, 1990), tendon compliance (Berkemeier and Desai, 1996), interlimb coordination (Crespi et al., 2013; Owaki et al., 2013), and locomotion control (Manoonpong et al., 2007; Pfeifer et al., 1998). For more comprehensive reviews, refer to these sources: Ijspeert (2014), Zhou and Bi (2012), and Webb (2001).

Another significant advantage of bio-inspired robots is that they lead to the development of unconventional technology (Iida and Ijspeert, 2016). An example is serial elastic actuation, inspired by muscle compliance in biological movement and now used in various engineering applications (Lee et al., 2013). Even unsuccessful attempts to replicate target biological capacities can help form new assumptions about how the neuro-musculoskeletal system operates (Nishikawa et al., 2007).

It is worth noting that bio-inspired robotic research does not eliminate the need for simulation studies or biological experiments. Instead, it offers a complementary experimental platform. For example, Kalveram and Seyfarth (2009) proposed the concept of a "test trilogy". In this methodological framework, the authors propose bio-robotic experiments as critical tools for validating simulation models against real-world physics. Functioning as "reality checkers", tests with robots can help justify behavioral comparisons between simulated and observed biological data.

3.3 Hopping model

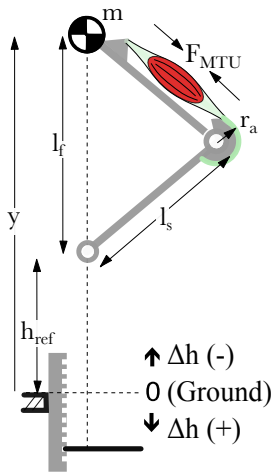

Figure 3.2: Biomechanical model used for simulating muscle-driven vertical hopping in Chapters 4 to 6. Figure extracted from Figure 1**b** in Izzi et al. (2023).

The computational research in this dissertation implements simulations of a two-segment leg performing vertical hopping. In Chapters 4 to 6, the vertical hopper is driven by a muscle-tendon unit, with the model parameters based on human anatomy (according to Geyer et al. (2003)). Chapter 7 implements a simplified version of the model, where knee actuation is reduced to a spring and damper in parallel. In this simplified version, model parameters were chosen to match the robotic leg tested in the same chapter.

The current section describes the muscle-driven vertical hopper, as illustrated in Figure 3.2– for details about its simplified version or the robotic hardware, refer to Chapters 7 and 8. The biomechanical structure of the muscle-driven model was developed in Geyer et al. (2003). It consists of a two-segment leg with motion constrained to the vertical direction, allowing only a single degree of freedom, the knee rotation. Each leg segment is equal to $l_s = 0.5\,\text{m}$. The model's mass is lumped at the hip and equal to $m = 80\,\text{kg}$.

A knee extensor muscle drives the model vertical hopping with an extending torque (T) equal to:

$$T = r_a F_{MTU}$$

where r_a is the lever arm at the knee joint, and F_{MTU} is the force produced by the muscle-tendon unit. For our studies, we used the muscle-tendon architecture developed in Haeufle et al. (2014b), with activation dynamics from Hatze (1977); Rockenfeller et al. (2015). A more detailed description of these models can be found in the next sections (section 3.4 and section 3.4.5, respectively). The knee extensor muscle acts on the knee joint only during the stance phase, which is the hopping phase with ground-foot contact. Outside the stance phase, the leg geometry is fixed, with knee angle corresponding to a leg length $l_f = 0.99\,\text{m}$. Tables 4.1, A1.1 and A2.1 contain the comprehensive lists of model parameters used for implementing the hopping model in Chapters 4 to 6.

Given a specific muscle setting and stimulation, the model performs vertical hopping. We defined h_{ref} as the reference hopping height, i.e., the initial drop height resulting in the same apex height by the end of one hopping cycle. We simulated fast perturbed locomotion by applying small step perturbations (Δh) to the reference hopping height for chosen model settings. A step-down perturbation (Δh (+)) comported an increment in the initial drop height, while a step-up perturbation (Δh (-)) a reduction. The hopping motion is asymptotically stable if the change in drop height produced by a step perturbation tends to zero over the following hopping cycles. The hopping is stable, but not asymptotically, if the change remains constant. Finally, the hopping is unstable if the change increases over time.

Vertical hopping simplifies fast perturbed locomotion by constraining the dynamics to a single dimension, the vertical axis. Despite being an approximation, this modeling choice facilitates the analysis by reducing the number of redundant solutions for rejecting step perturbations. For example, in planar hopping, hip-torque strategies can assist hopping stabilization by adjusting leg orientation (Shen and Seipel, 2012). In our model, only the knee torque can regulate leg motion, thereby centering the analysis on the functional role of the embedded tunable mechanical damping. While this simplification facilitates our analysis, it also emphasizes the function of knee damping. Therefore, omitting concurrent regulatory strategies in other joints likely influences our investigations. Limiting our research to the knee joint was motivated by consistent evidence of its crucial role as an absorber of negative work in downslope walking (Alexander et al., 2017; Lay et al., 2007; Montgomery and Grabowski, 2018), acceleration and deceleration (Qiao and Jindrich, 2016), and landing from different heights (Zhang et al., 2000). Nevertheless, future work should extend our studies to more comprehensive biomechanical structures to understand the generalizability of our findings.

3.4 Muscle model

Haeufle et al. (2014a) created the Hill-type muscle model used in this dissertation's computational studies. As illustrated in Figure 3.3a, the model consists of four elements: a contractile element (CE), a parallel elastic element (PEE), a serial elastic element (SEE), and a serial damper element (SDE). The geometry of the muscle-tendon unit (MTU) is such that the CE and PEE operate in parallel against the parallel SEE and SDE. Therefore, the force equilibrium in the muscle-tendon unit is:

$$F_{MTU} = F_{CE} + F_{PEE} = F_{SEE} + F_{SDE} \tag{3.1}$$

Due to the model geometry, if l_{MTU} represents the muscle-tendon unit length, the following equivalences

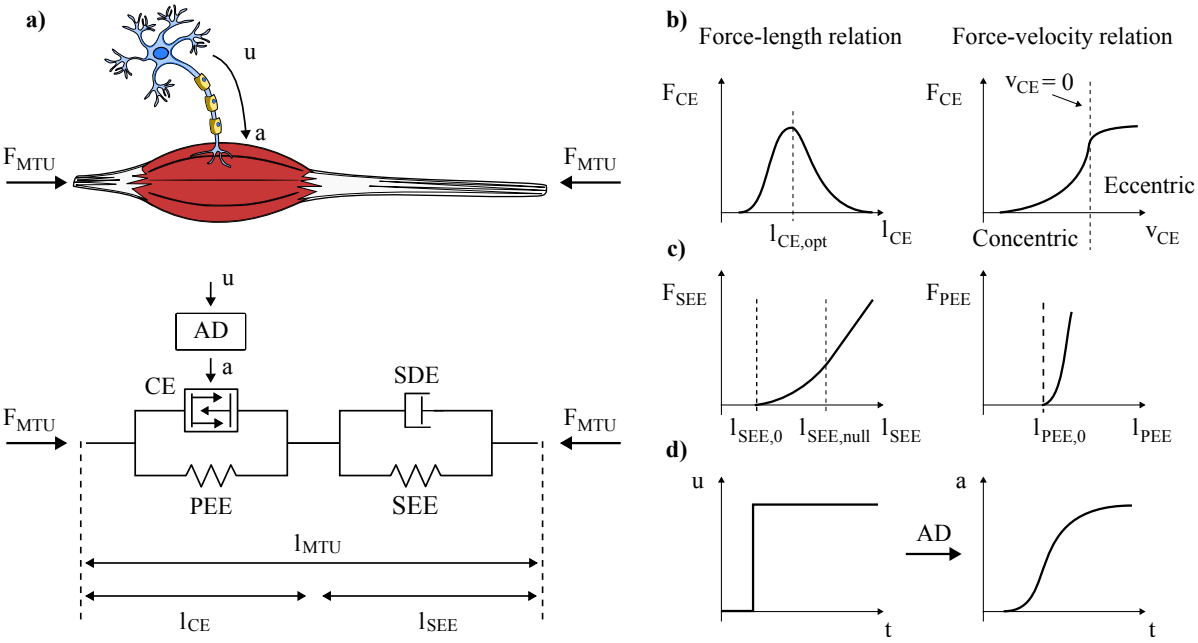

Figure 3.3: The muscle model implemented in this dissertation. **a)** Muscle-tendon unit and associated motor neuron (top) and corresponding architecture of the Hill-type model (bottom). AD stands for Activation Dynamics and converts the neuronal stimulus u into muscle activity level a. **b)** Sketches of the force-length and force-velocity relations characterizing the contractile element (CE). **c)** Sketches of the force-length profiles characterizing the serial elastic element (SEE) and parallel elastic element (PEE). **d)** Example of how the activation dynamics convert a step stimulus u into a smooth rise of muscle activation level a.

also hold:

$$\begin{aligned} l_{CE} &= l_{PEE} \\ l_{SEE} &= l_{SDE} \\ l_{MTU} &= l_{CE} + l_{SEE} \end{aligned} \tag{3.2}$$

where l_i is the length of the i-th element in the muscle model. Identical equations characterize the relationship between the elements' velocities ($\dot{l}_i$). Therefore, the muscle model relies on an internal equilibrium between the parallel dynamics of the contractile and parallel elastic elements and those of the serial elastic and damper elements. The following provides a brief overview of how the model describes the dynamics of each element. The explicit formulation of the various parameters in the model is superfluous for understanding their overall function, and therefore it will be omitted. For more information, refer to Günther et al. (2007); Haeufle et al. (2014a).

3.4.1 Contractile element (CE)

The contractile element captures the collective contraction of the active fibers in a biological muscle. According to Hill-type experiments, the force produced by the contractile element exhibits force-length

and force-velocity relations. The force-length relation is modeled as follows:

$$F_{isom}\left(l_{CE}\right) = \exp\left\{-\left|\frac{l_{CE}/l_{CE,opt} - 1}{\Delta W_{limb}}\right|^{\nu_{CE,limb}}\right\} \tag{3.3}$$

Equation (3.3) describes a bell curve with two limbs, one ascending ($l_{CE} \leq l_{CE,opt}$) and one descending ($l_{CE} > l_{CE,opt}$). ΔW_{limb} and $\nu_{CE,limb}$ are constant parameters that characterize the bell curve's width and exponent for each limb, respectively. $l_{CE,opt}$ is a constant parameter that describes the muscle fiber length for which the isometric force of the muscle fibers (F_{isom}) is maximal. Therefore, F_{isom} is a function of only one state of the muscle-tendon unit, l_{CE}.

To account for the force-velocity relation and activity dependence of the muscle fiber force, the formulation of F_{isom} is extended as follows:

$$F_{CE,k}\left(l_{CE}, \dot{l}_{CE}, a\right) = F_{\max}\left(\frac{a\,F_{isom} + A_{rel,k}}{1 - \frac{\dot{l}_{CE}}{B_{rel,k}\,l_{CE,opt}}} - A_{rel,k}\right) \tag{3.4}$$

where k indicates parameters whose formulation depends on whether muscle fiber velocity is concentric ($\dot{l}_{CE} < 0$) or eccentric ($\dot{l}_{CE} > 0$). According to eq. (3.4), $F_{CE,k}$ is a function of three state variables: muscle fiber length (l_{CE}), velocity ($\dot{l}_{CE}$) and activation level (a). With respect to $\dot{l}_{CE}$, eq. (3.4) describes a hyperbola that characterizes the force-velocity relation; $A_{rel,k}$ and $B_{rel,k}$ set the hyperbola axes. During concentric contraction ($k = c$), $F_{CE,c}$ reduces with larger concentric velocities, while $F_{CE,e}$ increases with larger eccentric velocities during eccentric contraction ($k = e$). With respect to a, $F_{CE,k}$ increases as muscle fibers are more excited and reduces otherwise. Equation (3.4) also implies that a scales the curve of the force-velocity relation. Finally, F_{max} represents the max isometric force produced by the muscle fibers. This parameter serves to denormalize and scale eq. (3.4), allowing to simulate muscles of different sizes and actuation capacities. Figure 3.3b illustrates the force-length and force-velocity relations characterizing CE contraction dynamics.

3.4.1.1 The force-velocity relation

The force-velocity relation is a fundamental mechanical property of muscle physiology. It describes a phenomenological dependence between muscle force and muscle contraction velocity. According to Alcazar et al. (2019), the first mention of this property dates back to 1922, when Archibald Hill (1922) observed that the force exerted by human muscles during in vivo experiments is greatest the slower the motion.

Since then, numerous experiments with active shortening and lengthening of muscles (or muscle fibers) have been conducted to determine the force-velocity relation's shape (Alcazar et al., 2019). A classic experimental protocol is the quick-release experiment (Haeufle et al., 2012b), where a muscle is fixed at a desired length (usually the optimal length of isometric contraction) and fully activated. After the initial contraction stabilizes, one muscle end is quickly released against a predefined resistance, usually an attached mass. This process is repeated with multiple loads, resulting in different contraction velocities. The force-velocity relation is eventually computed by fitting a mathematical function to the measured force-velocity data pairs.

While it's widely accepted that the shape of the force-velocity relation is nonlinear, the exact formulation for the fitting function remains a topic of debate (Alcazar et al., 2019). A typical strategy

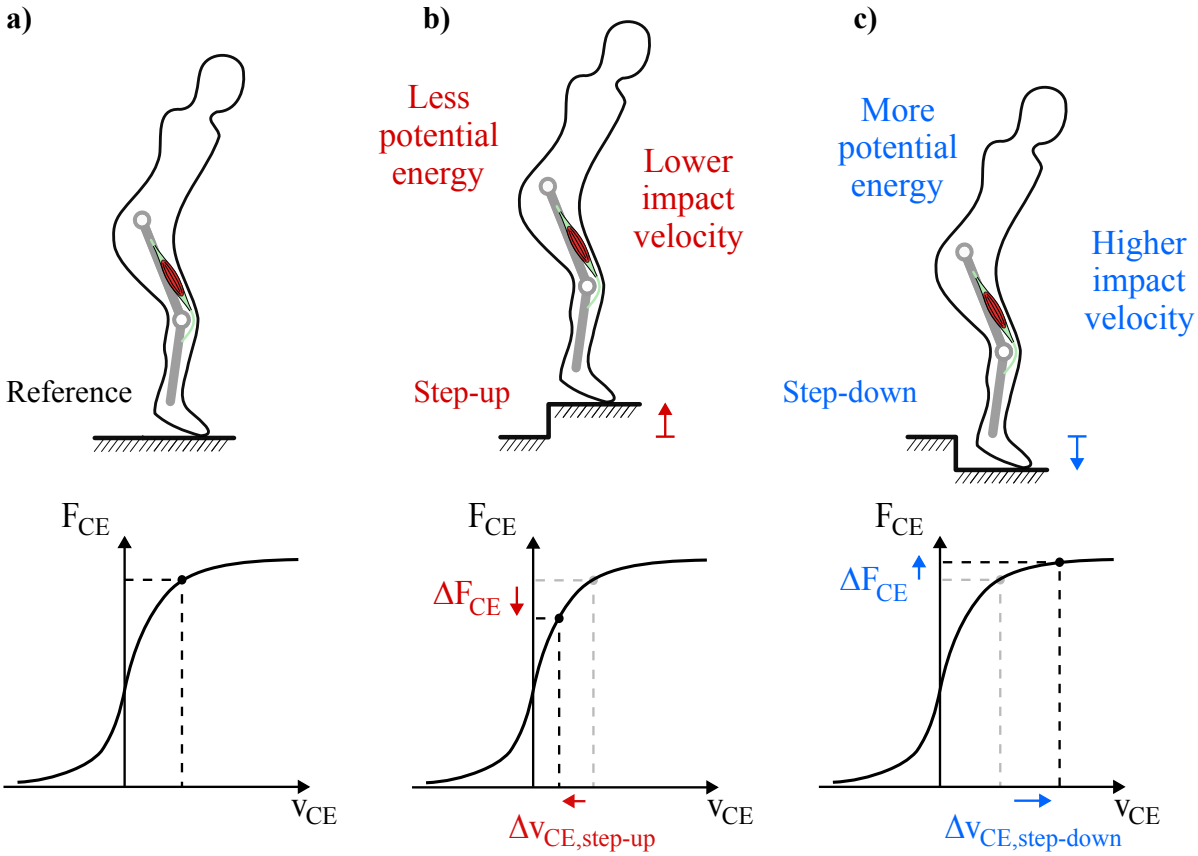

Figure 3.4: The expected contribution of the force-velocity relation during fast perturbed locomotion. **a)** Reference unperturbed hopping, occurring with an initial $\{F_{CE}, v_{CE}\}$ state. **b)** Step-up perturbation, causing lower impact velocity at touchdown and a reduction in the system's potential energy. The slower impact velocity comports a reduction in the extensor's eccentric velocity at touchdown ($\Delta v_{CE,step\text{-}up}$), with the consequent reduction in muscle fiber force due to the force-velocity relation. This force reduction should diminish muscle energy dissipation during knee flexion, counteracting the effect of the step-up perturbation on the system's potential energy. **c)** Step-down perturbation, representing the inverse scenario to the step-up perturbation.

involves modeling the force-velocity relation with hyperbolic functions, separating it into eccentric and concentric portions.

The concentric portion involves muscle fiber velocities that produce shortening contraction. In this part of the force-velocity relation, the muscle fiber force decreases as the shortening velocity increases. In his seminal study, Hill (1938) found that a rectangular hyperbola could fit the curvilinear distribution of force-velocity data that characterizes shortening contraction experiments. Although later studies demonstrated that Hill's regression loses accuracy at very slow and very fast concentric velocities (Claflin and Faulkner, 1985; Edman and Hwang, 1977; Edman et al., 1976; Julian et al., 1986), single-hyperbolic fitting is still frequently used in Hill-type muscle models due to its good correlation with experimental data (Alcazar et al., 2019). For example, the muscle model implemented in this dissertation (Haeufle et al., 2014b) uses such a hyperbolic fitting.

The eccentric portion of the force-velocity relation involves lengthening muscle contractions. Contrary to shortening contractions, faster lengthening velocities increase the force a muscle can produce. This

can lead to force increments up to 1.8 times the maximum voluntary isometric force, as reported in Hahn (2018).

The eccentric portion of the force-velocity relation has been studied less than the concentric part. As reviewed in Alcazar et al. (2019), it is generally accepted that its shape is concave, with most force augmentation occurring at low eccentric velocities (i.e., v_{CE} close to zero). At moderate to high eccentric velocities, the force augmentation levels off, resulting in a flattening profile of the force-velocity relation (Krylow and Sandercock, 1997; Lännergren, 1978; Stienen et al., 1992). The results in Rijkelijkhuizen et al. (2003) even suggest a potential decrease from maximal eccentric force when lengthening velocities are sufficiently high. This evidence suggests that the force regulation by the eccentric side of the force-velocity relation may become less effective for very fast lengthening contractions.

While the exact shape of the eccentric part of the force-velocity relation remains uncertain, muscles must certainly dissipate mechanical energy during eccentric contractions. This is because muscles are unidirectional actuators, capable of only exerting pulling forces. In a lengthening contraction, muscle force and contraction velocity have opposite directions, generating negative mechanical power. Consequently, the eccentric portion of the force-velocity relation could embed muscles with mechanical viscous damping capacities. This feature would be useful against external disturbances.

Figure 3.4 offers an insight into how the force-velocity relation could aid in rejecting step perturbations during hopping. In this example, an extensor muscle drives the hopping model, with reference hopping occurring at an initial $\{F_{CE}, v_{CE}\}$ state. The knee flexion following touchdown leads to muscle lengthening at a certain eccentric velocity. Let us now assume that a step-up perturbation occurs during the initial flight phase. In this scenario, the reduction in drop height would diminish both ground impact velocity and the hopper's potential energy. The diminished impact velocity would produce a slower initial knee flexion, resulting in less eccentric muscle velocity. With less eccentric velocity, the force-velocity relation would diminish muscle force, promoting less energy dissipation and thus compensating for the lost potential energy. The inverse would occur with a step-down perturbation: the higher impact velocity and extra potential energy due to the perturbation would be compensated by more muscle force and energy dissipation. What is common to both perturbed conditions is that hopping robustness would be promoted by a viscous-like regulation inner to the muscle mechanics, thus without needing sensing and feedback control.

Unfortunately, evidence supporting the functional damping role of the force-velocity relation is both scarce and largely qualitative. Gerritsen et al. (1998) discovered that removing the force-velocity relation from Hill-type models during multibody biomechanical simulations compromises the system's ability to reject dynamic disturbances. Similarly, Haeufle et al. (2010) found that removing or simplifying the shape of the force-velocity relation in a minimalistic muscle-driven hopper diminished the system's ability to stabilize step perturbations. Both studies provide evidence for a stabilizing role of the force-velocity relation, but they fail to quantify its exact contribution and interplay with other muscle properties. In this regard, van der Krogt et al. (2009) suggested that the force-velocity relation may contribute less to perturbation rejection than expected. Their study found that during unexpected changes in ground stiffness, the interaction between feedforward stimulation and change in surface hardness was more meaningful in correcting leg stiffness than muscle inner mechanics.

The suggested importance of the force-velocity relation for enabling stable motion in biomechanical simulations, combined with the lack of a quantitative understanding of its contribution within the nonlinear muscle contraction dynamics, has been a primary motivation for this dissertation's research.

3.4.2 Parallel elastic element (PEE)

The parallel elastic element approximates the passive elastic properties of muscle fibers' bundles. The mathematical formulation of PEE in the model of Haeufle et al. (2014b) is:

$$F_{PEE}\left(l_{CE}\right) = \begin{cases} 0, & l_{CE} < l_{PEE,0} \\ K_{PEE}\left(l_{CE} - l_{PEE,0}\right)^{v_{PEE}}, & l_{CE} \geq l_{PEE,0} \end{cases} \tag{3.5}$$

Equation (3.5) describes a nonlinear elastic element, with curvature defined by K_{PEE} and v_{PEE}. This element only engages when muscle fibers have stretched beyond a certain threshold ($l_{CE} \geq l_{PEE,0}$), a property observed during isometric contraction experiments with biological muscles. Note that while v_{PEE} is a free parameter of the muscle model, K_{PEE} comprises two additional free parameters in its explicit formulation (here omitted). Figure 3.3c (right) illustrates the force-length profile characterizing PEE dynamics.

3.4.3 Serial elastic element (SEE)

The serial elastic element captures the elastic properties of tendons and aponeuroses. Its mathematical expression in Haeufle et al. (2014b)'s model is:

$$F_{SEE}\left(l_{SEE}\right) = \begin{cases} 0, & l_{SEE} < l_{SEE,0} \\ K_{SEE,nl}\left(l_{SE} - l_{SEE,0}\right)^{v_{SEE}}, & l_{SEE,0} \leq l_{SEE} < l_{SEE,nll} \\ \Delta F_{SEE,0} + K_{SEE,l}\left(l_{SEE} - l_{SEE,nll}\right), & l_{SEE} \geq l_{SEE,nll} \end{cases} \tag{3.6}$$

Equation (3.6) describes the serial elastic element as a nonlinear toe-zone with a linear continuation. Below a certain threshold $l_{SEE,0}$, the serial elastic element is not engaged in force production. In the range of $l_{SEE,0} \leq l_{SEE} < l_{SEE,nll}$, a nonlinear elastic force is produced as a function of l_{SEE}. Here, $K_{SEE,nl}$ and v_{SEE} define the nonlinear curvature. For more extended stretching ($l_{SEE} \geq l_{SEE,nll}$), the serial elastic element produces a linear elastic force with stiffness coefficient $K_{SEE,l}$. The parameter $\Delta F_{SEE,0}$ guarantees force continuity between the nonlinear and linear branches of the serial elastic element. Figure 3.3c (left) illustrates the force-length profile characterizing SEE dynamics.

3.4.4 Serial damper element (SDE)

The serial damper element captures de-localized musculo-tendinous damping, consistent with observations of physiologically damped eigenoscillations in real muscles (Günther et al., 2007). SDE is formulated by Haeufle et al. (2014b) as follows:

$$\begin{aligned} &F_{SDE}\left(l_{CE}, \dot{l}_{CE}, \dot{l}_{MTU}, q\right) \\ &= D_{SDE,\max} \cdot \left(\left(1 - R_{SDE}\right) \cdot \frac{F_{CE}\left(l_{CE}, \dot{l}_{CE}, q\right) + F_{PEE}\left(l_{CE}\right)}{F_{\max}} + R_{SDE} \right) \cdot \left(\dot{l}_{MTU} - \dot{l}_{CE}\right) \end{aligned} \tag{3.7}$$

According to eq. (3.7), the serial damper element produces a viscous damper-like force, with the damping coefficient proportional to the muscle-tendon force ($F_{MTU} = F_{CE} + F_{PEE}$). The coefficient R_{SDE}, which is ≤ 1, represents the damping at $F_{MTU} = 0$; $D_{SDE,max}$ represents the maximum damping coefficient at $F_{MTU} = F_{max}$.

3.4.5 Activation dynamics

In this dissertation, muscle contraction dynamics during hopping simulations include the activation dynamics from Hatze (1977); Rockenfeller et al. (2015). The activation dynamics describe the electrochemical processes that convert neuronal stimulation (u) into the activity of the contractile element (a). Neuronal stimulation refers to the electrical signal that arrives at the muscle membrane, modeled by a normalized continuous variable $u \in [0,1]$. Therefore, u represents the control signal for muscle contraction. A value of $u = 1$ implies complete recruitment of the muscle unit, whereas a value of $u = 0$ indicates the nervous system is not recruiting the muscle unit.

The normalized continuous variable a is the output of the activation dynamics and represents the concentration of bound Ca^{2+}-ions. Such concentration is associated with the number of attached cross-bridges in the muscle fibers and thus defines the force the muscle unit exerts. $a = 1$ implies that the maximum concentration of Ca^{2+}-ions is reached, resulting in maximal muscle contraction. Contrary to u, a is never zero. Its minimum threshold is $a = a_0$, where a_0 indicates the minimum concentration of bound Ca^{2+}-ions persisting in the muscle when no neuronal stimulation is received. Therefore, $a \in [a_0, 1]$.

The activation dynamics link u and a as functions of time through the following nonlinear differential equation:

$$\dot{a}(t) = \frac{\nu \cdot m}{1 - a_0} \cdot \left[u(t) \cdot \rho\left(\ell_{\text{CErel}}\right) \cdot (1 - a(t))^{1+1/\nu} \cdot (a(t) - a_0)^{1-1/\nu} - (1 - a(t)) \cdot (a(t) - a_0)\right] \tag{3.8}$$

for which the following definitions hold

$$\begin{aligned} \rho\left(\ell_{\text{CErel}}\right) &= \rho_c \cdot \left(\left(\ell_\rho - 1\right) / \left(\ell_\rho / \ell_{\text{CErel}} - 1\right)\right) \\ \rho_c &= \rho_0 \cdot c \\ \ell_{\text{CErel}}(t) &= \ell_{\text{CE}}(t) / \ell_{\text{CE,opt}} \end{aligned} \tag{3.9}$$

In eqs. (3.8) and (3.9), ν, m, ρ_0, c, and ℓ_ρ are empirical values (for a more careful description, see Rockenfeller et al. (2015)). It should be noted that eq. (3.8) includes a length dependency, expressed by $\rho\left(\ell_{\text{CErel}}\right)$. This feature is based on experimental evidence of a relation between the contractile element's length and the muscle fibers' activity level. Figure 3.3d provides an intuitive example of how the activation dynamics (AD) convert a step stimulus u into a smooth rise of muscle activity level a.

3.5 Decomposition algorithm

One research objective of this doctoral project was investigating damping-like regulation by the force-velocity relation during fast perturbed locomotion. This requires measuring the amount of force produced by the force-velocity relation, a quantity not available in biological experiments and not directly accessible in Hill-type simulations. As indicated by eq. (3.4), the force produced by the muscle fibers depends on nonlinear dynamics combining the contribution of the force-velocity relation with other muscle properties, such as force-length relation and activation level. Therefore, we developed the decomposition algorithm, a computational method to isolate and quantify the muscle fiber force produced by the force-velocity relation during Hill-type simulations. This algorithm is a fundamental contribution to this doctoral thesis. It enables a quantitative understanding of preflexes and eliminates the need to restrain muscle contraction to unrealistic trajectories to study the individual contribution of muscle inner mechanics.

The decomposition algorithm is based on the concept of the total derivative. Given a time-dependent function $G = g(t)$ and a small time increment Δt, the total derivative of G represents its best linear approximation at $t + \Delta t$:

$$G(t + \Delta t) = G(t) + \frac{dG}{dt}(t)\,\Delta t + \varepsilon(\Delta t) \tag{3.10}$$

where dG/dt is the total derivative of G calculated at t, and $\varepsilon(\Delta t)$ is the approximation error. Notice that the approximation error depends on the time increment Δt. For an infinitesimal time increment dt, the approximation error is zero. Therefore, given an initial time instance t_0, the value of G at any desired future time instance t_x can be computed as:

$$G(t_x) = G(t_0) + \int_{t_0}^{t_x} \frac{dG}{dt}(t)\,dt \tag{3.11}$$

Intuitively, eq. (3.11) can be considered as the continuous form of eq. (3.10). The integral in eq. (3.11) indicates that the change in G that occurs from t_0 to t_x is the continuous and cumulative summation of the infinitesimal change of G across each integration step. Therefore, the integral of the total derivative dG/dt describes the evolution of G as a function of time.

Let's now generalise eq. (3.11) for a multi-input function $G = g(x, y, z)$, where each input variable is time-dependent, i.e., $x(t)$, $y(t)$, $z(t)$. For the sake of simplicity, only three input variables are considered, yet the following can be easily generalized to n-dimensions. The total derivative of $G = g(x, y, z)$ becomes:

$$\frac{dG}{dt} = \frac{\partial G}{\partial x}\frac{dx}{dt} + \frac{\partial G}{\partial y}\frac{dy}{dt} + \frac{\partial G}{\partial z}\frac{dz}{dt} \tag{3.12}$$

where Leibniz chain rule was applied and time-dependencies removed for clarity. $\partial G/\partial k$ indicates the partial derivative of G with respect to its k-th input variable. Applying eq. (3.12) to eq. (3.11) gives:

$$\begin{aligned} G(t_x) &= G(t_0) + \int_{t_0}^{t_x} \left(\frac{\partial G}{\partial x}\frac{dx}{dt} + \frac{\partial G}{\partial y}\frac{dy}{dt} + \frac{\partial G}{\partial z}\frac{dz}{dt} \right) dt \\ &= G(t_0) + \int_{x(t_0)}^{x(t_x)} \frac{\partial G}{\partial x}dx + \int_{y(t_0)}^{y(t_x)} \frac{\partial G}{\partial y}dy + \int_{z(t_0)}^{z(t_x)} \frac{\partial G}{\partial z}dz \\ &= G(t_0) + \Delta G_x(t_x) + \Delta G_y(t_x) + \Delta G_z(t_x) \end{aligned} \tag{3.13}$$

with $\Delta G_k(t_x) = \int_{k(t_0)}^{k(t_x)} \frac{\partial G}{\partial k}dk$ and k indicating the k-th input variable. In eq. (3.13), each integral represents the individual contribution of the k-th input variable to the change in G between t_0 and t_x. Therefore, each $\Delta G_k(t)$ is a time-dependent function that describes the separate contribution of the k-th input variable to the evolution of G in time t.

Equation (3.13) is the key formula implemented by our decomposition algorithm. According to eq. (3.13), the decomposition algorithm exploits the total time derivative and the Leibniz chain rule to reformulate the evolution in time of a multi-variable function G. In this reformulation, the separate contribution of each input variable emerges explicitely. Section 4.2.3 describes the application of the decomposition algorithm to the Hill-type formulation of muscle contraction. The main steps for implementing the decomposition algorithm to simulated muscle contraction are:

1. Simulate the motion of a desired biomechanical model. In our study, we simulated vertical hopping of a two-segment leg actuated by an extensor muscle.

2. Record the time traces of the muscle model's input variables throughout the simulated movement. In our study, the input variables for the muscle model were muscle fiber length, velocity, and activation level.

3. Compute the partial derivatives in eq. (3.13) from the analytical formulation of the muscle model used for the simulations. In our study, the muscle model implemented the Hill-type formulation defined in Haeufle et al. (2014b).

4. Numerically integrate these partial derivatives according to eq. (3.13), using the recorded values of the muscle model's input variables as integration nodes.

These steps collectively form the decomposition algorithm. We used this algorithm to compute offline the change in muscle fiber force produced by each input variable of the muscle model. Precisely, the change produced by the muscle fiber velocity quantifies the force contribution of the force-velocity relation to muscle contraction (see Chapter 4 for more details).

4 Muscle prestimulation tunes velocity preflex in simulated perturbed hopping

Hill-type muscle models feature the force-velocity relation, a phenomenological function that characterizes the viscous-like behavior of muscle fibers observed during contraction experiments. It is hypothesized that the force-velocity relation grants muscle fibers viscous mechanical damping. However, validating this hypothesis is complex due to the highly nonlinear dynamics of muscle contraction. For this reason, in vitro studies use unrealistic contraction trajectories to isolate the contribution of the force-velocity relation to muscle force generation. Computer simulations with Hill-type models can simulate more complex conditions. Nevertheless, even their mathematical formulation nonlinearly combines the force-velocity relation with other factors, such as the force-length relation and muscle fibers' activity level.

In this study, we present the decomposition algorithm, a novel approach to isolate and quantify the force produced by the force-velocity relation in Hill-type musculoskeletal simulations. We used this technique to analyze the muscle response to ground-level perturbations in simulated vertical hopping. Our analysis focused on the preflex phase—the first 30 ms after impact—where neuronal delays render a controlled response impossible. We found that muscle force at impact and dissipated energy increase with perturbation height, helping reject the perturbations. However, the muscle fibers reject only 15% of step-down perturbation energy with constant stimulation. An open-loop rising stimulation, observed in locomotion experiments, amplified the regulatory effects of the muscle fiber's force-velocity relation, resulting in 68% perturbation energy rejection. We conclude that open-loop neuronal tuning of muscle activity around impact allows for adequate feedforward tuning of muscle fiber viscous-like capacity, facilitating energy adjustment to unexpected ground-level perturbations.

Note: a large portion of this chapter uses content published in *Scientific Reports* (Izzi et al., 2023). For details on this journal article, including the list of authors and my contribution, see Section 2.1.1.

4.1 Introduction

Muscles are smart actuators; they generate forces and movements and contribute to controlling them. Thanks to muscles' nonlinear mechanical characteristics, they can react to unexpected perturbations instantly (Haeufle et al., 2020a,b; John et al., 2013; Patla, 2003; van der Krogt et al., 2009) and without the inherent delays of neuronal reflexes (More and Donelan, 2018). This zero-delay capacity is known as "preflex" (Loeb, 1995). Preflexes allow mitigating neuro-transmission delays, which otherwise produce significant reaction latencies (animal size dependent, $> 30\,\text{ms} \ldots 50\,\text{ms}$) and hinder the control of quick movements (More and Donelan, 2018; Patla, 2003).

Among the mechanical properties of muscle fibers is the capacity to produce more negative power when lengthening (eccentric contraction) than positive power when shortening (concentric contraction) (Biewener, 1998; Herzog, 2018; Joyce et al., 1969; Siebert and Rode, 2014). Macroscopic muscle models describe this asymmetry as a "force-velocity relation" (Haeufle et al., 2014b; van Soest and Bobbert, 1993), i.e., a phenomenological relation between muscle fiber velocity and force (fig. 5.1d).

Simulation studies have shown that the force-velocity relation can contribute to the stability of hopping and walking (Gerritsen et al., 1998; Haeufle et al., 2010; John et al., 2013). However, it is still unclear how the force-velocity relation contributes to the preflex mechanics. Previous research argued that the force-velocity relation implements a stabilizing velocity preflex in muscle fibers (Geyer et al., 2003; Haeufle et al., 2010). If the impact velocity changes due to an unexpected ground height, the muscle's force-velocity characteristics would instantly lead to an adjusted force (fig. 5.1a). Similar self-regulating mechanisms are documented for parallel-elastic viscous damper systems during legged locomotion (Abraham et al., 2015; Heim et al., 2020; Mo et al., 2020).

Much functional research concerns the existence and shape of the force-velocity relation, and is often qualitative (Gerritsen et al., 1998; Haeufle et al., 2010). Multiple mechanisms rejecting ground perturbations are plausible; variables such as fiber length and neuronal activity shape the nonlinearity of muscle dynamics. For example, a ground perturbation during the rise of the muscle stimulation would trigger a change of muscle excitation at touchdown, leading to velocity-dependent regulation of muscle force similar to a velocity preflex. Furthermore, a change in impact velocity can also alter the muscle fiber stretch, which indirectly adapts muscle forces. Therefore, a quantitative analysis is necessary to test if the force-velocity relation leads to a velocity-dependent rejection of external disturbances, and if so, to what extent.

In this study, we use computer simulations to quantify velocity-dependent regulation of muscle fiber force when ground perturbations affect vertical hopping. The novelty of our analysis consists in the explicit quantification of the preflex response generated by the muscle fibers' force-velocity relation, force-length relation, and neuronal activity. With this approach, we study the complex nonlinearity of muscle contraction, discerning the net contribution of the force-velocity relation from other regulating factors. Our results suggest that the force-velocity relation can regulate muscle forces during perturbed hopping in a velocity-dependent manner. However, we observe a substantial, stabilizing response only if low-level neuronal stimulation interacts with the muscle's force-length-velocity characteristics.

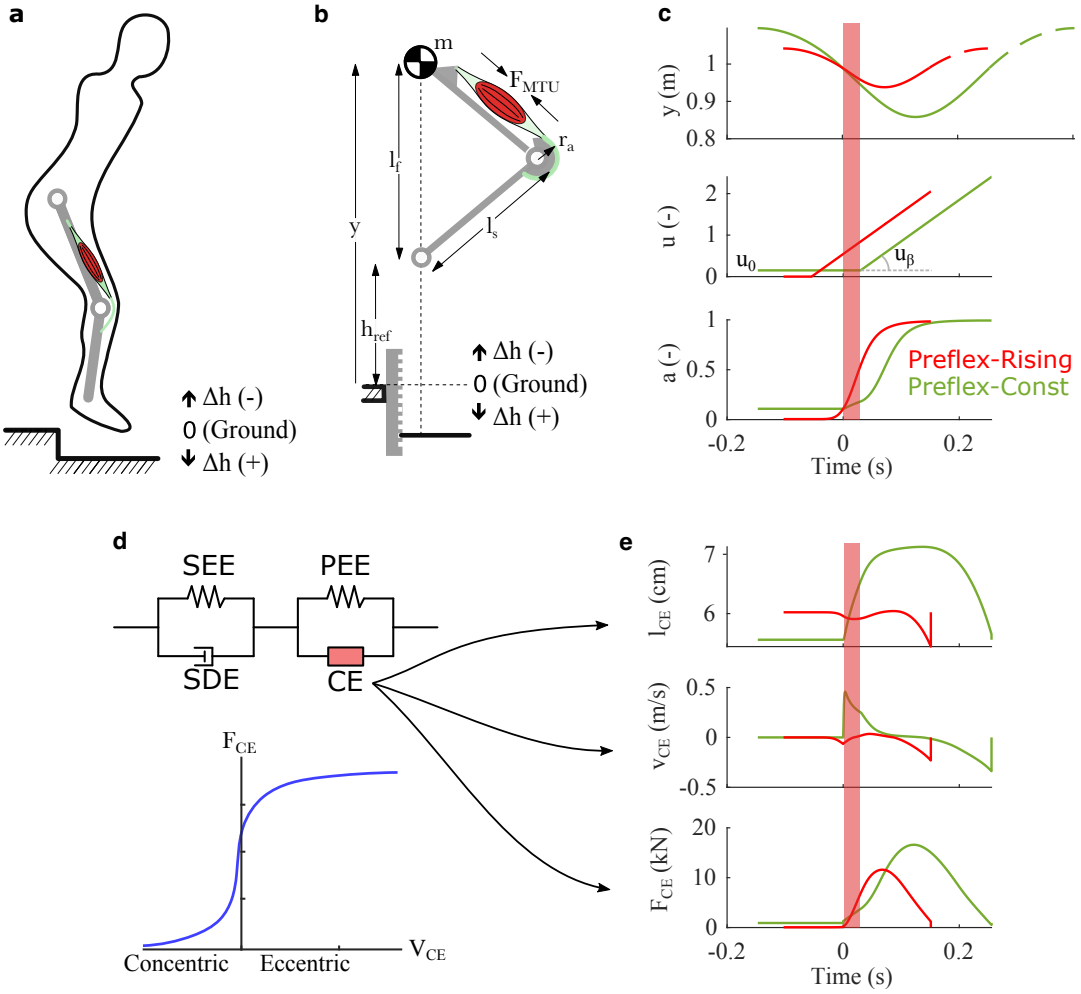

Figure 4.1: Study design. (a) Step perturbations present a challenge during agile locomotion because neurotransmission delay affects a considerable fraction of the stance duration. Because of their instantaneous response to ground disturbances, the mechanical properties of muscle-tendon units may be critical to prevent falling. (b) We simulate vertical hopping of a massless, two-segment leg model to investigate the stabilizing response of the muscle fiber's force-velocity relation to step disturbance Δh. Here, h_{ref} indicates the unperturbed periodic hopping height, and y is the vertical position of the point-mass m. Leg length during flight and leg segment length are indicated by l_f and l_s, respectively. F_{MTU} is the force exerted by the muscle-tendon unit and r_a the associated lever arm. (c) To stimulate the muscle and generate periodic hopping, we apply a ramp signal, with prestimulation value u_0 and slope u_β. In Preflex-Const, the muscle stimulation starts at the actual touchdown and stays constant ($u = u_0$) until the end of the preflex duration (30 ms post-touchdown, indicated by the colored bar, with $t = 0$ s being touchdown). In Preflex-Rising, the muscle stimulation starts before the expected touchdown with $u_0 = 0$. Here, the stimulation onset is fixed in time and thus independent of the actual touchdown timing. We use the activation dynamics in Hatze (1977); Rockenfeller et al. (2015) to convert the stimulation signal u into muscle activity a. We tuned Preflex-Const and Preflex-Rising to produce the same muscle activity at touchdown during unperturbed hopping: y shows the vertical trajectory of the center of mass for each stimulation strategy. Initial and final mass heights y are identical for each trajectory, indicating that both Preflex-Const and Preflex-Rising produced periodic hopping. (d) For our simulations, we use the Hill-type muscle model developed in Haeufle et al. (2014b), which includes a contractile element (*CE*), a parallel elastic element (*PEE*), a serial elastic element (*SEE*), and a serial damper element (*SDE*). The force-velocity relation models the dependence of the muscle fiber force F_{CE} on the muscle fiber velocity v_{CE}. Shortening velocities (negative v_{CE}) define the concentric region of the force-velocity relation, while lengthening velocities (positive v_{CE}) define the eccentric region. (e) Length (l_{CE}), velocity (v_{CE}), and force traces (F_{CE}) of the muscle fibers during unperturbed hopping with Preflex-Const and Preflex-Rising

4.2 Methods

4.2.1 Musculoskeletal model

For our study, we used a modified version of the musculoskeletal model developed in Geyer et al. (2003), with identical kinematics but a revised muscle-tendon unit (Haeufle et al., 2014b). The model is a minimalist representation of vertical, perturbed hopping (fig. 4.1a). It consists of a two-segment leg with total mass lumped at the hip and motion constrained to the vertical axis (figure fig. 4.1b). During stance, an extensor muscle-tendon unit actuates the knee joint with a force outcome F_{MTU} that corresponds to a torque

$$T_{knee} = r_a F_{MTU} \tag{4.1}$$

with r_a being the muscle lever arm. During the flight phase, the knee motion was always constrained, and the leg length was fixed to l_f. This solution guaranteed the same leg geometry at touchdown despite the absence of antagonistic muscles in our model. Because of the simplified flight phase, we could reduce the analysis of each hopping scenario to the first hopping cycle (apex-to-apex). Each simulation started with the model in flight phase. Touchdown occurred when the mass vertical position $y \leq l_f$, and take-off when either $y > l_f$ or the ground reaction force $F_{leg} \leq 0N$ (positive F_{leg} was upwards directed).

For our muscle-tendon unit, we used the Hill-type model in Haeufle et al. (2014b). It consists of four elements, as shown in fig. 4.1d: a contractile element (CE), a parallel elastic element (PEE), a serial elastic element (SEE), and a serial damping element (SDE). These four components fulfill the force equilibrium:

$$F_{MTU} = F_{CE} + F_{PEE} = F_{SEE} + F_{SDE} \tag{4.2}$$

The contractile element represents the collective contribution of the muscle fibers to muscle contraction. In our model, the parallel elastic element (PEE) engages when $l_{CE} > 95\% l_{opt}$, i.e., when the muscle fiber length (l_{CE}) is close to the muscle fiber optimal length (l_{opt}). This condition never occurred in our simulations, which means that in our study, the force produced by the muscle fibers (F_{CE}) was equal to the total force produced by the muscle-tendon unit (F_{MTU}).

The force of the contractile element F_{CE} is a nonlinear function of the fiber velocity v_{CE} (force-velocity relation), fiber length l_{CE} (force-length relation), and muscle activity a, the latter in turn dependent on the neuronal stimulation u received by the muscle fibers. The force-velocity relation comprises two regions, shown in fig. 4.1d: the concentric and the eccentric contraction regions, characterized by shortening velocities ($v_{CE} \leq 0\,\text{m/s}$) and stretching velocities ($v_{CE} > 0\,\text{m/s}$) of the muscle fibers, respectively. The force-velocity relation predicts a flattening profile of F_{CE} for increasing eccentric velocities. Such flattening is suggested by experimental data and commonly implemented in biomechanical models; for an overview see Fig.3 of Klute et al. (2002).

We implemented our model in Simulink R2018a (Mathworks Inc., Natick, MA, USA). We used ode45 as numerical solver, with a maximum step size of 1×10^{-4} s, and absolute and relative error tolerances of 1×10^{-8}. Model parameters are listed in Table 4.1. A more in-depth list of model variables can be found in the electronic supplementary materials (Table A1.1). Note that our model requires a large value for the maximum isometric force F_{max} to compensate for the lack of additional muscle-tendon units, as explained in Geyer et al. (2003).

4.2.2 Muscle stimulation

This study focuses on the preflex phase, i.e., the first 30 ms after touchdown, during which neuronal feedback is absent because of neuronal delays (More and Donelan, 2018). To initialize hopping, muscle fibers receive a ramp signal as neuronal stimulus $u(t)$ (fig. 4.1c). The ramp signal is inspired by the observation that knee extensor's activity rises during locomotion around and after impact (Moritz and Farley, 2004; Müller et al., 2015, 2020). We implemented two stimulation protocols: Preflex-Const (u_C) and Preflex-Rising (u_R).

With Preflex-Const, the ramp signal is kept constant during the first 30ms after touchdown. After the preflex phase, the muscle stimulation rises linearly:

$$u_C(t) = \begin{cases} u_0 + u_\beta \, (t - t_{TD} - \delta_C) & \text{, for } t > t_{TD} + \delta_C \\ u_0 & \text{, otherwise} \end{cases} \tag{4.3}$$

where u_0 is the muscle prestimulation level, u_β the slope of the ramp stimulus, t_{TD} the time of touchdown, and $\delta_C = 30\,\text{ms}$ the neuronal delay. The Preflex-Const protocol enabled us to study the isolated response of the muscle fibers' inherent mechanical properties. The Preflex-Const protocol also served as design reference for Preflex-Rising.

With Preflex-Rising, the muscle stimulation $u(t)$ rises linearly starting 54 ms before the expected touchdown, with the same linear coefficient as in Preflex-Const (u_β):

$$u_R(t) = \begin{cases} u_\beta \, (t - t^*_{TD} + \delta_R) & \text{, for } t > t^*_{TD} - \delta_R \\ 0 & \text{, otherwise} \end{cases} \tag{4.4}$$

where t^*_{TD} is the expected touchdown event, i.e., the time in which touchdown occurs during unperturbed hopping, and $\delta_R = 54\,\text{ms}$. We applied the particular time offset δ_R to ensure that both Preflex-Rising and Preflex-Const produced unperturbed periodic hopping with the same amount of muscle activity at touchdown. Therefore, Preflex-Const and Preflex-Rising guarantee the same muscle pre-activation level at touchdown, as shown by the a-signal in fig. 4.1c. However, while the onset of Preflex-Const depends on the real touchdown t_{TD}, Preflex-Rising is an open-loop signal with the onset at the expected touchdown (t^*_{TD}), and therefore independent of the actual ground height. The Preflex-Rising protocol allowed comparing Preflex-Const results with those of a more biologically feasible stimulation, for which inherent mechanics and feedforward control of muscle fibers interact to generate a first response to ground perturbations.

Regardless of the stimulation protocol in use, our model includes the activation dynamics described in Hatze (1977); Rockenfeller et al. (2015), which consists of a first-order differential equation incorporating fiber length dependency. The activation dynamics turn the stimulation signal $u(t)$ into muscular activity $a(t)$ before reaching muscle fibers, limiting muscle activity between 0.005 and 1.

4.2.3 Muscle fiber force decomposition

We aimed to quantify the force-velocity relation's contribution to the force produced by the muscle fibers during the preflex phase. We further separated the contributions of fiber elasticity and muscle activity. In our simulations, the muscle fibers exert a force

$$F_{CE}(t) = f_{CE}\left(v_{CE}(t), l_{CE}(t), a(t)\right) \tag{4.5}$$

which is a nonlinear function of the muscle fiber velocity $v_{CE}(t)$, length $l_{CE}(t)$, and muscle activity $a(t)$. For better readability, we will omit the time dependency in the following.

According to what described in section 3.5, we can separate the three contributions by interpreting f_{CE} as follows:

$$f_{CE} = \int_{t_{TD-1}}^{t_x} \frac{df_{CE}(v_{CE}, l_{CE}, a)}{dt} dt + F_{CE}^0 \tag{4.6}$$

where F_{CE}^0 is the force exerted by the muscle fibers immediately before touchdown, t_{TD-1} is the time instance just before touchdown, and t_x any later time within the stance duration. After applying the chain rule in eq. (4.6), we can rewrite eq. (4.5) as the sum of four components:

$$\begin{aligned} F_{CE} &= F_{CE}^V + F_{CE}^L + F_{CE}^A + F_{CE}^0 \\ F_{CE}^V &= \int_{t_{TD-1}}^{t_x} \frac{\partial f_{CE}}{\partial v_{CE}} dv_{CE} \\ F_{CE}^L &= \int_{t_{TD-1}}^{t_x} \frac{\partial f_{CE}}{\partial l_{CE}} dl_{CE} \\ F_{CE}^A &= \int_{t_{TD-1}}^{t_x} \frac{\partial f_{CE}}{\partial a} da \end{aligned} \tag{4.7}$$

where F_{CE}^V is the force contribution of the force-velocity relation, F_{CE}^L of the force-length relation, and F_{CE}^A of the muscle activity, the latter in turn associated with the stimulation signal received by the muscle fibers.

We implemented this decomposition algorithm offline, using the trapezoidal rule to solve each integral in eq. (4.7) numerically (*cumtrapz*, Matlab R2018a, Mathworks Inc., Natick, MA, USA). Touchdown ($t = t_{TD}$) occurs instantly in our model. Hence, we computed the initial values of the numerical integration of eq. (4.7) algebraically:

$$\begin{aligned} F_{CE}^L(t_{TD}) &= F_{CE}^A(t_{TD}) = 0 \\ F_{CE}^V(t_{TD}) &= F_{CE}(t_{TD}) - F_{CE}^0 \end{aligned} \tag{4.8}$$

Equation (4.8) shows that changes in muscle fiber force at touchdown must derive from the contribution of the force-velocity relation since muscle fiber length (l_{CE}) and activity (a) remain constant at the instantaneous ground impact.

4.2.4 Hopping motion and perturbation modeling

To explore the contribution of muscle fibers to preflexes during perturbed hopping, we established reference hopping conditions for both stimulation protocols, i.e., Preflex-Const and Preflex-Rising.

We started by tuning the Preflex-Const stimulus to produce periodic hopping with physiologically plausible muscle activation values: prestimulation value $a_0 = 0.11$, reaching 90 % saturation in 117 ms. Setting $u_0 = 0.15$ and $u_\beta = 10$ resulted in vertical hopping with 10.6 cm apex height (h_{ref}) and the muscle activity shown in fig. 4.1c. The resulting stance duration was 255 ms and the hopping frequency 1.8 Hz, consistent with periodic hopping investigated by previous research (Geyer et al., 2003). Although the Preflex-Const stimulation u_C remained constant throughout the preflex phase, in accordance to eq. (4.3), a small increase of muscle activity a occurred within the preflex duration (see bottom plot,

green line in fig. 4.1c). This increase is a result of the activation dynamics' dependency on the muscle fiber length and stretch throughout the preflex duration.

We designed the Preflex-Rising stimulation using Preflex-Const as reference: we set $\delta_R = 54\,\text{ms}$ to have the same amount of muscle activation a at touchdown ($a_0 = 0.11$), and $u_\beta = 10$ for an equal rate of muscle stimulation – producing 90 % saturation of a-signal in 70 ms after touchdown. These settings resulted in a Preflex-Rising muscle activity comparable to that produced by Preflex-Const, as shown in fig. 4.1d. The major difference is a time shift due to the lack of a constant stimulation phase during the preflex. The Preflex-Rising stimulation produced periodic hopping with an apex height h_{ref} of 5.2 cm, a stance duration of 151 ms, and a hopping frequency of 2.8 Hz. These features imply that Preflex-Rising caused stiffer reference hopping than Preflex-Const, as also seen by the smaller change in the l_{CE} and v_{CE} time traces in fig. 4.1e. Nonetheless, the characteristics of the stiffer reference periodic hopping remain in line with earlier studies (Geyer et al., 2003).

A second difference in the periodic hopping associated with Preflex-Rising and Preflex-Const was the muscle fiber's force at touchdown: 179 N during Preflex-Rising, and 1260 N during Preflex-Const. The difference in touchdown conditions occurs as the muscle stimulation starts before touchdown in the periodic hopping caused by Preflex-Rising. As a result, muscle fibers are shortening at ground contact with Preflex-Rising, and this causes the concentric side of the force-velocity relation to diminish the muscle fiber force at touchdown. Figure 4.1e further illustrates the time trace of F_{CE} for both stimulation protocols.

After selecting these reference hopping conditions for the two investigated stimulation protocols, we simulated unexpected ground perturbations by applying changes Δh to the reference hopping height. We applied a total of six height perturbations, consisting of two step-up ($\Delta h = -5.0\,\text{cm}$ and $-2.5\,\text{cm}$) and four step-down perturbations ($\Delta h = 2.5\,\text{cm}$, 5.0 cm, 7.5 cm and 10.0 cm). Hence, ground perturbations ranged from -5 % to 10 %, in reference to a leg length of $l_f = 99\,\text{cm}$. Limiting the largest step-up perturbation to $-5\,\text{cm}$ was because $h_{ref} = 5.2\,\text{cm}$ during reference periodic hopping with Preflex-Rising.

The apex-return map visualizes the stability of Preflex-Const and Preflex-Rising reference hopping against the tested step perturbations (fig. 4.2). The apex-return map plots each tested drop height ($h_0 = y(t_{TD}) - l_f$) against the apex height at the end of the first hopping cycle (h_1) – which would become the follow-up drop cycle height. A horizontal apex-return profile would show complete rejection of any ground disturbance since any perturbation intensity will produce a return apex coincident with the reference hopping height. If the apex-return profile coincides with the diagonal line, the result is periodic hopping at the perturbed hopping height. The hopping height would not converge back to the initial reference hopping height, and the perturbation would not be rejected. Finally, any apex-return profile with a slope outside the area enclosed by (1) the diagonal line and (2) its perpendicular line at the periodic hopping height represents unstable hopping: the return apex will move away from the reference hopping height at each new hopping cycle.

Figure 4.2 shows that reference hopping of Preflex-Const and Preflex-Rising were asymptotically stable for the set of step perturbations studied here. Preflex-Rising showed faster rejection of the step-down perturbations, based on its more horizontal apex-return profile in fig. 4.2.

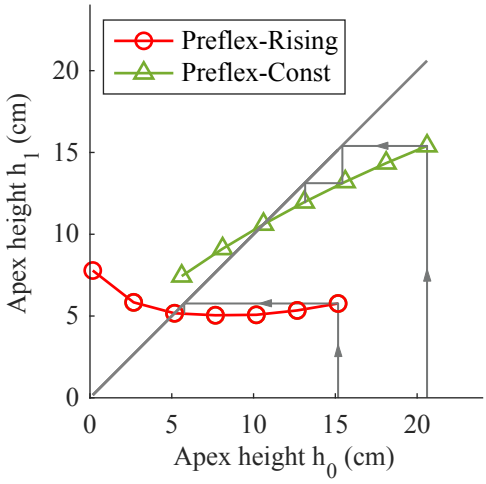

Figure 4.2: Apex return map for Preflex-Const (green) and Preflex-Rising (red). h_0 is each initial drop height tested in our study, and h_1 each associated return apex after one hopping cycle. Notice that h_1 would be the initial drop height for the following hopping cycle during continuous hopping. Intersections with the diagonal line represent periodic hopping heights. The rather horizontal return-map for Preflex-Rising around its periodic hopping height represents a faster rejection of ground perturbations: the arrows indicate the faster convergence to periodic hopping within fewer hopping cycles.

4.3 Results

4.3.1 Touchdown response (at $t = 0$ ms)

At touchdown, Preflex-Const produced little adjustments of muscle fibers' force in response to ground perturbations, while Preflex-Rising produced larger adjustments. This finding is visible at the touchdown events in fig. 4.3, indicated by circle symbols. Figure 4.4a shows that during Preflex-Const, the muscle fiber force F_{CE} ranged from 1.15 kN to 1.35 kN at impact. Also, changes in F_{CE} became smaller as the drop height increased. During Preflex-Rising, F_{CE} at impact displayed a wider range of adjustment (from 0.06 kN to 4.20 kN, fig. 4.4b). Here, the majority of change occurred along the step-down perturbations. This finding is expected since with Preflex-Rising, the concomitant effects of delayed ground impacts and rising stimulation produce larger muscle excitation at touchdown during step-down perturbations.

By separating the individual components contributing to the muscle force at touchdown, it becomes clear that different mechanisms lead to the touchdown adjustment of F_{CE} (fig. 4.4a,b), depending on the stimulation protocol. During Preflex-Const, the force-velocity relation was the main factor driving F_{CE} adjustment, as shown by changes in F_{CE}^V and constant values of F_{CE}^0 across the tested conditions (fig. 4.4a). During Preflex-Rising, changes in both F_{CE}^V and F_{CE}^0 produced F_{CE} adjustment, with F_{CE}^0 contributing the most (fig. 4.4b). This shows that the adjustment of muscle stimulation at touchdown, which occurs during Preflex-Rising but not during Preflex-Const, plays a major role in adjusting the initial preflex response to the perturbation intensity.

We hypothesized that the force-velocity relation contributes to regulate ground perturbations by means of a velocity preflex. Such a velocity-dependence can be seen when plotting the force component F_{CE}^V against muscle fiber velocities v_{CE} at impact (fig. 4.4c,d). The plot reveals that the touchdown event of Preflex-Const trials always occurred in the eccentric contraction, and that increasing drop heights led to

Table 4.1: Model parameters, adapted from (Geyer et al., 2003).

Parameter	Value
Body weight m	80 kg
Gravitational constant g	9.81 m/s^2
Assumed flight leg length ℓ_f	0.99 m
Segment length ℓ_s	0.5 m
Optimum length ℓ_{opt}	0.1 m
Lever arm r_a	0.04 m
Maximum isometric force F_{max}	22 kN
Activation dynamics time constant τ	88.5 ms

faster v_{CE} but flatter adjustment of F_{CE}^V. The flattening of F_{CE}^V adjustment is a result of the eccentric side of the force-velocity relation in our muscle model, which predicts a decrease in the velocity-produced adjustment of the muscle force as v_{CE} increases (fig. 4.1d). No flattening adjustment of F_{CE}^V occurred during Preflex-Rising trials. In contrast, the rising muscle stimulation caused an almost linear trend along step-down perturbations. Furthermore, during Preflex-Rising trials, touchdown occurred in concentric contraction. Exceptions were the two step-up perturbations, which produced touchdown with almost steady conditions ($|v_{CE}| < 0.01$ m/s) and minimal muscle activity due to the short time for the muscle stimulation to rise.

4.3.2 Preflex response ($t = 0$ ms to 30 ms)

Work loop trajectories of Preflex-Const trials were almost identical during preflexes ($t = 0$ ms to 30 ms). They mainly differed by the amount of stretch reached by muscle fibers at the end of the preflex duration, shown by the box symbols in fig. 4.3a shifting to the right. Hence, differences in the muscle fiber velocity between trials resulted in a minimal adjustment of the muscle fiber force throughout the preflex duration. Therefore, in Preflex-Const trials, increased energy dissipation during preflexes was mainly caused by larger fiber stretch.

In contrast, work loop trajectories of Preflex-Rising trials show more complex preflex adjustments, visible by the variety of work loop shapes (fig. 4.3b). Step-up perturbations of higher intensity resulted in more eccentric stretch of muscle fibers and lower rise in muscle fiber force during preflexes, as shown by the two darker lines in fig. 4.3b. This trend emerges because larger step-up perturbations move the touchdown event closer to the onset of muscle stimulation. This leads to less excited and, therefore, more compliant muscle fibers during preflexes. For instance, the −5.0 cm step-up perturbation shifted the touchdown event about 30 ms before the muscle stimulation onset, making the muscle fibers relaxed for 99 % of the preflex phase and dissipate almost no energy. The step-down perturbations consisted of an initial phase of concentric shortening, followed by an eccentric stretch of the muscle fibers. Larger perturbations caused more prominent eccentric phases with larger muscle fiber forces, resulting in more energy dissipated by muscle fibers during preflexes.

To investigate the amount of energy regulation, we calculated the change in muscle fiber work during preflexes in response to each ground perturbation (ΔW_{CE}, green lines in fig. 4.5). The light-blue line

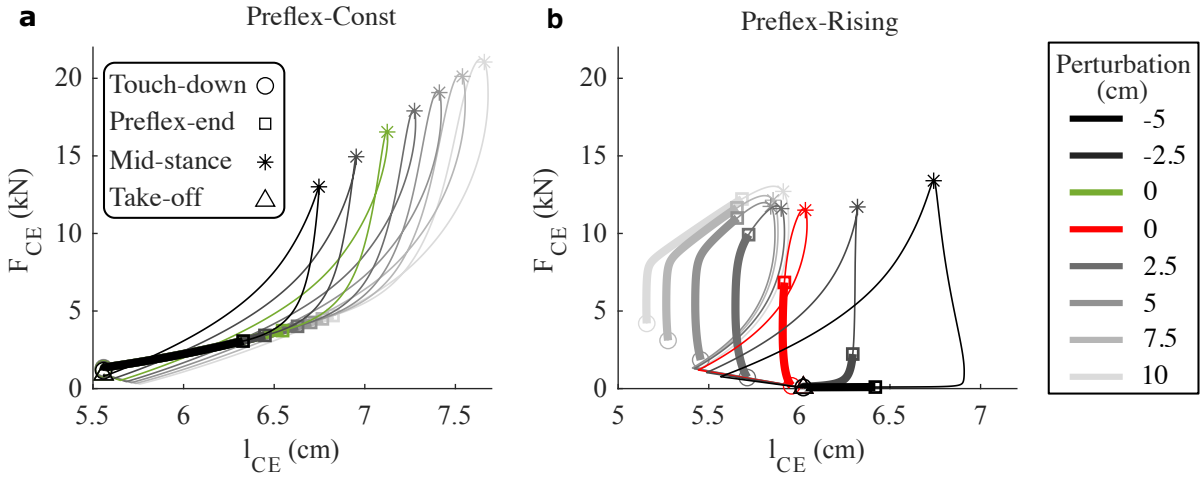

Figure 4.3: Muscle fiber work loop results for (a) Preflex-Const and (b) Preflex-Rising. Data is plotted from touchdown ○ to take-off △. The preflex phase is emphasized with thicker lines. Each □ indicates the end of the preflex duration; each * indicates mid-stance. The drop height increases from darker to lighter colors: the darkest and lightest work loops are produced by the largest step-up and step-down perturbations, respectively. Reference hopping conditions are colored green and red for Preflex-Const and Preflex-Rising, respectively.

(ΔE_P in fig. 4.5) indicates the amount of potential energy altered by each step perturbation. As such, ΔW_{CE} matching ΔE_P indicates the full rejection of ground perturbations by the end of the preflex phase.

Results show that Preflex-Rising produced a consistently better regulation of muscle fiber work than Preflex-Const during step-down perturbations. For example, during the largest step-down perturbation, $\Delta W_{CE} = 53.4\,\mathrm{J}$ with Preflex-Rising, and $\Delta W_{CE} = 11.9\,\mathrm{J}$ with Preflex-Const. This means that Preflex-Rising could reject 68 % ΔE_P, while Preflex-Const only 15 % ΔE_P.

Preflex-Const adapted well to step-up perturbations by reducing muscle fiber work (negative x-axis, fig. 4.5a). During the largest step-up perturbation, $\Delta W_{CE} = -7.5\,\mathrm{J}$ with Preflex-Const, meaning 19 % ΔE_P rejection. In contrast, Preflex-Rising failed to adjust muscle fiber work during step-up perturbations (negative x-axis, fig. 4.5b). Instead, muscle fiber work slightly increased: ΔW_{CE} was equal to 1.0 J and 0.3 J for −2.5 cm and −5.0 cm step-up perturbations, respectively.

We hypothesized that the force-velocity relation is important to regulate the muscle fiber work in response to perturbed ground contacts. We were able to test our hypothesis with our new approach, separating the components that produce ΔW_{CE}. We identified different principles of work regulation between Preflex-Const and Preflex-Rising. During Preflex-Const, we found a similar contribution from the force-velocity relation (ΔW^V_{CE}, dark-blue line), force-length relation (ΔW^L_{CE}, red line), and muscle excitation (ΔW^A_{CE}, yellow line). In particular, ΔW^V_{CE} contributed the least to ΔW_{CE} during Preflex-Const trials. In contrast, during Preflex-Rising ΔW^V_{CE} contribution was predominant over ΔW^L_{CE} and ΔW^A_{CE}. These results show that by adjusting muscle prestimulation at touchdown, the regulatory effect of the force-velocity relation on the muscle fiber work is most effective.

4.4 Discussion

In this study, we tested whether muscle fibers can produce a velocity preflex, i.e., a mechanical velocity feedback, to reject step perturbations, and how much the force-velocity relation contributes. We tested

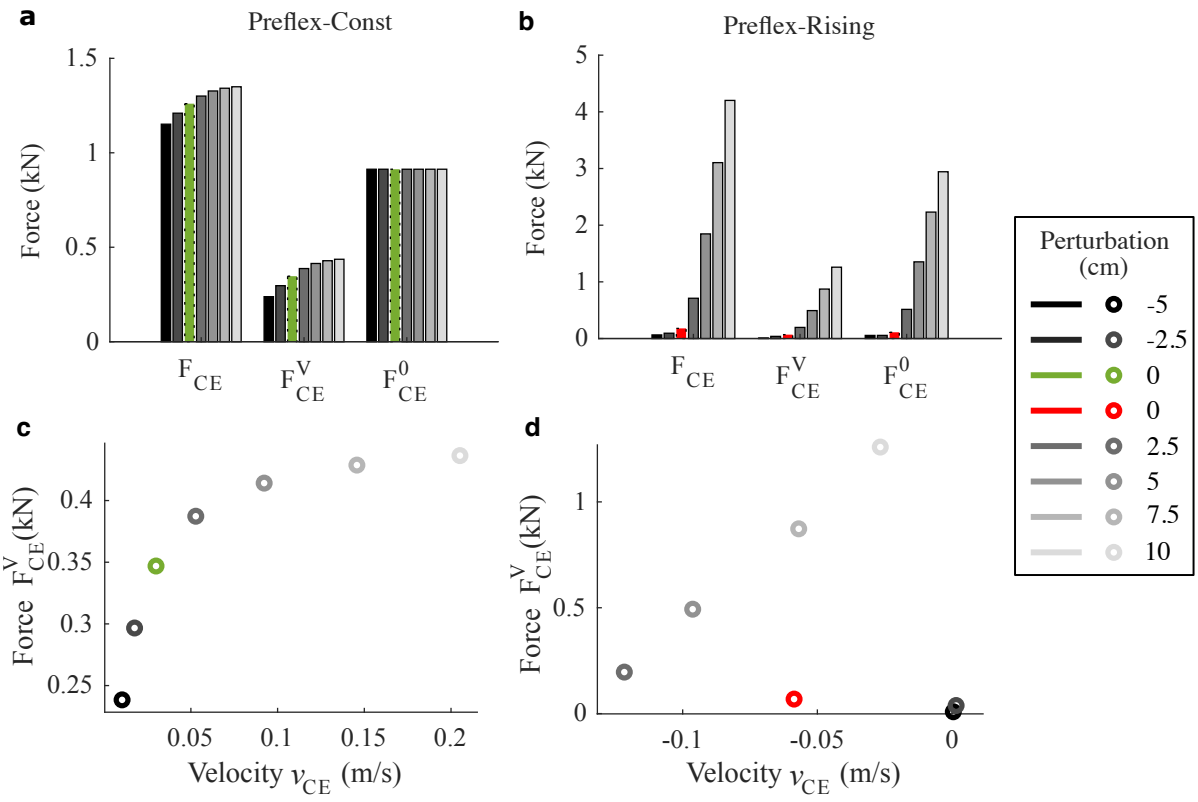

Figure 4.4: Touchdown results. (a, b) Force values: F_{CE} is the net muscle fiber force, F_{CE}^{V} the force component due to the force-velocity relation and F_{CE}^{0} the muscle fiber force just before touchdown. (c, d) Touchdown dependence of the muscle fiber force component due to the force-velocity relation (F_{CE}^{V}) on the muscle fiber velocity (v_{CE}). (a, c) Results for Preflex-Const, with reference hopping condition in green. (b, d) Results for Preflex-Rising, with reference hopping condition in red.

two stimulation protocols; in Preflex-Const, the stimulation of muscle fibers is kept constant around impact as an artificial measure to isolate the mechanical contribution of the muscle fibers to preflexes. The more physiologically plausible Preflex-Rising case permits to study the interplay between low-level control and muscle fibers' mechanical properties. Thanks to our suggested analytical approach to quantify force components produced by muscle fibers' mechanical properties, we found that the force-velocity relation does not produce a substantial velocity preflex in isolation, i.e., it produces only a minor adjustment of muscle fiber's force to variable impact velocity. However, its regulating effect can be maximized by feedforward control.

4.4.1 Reflection on literature hypothesis

By completely removing the force-velocity relation, previous research showed that the force-velocity relation is crucial to reject dynamic perturbations (Gerritsen et al., 1998; Haeufle et al., 2010; John et al., 2013). It was suggested that the force-velocity relation stabilizes locomotion by providing damping capacities to the muscle fibers (Geyer and Herr, 2010; Geyer et al., 2003; Haeufle et al., 2010). According to this hypothesis, in the event of a sudden step perturbation, the force-velocity relation would adjust the muscle fiber force in response to the new impact velocity. With this velocity preflex, that is, a mechanical

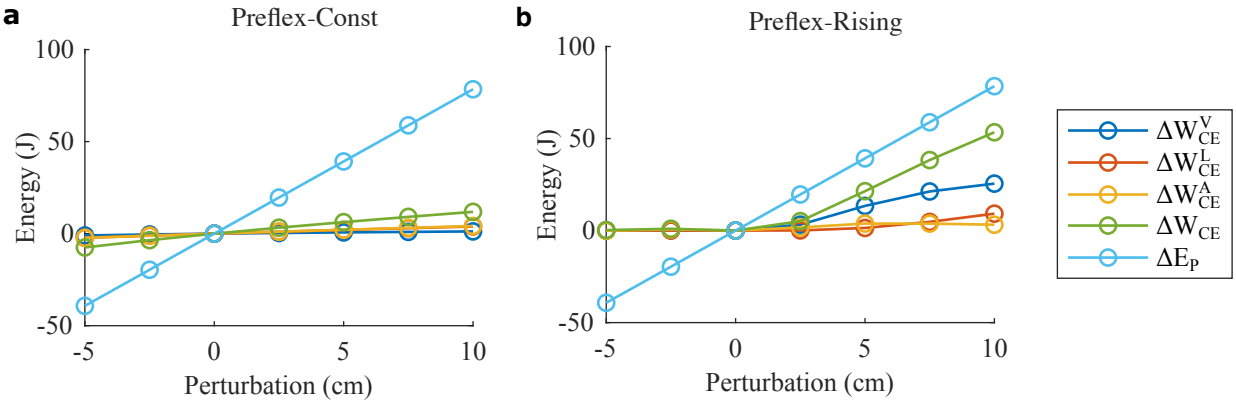

Figure 4.5: Change in muscle fiber work caused by each step perturbation (circles) with respect to the reference hopping condition. ΔE_P (light blue) is the amount of work adjustment required to reject, within the preflex duration, the potential energy change caused by each step perturbation. ΔW_{CE} (green) is the net change in muscle fiber work. ΔW^V_{CE} (dark blue) is the change in muscle fiber work induced by the force-velocity relation; ΔW^L_{CE} (red) by the force-length relation; ΔW^A_{CE} (yellow) by the muscle excitation. (a) Preflex-Const and (b) Preflex-Rising.

velocity feedback embedded in the muscle fibers, the force-velocity relation can mitigate delays caused by neuro-transmission and reduce feedback control by the nervous system.

By explicitly quantifying the preflex response of muscle fibers during perturbed hopping with constant muscle stimulation around impact (Preflex-Const), we observed that the muscle fiber force does, indeed, adjust to the perturbed impact velocity because of the force-velocity relation (fig. 4.4a) as previously hypothesized. However, this regulatory action of the force-velocity relation was small and quickly faded (< 5 ms) during preflexes (Figure A1.1a, in supplementary material). As a result, the force-velocity relation produced minimal adjustment of the muscle work and had little effect on rejecting the potential energy induced by each step perturbation (fig. 4.5a).

One aspect that seems to limit the contribution of the force-velocity relation is its flattening shape along the eccentric side (fig. 4.1d). It predicts a diminishing influence on the muscle fiber force for sufficiently large muscle fiber velocities. Inspection of the time traces (Figure A1.1-A1.2, in supplementary material) confirms that shortly after touchdown, a rapid increase in the stretching velocity of muscle fibers occurs, leading to a convergence of multiple F^V_{CE} trajectories. This convergence explains why work loop trajectories of Preflex-Const trials were mostly aligned during the preflex duration (fig. 4.3a).

Our Preflex-Const tests reveal a limited energy regulation by the mechanical damping action associated with the force-velocity relation. Still, some energetic adaptation is achieved (fig. 4.5a), but this is rather a result of the change in muscle fiber stretch during preflexes, as can be seen from the area under the thick lines in the work loops (fig. 4.3a).

Overall, our simulation results of Preflex-Const support the literature hypothesis about a velocity preflex induced by the force-velocity relation in musculoskeletal models. We also demonstrate its inefficacy in regulating ground perturbations in a purely passive mechanical manner. In contrast, the force-velocity relation becomes the predominant element in regulating perturbed hopping with Preflex-Rising. Here, a minimalist, low-level stimulation was sufficient to enhance the regulating action of the force-velocity relation, resulting in surprisingly complex stabilizing mechanics.

4.4.2 Details about perturbation rejection by Preflex-Rising

Preflex-Rising produced better regulation of step-down perturbations. Its central aspect is the rising stimulation that amplified regulatory effects of the force-velocity relation (fig. 4.5b). In human locomotion, such rising stimulation can be found in knee extensor muscles (Moritz and Farley, 2004; Müller et al., 2015, 2020). Several previous computer simulations applied such control when investigating the role of the force-velocity relation or stability of gait (Dzeladini et al., 2014; Gerritsen et al., 1998; Haeufle et al., 2010, 2018; John et al., 2013).

The underlying regulatory mechanism generated by Preflex-Rising shows an intricate interaction between muscle fiber force and velocity profile. The central effect is that increasing drop heights postponed ground impact and, therefore, lead to more excited muscle fibers at touchdown. On the one hand, the muscle is stiffer with rising activity and, therefore, resists shifting to eccentric velocities, where more energy can be dissipated. On the other hand, the rising activity consistently increased the force of the muscle fiber at impact with larger step-down perturbations. Furthermore, with more excited muscle fibers, the force-velocity relation scales vertically so that the change in muscle fiber velocity produces a larger response from the force-velocity relation, as shown in fig. 4.4d. This scaling effect was already observed in van der Krogt et al. (2009). Combined, these effects result in a substantial adaptation of the preflex energy dissipation to the perturbation height (fig. 4.5b).

Now the intricate details: Preflex-Rising initiated a muscle contraction before impact, which led to an initial concentric contraction and then eccentric stretch during the preflex duration (Figure A1.2b, in supplementary material). With increasing step-down perturbations, this initial contraction starts earlier and, depending on the timing of the perturbation, it shifts the shortening velocity of the fibers at impact (Figure A1.2b, in supplementary material). For medium perturbations, the contraction velocity was larger than in reference hopping. For large perturbations, it was smaller, as muscle-tendon forces approached equilibrium (the knee is fixed in flight). In all cases, the ground impact causes a shift in fiber velocity towards eccentric velocities. In particular, larger step-down perturbations produced a faster transition to the eccentric mode and higher maximum eccentric velocity during preflexes (Figure A1.2b, in supplementary material). During Preflex-Rising, the dynamic effect of the step-down perturbation, which caused more eccentric stretch of the muscle fibers due to larger impact velocities, overcame the muscle fiber stiffening caused by the increasing muscle activity at touchdown. In combination with the faster rising of F_{CE}^{V} due to the scaling of the force-velocity relation (Figure A1.1b, in supplementary material), this specific trend in velocity profile resulted in muscular power generation that rose earlier, faster and created a larger area during the preflex phase with increasing step-down height (Figure A1.3b, in supplementary material).

It is worth noticing that the intricate details of how knee joint flexion is transmitted into fiber stretch velocity depend on the internal stiffness of muscle fibers and tendons. At landing, changing the tendon's stiffness affects both the way the impact velocity is transmitted to the muscle fibers and the overall stiffness of the muscle-tendon unit. These two aspects affect v_{CE} in opposite ways and can (potentially) balance each other. From one side, more compliant tendons will decouple the muscle fibers from the joint action (Roberts and Azizi, 2010), thus favoring reduced v_{CE} values just after landing. However, the muscle-tendon unit will be more compliant overall, meaning that reference hopping will occur at higher hopping heights due to more elastic recoil during the stance phase. This increased hopping height favors higher impact velocities and, as a consequence, higher v_{CE} values. Changing the tendon's stiffness also alters how much v_{CE} changes following a step perturbation. Stiffer tendons will comport larger changes in v_{CE}. Notice, however, that the force-velocity relation has a plateau on its eccentric

side (fig. 4.1d). For this reason, larger increments in v_{CE} comport minor adjustment of F_{CE} after a certain range of v_{CE} values is reached (fig. 4.4c shows that this reduced F_{CE} adaptation occurs already for $v_{CE} = 0.1\,\text{m/s}$). Therefore, we expect that a different compliance of the tendon affects the hopping pattern of our model and the operative point on the force-velocity relation at touchdown, and, thus, the magnitude of the force-velocity contribution. However, we do not expect tendon compliance to affect our main finding, i.e., that the force-velocity relation contributes to a velocity preflex in the presence of low-level feedforward stimulation. This is because feedforward stimulation will always contribute to scale the force-velocity relation, regardless of the force-velocity state at landing and during the preflex duration. As a future research direction, we propose to quantify the force-velocity contribution over a range of different muscle fiber to tendon length ratios (Mörl et al., 2016), which could give insights into the role of different muscle-tendon unit morphologies in locomotion.

4.4.3 Muscle model considerations

The muscle model used here is a variant of a macroscopic Hill-type muscle model described in Haeufle et al. (2014b). Originally, Archibald Hill developed a mathematical formulation to fit his experimental data on frog muscle fiber contraction (Hill, 1938). Later models included explicit elements, i.e., mathematical formulations, for the tendon and connective tissue parts too. Several different arrangements of such mechanical elements exist, all being in series or parallel to the fiber formulation. The model used here additionally includes an explicit damper element (SDE) in series to the contractile element (CE). This Hill-type muscle model with added SDE fits the biological data for all muscle contraction experiments better than muscle models without added serial damper (Günther et al., 2007). Additionally, the added SDE allows to observe an impact velocity distribution between the fiber and the tendon part. A purely elastic tendon formulation, as used in other variants of Hill-type models, does not provide such capability. Consequently, the Hill-type model with an added damper in series has shown great accuracy when modeling dynamic motions. Similar to the parallel damping element in Millard et al. (2013), the serial damper element in Haeufle et al. (2014b) is intended to capture the macroscopic effects of viscosity in muscle-tendon units, but in series to the fiber. It is, therefore, ideally suited for the analyses of such a contribution on a macroscopic level.

The Hill-type muscle model used in this study also replicates the flattening of the force-velocity relation at high fiber-stretching velocities, which is consistent with previous experimental research on the eccentric contraction of the muscle fibers (Joyce et al., 1969). However, the data on eccentric contractions is relatively sparse, and the real dynamics are more complicated, especially its inter-dependency with the force-length relation (Till et al., 2008). Nonetheless, our – or similar – implementations of the force-velocity relation allows to simulate realistic locomotion patterns (Geyer and Herr, 2010; John et al., 2013), which are further used to investigate perturbations in locomotion (Gerritsen et al., 1998; Günther and Ruder, 2003; Haeufle et al., 2018; Schreff et al., 2022; Song and Geyer, 2017).

Generally, Hill-type muscle models are macroscopic, phenomenological approximations of biological muscle-tendon complexes. As such, they present several shortcomings when compared to experimental data of muscle fibers' contraction. For example, experimental studies show that parameters for Hill-type models, which are usually obtained from maximally activated muscles, adjust based on complex relations with the activation level (Holt and Azizi, 2016). For this reason, Hill-type models are less accurate for simulating muscle force with variable excitation level, as occurring in our study. Over the last years, attempts have been made to derive the macroscopic formulation of muscle-tendon dynamics from a microscopic, biophysical perspective (Günther et al., 2018; Rosenfeld and Günther, 2014). Thus, the

macroscopic force-velocity relation, as used here, becomes the result of a first principles ansatz and a stringent derivation using few additional assumptions (Günther et al., 2018). Looking inside biophysical models reveals explicit formulations of damping components inside the CE. Such formulations would facilitate the research presented here by enabling to directly quantify the damping rate at the muscle fiber level. Unfortunately, the existing models that incorporate explicit damping cannot yet predict the mechanical response of muscles during eccentric contractions (Günther et al., 2018; Rosenfeld and Günther, 2014). This drawback leaves these more physiological-biophysical models currently insufficient to apply here, as the eccentric contraction is the main working mode during preflexes.

4.4.4 Implication of our results

Our study shows that the force-velocity relation contributes with a velocity preflex to reject unexpected ground perturbations, but it needs low-level control for maximum efficacy. This is consistent with van der Krogt et al. (2009), where it was observed that time-based muscle stimulation drives the regulating response of muscle fiber viscoelasticity to variations in ground stiffness. In our simulation, the basic rising stimulation considered in Preflex-Rising was sufficient to amplify the regulatory effects of the force-velocity relation. However, even more simple stimulation strategies might produce similar effects. For example, Preflex-Const with prestimulation level proportional to the drop height, i.e, with tunable u_0 (see eq. (4.3)), will produce the same vertical scaling of the force-velocity relation observed in Preflex-Rising, potentially leading to similar stabilizing effects. From a biological perspective, our findings raise the question of how much morphological computation, as described in Ghazi-Zahedi et al. (2016); Zahedi and Ay (2013), is carried by the force-velocity relation, and whether a trade-off exists between the force-velocity relation's stabilizing effect and control effort. From a technical perspective, understanding low-level control of the force-velocity relation can promote bio-inspired designs for assistive robotic devices, as numerous studies have suggested that implementing (tunable) dampers can improve the system performance and facilitate robustness against external perturbations (Mo et al., 2020; Monteleone et al., 2022).

Previous research has qualitatively described a velocity preflex produced by the muscle fiber's force-velocity relation to regulate locomotion (Gerritsen et al., 1998; Geyer et al., 2003; Haeufle et al., 2010). With our quantitative analysis, which was made possible by our decomposition algorithm (see Section 4.2.3), we could test the mechanical principles expected to produce such a velocity-based regulation by preflexes. Our study shows that preflex regulation of perturbed hopping emerges from a complex coupling between muscle fiber stretching trajectories and muscle fiber force. The amount of preflex force produced by muscle fibers depends on the muscle fiber length-velocity state, which is in turn affected by the action of the preflex force on the knee joint flexion. In addition to low-level control, this intricate interaction is likely affected by several elements, such as ground impact dynamics, terrain stiffness, leg geometry, and internal stiffness of the muscle-tendon unit. Therefore, future studies could consider more comprehensive musculoskeletal models to unveil the functionality of muscular preflex and to allow direct comparison with experimental studies, such as the running investigation carried out in Daley et al. (2009). In this context, the decomposition algorithm that we present here can become a central tool, as it permits to explicitly quantify the force components associated with muscular preflexes despite the model's complexity.

5 Influence of the operative side of the force-velocity relation on preflexes

As described in section 3.4.1.1, the force-velocity relation presents a flattening profile (plateau) for high eccentric velocities. The analysis in Chapter 4 suggests that this flattening profile reduces the mechanical damping that the force-velocity relation can produce without neuromodulation. As a result, the effectiveness of biological damping might be sensitive to the reference impact velocity of periodic locomotion. We hypothesized that if the touchdown velocity during periodic locomotion lies on the flattening side of the force-velocity relation (plateau-side), the preflex regulation in response to step perturbations is compromised. This chapter (Chapter 5) explores this hypothesis by using the simulation framework defined in Chapter 4. We selected numerous Preflex-Const stimulation settings to generate periodic hopping with different touchdown velocities. We then classified these conditions based on whether the touchdown velocity was on the rising- or plateau-side of the force-velocity relation. Surprisingly, we found lower periodic hopping stability for the rising-cases. However, the detailed analysis of two single cases (one plateau-case and one rising-case) supported our original hypothesis, revealing reduced regulation of touchdown force and preflex work for the plateau-case.

Note: a large portion of this chapter uses content from our pre-print in *arXiv* (Izzi et al., 2022). For details on this pre-print, including the list of authors and my contribution, see Section 2.2.1.

5.1 Introduction

Simulations of musculoskeletal models have shown that the force-velocity relation contributes to the robustness of hopping and walking (Gerritsen et al., 1998; Haeufle et al., 2010). By embedding nonlinear viscosity in a muscle-driven system (Geyer et al., 2003; Haeufle et al., 2010), the force-velocity relation is expected to mitigate sudden perturbations without additional control load on the central nervous system. As such, the force-velocity relation could play a major role in the muscle preflex response during fast, agile locomotion. For example, it may facilitate the quick rejection of step perturbations by instantly adapting the muscle force to a new impact velocity, similar to what has been observed when implementing a parallel viscous damper in a legged system (Abraham et al., 2015; Heim et al., 2020; Mo et al., 2020). According to Joyce et al. (1969); Till et al. (2008), however, the force-velocity relation may plateau at high fiber-stretching velocities. This could result in an undesirable decrease in its damping capacity during severely perturbed conditions, for which viscous stabilization could be particularly beneficial. It is still unclear how and to what extent periodic hopping with touchdown velocity on this plateau-side affects the preflex regulation that the force-velocity relation can produce in response to ground perturbations. In this study (Chapter 5), we use the computational framework developed in Chapter 4 to quantify how the mechanical damping response of the force-velocity relation

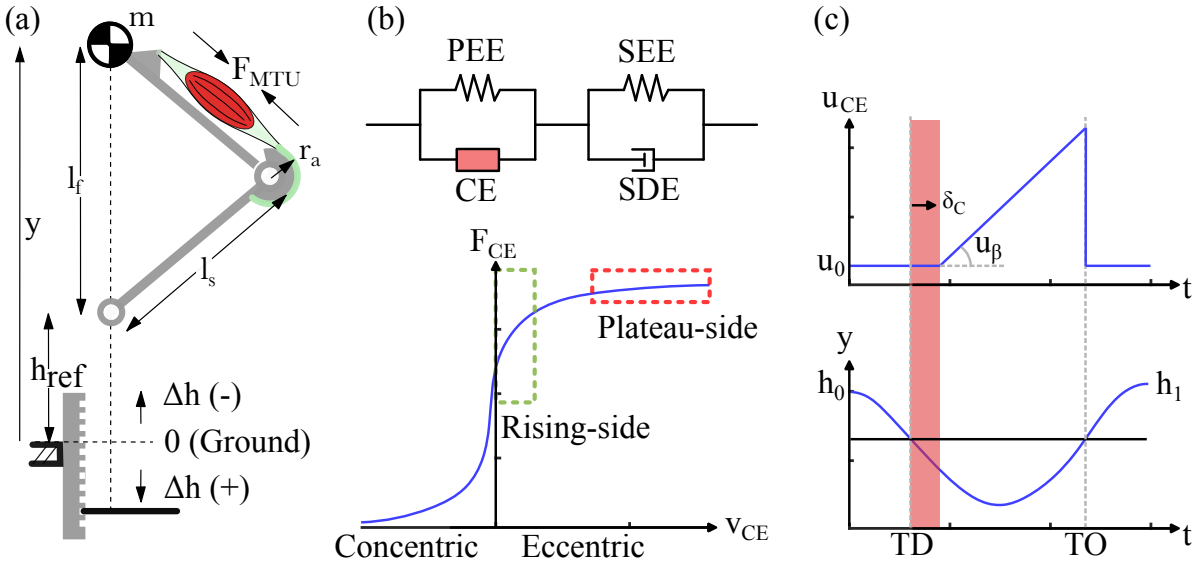

Figure 5.1: (a) For this study, we implemented the same neuro-musculoskeletal model described in Chapter 4. Thus, refer to fig. 4.1's caption for more details. (b) Architecture of the Hill-type muscle model implemented in our study (note: the model was developed in Haeufle et al. (2014b)). In this study, we divided the eccentric portion ($v_{CE} > 0$ m/s) of the force-velocity relation into two zones to classify periodic hopping conditions based on their operative velocity at touchdown. Inside the plateau-side, the force-velocity relation is mostly flat, and hence little variation in muscle fiber force (F_{CE}) occurs as a result of changes in muscle fiber velocity (v_{CE}). The opposite is true within the rising-side. (c) To stimulate the muscle and generate periodic hopping, we implemented Preflex-Const stimulation, as described in Chapter 4. We systematically adjusted u_0 and u_β to find periodic hopping conditions in the rising-side (rising-cases) or plateau-side (plateau-cases). The preflex duration (defined by δ_C) was equal to 30ms for all conditions. TD indicates touchdown, TO take-off. h_0 is the initial drop height, and h_1 is the drop height at the end of the hopping cycle.

depends on its operational velocity at touchdown.

5.2 Methods

The neuro-musculoskeletal model and most of the methods used in this study are identical to those described in Chapter 4. In this section, only the differences will be reported. For all remaining information, refer to section 4.2.

5.2.1 Definition of plateau- and rising-side

As shown in Fig.5.1b, the force-velocity relation comprises both positive and negative muscle fiber velocities. Negative velocities ($v_{CE} \leq 0$ m/s) define the concentric region of the force-velocity relation, where muscle contraction involves shortening muscle fibers. Positive velocities ($v_{CE} > 0$ m/s) form the eccentric region, where muscle contraction occurs with lengthening muscle fibers. The eccentric region of the force-velocity relation was the focus of our analysis. This was because, with the Preflex-Const stimulation, muscle fibers are in static equilibrium before touchdown. As impact occurs, knee flexion causes the extensor muscle to lengthen, resulting in eccentric contraction of the muscle model around

touchdown.

For our analysis, we separated the eccentric region into two sides of interest: the rising-side and the plateau-side. Along the rising-side, a deviation in muscle fiber velocity produces a large deviation in muscle fiber force (F_{CE}), while along the plateau-side, F_{CE} mostly saturates. Mathematically, we defined these two sides as:

$$\begin{cases} \text{rising-side} & \text{if } F_{CE}(t_{TD}) < 0.95\,\tilde{F}_{CE} \\ \text{plateau-side} & \text{if } F_{CE}(t_{TD}) > 0.99\,\tilde{F}_{CE} \end{cases} \tag{5.1}$$

where t_{TD} is the touchdown time, and $\tilde{F}_{CE}$ is the force that the contractile element would produce if $v_{CE} = 1.5\,\text{m/s}$ at ground impact. Therefore, $\tilde{F}_{CE}$ represents the largest expected force that the contractile element can produce at touchdown. Fig.5.2 further visualizes our classification approach. We hypothesized that if periodic hopping occurs with muscle fibers operating within the rising-side at touchdown, the preflex response would effectively adjust to ground perturbations; in contrast, we expected reduced adjustment if within the plateau-side.

5.2.2 Experimental procedure

In this study, we only considered Preflex-Const stimulations (see section 4.2.2 for details). First, we identified periodic hopping conditions for a grid of stimulation inputs $u_0 = [0.01 : 0.01 : 0.2]$ and $u_\beta = [1 : 1 : 20]$. For each $\{u_0, u_\beta\}$ input pair, we used optimization to compute the drop height (h_{ref}) that produces the smallest change in subsequent apex height (h_1). We used $min(h_1 - h_{ref})^2$ as the cost function and *fmincon* (Matlab R2018a) as the optimizer algorithm. We discarded all input pairs producing unstable hopping, which we defined to occur when $h_{ref} \leq 1\,\text{cm}$ or $|h_1 - h_{ref}| \geq 0.01\,\text{mm}$. We classified each periodic hopping condition according to the operative side of the force-velocity relation at touchdown, as defined in eq. (5.1). Furthermore, we measured the stability of each periodic hopping by applying a small perturbation (Δ_s) to the reference hopping height and then computing

$$S = \frac{h_1^* - h_{ref}}{\Delta_s} \tag{5.2}$$

where h_1^* is the return apex height following the perturbation. $|S|$ values closer to 0 indicate more (asymptotically) stable periodic hopping. For completeness, we tested bidirectional perturbations ($\Delta_s = \pm 0.1\,\text{cm}$).

For a more detailed analysis, we selected two periodic hopping conditions, one rising-case and one plateau-case. The rising-case was the hopping condition studied as Preflex-Const in Chapter 4. The plateau-case used the same Preflex-Const stimulation rate (u_β) but lower prestimulation (u_0). For each of these two conditions, we tested the mechanical response of the muscle fibers for an array of step perturbations $\Delta h = [-5, -2.5, 0, 2.5, 5, 7.5, 10]$ cm, where a negative sign indicates a step-up and a positive sign indicates a step-down perturbation. Considering that our model has a reference leg length $l_f = 0.99\,\text{m}$, these ground perturbations were within [-5,10]% l_f range. As in Chapter 4, the focus of our in-depth analysis was the preflex duration, which we defined as the first 30 ms following touchdown. Furthermore, we applied the same decomposition algorithm to study the adjustment of touchdown force and preflex work to each perturbation, isolating and quantifying the specific contribution of the force-velocity relation.

5.3 Results

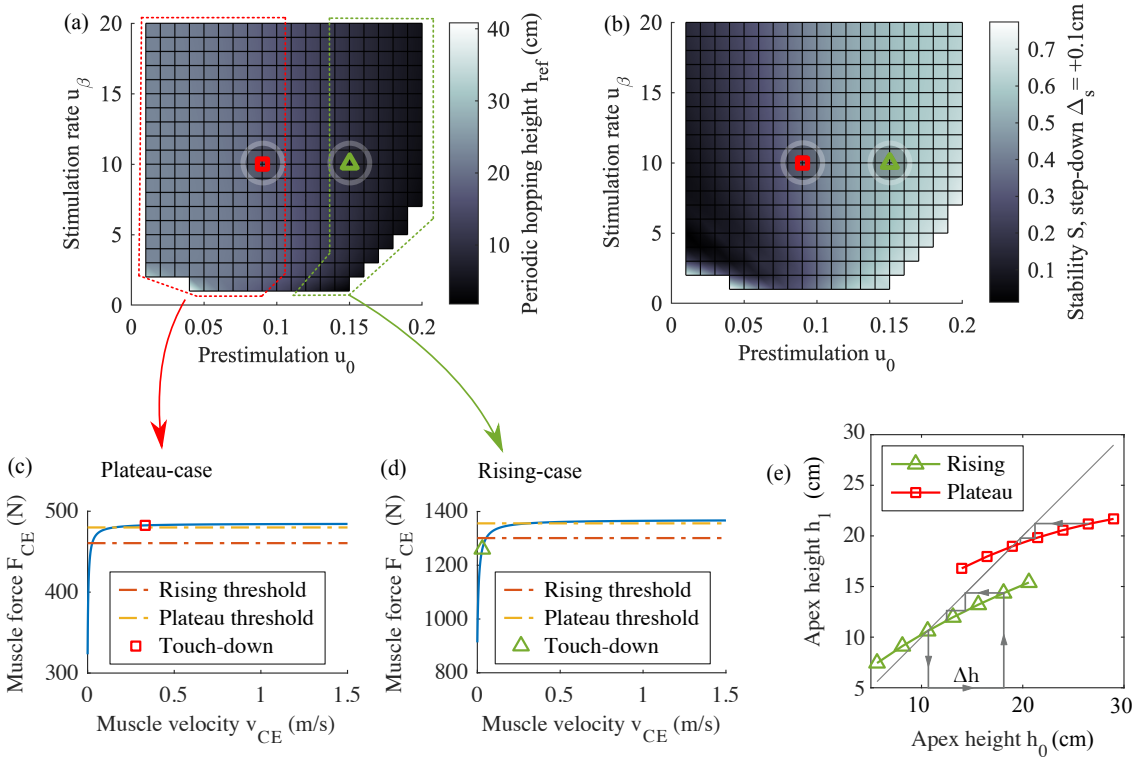

Figure 5.2: (a) Periodic hopping heights h_{ref} for different stimulation input pairs $\{u_0, u_\beta\}$. Preflex-Const (as defined in section 4.2.2) was the stimulation protocol for all conditions. Enclosing lines separate the plateau-cases from the rising-cases, i.e., conditions with the force-velocity relation operating on either the plateau-side or rising-side at touchdown. The square and triangle symbols indicate the two hopping conditions that we selected for in-depth analysis: one plateau-case and one rising-case, respectively. (b) Stability analysis for step-down disturbance ($\Delta_s = 0.1$ cm). Stability analysis for step-up disturbance ($\Delta_s = -0.1$ cm) yielded similar results. (c-d) Shape of the force-velocity relation at touchdown for the selected plateau-case and rising-case. The markers (square and triangle) indicate their specific force-velocity states at touchdown. Dashed lines indicate the thresholds separating the plateau- and rising-side, according to eq. (5.1). A rising-case occurred when the $\{F_{CE}, v_{CE}\}$ state at touchdown was below the rising threshold; a plateau-case occurred when the $\{F_{CE}, v_{CE}\}$ state at touchdown was above the plateau threshold. (e) Apex return map for the selected plateau- and rising-case, with h_0 indicating each starting apex height and h_1 the associated return apex after one hopping cycle. Intersections with the diagonal line indicate periodic hopping heights. More horizontal inclinations indicate faster perturbation rejection, requiring fewer hopping cycles to converge to reference hopping.

5.3.1 Periodic hopping analysis

Out of 400 tested conditions, we found 381 input pairs $\{u_0, u_\beta\}$ to produce periodic hopping (Fig.5.2a), which was always asymptotically stable (Fig.5.2b). Stable periodic hopping was possible with the touchdown state $\{F_{CE}, v_{CE}\}$ anywhere on the eccentric side of the force-velocity relation: either within the plateau-side, rising-side, or in-between (Fig.5.2a). We found a sharp clustering of plateau-cases and

rising-cases, which predominantly depended on the muscle prestimulation level u_0 (see enclosing dotted lines in Fig.5.2a). Plateau-cases were characterized by larger hopping heights than the rising-cases (21.2 ± 2.5cm and 7.9 ± 2.6cm, mean $\pm$ st.d. respectively). In contrast to our expectation, plateau-cases were also more stable than rising-cases ($|S|$, mean $\pm$ st.d.: 0.25 ± 0.13 for plateau-cases vs. 0.60 ± 0.04 for rising-cases).

5.3.2 Preflex response (in-depth analysis)

To investigate muscle fibers' preflex response to ground perturbations, we selected two periodic hopping conditions, one with muscle fibers' touchdown velocity inside the plateau-side of the force-velocity relation ($u_0 = 0.09$, $u_\beta = 10$), and one inside the rising-side ($u_0 = 0.15$, $u_\beta = 10$) (Fig.5.2c,d). For clarity, we will refer to these two experimental conditions as plateau-case and rising-case, respectively. These two conditions served as baseline scenarios for our analysis. Notice that the rising-case in this study is the same Preflex-Const hopping scenario presented in Chapter 4. Instead, the plateau-case was a novel hopping condition that we obtained by applying the same stimulation as in the rising-case, but with a lower prestimulation value u_0.

The plateau-case featured about 19 cm reference hopping height (h_{ref}) and 338 ms stance duration, while the rising-case had about 11 cm h_{ref} and 255 ms stance duration. Muscle pretension force (F^0_{CE}) values were 323 N and 913 N for the plateau- and rising-case, respectively. Each reference case was tested against ground perturbations $\Delta h = [-5, -2.5, 0, 2.5, 5, 7.5, 10]$ cm, for a total of two step-up (negative sign) and four step-down perturbations (positive sign). Inspection of the apex return map confirms stronger asymptotic stability for the plateau-case (Fig. 5.2e). Leg compression during the stance duration was never sufficient to engage the parallel elastic element (PEE) in either the plateau- or rising-case, perturbed or not. Therefore, according to eq. (3.1), muscle fiber force (F_{CE}) always represented the net force of the muscle-tendon-unit in our in-depth analysis.

Across all the tested conditions, the force-velocity relation produced an instantaneous, breaking force at touchdown (F^V_{CE} in Fig.5.3a,d). This was expected because the massless leg and the instantaneous ground impact generate a jump in muscle-tendon velocity (v_{MTU}) and thus muscle fiber velocity (v_{CE}); in contrast, muscle geometry and stimulation level stay constant at touchdown (see eq.4.8). The jump in muscle force at touchdown was substantial: during unperturbed hopping, F^V_{CE} was equivalent to approximately 49% (plateau-case) and 38% (rising-case) of the original values of muscle pretension (F^0_{CE}).

To check for a possible viscous-like response produced by the force-velocity relation, we looked at how F^V_{CE} changed with different step perturbations. For the rising-case, the touchdown value of F^V_{CE} adapted to the ground perturbation intensity, ranging from 238 N to 436 N (26% and 48% of the original muscle pretension). However, a similar adaptation was absent for the plateau-case. This finding confirms our hypothesis that the initial adaptation to ground perturbations produced by the muscle fibers depends on the operative side of the force-velocity relation at touchdown.

The adaptation of F^V_{CE} observed for the rising-case was not proportional to the change in v_{CE} that followed each step perturbation, as one would expect from an ideal viscous response (Fig. 5.3d vs. e). While the v_{CE} increments grew in size with higher drop heights, the corresponding F^V_{CE} increments lessened. These two opposite trends imply that incremental impact velocities move the touchdown state of the force-velocity relation towards the plateau-side, thereby reducing the touchdown adaptation of F^V_{CE}.

Impact transmission to the muscle fibers differed between the plateau- and rising-case. During the

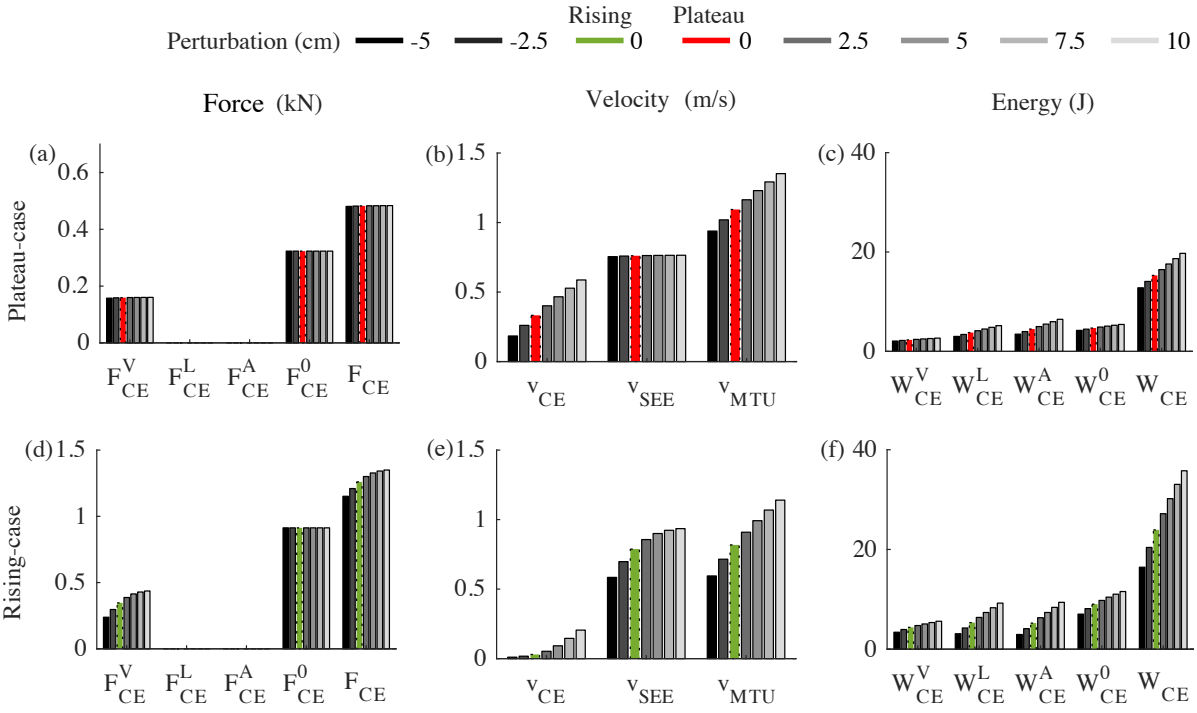

Figure 5.3: (a,d) Muscle fiber force at touchdown, separated into the contribution of: the force-velocity relation (F^V_{CE}), force-length relation (F^L_{CE}), muscle activity (F^A_{CE}), and muscle prestimulation (F^0_{CE}). For the sake of comparison, F_{CE} is the net force produced by the muscle fibers at touchdown ($F_{CE} = F^V_{CE} + F^L_{CE} + F^A_{CE} + F^0_{CE}$). (b,e) Touchdown muscle fibre velocity (v_{CE}), tendon velocity (v_{SEE}) and muscle-tendon unit velocity ($v_{MTU} = v_{CE} + v_{SEE}$). (c,f) Energy dissipated by the muscle fibers throughout the preflex duration, separated into the contribution of: the force-velocity relation (W^V_{CE}), force-length relation (W^L_{CE}), muscle activity (W^A_{CE}), and muscle prestimulation (W^0_{CE}). For the sake of comparison, W_{CE} is the net energy dissipated by muscle fibers ($W_{CE} = W^V_{CE} + W^L_{CE} + W^A_{CE} + W^0_{CE}$). The results illustrate the plateau-case (a-c) and rising-case (d-f) under different levels of ground perturbation.

plateau-case, the dependence of v_{CE} on the step perturbation intensity closely matched the trend of v_{MTU}, while v_{SEE} remained about constant across conditions (Fig.5.3b). This means that in the plateau-case, the change in impact condition almost exclusively affected the muscle fiber velocity and not the tendon velocity. In comparison, during the rising-case, v_{MTU} showed a profile more similar to that of v_{SEE}, especially during step-up and mild step-down perturbations (Fig.5.3e). This means that the tendon velocity was now the most affected by the ground perturbation at touchdown. Overall, these results demonstrate that impact velocity and muscle fiber velocity at touchdown are not directly proportional. Rather, there is a complex mapping that depends on the operating conditions of the force-velocity relation and on the level of prestimulation. This further supports our hypothesis that the operative side of the force-velocity relation influences muscle fibers' behavior.

In spite of the differences observed at touchdown, both the plateau-case and rising-case produced stabilizing responses within the preflex duration, as indicated by the finding that the total dissipated energy (W_{CE}) adjusted as a function of the step perturbation intensity (Fig.5.3c,f). For the plateau-case, the highest step-up and step-down perturbations resulted in a W_{CE}'s change of −2.5 J and 4.4 J, respectively; −7.5 J and 11.9 J for the rising-case. This means that by the end of the preflex duration,

the plateau-case rejected around 6.4% and 5.6% of the change in system energy caused by the biggest step-up and step-down perturbations, respectively; the rising-case rejected 19.1% and 15.1%. This indicates that in terms of net dissipated energy during preflexes (W_{CE}), muscle fibers rejected ground perturbations better in the rising-case.

The force-velocity relation, along with the force-length relation, muscle pretension, and even muscle activity, all contributed to counter the step perturbation during the preflex phase in the form of negative work. It is worth noting that the negative work produced by the muscle activity (W^A_{CE}) was not zero during preflexes, despite the constant stimulation signal ($u = u_0$). This is because the activation dynamics include an internal muscle-length dependency that alters muscle activity and, thus, muscle force according to changes in muscle fiber length. The energy dissipated by the force-velocity relation (W^V_{CE}) contributed the least to the total dissipated energy (W_{CE}) across almost all examined scenarios. Changes in W_{CE} in response to each step perturbation were mainly driven by the force-length relation (W^L_{CE}) and activity-induced changes (W^A_{CE}) (Fig.5.3c,f). However, compared to the plateau-case, the rising-case showed a more than threefold adaptation of W^V_{CE} to the ground perturbation intensity, ranging from 3.4 J to 5.6 J compared to 2.1 J and 2.7 J, respectively.

To further understand how the force-velocity relation dissipates energy during preflexes, we inspected the time progression of the associated force component (F^V_{CE}), fiber velocity (v_{CE}), and power (P^V_{CE}) (Fig.5.4). For both the plateau- and the rising-case, F^V_{CE} trajectories showed minimal dependence on the ground perturbation level (Fig.5.4a,d). This occurs because v_{CE} rapidly rose following an impact (Fig.5.4b,e), causing the muscle to operate outside the rising-side of the force-velocity relation throughout most of the preflex duration (see markers in Fig.5.4a,d). As a consequence, even in the rising-case, F^V_{CE} trajectories exhibit little variability early after impact. On the contrary, the trajectory of v_{CE} changed noticeably across ground perturbations (Fig.5.4b,e), with trends similar to those of P^V_{CE} (Fig.5.4c,f). This means that changes in the muscle fiber velocity's profile, rather than adjustments in F^V_{CE} trajectories, were primarily responsible for adjusting the energy dissipated by the force-velocity relation to each step perturbation. The fact that v_{CE} adjustments played a major role in energy regulation during the preflex phase is also supported by the finding that the energy dissipated by muscle pretension (W^0_{CE}) changed across step perturbations (Fig.5.3c,f). Since F^0_{CE} was constant throughout the preflex duration, only changes in v_{CE} trajectory can explain the observed W^0_{CE} adjustment.

5.4 Discussion

In this study, we quantified the capacity of the Hill-type force-velocity relation to regulate ground perturbations during vertical hopping. Our analysis focused on the early stance duration (preflex phase, $\delta_C = 30$ ms after touchdown), during which a viscous-like response from the muscle fibers was expected to play a significant role (Geyer et al., 2003; Haeufle et al., 2010). We hypothesized that the contribution of the force-velocity relation to the perturbation rejection would depend on its initial state at touchdown. To test this hypothesis, we simulated a variety of periodic hopping conditions having the force-velocity relation operating with different $\{F_{CE}, v_{CE}\}$ states at touchdown. Of this set, we analyzed in-depth two single cases: a plateau-case, where $\{F_{CE}, v_{CE}\}$ at touchdown was within the flattening side of the force-velocity relation, and a rising-case, where $\{F_{CE}, v_{CE}\}$ was on the steep incline (Fig.5.2c,d). We predicted that by producing more viscous damping, the rising-case would reject ground disturbances better than the plateau-case.

Our results support this hypothesis, showing that the rising-case could better adjust muscle fibers'

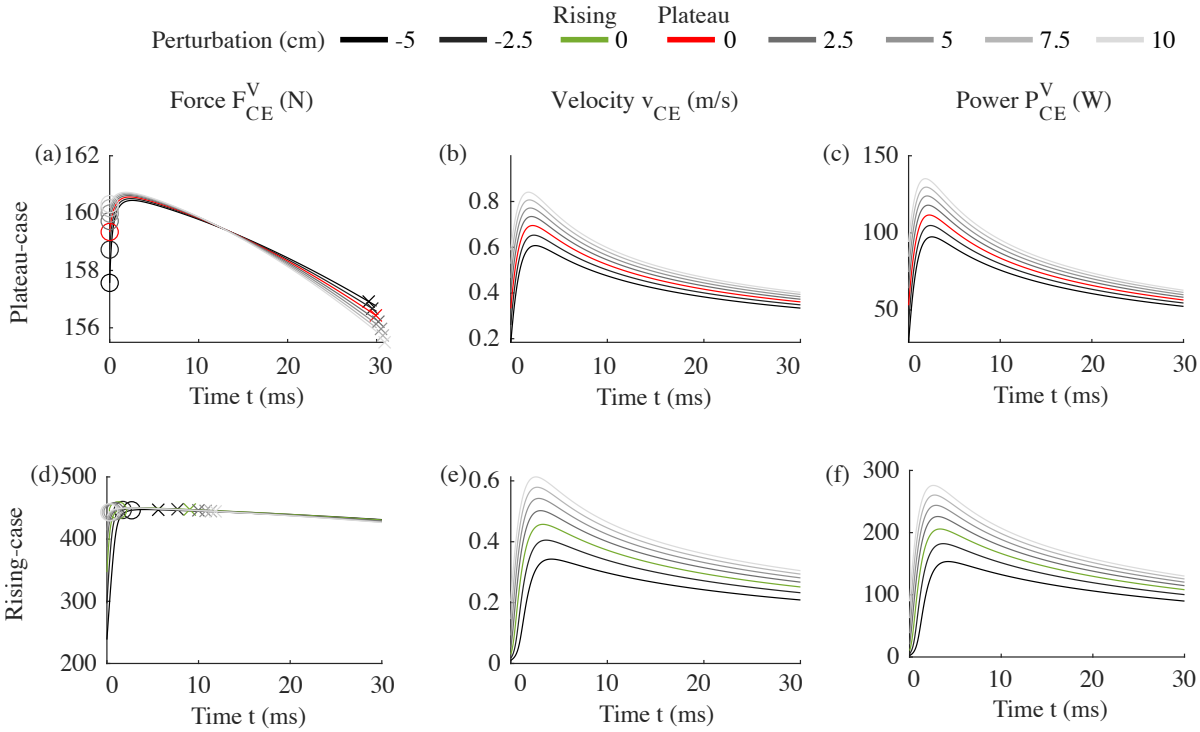

Figure 5.4: (a,d) Time trajectories of the force contribution from the force-velocity relation (F^V_{CE}). Circles indicate the entry of the muscle state $\{F_{CE}, v_{CE}\}$ inside the plateau-side; crosses indicate the exit from the plateau-side. In no case did $\{F_{CE}, v_{CE}\}$ return to the rising-side for the remaining preflex duration. (b,e) Time trajectories of the muscle fiber velocity (v_{CE}). (c,f) Time trajectories of the power produced by the force-velocity relation: $P^V_{CE} = F^V_{CE} \cdot v_{CE}$. Positive values indicate energy dissipation (negative work). Results illustrate the plateau-case (a-c) and the rising-case (d-f) from touchdown to the end of the preflex duration and in response to various ground perturbation levels.

touchdown force (F_{CE}) and preflex work (W_{CE}) in response to step perturbations than the plateau-case. In the plateau-case, touchdown regulation of F_{CE} was diminished by a severe reduction in F^V_{CE} adjustments. Although each step perturbation caused a new muscle fiber touchdown velocity (v_{CE}), the flattening side of the force-velocity relation saturated the ability of muscle fibers to adjust their force to the new impact condition. Since the force-velocity relation is the only factor that can adjust muscle fiber force at touchdown when constant preflex stimulation is considered, lack of F^V_{CE} adjustments resulted in negligible F_{CE} regulation for the plateau-case's touchdown.

It is worth noting that the extra touchdown regulation of F^V_{CE} and thus F_{CE} that we observed during the rising-case diminished in magnitude as we tested larger step-down perturbations (Fig.5.3d). This finding occurs because our demarcation between rising-cases and plateau-cases is based on unperturbed hopping. As the impact velocity increased with increasing step-down perturbations, the touchdown $\{F_{CE}, v_{CE}\}$ state of the rising-case moved closer to the plateau-side. For example, when we perturbed the rising-case with $\Delta h = [5, 7.5, 10]$ cm, the operative state of force-velocity relation at touchdown was within the transition zone between the rising-side and plateau-side. As a result, the rising-case became

less capable of adjusting touchdown preflex forces as step-down perturbations increased in magnitude.

Concerning the preflex work, the negative work produced by the force-velocity relation (W^V_{CE}) also adjusted to step perturbations better in the rising-case compared to the plateau-case (Fig.5.3, c vs. f). However, it is important to note that the force-velocity relation had a minor role in the preflex adjustment of the total dissipated energy (W_{CE}) for both the rising- and plateau-case. From the largest step-up to the largest step-down perturbation, the change in W^V_{CE} accounted for only 11.4 % and 8.5 % of the change in W_{CE} for the rising- and plateau-case, respectively. This finding aligns with previous observations that a lack of neuronal modulation severely limits viscous-like preflex regulation by the force-velocity relation (Izzi et al., 2023; van der Krogt et al., 2009).

When we inspected the mechanisms of W^V_{CE} adjustment, we discovered that the force component produced by the force-velocity relation (F^V_{CE}) had minimal impact. F^V_{CE} time trajectories converged to the same profile shortly after touchdown. This indicates that outside the touchdown event, regulation of F^V_{CE} to the perturbation level was negligible. Surprisingly, we found this behavior not only for the plateau-case, where the force-velocity relation struggles to adjust muscle fiber force in response to changes in muscle fiber velocity, but also for the rising-case (Fig.5.4a,d). The lack of F^V_{CE} adjustment during the preflex phase of the rising-case was due to a rapid shift in the force-velocity relation's operative state early after touchdown. Shortly after touchdown, muscle fiber stretching velocity rapidly increased, causing the $\{F_{CE}, v_{CE}\}$ state to leave the rising-side and operate outside it for the rest of the preflex duration. This resulted in the force-velocity relation operating outside the rising-side for $99.2 \pm 1.1\%$ of the preflex duration— mean and st.d. across the seven ground heights that we tested. As a result, any initial touchdown regulation of F^V_{CE} that we observed in the rising-case quickly faded throughout the preflex phase.

During preflexes, the muscle fibers elongate, increasing muscle activity due to the dependence of the activation dynamics on the muscle fiber length. In our muscle model, the shape of the force-velocity relation scales with changes in either muscle fiber length or muscle activity, similar to what is described in Fig.7G-H in van der Krogt et al. (2009). When the curvature of the force-velocity relation becomes steeper, the overall sensitivity of muscle fiber force to muscle fiber velocity increases, potentially enhancing the capacity of modulating F^V_{CE} within the preflex phase. However, our results indicate that muscle fiber elongation and consequent increase in muscle activity were insufficient to alter the force-velocity relation's shape in a way to modulate F^V_{CE} trajectories within the preflex duration.

Instead, our data suggest that W^V_{CE} adjustment was primarily driven by changes in v_{CE} trajectory (Fig.5.4b,e). This indicates that energy regulation in response to step perturbations is mainly driven by the spontaneous change in leg kinematics that follows the altered impact conditions. This kinematic change could be sufficient to allow a constant damping force to adjust energy dissipation to the perturbation intensity. Enabling this constant damping force to be tunable in magnitude could further enhance the resulting energy regulation. These considerations present an intriguing new paradigm for implementing tunable mechanical damping in legged locomotion. For example, a simple friction damper with controllable braking force could be an effective technical solution for a hopping robot. A similar implementation could offer a simple alternative to more complex designs exploiting viscous damping, as those simulated in Abraham et al. (2015); Heim et al. (2020). As later discussed, this intuition motivated the simulation analysis in Chapter 7.

Surprisingly, hopping with the force-velocity relation on the rising-side at touchdown did not produce higher hopping stability. In fact, we found the plateau-cases to produce more stable hopping than the rising-cases (Fig.5.2b,e). As observed in Chapter 4, preflex regulation is limited with constant preflex stimulation. For this reason, it is possible that the level of preflex regulation in our plateau- and

rising-cases was small enough to play a marginal impact on the overall hopping stability. Therefore, we cannot exclude that mechanics beyond preflexes were more critical in determining hopping stability across the tested conditions.

Altogether, our analysis supports the findings of Chapter 4, demonstrating that previous explanations of how the force-velocity relation regulates ground perturbations (Geyer et al., 2003; Haeufle et al., 2010) may oversimplify more complex mechanisms, involving a nonlinear coupling between system kinematics, muscle inner mechanics, and perturbation intensity.

5.4.1 Limitations

Our study presents some limitations. Our muscle model (Haeufle et al., 2014b) lacks muscle characteristics that could influence preflex generation, such as history-dependent force production (Daley et al., 2009) and short-range stiffness (Rack and Westbury, 1974). Furthermore, we only investigated a single stimulation strategy. More realistic muscle models and alternative stimulations may modify the distribution of plateau- and rising-cases, along with their hopping stability and engagement of the force-velocity relation. Notice, however, that similar limitations were present in previous research on the topic (Gerritsen et al., 1998; Haeufle et al., 2010; van der Krogt et al., 2009).

The analysis in this study focuses on the influence of preflex regulation on hopping stability. Considering hopping stability as the only performance metric is limiting as locomotion is likely optimized for multiple objectives (Birn-Jeffery et al., 2014). Our choice was motivated by the simplified nature of vertical hopping, for which testing more complex metrics, such as resistance to falling, is challenging. Future studies should extend our analysis to more complex locomotion tasks, which would enable testing the influence of the force-velocity relation on additional performance metrics. Similarly, implementing more complex neuro-musculoskeletal models, including multiple muscles and ground-impact dynamics, would help validate our hypothesis over more realistic conditions.

In this study, we examined only two periodic hopping conditions in detail, one of which is coincident with Preflex-Const in Chapter 4. This limitation narrows the generalizability of our results and partially promotes alignment with previous findings (Chapter 4). Extending our in-depth analysis to more cases is thus necessary for further validation. Considering more periodic hopping conditions would also help exclude the existence of other stabilizing mechanisms beyond those discussed.

Despite these limitations, the findings in this study provide further evidence supporting a renewed interpretation of how the force-velocity relation produces preflexes. Specifically, this study highlights a previously unconsidered sensitivity of the force-velocity relation on its starting operative side at touchdown.

5.5 Conclusion

In summary, the intrinsic mechanical characteristics of muscle fibers play an essential role during agile locomotion. The zero-delay response to ground perturbations generated by muscle inner mechanics may be essential for compensating for neurotransmission delays, particularly early after touchdown. While it is argued that the force-velocity relation is a crucial factor in producing such an instantaneous response, we found that the touchdown state of the force-velocity relation influences the mechanical damping produced. Hopping with the touchdown state of the force-velocity relation on the flattening side reduced the regulation of muscle preflexes. Nevertheless, this did not lead to a reduction in hopping

stability. We also found that when preflex stimulation is constant, muscle mechanical damping mainly relies on the complex coupling between hopping kinematics and step perturbation intensity. From an engineering perspective, this finding suggests that a constant friction damper with tunable magnitude may be sufficient to provide some tunable mechanical damping in a legged robot.

6 Muscle Preflex Response to Perturbations in locomotion: In vitro experiments and simulations with realistic boundary conditions

The computational research in the previous two chapters relies on Hill-type muscle models. These models are common in computational studies of motion control. However, it is well known that they can only approximate the contraction dynamics of biological muscles. Hill-type models implement phenomenological functions that describe muscle mechanical properties (active and passive) during constrained experimental conditions. Therefore, they may perform poorly in predicting more dynamic contractions (Millard et al., 2023). These approximations might impact the reliability of simulations involving non-standard contraction conditions, such as the simulated perturbed hopping in Chapters 4 and 5. The study in the current chapter investigates the influence of the Hill-type formulation in this thesis's computational research.

We performed in vitro experiments with biological muscle fibers under physiological boundary conditions, which we defined using computer simulations of perturbed hopping. We measured the mechanical work and force modulation in biological muscle fibers during preflexes and compared the results to Hill-type predictions. Our findings show that muscles initially resist impacts with a stereotypical stiffness response—identified as short-range stiffness—regardless of the perturbation condition. We then observed a velocity adaptation of the muscle force related to the amount of perturbation, similar to a damping response. The main contributor to the preflex work modulation was not the change in force due to the change in fiber stretch velocity (fiber damping characteristics) but the change in magnitude of the stretch due to the leg dynamics in the perturbed conditions. Our results confirm previous findings that muscle stiffness is activity-dependent and show that also damping characteristics are activity-dependent. These results indicate that neural control could tune the preflex properties of muscles in expectation of ground conditions leading to previously inexplicable neuromuscular adaptation speeds.

Note: a large portion of this chapter uses content published in *Frontiers in Bioengineering and Biotechnology, section Biomechanics* (Araz et al., 2023). For details on this journal article, including the list of authors and my contribution, see Section 2.1.2.

6.1 Introduction

Legged locomotion on uneven terrain is a complex motor control task performed seemingly effortless by humans and other animals (Blickhan et al., 2007). Animals reject unexpected ground perturbations (Daley and Biewener, 2006; Müller et al., 2014), despite considerable sensorimotor transmission delays affecting the feedback control (More et al., 2010; More and Donelan, 2018). This ability has long

puzzled researchers in biomechanics and motor control science. In vivo research on perturbed legged locomotion suggests that the intrinsic mechanical properties of muscles are essential for dynamic stability during the first 30 ms to 50 ms after touchdown (Daley et al., 2009; Gordon et al., 2020; Nishikawa et al., 2007). During this brief interval, muscles and tendons react instantly through elastic and viscous-like properties. Brown and Loeb (2000, p. 161) labeled it preflex: the "... zero-delay, intrinsic response of a neuromusculoskeletal system to a perturbation".

In vivo walking experiments are essential for understanding robust locomotion. However, the functional mechanical and control coupling of muscle groups during whole-body movement complicates unveiling the regulatory principles behind preflexes, reflexes, and voluntary neuromuscular control. By artificially contracting individual muscle fibers, in vitro research allows for precise isolation and investigation of muscles' mechanical properties (Weidner et al., 2022). So far, a wide range of contraction settings have been explored, such as isometric, isotonic, and isovelocity (Brown et al., 2003; Gilliver et al., 2011; Tomalka et al., 2020). Yet, the exact boundary conditions of physiological muscle contraction are hard to replicate during in vitro experiments. Cyclic fiber contractions during in vitro experiments and follow-up work loop analyses are relatively realistic (Josephson, 1985). Even though it is possible to extract physiological kinematic trajectories of muscle contraction with the sonomicrometry method during in vivo experiments (Daley et al., 2009; Gordon et al., 2020), extracting the preflex phase is still challenging due to the relative oscillations of soft tissue at impact (Christensen et al., 2017). Therefore, stretch-shortening cycle investigations that are limited to sinusoidal length trajectories (Darby et al., 2013) only roughly present locomotion conditions.

Previous simulation studies support the hypothesis that intrinsic muscle properties play a crucial role in stabilizing locomotion against disturbances (Gerritsen et al., 1998; John et al., 2013; van der Krogt et al., 2009). Simulation studies revealed that feedforward adjustment of muscle stimulation, as observed during human locomotion (Müller et al., 2015), may allow to adjust muscle mechanics according to perturbed impact conditions (Haeufle et al., 2010, 2018). As a means of investigation, computer simulations combine the advantages of in vivo and in vitro investigations. They enable the analysis of complex whole-body movements similar to in vivo research while providing access to difficult-to-measure variables, similar to in vitro experiments. Nevertheless, computer models depend on simplified assumptions. Most investigations of muscle preflexes use classic Hill-type muscle models, which are restricted in their ability to describe muscle contraction outside of specific conditions (Siebert et al., 2021). Hill-type muscle models are parameterized with empirical data from isometric, isotonic, and isovelocity muscle fiber experiments, mostly at maximum activity, which are controlled experimental conditions differing greatly from in vivo muscle loading. Compared to data from gait recordings, Hill-type muscle models were inaccurate in predicting muscle force during high-speed locomotion (Dick et al., 2017; Lee et al., 2013). Furthermore, several studies showed that Hill-type muscle models can only predict accurate joint kinetics and kinematics for perturbed quiet stance (De Groote et al., 2017; Hu et al., 2011) if they consider a model extension accounting for short-range stiffness (Cui et al., 2008). Therefore, it still needs to be discovered to what extent simulation studies with Hill-type models can validate experimental research on muscle preflexes. On the other hand, in vitro experiments are required to test individual muscle fibers' response to unexpected perturbation.

This study aims to understand how individual muscle fibers exploit their intrinsic mechanical properties to respond to perturbations in realistic settings (in terms of physiological boundary conditions). We focus on how muscles' elastic and viscous properties regulate energy absorption during the preflex phase to reject perturbations during locomotion impacts. We hypothesize that (1) the muscle's force and mechanical work during and after the short-range stiffness (SRS) period, but within the 30 ms preflex

period, changes in reaction to differences in stretch velocities induced by step-up and step-down ground level perturbations, and (2) mechanical muscle properties can be tuned by changing activity level in advance to touchdown. We conducted muscle fiber experiments with realistic kinematic trajectories at three different activity levels to prove our hypotheses. We obtained the kinematic trajectories by simulating vertical human hopping driven by a Hill-type muscle model under three levels of perturbations: step-up, no step, and step-down. Further, we derived a quasistatic-scenario for muscle fiber experiments with the same lengthening patterns over a much larger time to eliminate fiber's velocity effect on the muscle force production. These quasistatic-scenario experiments permit separating the elastic response from the viscous response of muscle fibers. Finally, we compared simulations with muscle fiber experiments to test the accuracy of Hill-type models in explaining fiber response. Our results show that during the preflex phase, intrinsic muscle characteristics adjust the muscle force in response to the perturbation level. Our findings corroborate that muscle activity can tune mechanical muscle properties in advance. On the other hand, we confirm previous findings that classical Hill-type muscle models—as the one used in our study—cannot accurately predict the force response in the preflex phase. This is not only the case within the SRS phase (De Groote et al., 2017; Hu et al., 2011), but also after the SRS, where the change in force with stretch velocity (Weidner et al., 2022) is not predicted by the model.

6.2 Materials and Methods

The goal of this study was to test the force response of muscle fibers in realistic perturbation scenarios. Boundary conditions for in vitro muscle fiber experiments were derived from a human hopping simulation (Figure 6.1A). Notice that the neuro-musculoskeletal model in this study is the same as in Chapter 4. The model consists of a point mass, a single leg with two segments, and a classical Hill-type muscle model connected as a knee extensor (Geyer et al., 2003; Haeufle et al., 2014b; Izzi et al., 2023) (for more details, see section 3.3). We performed three simulations with the hopping model: a no-perturbation reference hopping (P0), a step-up perturbation (P↑), and a step-down perturbation (P↓). Figure 6.1B shows the stimulation profile applied during the hopping simulation. During the first 30 ms (preflex phase), the stimulation is kept constant due to the delay of neural transmission, and response against the perturbation is dependent only on elastic and viscous intrinsic properties of the muscle. Then, stimulation rises linearly with time (approximated from experimental findings for hopping (Moritz and Farley, 2004) and walking (Müller et al., 2015, 2020)). Note that the muscle stimulation for this study is identical to Preflex-Const stimulation in Chapter 4. We extracted kinematic trajectories and the stimulation state during the preflex phase (Figure 6.1B) of the contractile element. These data were used as boundary conditions for muscle fiber experiments (conducted with the fibers taken from rat muscles) and their corresponding simulations of the isolated contractile element (Figure 6.1C-D). Notice that in the vertical hopping model (Figure 6.1A), the neural stimulation (u) is first filtered by activation dynamics (Hatze, 1977; Rockenfeller et al., 2015). However, in the simulation of the isolated contractile element, no activation dynamics are included. Thus, the neural stimulation sent to the muscle and the muscle activation level are equal ($u = a$). This was necessary since the simulation of the isolated contractile element mimics the in vitro muscle fiber experiments for which no activation dynamics take place. The highlighted preflex phase (Figure 6.1B, shaded area)— is the focus of our study. Figure 6.1B also shows the behavior shortly after the preflex phase. However, the data after preflexes is measured with constant activity levels, as the in vitro setup does not allow for a time-controlled activity change. In the hopping simulation, the muscle activity rises after the preflex phase. We recorded force-length traces

during these experiments and matching simulations and analyzed the preflex phases of work loops for the mechanical work of the muscle fiber. The following sections provide details of the experiments and simulations conducted.

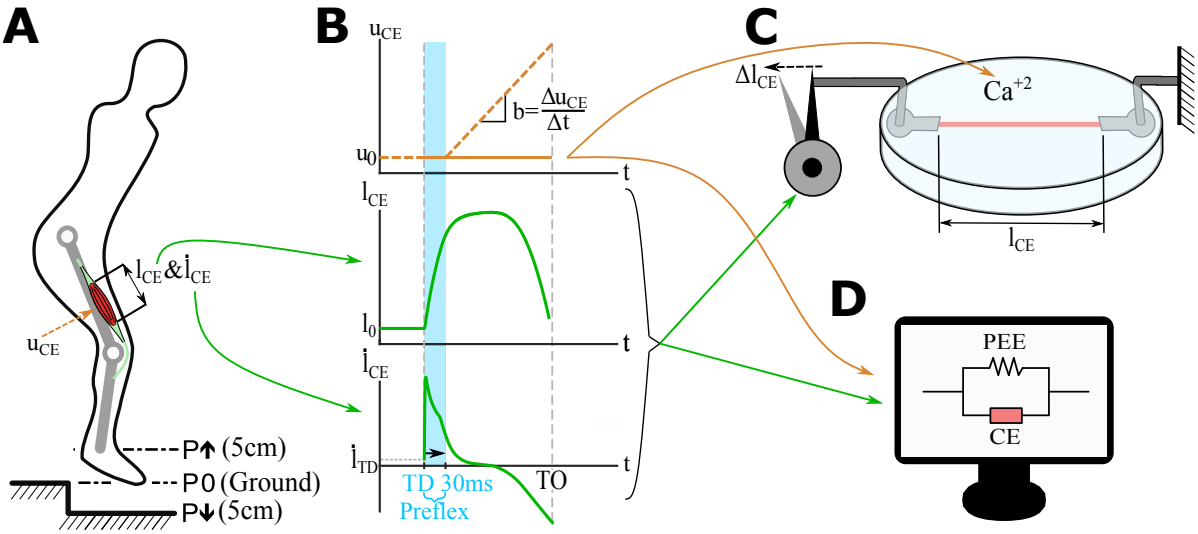

Figure 6.1: Simulations and in vitro experiments applied in this study. A Hill-type model muscle-tendon unit drives a knee extensor unit of the hopper (Geyer et al., 2003; Haeufle et al., 2014b; Izzi et al., 2023). The hopping model is the same as in Chapter 4 (for more details, see section 3.3). Single-leg hopping is computer-simulated (**A**) with three perturbation scenarios: 5 cm step-up (P↑), no perturbation (P0), and 5 cm step-down (P↓). The model outputs are length changes of the contractile element (l_{CE}, (**B**)), and contraction velocities ($\dot{l}_{CE}$, (**B**)). One hopping cycle from touchdown (TD) to toe-off (TO) is extracted for the analysis. Since the focus of this study is the muscle behavior during the preflex phase of a hopping cycle (the first 30 ms of the stance phase), we focused on the time zone shown with the blue area (**B**). In this time zone, there is no influence of reflexes on the muscle activation, and we assume no activity rise due to feedforward muscle activation. Thus, constant stimulation profile (u_{CE}-orange line is shown only for 15% stimulation level, (**B**)) is then applied to in vitro muscle fiber experiments (**C**) and isolated contractile element (CE) simulations (**D**). Constant stimulation in experiments and isolated contractile element simulations were used since the in vitro setup does not allow changing stimulation levels within a stretch-shortening cycle. Since the muscle fibers used in in vitro experiments (**C**) were isolated from the tendon, the contractile element (CE) and parallel elastic element (PEE) of the Hill-type muscle model were also isolated from the tendon unit (**D**).

6.2.1 Muscle Fiber Experiments

6.2.1.1 Fiber Preparation

One M. extensor digitorum longus (EDL) was extracted from a single female Wistar rat, which was sacrificed with an overdose of CO_2 shortly before. We used n = 9 fibers from the extracted EDL muscle for our experiments. The specimen's age was 8 to 10 months, at a body weight of 300 g to 350 g. The specimen was kept at a 12 h light and 12 h dark cycle at a housing temperature of 22 °C. The EDL muscle was obtained from the left hind limb. The experiment was conducted according to the guidelines of ARRIVE and approved according to the German animal protection law (Tierschutzgesetz §4(3), permit no. T170/18ST).

The techniques used for muscle preparation, storage, and activation of skinned single muscle fibers

were carried out as described in detail in Tomalka et al. (2017). In summary, the EDL was prepared in 6 to 8 small fiber bundles, which were permeabilized in a skinning solution (see “Solutions"; Section 6.2.1.3) at 4 °C temperature directly after preparation. Fiber bundles were transferred to a storage solution made of 50% glycerol and 50% skinning solution and kept at −22 °C for 6 to 8 weeks. Prior to conducting experiments, fibers were removed from the bundle using a dissecting microscope and fine forceps. Single fibers were cut into smaller muscle fiber segments with a length of 1 mm. Aluminum T-shaped clips were folded around both ends of the fiber. The fiber was then treated with a skinning solution consisting of a relaxing solution with 1% vol/vol Triton-X 100 for 3 min at 4 °C until the complete removal of internal fiber membranes (Linari et al., 2007).

6.2.1.2 Experimental Setup

The skinned muscle fiber was transferred from the skinning solution to the experimental chamber of the fiber test apparatus (600A, Aurora Scientific, ON, Canada). One clipped end was attached to a length controller (model 308B, Aurora Scientific, ON, Canada) and the other end to a force transducer (model 403A, Aurora Scientific, ON, Canada). Both attached ends were fixed with fingernail polish diluted with acetone (Getz et al., 1998). Transitions from the fiber end to the clip were treated with glutaraldehyde in rigor solution to improve mechanical performance and stability during the experiment (Hilber and Galler, 1998).

The central fiber segment was focused in the microscope and used to optically measure the sarcomere length (Weidner et al., 2022), which was set to 2.5 µm (means ± standard deviation) in the beginning. At this optimal sarcomere length, the fiber produces its maximum force F_{max}(Stephenson and Williams, 1982). The corresponding muscle fiber length is defined as l_{opt}. The height (h) and width (w) of the fiber were measured in 0.1 mm increments over the entire length of the fiber using a 10 x extra long working distance dry lens (NA 0.60, Nikon, Japan) and a 10 x eyepiece. The cross-sectional area of all tested muscle fibers was determined 5.25×10^{-9} m^2 ($\pm 1.5 \times 10^{-9}$) assuming an elliptical cross-section ($\pi \times h \times w/4$).

A high-speed video system (Aurora Scientific, 901B, Canada) in combination with a 10 x extra long working distance dry objective (NA 0.40, Nikon, Japan) and an accessory lens (2.5 x, Nikon, Japan) visualized and tracked dynamic changes in the sarcomere length. Videos were recorded at 300 Hz recording frequency.

6.2.1.3 Solutions

The relaxing solution contained 0.1 mol TES, 7.7 mmol $MgCl_2$, 5.44 mmol Na_2ATP, 25 mmol EGTA, 19.11 mmol Na_2CP, 10 mmol GLH (pCa 9.0). The preactivating solution contained 0.1 mol TES, 6.93 mmol $MgCl_2$, 5.45 mmol Na_2ATP, 0.1 mmol EGTA, 19.49 mmol Na_2CP, 10 mmol GLH, and 24.9 mmol HDTA. The skinning solution contained 0.17 mol potassium propionate, 2.5 mmol $MgCl_2$, 2.5 mmol Na_2ATP, 5 mmol EGTA, 10 mmol IMID, and 0.2 mmol PMSF. Recipes for activation solutions (‘ACT’) are shown in Table 6.1. The storage solution is the same as the skinning solution, except for the presence of 10 mmol GLH and 50 % glycerol vol/vol. Cysteine and cysteine/serine protease inhibitors [trans-epoxysuccinyl-L-leucylamido-(4-guanidino) butane, E-64, 10 mM; leupeptin, 20 mg/mL] were added to all solutions to preserve lattice proteins and thus sarcomere homogeneity (Linari et al., 2007; Tomalka et al., 2017). KOH was applied to adjust to a pH 7.1 at 12 °C. Then, 450 U/mL of creatine kinase were added to all except skinning and storage solutions. Creatine kinase was obtained from

Roche, Mannheim, Germany, and the remaining chemicals were obtained from Sigma, St Louis, MO. According to our calibration curve (Figure A2.1) we chose concentrations of 6.73 pCa, 6.34 pCa and 6.3 pCa to best match the simulations boundary conditions.

Table 6.1: Recipe of activation solutions used, values are in [mmol].

ACT	5 %	15 %	25 %	100 %
TES	100.000	100.000	100.000	100.000
$MgCl_2$	7.183	6.995	6.980	6.760
EGTA	11.250	6.250	5.852	0.000
CaEGTA	13.750	18.750	19.147	25.000
Na_2ATP	5.451	5.455	5.455	5.460
KPi	0	0	0	0
Na_2CP	19.319	19.395	19.401	19.490
GSH	10.000	10.000	10.000	10.000

6.2.1.4 Experimental Protocol

All experimental trials were conducted at a solution temperature of 12 °C (±0.1). At this temperature, the skinned muscle fibers proved stable during work loop experiments (Tomalka et al., 2020, 2021). Fibers can tolerate activation and active stretch protocols over a long period (Ranatunga, 1982, 1984). A three-step approach was used to activate the fibers by calcium diffusion. First, muscle fibers were immersed for 60 s in a preactivation solution for equilibration. The fiber was then transferred to the activation solution. This led to a rapid increase in force until a plateau was reached. We defined the plateau as an isometric force increase of less than 1% rise of force within 1.5 s. After reaching the plateau, the perturbation was carried out. In the last step, the fiber was transferred to the relaxing solution, in which it was prepared for the subsequent activation for 400 s using cycling protocols (Tomalka et al., 2017).

The in vitro experiment included isometric contractions at optimal fiber length and three hopping stretch-shortening cycles based on the simulation data of the hopping model (Section 6.2.2). First, the activity level of the fiber in three sub-maximal conditions was checked using isometric contractions in 5 %, 15 %, 25 %, and supra maximal activation solution at optimal fiber length. This step ensured matching boundary conditions with the simulation data. A flow chart of an experimental day for a single fiber is shown in Supplementary Figure A2.2. Hopping stretch-shortening cycles were applied to the fiber according to length and velocity data extracted from the simulations in the simulated dynamic-scenarios and modified quasistatic-scenarios (see Section 6.2.2 for more details).

Both the order of stretch-shortening profiles and the order of activity levels within a perturbation, called a “block", were randomized. Each block was surrounded by isometric reference contractions at optimal fiber length and full activity to take into account fiber degradation during force data normalization (Supplementary Figure A2.2).

Velocity, force, and length data were recorded at 1 kHz for isometric and quasistatic-scenario trials and 10 kHz for high-speed trials with an A/D interface (604A, Aurora Scientific, ON, Canada). The data acquisition was carried out with real-time software (600A, Aurora Scientific, ON, Canada). Data were loaded into MATLAB (MathWorks, MA, United States) and analyzed with a custom-written script.

Forces during perturbation trials for every single fiber were divided by individual F_{max}, and likewise, fiber length l by individual l_{opt}, to normalize them.

6.2.2 Simulations

6.2.2.1 Generating Hopping Trajectories in Simulation

To identify realistic boundary conditions for in vitro muscle fiber experiments, we extracted contractile element kinematics from a single-leg hopper simulation (Izzi et al. (2023) based on the model by Geyer et al. (2003)). The hopping model is the same as in Chapter 4. The single-leg hopper is driven by a Hill-type muscle-tendon unit (MTU) model. The MTU model considers four elements: a contractile element representing the muscle fibers (CE), a parallel elastic (PEE), a serial elastic (SEE), and a series damping (SDE) element (Haeufle et al., 2014b). The modeled muscle-tendon unit extends the knee joint (Figure 6.1A). The leg features two massless segments connected by the knee hinge joint. The body mass is represented as a point mass located at the hip joint. For further details on the model, see section 3.3.

We simulated stable periodic hopping with the hopper model and introduced a step-up and a step-down perturbation (Figure 6.1A). During the flight phase, the muscle was stimulated with 15 % constant stimulation, and the knee joint was fixed. After touchdown, the constant stimulation level continued for 30 ms throughout the preflex phase and then increased with a ramp input ($b = 10\,\mathrm{s}^{-1}$, Figure 6.1B). Thus, the stimulation was identical to the Preflex-Const stimulation described in Chapter 4. Despite the constant stimulation during the preflex phase, the contractile element can change its force due to its elastic and viscous intrinsic properties, which are related to the force-length and the force-velocity relations, respectively. Since the Hill-type muscle is extending the knee in the hopping simulation, muscle-tendon unit and contractile element are stretched at the initial phases of the stretch-shortening cycle. Thus, the model operates on the eccentric section of the force-velocity relation (Haeufle et al., 2014b):

$$F_{CE,e}\left(\dot{l}_{CE} > 0\right) = F_{\max}\left(\frac{aF_{\mathrm{isom}} + A_{\mathrm{rel,e}}}{1 - \frac{\dot{l}_{CE}}{B_{\mathrm{rel,e}} l_{\mathrm{opt}}}} - A_{\mathrm{rel,e}}\right) \tag{6.1}$$

Here $\dot{l}_{CE}$ is the fiber contraction velocity, F_{max} is the maximum isometric force that the contractile element can generate, F_{isom} is the isometric force that the contractile element generates according to the current muscle length, $A_{rel,e}$ and $B_{rel,e}$ are the normalized Hill parameters for the eccentric phase, and a is the activity level. Figure 6.2 shows force-velocity traces predicted by the Hill-type muscle model for sub-maximal (5 %, 15 % and 25 %), and full activity (100 %).

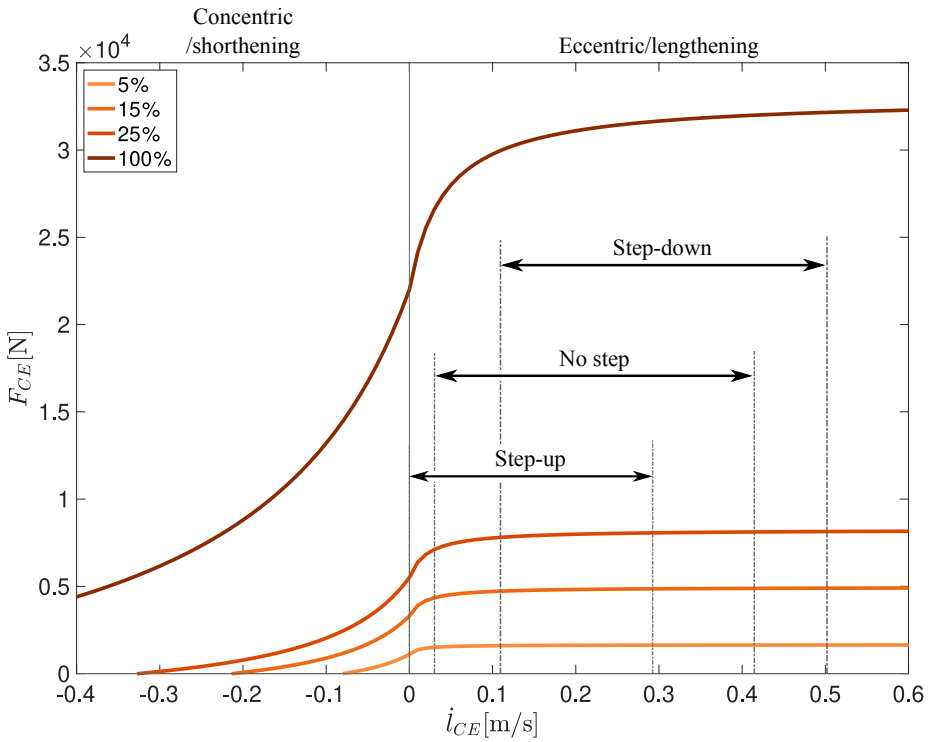

Figure 6.2: Force-velocity relation for the contractile element for activity levels of 5 %, 15 %, 25 % and 100 %. Shown intervals for each perturbation represent the stretch velocity ranges from touchdown to the end of the preflex phase.

For a comparison between the biological muscle fiber and the Hill-type muscle model behavior, the parameters of the isometric force-length curve of the model were optimized to fit experimental data (Stephenson, 2003). More precisely, the width of the normalized bell-curve ΔW_{limb} and its exponent $\nu_{CE,limb}$ of the ascending limb were optimized with the *lsqcurvefit* function (MATLAB 2021b). All other parameters are based on (Bayer et al., 2017; Kistemaker et al., 2006; Mörl et al., 2012) and tabulated in the Supplementary table A2.1.

6.2.2.2 Extracting Boundary Conditions

We simulated hopping for no-perturbation locomotion on ground level (P0), 5 cm step-up perturbation (P↑), and 5 cm step-down perturbation (P↓). Beyond step-up perturbations of 5 cm, the single-leg hopper generates unstable hopping patterns. Thus, we decided to use a maximum perturbation height of 5 cm. The contractile element length and velocity profiles were extracted for each perturbation level. These kinematic data were used in muscle fiber experiments and isolated contractile element simulations to compare their reactions to the perturbations during the preflex phase.

We further derived quasistatic-scenario boundary conditions to differentiate between the muscle fibers' velocity-dependent and length-dependent force modulation. To create a length-dependent force modulation, we generated quasistatic-scenario boundary conditions for each perturbation level. In these conditions, the time duration of the contractile element lengthening profiles obtained from each perturbation level was expanded by 80 times compared to the original duration. Thereby, the

contraction velocity was decreased to negligible levels without exceeding the minimum speed limits of the experimental setup. Hence, the viscous contribution was minimized from the muscle fiber force response, and the muscles only reacted with their elastic properties to the perturbations.

6.2.2.3 Simulating Isolated Contractile Element Response

In the hopping simulation, the Hill-type muscle model calculates contractile element kinematics according to the dynamic balance of the serial (SEE and SDE) and contractile (CE and PEE) side of the model. However, in vitro experiments are conducted only with isolated muscle fascicles. To match in vitro conditions, we ran simulations solely with an isolated contractile element. Thereby, the isolated responses of the CE—corresponding to the muscle fibers—were calculated according to the provided contractile element length (l_{CE}), contraction velocity ($\dot{l}_{CE}$) and activity (a):

$$F_{CE} = f(l_{CE}, \dot{l}_{CE}, a) \tag{6.2}$$

We obtained the kinematic data of contractile element from hopping simulations for step-up, no step, and step-down perturbations. All perturbation cases were applied as input to the isolated contractile element model with constant activity levels of 5 %, 15 % and 25 %. Although the activity level increases after the preflex phase during hopping simulations, isolated contractile element model simulations must be kept constant to reproduce the conditions of in vitro muscle fiber experiments. In the experimental setup, the stimulation level is arranged with chemical baths, as explained in Section 6.2.1.3. The setup allows only a single stimulation level for each stretch-shortening cycle. Therefore, stimulation levels were kept constant in isolated contractile element simulations to match the experimental in vitro conditions.

6.2.3 Data Analysis and Statistics

6.2.3.1 Data Analysis

The analysis of stretch-shortening cycles of both experimental and simulated fiber contractions focused on the preflex phase, which is the first 30 ms of the dynamic-scenario scenarios. We analyzed data in quasi-scenarios until the fiber lengthening reached the same level as at the end of the preflex phase in the dynamic-scenario conditions. We calculated the areas under force-length curves with the *trapz* function (MATLAB 2021b) to measure the work done by the muscle fibers and the isolated contractile element model. In addition, we estimated the muscle fiber's short-range stiffness from the slope of fitted force-length curves during the initial phase of preflex, from 0.57 to 0.59 $\tilde{l}_{CE}$, with $\tilde{l}_{CE} = l_{CE}/l_{opt}$. This initial phase begins where muscles start to generate force ($\approx 0.57\ \tilde{l}_{CE}$) and ends where the force responses start to deviate due to the stretch velocities ($\approx 0.59\ \tilde{l}_{CE}$). Then, to observe the effect of velocity on stiffness, we calculated the stiffness during the quasistatic-scenario stretch for the same boundary conditions.

6.2.3.2 Statistics

SPSS 27 (IBM Corp., Armonk, NY) was used for the statistical analysis, with a significance level of $p = 0.05$. Initially, we tested for normal data distribution by running a Shapiro-Wilk, which was negative. Hence, we used a Friedman test to elucidate differences between the applied perturbations within one activity level. We executed comparisons pairwise for post hoc experimental data analysis. Results were

fed into a Bonferroni correction to take multiple testing into account. We tested for differences between similar activity levels and applied perturbation between dynamic-scenario and quasistatic-scenario conditions with a two-sample paired sign test. Effect sizes for the pairwise comparisons were classified as small ($d < 0.3$), medium ($0.3 < d < 0.5$), and large ($d > 0.5$) using Cohen's d (Cohen, 1988).

6.3 Results

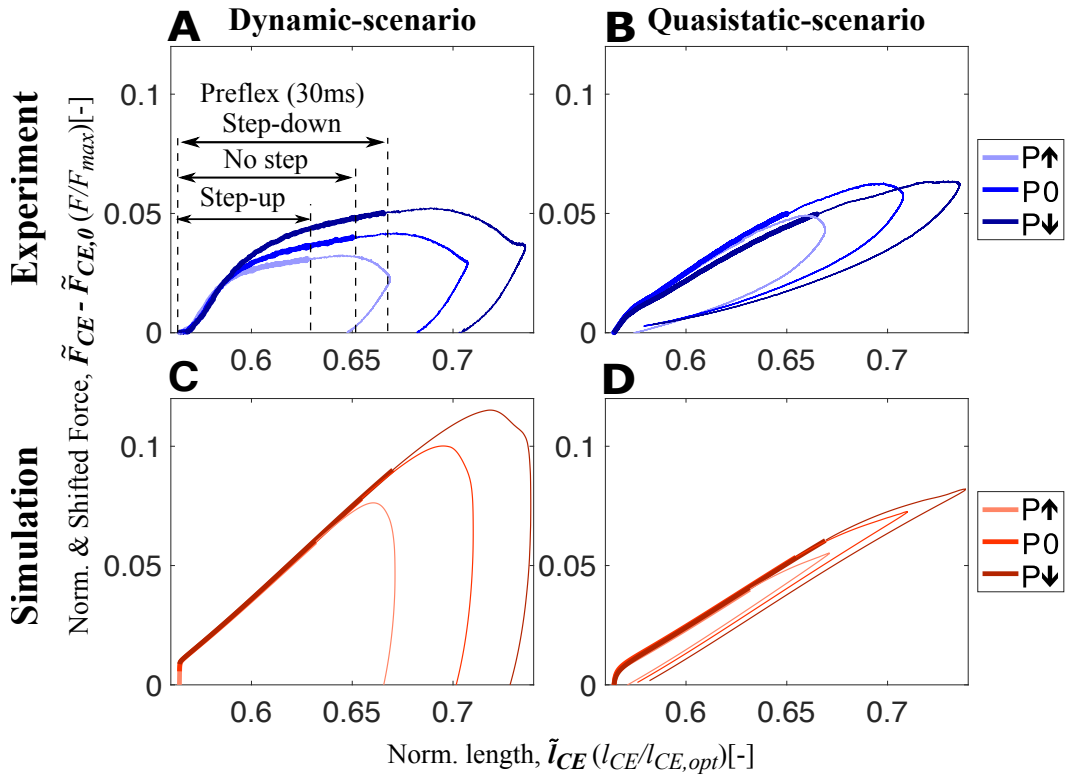

Figure 6.3: Shifted work loops for dynamic-scenario and quasistatic-scenario analysis step-up (P↑), no (P0) and step-down (P↓) perturbations for both experiments (**A, B**) and simulations (**C, D**) at 15 % activity level (work loops for 5 % and 25 % are shared in Supplementary Figures A2.3 and A2.4, respectively). The experimental data presented on (**A, B**) show the mean of all experimental trials. From touchdown to toe-off, all stretch-shortening cycle loops are plotted in the clockwise direction, and the thick and thin sections of the loops represent the preflex and remaining part of the stretch-shortening cycle, respectively. The preflex stretch gets longer from step-up to step-down perturbation since the muscle stretches faster in the same amount of time. The force-time curves for all experimental conditions with standard deviations can be found in Supplementary Figure A2.5 and Supplementary Figure A2.6 for dynamic-scenario and quasistatic-scenario, respectively.

During in vitro experiments, we found that intrinsic muscle properties adjust the force response to the perturbation condition within the preflex phase (Figure 6.3A, thick lines). Work loops of dynamic-scenario experiments for skinned fibers show muscle fibers are initially responding with similar force and with a linear and increasing trend between touchdown and 0.59 $\tilde{l}_{CE}$ in all perturbations (Figure 6.3A).

After $0.59\,\tilde{l}_{CE}$, the force differs depending on the perturbation level, i.e., force is highest in the step-down perturbation (Figure 6.3A).

The response we observed from the skinned fiber experiments does not match with the prediction of the isolated contractile element of the Hill-type muscle model (Figure 6.3A, C). For the Hill-type muscle model, an effect of the perturbation is only observed at touchdown ($0.56\,\tilde{l}_{CE}$, Figure 6.3C). Right after touchdown, the response of the Hill-type muscle model reaches the same force level regardless of the perturbation state and then increases with the same linear trend. Therefore, the model did not predict the modulation in the muscle's force response due to the perturbation.

Contrary to the dynamic-scenario experiments (Figure 6.3A), force responses of skinned fibers in quasistatic-scenario stretches do not change according to the perturbation level (Figure 6.3B), during preflexes. Initial force and the rise in force are similar for all perturbation levels. This result matches the prediction of the isolated contractile element of the Hill-type muscle model (Figure 6.3D).

We found that intrinsic muscle properties adjust the mechanical work during the preflex phase (preflex work) according to the perturbation condition. This is true in dynamic-scenario and quasistatic-scenario tests, both during experiments and simulations and for all activity levels (Figure 6.4).

The preflex work increases when comparing the step-up to the step-down perturbation, according to the dynamic-scenario analysis of skinned fibers (Figure 6.4A). Albeit no significant difference among perturbation states at 5 % activity level ($p = 0.169$), a perturbation influence on preflex work is observable for 15 % ($\chi^2 = 12.61; p = 0.002$) and 25 % ($\chi^2 = 14; p = 0.001$) activity levels (Supplementary Table A2.2).

Preflex work changes significantly between activity levels. For the same kinematic profiles, the work done by skinned fibers increases if they are activated more (5 % to 25 % activity level; $p = 0.001$). The work differences between the perturbation conditions increase with an increase in activity level. See the supplementary materials (Supplementary Table A2.3) for further details.

In the dynamic-scenario analysis, the muscle fibers' response is a combination of two mechanical features: elasticity and viscosity. To identify their individual contributions, we minimized the parameter responsible for the viscous contribution—the stretch velocity. We performed quasistatic-scenario experiments, where muscles were stretched with the same lengthening profiles as in dynamic-scenario experiments, but at super-low velocities. Hence, with this experimental design, we expect to see only the elastic muscle fiber response. Still, even at negligible stretch velocities, we observed a similar preflex work trend between perturbation levels in quasistatic-scenario experiments and dynamic-scenario experiments (Figure 6.4A, B).

Surprisingly, the Hill-type muscle model predicted the amount of preflex work accurately for the dynamic-scenario experiments (Figure 6.4A, C) and the quasistatic-scenario experiments (Figure 6.4B, D). Such correct prediction is an expected outcome for quasistatic-scenario experiments but not for dynamic-scenario experiments, as the model's dynamics differed compared to the muscle fiber dynamics (Figure 6.3A, C).

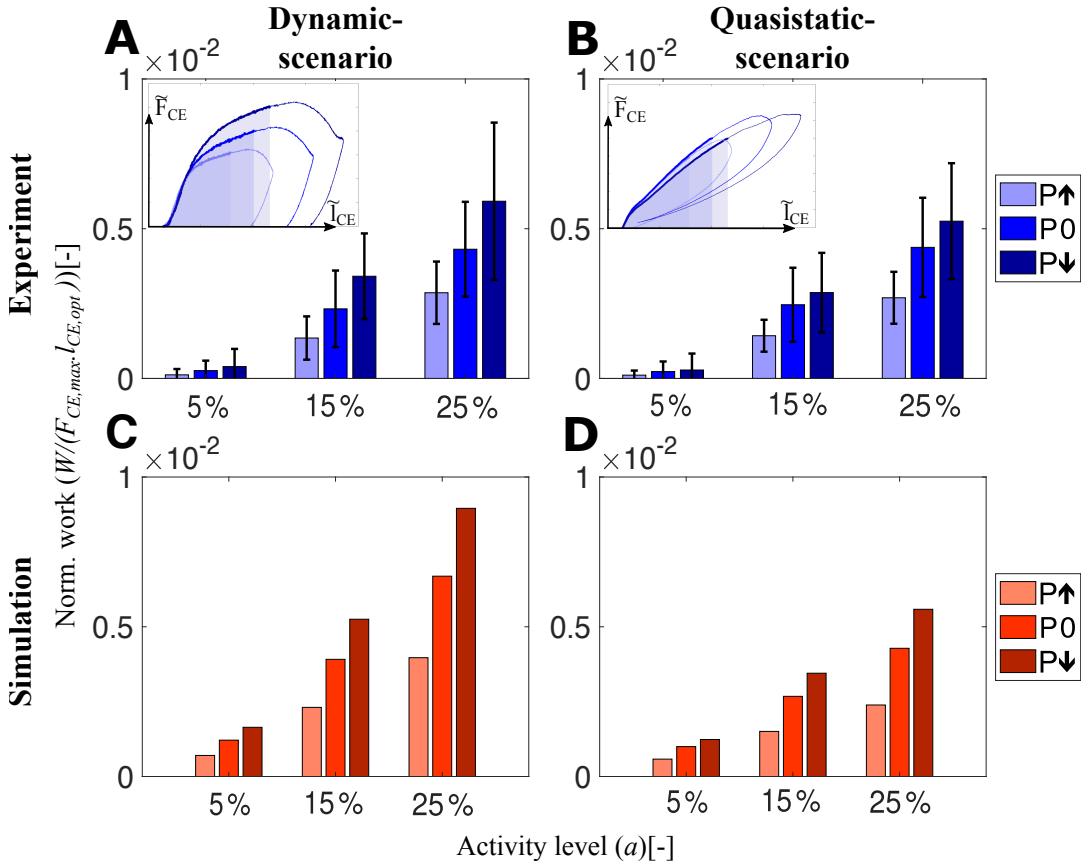

Figure 6.4: The amount of preflex work done by skinned fibers and the isolated contractile element of the Hill-type muscle model for all perturbation states and activity levels. In the dynamic-scenario analysis, work done during the preflex phase was calculated as the area under the force curve. Shaded areas in the insets (**A**) and (**B**) indicate changing perturbation levels. In the quasistatic-scenario analysis, the area till the lengthening reached at the end of the preflex phase was analyzed for each perturbation level. Bars in (**A, B**) and (**C, D**) indicate the work done by skinned muscle fibers and the isolated contractile element at dynamic-scenario and quasistatic-scenario, respectively. We calculated and indicated the area of the normalized work loops (Figure 6.3). Hence, there is no need to match the parameters of the hopping simulation to the experimental muscle size.

Work loops obtained from the dynamic-scenario analysis (Figure 6.3A, Supplementary Figure A2.3A, and Supplementary Figure A2.4A) show that the force response of the muscle fibers is almost identical within the short-range stiffness (Rack and Westbury, 1974) regardless of the velocity profile. The force-time curves of all experimental conditions with standard deviations can be found in Supplementary Figure A2.5 and Supplementary Figure A2.6 for the dynamic- and quasistatic-scenarios, respectively. Only after the short-range stiffness phase, the force and energy are affected by velocity (Figure 6.5). To understand the influence of velocity on the preflex work, we measure the area after the end of the short-range stiffness phase until the end of preflexes for the step-up perturbation condition (Figure 6.5A, inset: shaded areas). Work done in this phase is slightly higher for the faster stretches at 15 % and 25 % activity levels. However, the differences between the perturbation levels are not significant (15% activity: $\chi^2 = 4.67, p = 0.097$; 25 % activity: $\chi^2 = 3.56, p = 0.167$; See Supplementary Table A2.2 for more details).

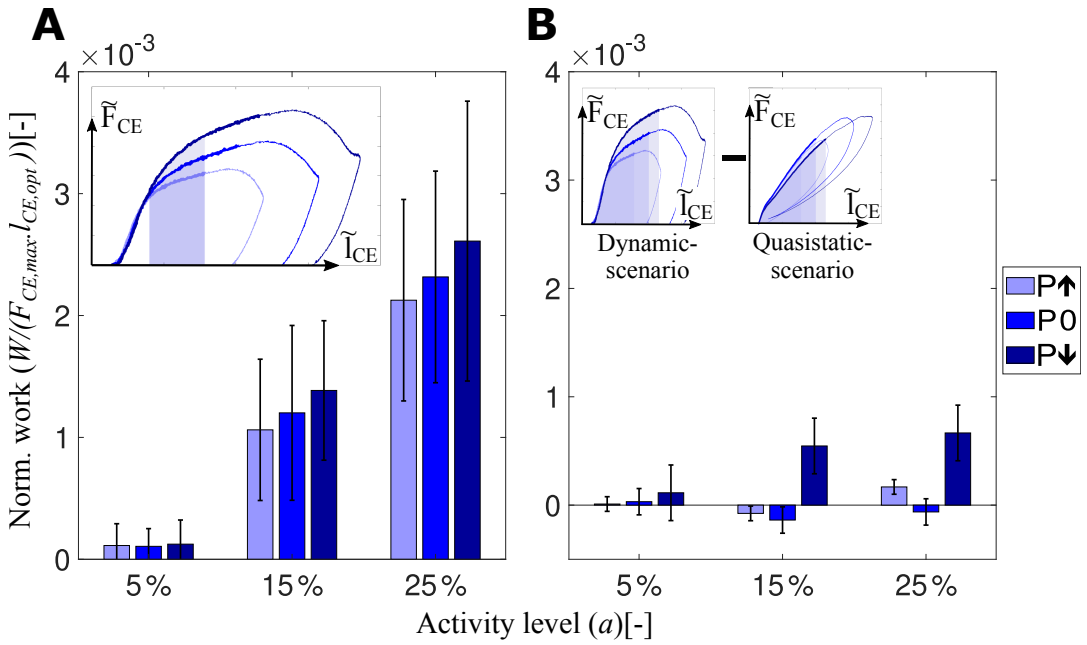

Figure 6.5: Influence of velocity adaptation on preflex work is represented. (**A**) shows the dissipated energies at dynamic-scenario experiments after the short-range stiffness till the end of the 'step-up' perturbation phase (shaded area shown in the inset). Elastic contribution is kept equal for all perturbation states. Thus, the difference in energy will be caused by the difference in velocity profiles. (**B**) shows the preflex work difference between the dynamic-scenario and quasistatic-scenario experiments for each perturbation level. The preflex work is shown in the insets as a shaded area and for multiple conditions.

We compared activity levels affecting muscle work to see whether muscles' viscous properties are tunable. Our results show that the activity level influences the amount of viscous contribution (Figure 6.5A) similar to the preflex work (Figure 6.4A). For the same kinematic profiles, a rising activity level causes a work increase by viscous characteristics of muscle fibers (15 % to 25 % activity level; $p = 0.001$).

To understand the velocity-related adaptation throughout the preflex phase, we subtract the work done in the quasistatic-scenario experiments from dynamic-scenario experiments, shown as inset in Figure 6.5B. Surprisingly, the amount of work done by muscle fibers at dynamic-scenario and quasistatic-scenario experiments are almost identical, and we measured no significant effect of the velocity on the preflex work (Supplementary Table A2.4). Both comparisons between perturbations and between dynamic- and quasistatic-scenarios showed that velocity differences had no significant effect on the preflex work.

Analysis of the short-range stiffness shows no difference between perturbations but significant differences between activity levels (Figure 6.6A). In quasistatic-scenario experiments, we found no significant differences between perturbation levels. However, short-range stiffness was less in quasistatic-scenario stretches (Figure 6.6B) than in dynamic-scenario experiments (Figure 6.6A), and the difference between them increased with higher activities (Supplementary Table A2.4). Hence, short-range stiffness is increasing from quasistatic-scenario (Figure 6.6D) to dynamic-scenario velocities (Figure 6.6C). However, short-range stiffness does not change according to the difference in velocity between the perturbation levels (Figure 6.6C, different shades of thick blue lines). Besides, the stiffness value can be

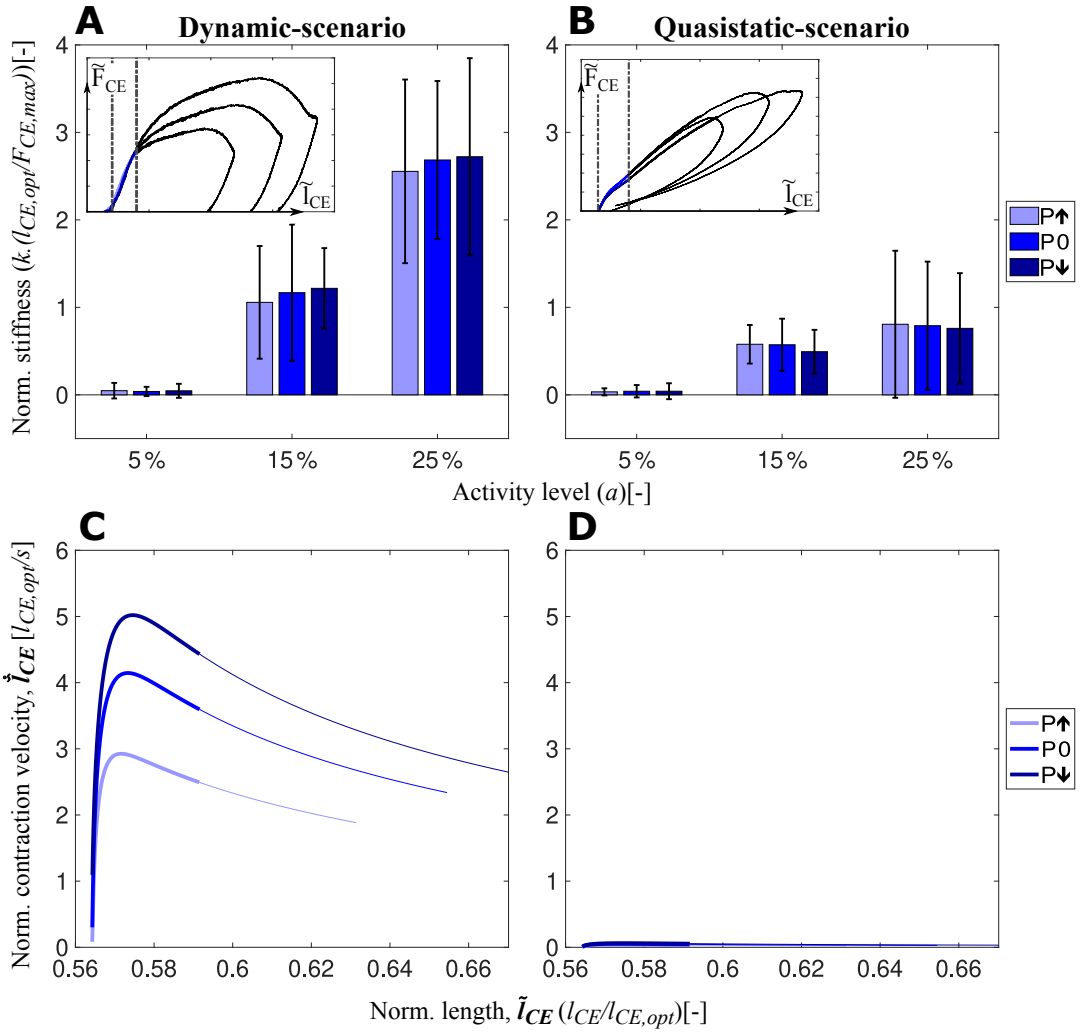

Figure 6.6: Short-range stiffness of muscle fibers during the dynamic-scenario (**A**). Stiffness amount during the short-range stiffness lengthening during quasistatic-scenario experiments (**B**) for all perturbation and activity levels are shown in the bar charts. Boundary conditions for the stiffness calculations for both speed conditions are shown as insets. In addition, velocity-length profiles during the preflex phase are presented in (**C**) and (**D**) for actual and quasistatic-scenario experiments, respectively. Thick lines show the short-range stiffness phase and thin lines present the remaining part of the preflex phase.

arranged by changing the activity level.

6.4 Discussion

In this study, we presented the first in vitro experiments conducted under realistic boundary conditions and activity levels of perturbed hopping. Our aim is to understand how intrinsic mechanical properties of an individual muscle fiber result in the modulation of the force output to perturbation during locomotion. We extracted the boundary conditions from a hopping simulation for three levels of perturbations. Here, we discuss surprising outcomes that we observed from our in vitro experiments and simulations. As

hypothesized, muscles modulate their force response to the stretch velocities. However, this modulation is not the main contributor to the preflex work. In addition, we observed that muscle's intrinsic properties are tunable by changing the activity level.

6.4.1 Muscle response to perturbations at dynamic-scenario

During dynamic-scenario experiments, muscle fibers initially react elastically to the sudden perturbation, known as short-range stiffness (Kirsch et al., 1994; Rack and Westbury, 1974). Muscles then transition into a viscoelastic behavior (Figure 6.3A). In the short-range stiffness region, we found no significant changes in fiber work, despite of different perturbations changed stretch velocities (Figure 6.6C). We calculated fiber work starting at the beginning of the stretch until the end of the short-range stiffness phase at $0.59\,\tilde{l}_{CE}$ (Figure 6.3A). Our observation is in agreement with the reported constant short-range stiffness for stretch velocity ranges similar to ours ($3\,l_{opt}$/s to $5\,l_{opt}$/s) (Pinniger et al., 2006; Rack and Westbury, 1974).

After the short-range stiffness phase, i.e., from $0.59\,\tilde{l}_{CE}$ to the end of preflexes, the force response became nonlinear, and velocity adaptation occurred. In this phase, higher stretch velocities cause higher forces (Figure 6.3A) and preflex work (Figure 6.4A). Both observations are in agreement with the reported work increment associated with increasing stretch velocity for the eccentric phase of ramp-like stretch-shortening cycles (Tomalka et al., 2021).

Two factors contribute to the increasing preflex work in our study. The first factor is the higher force when assuming the same stretch is considered for calculating the preflex work (Figure 6.5A, inset). For the specified area, all energetic differences between perturbations are the result of muscle fibers' viscous behavior since stretch amounts are identical. In that case, we observed no significant differences in preflex work between perturbations. Second, higher velocities cause a larger fibers' stretch in the preflex phase (Figure 6.3A). If the larger stretch is fully considered, differences in preflex work between the perturbation cases become significant (Figure 6.4A). We find a rising trend in dissipated energy with the increase of stretch velocity from step-up to step-down perturbations. Hence, muscles adjust their work response primarily due to a change of stretch caused by locomotion perturbation.

6.4.2 Tuning the force and energy response by activity level

Humans increase muscle activity in preparation for a step-down perturbation, as previously shown (Müller et al., 2012, 2015). The increased muscle activity strategy increases walking robustness (Haeufle et al., 2018). To test whether increased activity leads to higher muscle stiffness and work in this scenario, we conducted muscle fiber experiments with activity levels of 5 %, 15 % and 25 % for each perturbation case while keeping the kinematics identical.

The results confirm previous findings (Campbell et al., 2003) that the short-range stiffness increases with activity level (Figure 6.6A). As short-range stiffness is likely due to the stretch of attached cross-bridges (Getz et al., 1998; Pinniger et al., 2006), an increase in short-range stiffness can be explained by the increasing number of attached cross-bridges with increasing activity level (Metzger and Moss, 1990).

Additionally, we found that higher activity levels result in significantly higher preflex work (Figure 6.4A). Tomalka et al. (2021) likewise reported an increase in work with an increasing number of active cross-bridges in the eccentric phase of the ramp-like stretch-shortening cycles. An increase in preflex work with increasing activity level might be explained by an increasing number of forcibly detached

cross-bridges after the short-range stiffness phase. The number of forcibly detached cross-bridges might increase (at the given stretch kinematics) as a fraction of the increasing number of attached cross-bridges with activity level (Wahr and Rall, 1997). Forced detachment of cross-bridges is expected (Weidner et al., 2022) in the range of the tested stretch velocities (3 l_{opt}/s to 5 l_{opt}/s; Figure 6.6). Additionally, viscoelastic properties of non-cross-bridge structures (e.g., titin) might contribute to energy dissipation in a velocity-dependent manner (Freundt and Linke, 2019; Herzog et al., 2014; Tomalka et al., 2021). Furthermore, with higher activity, the differences between perturbation cases become more prominent, and, for 25 %, even significant (Figure 6.4A).

Consequently, humans and animals may tune their muscle stiffness during the short-range stiffness phase (Figure 6.6A) and their muscle work after the short-range stiffness phase (Figure 6.5A) utilizing the activity level. Thus, increased muscle stiffness and work in preparation for an expected perturbation are possible by increasing the muscle pre-activity level.

6.4.3 Dynamic- versus quasistatic-scenario

During the preflex phase of the quasistatic-scenario experiments, when muscles are stretched with negligible velocities, they respond with a linear force increase which is almost the same regardless of the perturbation case (Figure 6.3B). Comparison of dynamic-scenario and quasistatic-scenario experiments show that velocity is not only adding a viscous behavior to the response (Figure 6.3A, B), but also a visible short-range stiffness contribution (Figure 6.6). In previous isovelocity stretch experiments, the initial force response (i.e., short-range stiffness) was velocity dependent (Pinniger et al., 2006; Rack and Westbury, 1974), especially when the strain rate was varied over several orders of magnitude. For example, Pinniger et al. (2006) showed that the initial force response differs between slow (0.1 l_{opt}/s) and fast (2 l_{opt}/s) stretches. However, for contractions faster than 2 l_{opt}/s they observed no significant difference in the short-range stiffness. Weidner et al. (2022) observed differences in the short-range stiffness between 0.01 l_{opt}/s and 1 l_{opt}/s stretches. Our results align with these previous findings: while the short-range stiffness appears to be velocity-independent within the range of velocities tested in our dynamic-scenario experiments (reached peak velocities from 3 l_{opt}/s to 5 l_{opt}/s, Figure 6.6C), the comparison to the quasistatic-scenario experiments (reached maximum peak velocity of 0.05 l_{opt}/s, Figure 6.6D) revealed that the short-range stiffness actually reflects a muscle behavior that varies with large differences of velocity.

Interestingly, even though the dynamic behaviors during the preflex phase differ between quasistatic-scenario and dynamic-scenario conditions (Figure 6.3A, B), we observed almost equal amounts of mechanical work at quasistatic-scenario compared to dynamic-scenario stretches for each activity level (Figure 6.4A, B).

Possibly, myosin heads are detached forcibly from actin at high velocities during eccentric contractions. This will decrease muscle force generation (Weidner et al., 2022) observed during in situ and in vitro experiments (Fukutani et al., 2019; Griffiths et al., 1980; Krylow and Sandercock, 1997; Till et al., 2008; Tomalka et al., 2020; Weidner et al., 2022). On the other hand, during the quasistatic-scenario stretches, ultra-slow-speed stretches allow cross-bridges to bind easier and longer than during rapid contractions (Herzog, 2018; Huxley, 1957). Hence, similar forces during the preflex stretch phase result in similar amounts of energy dissipation in quasistatic-scenario and dynamic-scenario experiments.

6.4.4 Muscle fibers versus Hill-type muscle model

Since Hill's empirical investigations of muscle contraction dynamics, Hill-type models have played a crucial role in biomechanics research (Hill, 1938; Rode and Siebert, 2017). These models have been improved over the years, but they are still limited in predicting muscle forces, especially during eccentric (lengthening) contractions (Siebert et al., 2021; Till et al., 2008). Surprisingly, our results show that the magnitude and trends in mechanical work predicted by the Hill-type contractile element model are similar to the work of muscle fibers for fast eccentric contractions (Figure 6.4A, C). This is an unexpected outcome since the force responses of the Hill-type muscle model and muscle fibers differ (Figure 6.3A, C). We show that the main source of preflex work modulation to perturbation height is the amount of muscle stretch rather than the viscous force adaptation.

Our quasistatic-scenario experiments and simulations proved that the force-length relation of the Hill-type muscle model could accurately estimate the length-dependent force and mechanical work response of muscle fibers for the investigated conditions (relatively short muscle fibers at low activity levels). Because the length-dependent behavior of muscle fibers is the main force contributor during preflex, the Hill-type muscle model predicts work for the larger stretch in response to the fast contraction reasonably well.

Although the Hill-type muscle model estimates work during preflexes with good accuracy, it still requires improvements for better force prediction during fast contractions (Figure 6.3A, C). The short-range stiffness had previously been observed in other fiber experiments (Rack and Westbury, 1974; Tomalka et al., 2021; Weidner et al., 2022). We observed that the short-range stiffness was activity- and velocity-dependent (Figure 6.6), at least for the velocity difference between dynamic-scenario and quasistatic-scenario experiments (Figure 6.3A, B). However, our Hill-type muscle model cannot generate the high-stiffness response of a short-range stiffness, since short-range stiffness is not a built-in mechanical property (Haeufle et al., 2014b). So far, the short-range stiffness model proposed by Cui et al. (2008) has been implemented in several musculoskeletal simulations to study the influence of short-range stiffness on the endpoint stiffness of the human arm in static postures (Hu et al., 2011) and postural stability while standing (De Groote et al., 2017). These simulation studies showed that including short-range stiffness in a Hill-type muscle model improves the estimation of joint angles, torques, and stiffness (Hu et al., 2011), as well as postural stability against external perturbations (De Groote et al., 2017). Together with our results, we expect that Hill-type muscle models that feature short-range stiffness should provide a better force estimation at and immediately after impact. Therefore, we consider short-range stiffness an essential model feature for the understanding of gait mechanics leading to stable locomotion.

The force modulation to the perturbation velocity after the short-range stiffness (Figure 6.3A, C) is also not accurately modeled in the Hill-type muscle model. Here, the Hill-type muscle model operates in the plateau region of the eccentric force-velocity relation (Figure 6.2). The model, therefore, does not show any modulation of the force due to the perturbation-related changes in fiber velocity, in contrast to the observations in the experiments (Figure 6.3A, C). This plateau-form of the eccentric force-length relation was introduced by van Soest and Bobbert (1993). While their results are consistent with our simulation data, they do not explain the experimental results of the present study. Possible reasons for the deviation of the experiment can be the starting length of the contraction, the sub-maximal activity level or the underlying model. However, the results of Krylow and Sandercock (1997) suggest that the starting length has no influence on the point of occurrence of the eccentric force-velocity relation's plateau. Regarding the sub-maximal activity level and its effects, it is known that the calcium concentration has

an influence on the cross-bridge kinetics (Brenner, 1988). Nevertheless, to the best of our knowledge, there is no study that looked at the dependency of the eccentric force-velocity relation on the activity level within the contractile element only. A likely explanation for the discrepancy is a simplification of the contraction by the model. For example, the Hill-type muscle model lacks the implementation of “Give" (Flitney and Hirst, 1978), which, on the one hand, is speed-dependent and, on the other hand, occurs directly after the end of the short-range stiffness (Weidner et al., 2022). The force and work responses show that the modeling of eccentric muscle behavior needs to be modified for better estimation of the dynamic response to perturbations during fast eccentric contractions. In addition, the effect of the neural reflex response after the preflex phase will have a significant effect on the post-preflex force generation (Nichols and Houk, 1976) and should also be examined in further experiments with an appropriately updated experimental setup.

6.4.5 Study limitations

This study aimed to analyze how a single muscle fiber reacts to ground perturbations in real life. It is known that the temperature influences the muscle properties (e.g., F_{max}, V_{max}, (Ranatunga, 1984; Stephenson and Williams, 1985; Zhao and Kawai, 1994)) and thus the force response to disturbances. Therefore, temperature influences on the force response to perturbations should be investigated in future studies. We conducted single-leg hopping simulations using a Hill-type muscle model as a knee extensor muscle to generate kinematic boundary conditions for in vitro experiments. However, Hill-type muscle models have limitations discussed in previous chapters, and simulation and real-life muscle lengthening may differ. Additionally, our in vitro experimental setup allows only constant activity levels. Even though in the hopping simulations after the preflex phase activity rises, due to the setup limitations, we performed the kinematic analysis with the constant preflex activity level, which is not the case for in vivo hopping (Moritz and Farley, 2004) and locomotion (Müller et al., 2015). Thus, we only focused our analysis on the preflex phase. We assume a preflex time-span of 30 ms based on the reflex delay scaling found by More et al. (2010). Since we do not consider a full work loop, this study’s design does not directly allow us to calculate damping, i.e., the amount of energy dissipation in a full cycle. However, the velocity-dependent modulation of preflex work indicates a viscous-like response, which we identify as a damping behavior.

6.5 Conclusion

Previous experimental and simulation studies indicated that muscles’ preflex capability to adjust force to unexpected ground conditions is essential in stabilizing hopping and locomotion. Our study confirms these findings and shows three mechanisms: (1) muscle force adapts to the change in stretch velocity caused by a perturbation; (2) the overall fiber stretch in the preflex duration is larger for larger stretch velocities resulting in increased preflex work; (3) with increasing muscle activity short-range stiffness and muscle force increase. Mechanism (1) is the hypothesized viscous effect of the force-velocity relationship but plays a minor role compared to the mechanism (2). Together, (1) and (2) result in a beneficial and significant modulation of muscle force to perturbations and thus confirm the preflex hypothesis. Mechanism (3) allows for a simple neuronal strategy to tune the muscle properties to ground conditions and unexpected perturbations and aligns with feedforward strategies observed in human locomotion (Müller et al., 2012).

7 Effective viscous damping enables morphological computation in legged locomotion

This chapter describes our first investigation on principles of tunable mechanical damping in legged robotics. Muscle models and experimental observations suggest that mechanical damping benefits motion stabilization. Still, only a few implementations of mechanical damping exist in compliant, legged robots. Although its control-free capacity to generate adaptive forces and negative work is promising, it remains primarily unexplored how mechanical damping can be exploited in legged robotics.

Using a simplified numerical model of a robotic leg, we studied the benefit of viscous damping in regulating energy dissipation following step perturbations. Our simulations demonstrate that viscous damping consistently outperforms Coulomb friction damping. Based on these results, we investigated whether damping rate control of viscous dampers directly coupled to the knee joint effectively produces tunable mechanical damping in hardware experiments. We tested two damper designs: commercial hydraulic dampers and a custom-made pneumatic damper. The pneumatic damper exploits a rolling diaphragm with an adjustable orifice, minimizing Coulomb friction-damping effects while permitting adjustable resistance. Experimental results show that the leg-mounted hydraulic damper exhibits the most effective viscous damping. However, damping rate control did not adjust dissipated energy substantially in all the tested hardware, unlike what we observed in our numerical simulations. Consequently, our hardware experiments suggest that damping rate control of directly coupled viscous dampers may not be an effective solution to produce tunable mechanical damping in fast perturbed legged locomotion.

Note: a large portion of this chapter uses content published in *Frontiers in Robotics and AI, section Soft Robotics* (Mo et al., 2020). For details on this journal article, including the list of authors and my contribution, see Section 2.1.3.

7.1 Introduction

While less understood, damping likely plays an essential role in animal legged locomotion. Intrinsic damping forces can potentially increase the effective force output during unexpected impacts (Müller et al., 2014), reduce control effort (Haeufle et al., 2014b), stabilize movements (Abraham et al., 2015; Secer and Saranli, 2013; Shen and Seipel, 2012), and reject unexpected perturbations (Haeufle et al., 2010; Kalveram et al., 2012), e.g., sudden variations in the ground level (Figure 7.1). Stiffness, in comparison, has been studied extensively in legged locomotion. Its benefits have been shown both in numerical simulations, e.g., through spring-loaded inverted pendulum (SLIP) models (Blickhan et al., 2007; Mochon and McMahon, 1980), and mechanical springy leg implementations (Hutter et al., 2016;

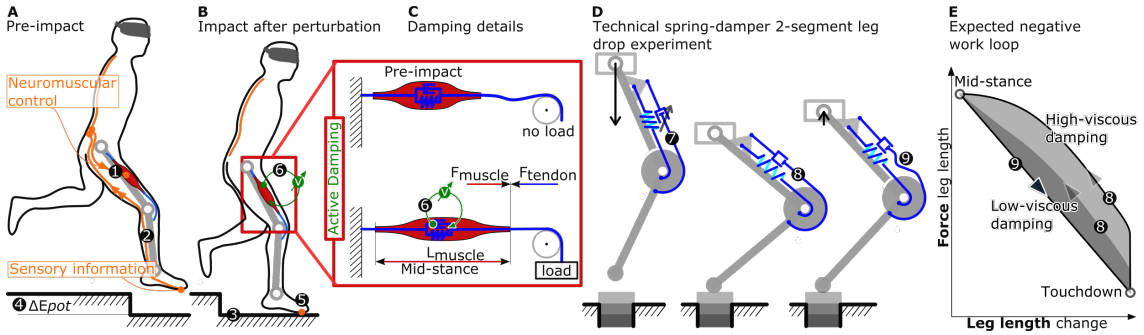

Figure 7.1: (A-C) Problem identification, and related research question. The limited nerve conduction velocity in organic tissue (More et al., 2010) ❷ presents a significant hazard in legged locomotion. Local neuromuscular strategies ❻ provide an alternative means of **timely and tunable force and power production**. Actuators like the indicated knee extensor muscle keep the leg extended during the stance phase (muscle length L_{muscle}) by producing the appropriate amount of muscle force (F_{muscle}), correctly **timed**. Neuromuscular control ❶ plays a major role in initiating and producing these active muscle forces, but works best only during unperturbed locomotion. Sensor information from foot contact travels via nerves bundles ❷ to the spinal cord, but with **significant time delays** in the range of $t = 40\,\text{ms}$ (More and Donelan, 2018, for 1 m leg length) and more. Hence, the locomotion control system can become **'sensor blind' due to conduction delays, for half a stance phase**, and can miss unexpected perturbations like the depicted step-down. During step-down perturbations ❸ additional energy ❹ is inserted into the system. Viscous damper-like mechanisms **produce velocity-dependent counter-forces and can dissipate kinetic energy**. Local neuromuscular strategies ❻ producing tunable, viscous damping forces would **act instantaneously and adaptively**. Such strategies ❻ could also be robust to uncontrolled and harsh impacts of the foot after perturbations ❺, better than sensor-based strategies. In this work **(D)**, we are testing and characterizing spring-damper configurations mounted to a two-segment leg structure, during rapid- and slow-drop experiments, for their feasibility to mechanically and instantaneously produce tunable, speed-dependent forces extending the leg. Work loops **(E)** will indicate how much effective negative work is dissipated between touchdown and mid-stance. Prior to impact ❼ and during the leg loading ❽ the spring-damper's tendons act equally. Starting at mid-stance, the main spring extends the knee, leading to leg extension and leaving the damper's tendon slack ❾.

Ruppert and Badri-Spröwitz, 2019; Spröwitz et al., 2013).

What combines both mechanical stiffness and intrinsic mechanical damping is their sensor- and computational-free action. A spring-loaded leg joint starts building up forces exactly at the moment of impact. Mechanical stiffness, or damping, acts instantaneously and is not subject to delays from post-processing sensor data (Grimminger et al., 2020), delays from limited nerve conductive velocities (More and Donelan, 2018), or uncertainties in the estimation of the exact timing of swing-to-stance switching (Bledt et al., 2018).

Legged robots commonly exploit *virtual damping*: actively produced and sensory-controlled negative work in the actuators (Grimminger et al., 2020; Havoutis et al., 2013; Hutter et al., 2012; Kalouche, 2017; Seok et al., 2015). Virtual damping requires high-frequency force control, and actuators mechanically and electrically capable of absorbing peaks in negative work. In comparison, mechanical damping-based systems (Garcia et al., 2011; Hu et al., 2019) act instantaneously, share impact loads with the actuator when in parallel configuration, and require no sensors or control feedback. The instantaneous mechanical response of a damper is especially relevant in biological systems, where the neuronal delay may be as large as 5 % to 40 % of the duration of a stance phase (More et al., 2010). In such a short time window, mechanical damping could help to reject the perturbation (Haeufle et al., 2010; Kalveram et al., 2012) by morphological computation, as it mechanically contributes to the rejection of the perturbation, a

contribution that otherwise would need to be achieved by a (fast) controller (Ghazi-Zahedi et al., 2016; Zahedi and Ay, 2013). Hence, mechanical damping has the potential to contribute to the *morphological computation* (Ghazi-Zahedi et al., 2016; Zahedi and Ay, 2013) of a legged system.

Compared to virtual damping with proprioceptive sensing strategies (Grimminger et al., 2020), a legged robot with mechanical damping requires additional mechanical components, e.g., a fluidic cylinder, and the mechanics to convert linear motion to rotary output. In a cyclic locomotion task, the energy removed by any damper must also be replenished. Hence, from a naive energetic perspective, both virtual and mechanical damping systems are costly.

Energy dissipation in the form of negative work has been quantified in running birds and identified as a potential strategy to '... reduce the likelihood of a catastrophic fall.' (Daley and Biewener, 2006, p. 185). In virtual point-based control strategies for bipedal running, positive work is inserted into hip joints, and negative work is then dissipated in equal amounts in the spring-damper leg (Drama and Badri-Spröwitz, 2020). In sum, either mechanical damping or virtual damping allows removing energy from a legged locomotion system. In this work, we focus on mechanical damping produced by a viscous damper. We aim towards an understanding of how mechanical damping can be exploited in legged locomotion and which requirements a damper must fulfill.

We consider two damping principles: viscous damping and Coulomb damping. Viscous damping reacts to a system motion with a force that is linearly (or nonlinearly) proportional to its relative acting speed. Coulomb damping generates a constant force, largely independent from its speed (Serafin, 2004). From a control perspective, viscous damping can be beneficial for the negotiation of perturbations in locomotion as it approximates the characteristics of a differential, velocity-dependent term. Yet, it is unknown how this intuition transfers into reality, where impact dynamics and nonlinearities of the leg geometry alter the stance-phase dynamics of locomotion.

Damping in legged locomotion can have other purposes besides dissipating energy. The authors of (Werner et al., 2017, p. 7) introduced a damping matrix in the control scheme, which reduced unwanted oscillations in the presence of modeling errors. Tsagarakis et al. (2013) mount compliant elements with some damping characteristics, which also could reduce oscillations of the system's springy components.

In this project, we focus our investigation on the effect of damping during the touchdown (impact) and mid-stance. We chose this simpler drop-down scenario as it captures the characteristics of roughly half a locomotion cycle. A complete cycle would require an active push-off phase and the leg's swing dynamics. Hence, we study the effectiveness of mechanical damping on the leg's energy dissipation within one drop (touchdown to lift-off) by quantifying its **effective dissipated energy** $E_{\text{effective}}$. We combine insights from numerical simulations and hardware experiments (Figure 7.2). By studying the response of two damping strategies (viscous and Coulomb damping) in numerical drop-down simulations, we investigate how mechanical damping can influence the dynamics of the impact phase. We then examine how these theoretical predictions relate to hardware experiments with two functionally different, mechanical dampers. Hence we explore and characterize the mechanical damper implementations in a robot leg for their effectiveness in drop-impacts.

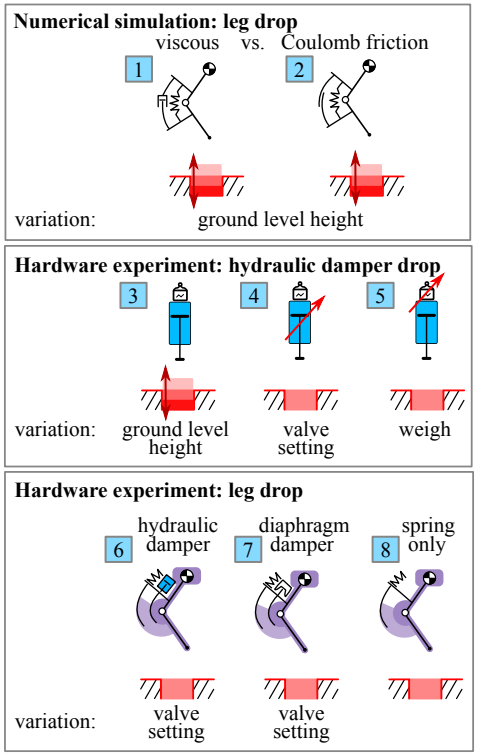

Figure 7.2: Overview: We study the *effective dissipated energy* $E_{\text{effective}}$ in drop experiments, i.e., the energy dissipation within one drop cycle between touchdown and lift-off (Figure 7.6). We focus on a system design with a damper and a spring, both acting in parallel on the knee joint (Figure 7.1D and Figure 7.3). No active motor is considered as it is not relevant for the drop scenario, but required for continuous hopping. In **numerical simulations**, we quantify the difference in energy dissipation between viscous 1 and Coulomb 2 damping for varying ground level heights (Section 7.2 and Figure 7.4). The **first set of hardware experiments** characterizes the industrial hydraulic damper. For this, we **drop the isolated damper** (damper only, not mounted in the leg) on a force sensor and calculate the energy dissipation. We vary the ground level height 3, the valve setting 4 and the drop mass 5, to investigate its dynamic characteristics (Section 7.4.1 and Figure 7.7). For the **second set of hardware experiments, we drop a 2-segment leg with dampers mounted in parallel to knee springs**. We investigate the energy dissipation dynamics of the hydraulic 6 and diaphragm damper 7 by comparing it to a spring-only condition 8, where the damper cable is simply detached (Section 7.4.2 and Figure 7.8). We also vary the valve setting on the dampers to test the dynamic adjustability of damping (Section 7.4.3 and Figure 7.9).

7.2 Numerical simulation

We use numerical simulations to investigate the energy dissipation in a leg drop scenario (Figure 7.2). In analogy to our hardware experiment (Section 7.3.3), a two-segment leg with a damper and a spring in parallel on the knee joint is dropped vertically (Figure 7.3a). Once in contact with the ground, the knee flexes, and energy is dissipated. We compare viscous vs. Coulomb damping to investigate which of these two theoretical damping strategies may be more suited for the rejection of ground-level perturbations. Also, we investigate how the adjustment of the damping characteristics influences the dissipated energy.

In all the damping scenarios investigated, the system is not energy-conservative. As we investigate the potential benefit of damping in the initial phase of the ground contact, i.e., from touchdown to mid-stance, we do not consider any actuation. Without actuation or control, the model's dissipated energy is not refilled, unlike in, for example, periodic hopping (Kalveram et al., 2012).

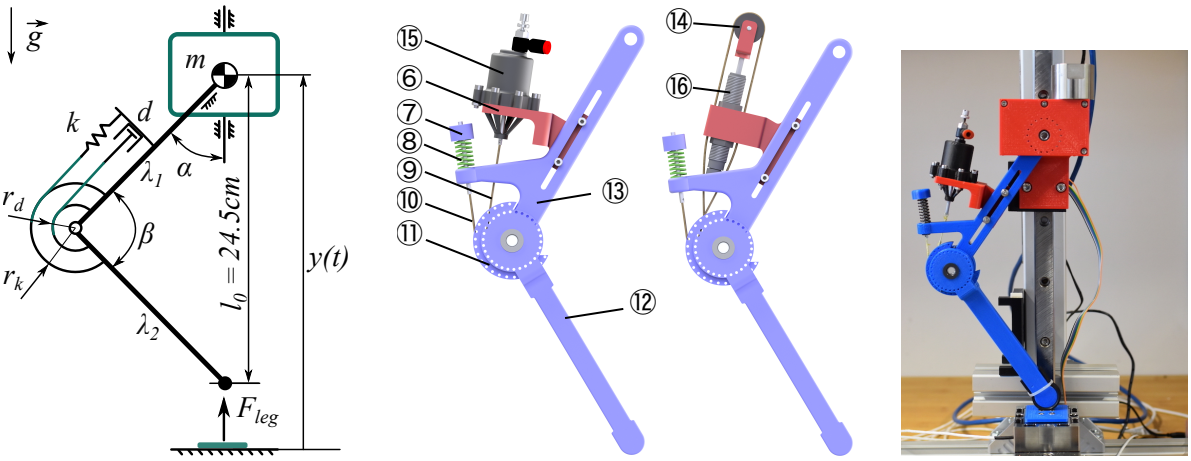

(a) Leg model **(b)** Leg design **(c)** Drop test bench

Figure 7.3: (a) two-segment spring-damper-loaded leg model used for simulation. **(b)** Mechanical design of the two-segment leg. The knee pulley⑪ is fixed with the lower segment⑫, coupled with the spring⑧ and the diaphragm damper⑮ or hydraulic damper⑯ via cables⑨⑩. **(c)** Drop test bench with the two-segment leg.

7.2.1 Model

The numerical model is a modified version of the two-segment leg proposed in Rummel and Seyfarth (2008) with an additional damper mounted in parallel to the knee-spring. The equation describing our leg dynamics is:

$$\ddot{y}(t) = \frac{F_{leg}(t)}{m} - g \tag{7.1}$$

where g is the gravitational acceleration, m is the leg mass (lumped at the hip), and $y(t)$ is the time-dependent vertical position from the ground. $F_{leg}(t)$ is the force transmitted to the hip mass - and the

ground - through the leg structure. As such, the force depends on the current phase of the hopping cycle:

$$F_{leg}(t) = \begin{cases} 0 & \text{, flight phase: } y(t) > l_0 \\ \dfrac{y(t)}{\lambda_1 \lambda_2} \dfrac{\tau(t)}{\sin(\beta(t))} & \text{, ground contact: } y(t) \leq l_0 \end{cases} \tag{7.2}$$

with segment length λ_i and knee angle $\beta(t)$ (Figure 7.3a); l_0 is the leg length at impact. $\tau(t)$ is the knee torque which is produced by the parallel spring-damper element, as in

$$\tau(t) = -k r_k^2 (\beta(t) - \beta_0) + \tau_d(t) \tag{7.3}$$

with k and r_k being the spring stiffness coefficient and lever arm, respectively. $\tau_d(t)$ is the damping torque, which is set to zero during leg extension, i.e., the damper is only active from impact to mid-stance:

$$\tau_d(t) = 0 \qquad \text{if } \dot{\beta}(t) > 0 \tag{7.4}$$

The modeled damper becomes inactive during leg extension, in accordance with our hardware: the tested mechanical dampers apply forces to the knee's cam via a tendon (Figure 7.1D, ❾), and this tendon auto-decouples during leg extension. By choosing different definitions of the damper torque $\tau_d(t)$, we can analyze different damper concepts. The model parameters are listed in Table 7.1.

Simulations were performed using MATLAB (the MathWorks, Natick, MA) with ODE45 solver (absolute and relative tolerance of 10^{-5}, max step size of 10^{-5} s). When searching for appropriate settings of the numerical solver, we progressively reduced error tolerances and the maximum step size until convergence of the simulation results in Table 7.2 to the first non-significant digit.

Table 7.1: Simulation and hardware parameters

Parameters	Symbol	Value	Unit
Mass	m	0.408	kg
Reference drop height	h_0	14	cm
Spring stiffness	k	5900	N/m
Leg segment length	λ_1, λ_2	15	cm
Leg resting length	l_0	24.6	cm
Knee resting angle	β_0	110	deg
Spring lever arm	r_k	2.5	cm
Damper lever arm	r_d	2	cm

7.2.2 Damping characteristics

We compared two damping concepts in our numerical simulation: (1) *pure* Coulomb damping, i.e., a constant resistance only dependent on motion direction, and (2) *pure* viscous damping, i.e., a damper torque linearly dependent on the knee angular velocity. Accordingly, we tested two different definitions of τ_d:

$$\tau_d(t) = \begin{cases} -d_c r_d \operatorname{sign}(\dot{\beta}(t)) & \text{, pure Coulomb damping} \\ -d_v r_d^2 \dot{\beta}(t) & \text{, pure viscous damping} \end{cases} \tag{7.5}$$

where r_d is the damper level arm, d_c (in N) and d_v (in Ns/m) the Coulomb damping and viscous damping coefficients, respectively.

7.2.3 Energy dissipation in numerical drop simulations

With this model, we investigate the difference in energy dissipation in response to step-up/down perturbations (cases 1 and 2 in Figure 7.2). For each drop test, the numerically modeled leg starts at rest ($\dot{y}(t) = 0$) with a drop height

$$h = y(t = 0) - l_0 \tag{7.6}$$

corresponding to the foot clearance at release. The total energy at release is $E_T(h) = m\,g\,h$. Given that all model parameters in Table 7.1 are fixed, the energy dissipated in a drop becomes a function of the drop height and the damping coefficients: $E_D = f_{E_D}(h, d_{c,v})$.

A simulated drop height h can be seen as a variation Δh from a reference value h_0:

$$h = h_0 \pm \Delta h \tag{7.7}$$

Equal to the hardware experiments, we use $h_0 = 14\,\text{cm}$ as reference drop height. In the reference drop condition, i.e., $h = h_0$, the energy dissipated by damping is $E_{D_0} = E_D(h_0) = f_{E_D}(h_0, d_{c,v})$. E_{D_0} only depends on the damping level, namely the chosen damping strategy (viscous or Coulomb damping) and the associated damping coefficient. We chose five different desired damping levels (set 1-5) as a means of scanning a range in which the damping could be adjusted: for each set, the amount of energy that is dissipated at the reference drop height E_{D_0} differs. The chosen E_{D_0} values (Table 7.2, column "Reference height") correspond to proportional levels ($[0.1, 0.2, \ldots, 0.5]$) of the systems potential energy in terms of the leg resting length l_0, as in

$$E_{D_0} \approx m\,g\,[0.1, 0.2, \ldots, 0.5]\,l_0 \tag{7.8}$$

This corresponds to damping configurations that dissipate between $\approx 17\,\%$ and $\approx 88\,\%$ of the system's initial potential energy at the reference height ($E_{T_0} = E_T(h_0) = m\,g\,h_0 = 560\,\text{mJ}$), as shown in Table 7.2, column "Reference height". To achieve these desired damping levels, we adjusted the damper parameters d_c and d_v accordingly (Table 7.2, column "Damping coeff."). As an example: for set 3, both damping values were adjusted such that at the reference height h_0 both dampers dissipate $E_{D_0} = m\,g\,0.3\,l_0 = 295\,\text{mJ}$, which corresponds to 53 % of the total energy E_{T_0}.

In the numerical simulations, we focus on the relation between a ground-level perturbation Δh and the change in energy dissipation – and their dependency on the damper characteristics. A drop from a height larger than h_0 corresponds to a step-down ($\Delta h > 0$), and a drop from a height smaller than h_0 to a step-up ($\Delta h < 0$). Each condition introduces a change in the total energy of $\Delta E_T = m\,g\,\Delta h$. The change in energy dissipation due to the perturbation is defined as

$$\Delta E_D(\Delta h) = E_D(h_0 + \Delta h) - E_{D_0} \tag{7.9}$$

which is the difference between the dissipated energy when released from a perturbed height and the dissipated energy when released from the reference height. As a reference, we further define the *full rejection* case where

$$\Delta E_D(\Delta h) = \Delta E_T = m\,g\,\Delta h \tag{7.10}$$

Table 7.2: Numerical simulation Total dissipated energy (E_D) in one drop cycle for different drop heights (h). *Reference height* is the reference drop height $h = h_0 = 14\,\text{cm}$. During *step-up(down)* condition, the drop height is reduced(increased) by $\Delta h = 2.5\,\text{cm}$. Percentage values indicate the change in dissipated energy (ΔE_D) relative to the change in system total energy (ΔE_T) due to the height perturbations. Each set simulates two separate mechanical dampers (pure viscous or pure Coulomb damping), with damping coefficients chosen to dissipate the same energy at the reference condition, i.e., E_{D_0}. Results of set 1, 3 and 5 are further described in Figure 7.4. For all tested conditions, viscous damping outperforms Coulomb damping, as indicated by the always higher percentage values (bold).

		Damping coeff.		*Step-up* $h = h_0 - \Delta h = 11.5\,cm$	*Reference height* $h = h_0 = 14\,cm$	*Step-down* $h = h_0 + \Delta h = 16.5\,cm$
		d_v	d_c	E_D ($\Delta E_D/\Delta E_T$)	E_{D_0} (E_{D_0}/E_{T_0})	E_D ($\Delta E_D/\Delta E_T$)
Set 1	Viscous	29.5 Ns/m	0 N	**82 mJ (15%)**	97 mJ (17%)	**112 mJ (15%)**
	Coulomb	0 Ns/m	7.7 N	88 mJ (9%)	97 mJ (17%)	104 mJ (7%)
Set 2	Viscous	68 Ns/m	0 N	**167 mJ (30%)**	197 mJ (35%)	**227 mJ (30%)**
	Coulomb	0 Ns/m	17.3 N	178 mJ (19%)	197 mJ (35%)	214 mJ (17%)
Set 3	Viscous	119.4 Ns/m	0 N	**249 mJ (46%)**	295 mJ (53%)	**341 mJ (46%)**
	Coulomb	0 Ns/m	29.3 N	264 mJ (31%)	295 mJ (53%)	323 mJ (28%)
Set 4	Viscous	197.1 Ns/m	0 N	**330 mJ (63%)**	393 mJ (70%)	**455 mJ (62%)**
	Coulomb	0 Ns/m	46.1 N	346 mJ (47%)	393 mJ (70%)	436 mJ (43%)
Set 5	Viscous	349.4 Ns/m	0 N	**411 mJ (81%)**	492 mJ (88%)	**572 mJ (80%)**
	Coulomb	0 Ns/m	76.3N	423 mJ (69%)	492 mJ (88%)	556 mJ (64%)

In human hopping, a full recovery within a single hopping cycle is not seen during experimental drop-down perturbations. Instead, a perturbation of $\Delta h = 0.1\,l_0$ is rejected in two to three hopping cycles (Kalveram et al., 2012). In our results, this corresponds to the partial rejections observed with viscous damping in sets 2 and 3 for $\Delta h = \pm 2.5\,\text{cm}$.

7.2.4 Simulation results

Figure 7.4a shows the relation between the change in drop height and the corresponding change in dissipated energy by the simulated dampers for set 1, 3 and 5 (continuous line for pure viscous, dashed for pure Coulomb damping). For the range of simulated drop heights, pure viscous and Coulomb dampers change the amount of dissipated energy with an almost linear dependence on the drop height. However, pure viscous damping has a slope closer to the *full rejection* scenario (blue line in Figure 7.4a), regardless of the set considered. In a step-down perturbation ($\Delta h > 0$ in Figure 7.4a), pure viscous damping dissipates more of the additional energy ΔE_T, while in a step-up perturbation ($\Delta h < 0$) it dissipates less energy than pure Coulomb damping. As such, the results show that a viscous damper can reject a step-down perturbation faster, e.g., within fewer hopping cycles, and it requires smaller correction by the active energy supply during a step-up perturbation.

Adjusting the damping parameters allows to change the reaction to a perturbation (Figure 7.4). Increasing the damping intensity, i.e., d_v and d_c from set 1 to 5, allows to better match the *full recovery* behavior (blue line in Figure 7.4a). However, this comes at the cost of a higher energy dissipation at the reference height, i.e., in the absence of a ground perturbation (Table 7.2, column 'reference height').

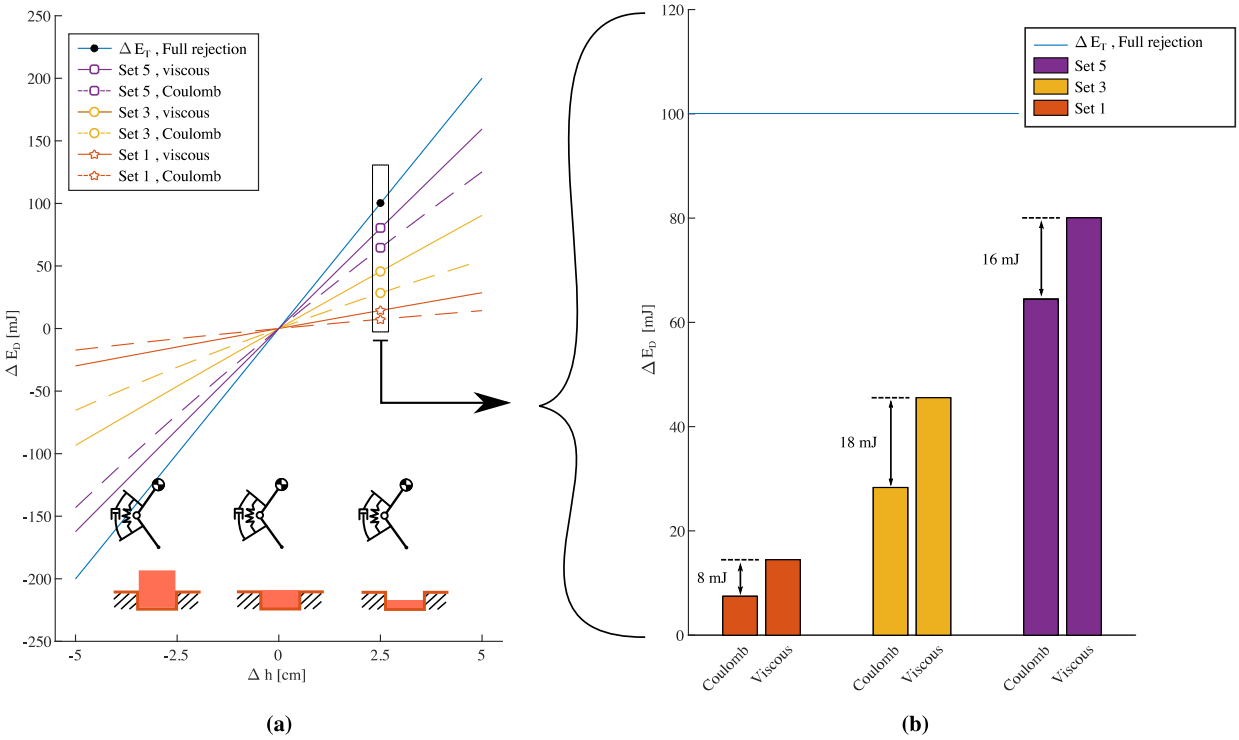

Figure 7.4: Numerical simulation Cases 1 and 2 from Figure 7.2, **(a)**: Change of dissipated energy vs. change of drop height for set 1, 3 and 5, with damping coefficients as in Table 7.2. Continuous lines are viscous damping results, dashed Coulomb damping. Positive perturbations, i.e., $\Delta h > 0$, correspond to step-down perturbations; step-up perturbations, otherwise. The steepest line indicates the slope needed for a *full rejection* of a Δh deviation. For each set (1, 3, 5), the damping parameters are matched such that viscous and Coulomb damping dissipate the same energy at the reference height h_0 (see Table 7.2). Within each set, the viscous damping line is closer to the desired *full rejection* line than the corresponding Coulomb damping line. This means that for the same cost (in the sense of dissipated energy at the reference height) viscous damping always rejects more of ground level perturbation than Coulomb damping. **(b)**: ΔE_D for $\Delta h = 2.5\,\text{cm}$. The horizontal line indicates the amount of energy to dissipate for *full rejection* of Δh. The energetic advantage of viscous damping over Coulomb damping, as indicated by the spread in the corresponding ΔE_D values, increases from set 1 to 3, and reduces from set 3 to 5.

Increasing the damping rate also affects the energetic advantage of viscous damping over Coulomb damping. Figure 7.4b shows this in detail for a *specific* step-down perturbation ($\Delta h = 2.5\,\text{cm}$): from set 1 to set 3, the spread between the ΔE_D values of the viscous damper and the Coulomb damper increases (from 8 mJ to 18 mJ). However, the difference in dissipated energy ΔE_D slightly reduces from set 3 to set 5 (from 18 mJ to 16 mJ).

Table 7.2 quantifies the previous findings by indicating the percentage of energy perturbation ΔE_T that each damping approach dissipates for $\Delta h = \pm 2.5\,\text{cm}$ and for all the tested sets of damping coefficients d_v and d_c. The data further confirms the observations from Figure 7.4, showing that:

1. within each set, viscous damping outperforms Coulomb damping for all the simulated conditions - its dissipated energy is always the closest to 100 % of ΔE_T, which means the closest to *full rejection*;

2. the energetic benefit of viscous damping over Coulomb damping, i.e., the spread in percentage

values of $\Delta E_D/\Delta E_T$, *does not monotonically increase* with higher damping rates, i.e., moving from set 1 to 5.

Furthermore, Table 7.2 shows that for low damping rates, i.e., set 1, viscous damping introduces only marginal benefits in energy management compared to Coulomb damping: $< 10\%$ spread between the corresponding $\Delta E_D/\Delta E_T$ values.

7.3 Hardware Description

With the previous results from our numerical simulation in mind, we tested two technical implementations (Figure 7.5) to produce tunable mechanical viscous damping. We implemented a two-segment leg hardware (Figure 7.3b) and mounted it to a vertical drop test bench to investigate the role of mechanical damping. The drop test bench produces velocity profiles during impact and stance phase similar to continuous hopping and allows us to test effective damping efficiently and repeatably.

7.3.1 Rolling Diaphragm Damper

The most common designs of viscous dampers are based on hydraulic or pneumatic cylinders (viscous damping) and can offer the possibility of regulating fluid flow by altering the orifice opening (adjustability). These mechanical dampers can display high Coulomb friction, caused by the mechanical design of the sliding seal mechanisms. Typically, the higher the cylinder pressure is, the higher the Coulomb friction exists. Ideally, we wanted to test one mechanical damper concept with the least possible amount of Coulomb friction. Inspired by the low-friction hydrostatic actuators (Whitney et al., 2014, 2016), we designed a low-Coulomb damper based on a rolling diaphragm cylinder. Its cylinder is 3D printed from Onyx material. Figure 7.5a illustrates the folding movement of this rolling diaphragm mounted on a piston. The rolling diaphragm is made of an elastomer shaped like a top hat that can fold at its rim. When the piston moves out, the diaphragm envelopes the piston. In the ideal implementation, only rolling contact between the diaphragm and the cylinder occurs and no sliding contact. Hence, Coulomb friction between the piston and cylinder is minimized. We measured $F_C \approx 0.3\,\mathrm{N}$ of Coulomb friction for our rolling diaphragm cylinder at low speed.

Our numerical simulation results promoted viscous and tunable damping for use in vertical leg-drop. By concept, both properties are satisfied by the diaphragm damper with an adjustable valve. When an external load F_{ext} pulls the damper piston (Figure 7.5a), the fluid inside the cylinder chamber flows through a small orifice, adjustable by diameter. This flow introduces a pressure drop $\Delta P(t)$, whose magnitude depends on the orifice cross-section area A_o and piston speed $v(t)$. As such, for a given cylinder cross-section area A_p, the diaphragm damper reacts to an external load F_{ext} by a viscous force $F_p(t)$ due to the pressure drop $\Delta P(t)$:

$$F_p(t) = A_p\,\Delta P(t) = A_p\,f(v(t), A_o) \tag{7.11}$$

We mounted a manually adjustable valve (SPSNN4, MISUMI) to set the orifice size A_o. For practical reasons (weight, leakage, complexity of a closed circuit with two cylinders), we used air in the diaphragm cylinder as the operating fluid instead of liquid (Whitney et al., 2014, 2016). Air is compressible, and with a fully closed valve, the diaphragm cylinder also acts as an air spring. This additional functionality can potentially simplify the overall leg design. With the pneumatic, rolling diaphragm-based damper

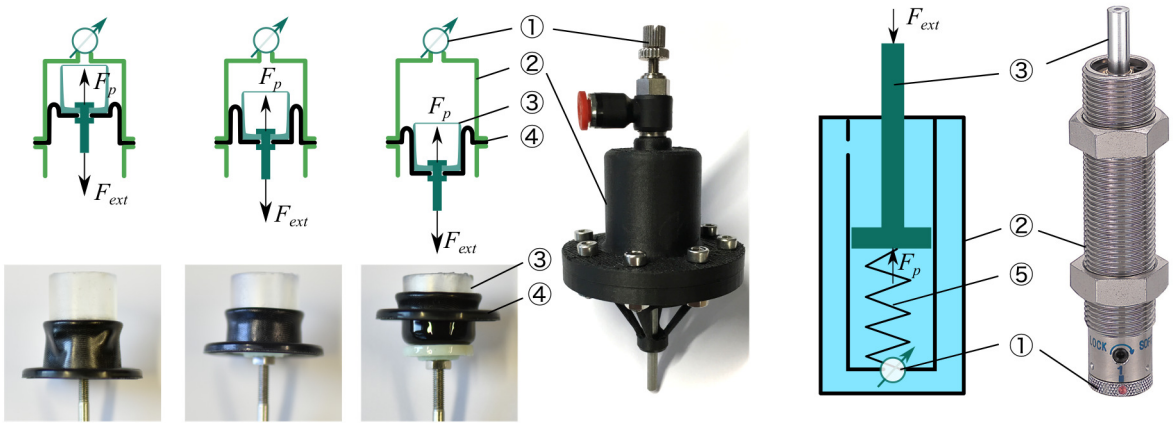

(a) Diaphragm damper **(b)** Hydraulic damper

Figure 7.5: (a) Left-top: schematic of a diaphragm damper, illustrating the motion of the rolling diaphragm, which includes an adjustable orifice①, a cylinder②, a piston③, and a rolling diaphragm④. **(b)** Right: schematic of a hydraulic damper: fluid is sealed inside the cylinder② with a recovery spring⑤ to reset the piston③.

implementation, we focused on creating a lightweight, tunable damper with minimal Coulomb friction and air as the operating fluid.

7.3.2 Hydraulic Damper

In the second technical implementation, we applied an off-the-shelf hydraulic damper (1214H or 1210M, MISUMI, Figure 7.5b), i.e., a commercially available solution for tunable and viscous damping. Tested against other hydraulic commercial dampers, we found these specific models to have the most extensive range of tunable viscous damping and the smallest Coulomb friction ($F_C \approx 0.7\,\mathrm{N}$). Similarly to the diaphragm damper, these hydraulic dampers produce viscous damping by the pressure drop at the adjustable orifice. The operating fluid is oil, which is in-compressible. Hence, the hydraulic damper should not exhibit compliant behavior. Other than the diaphragm damper, the hydraulic damper produces damping force when its piston is pushed, not pulled. This design also includes an internal spring to recover the piston position when unloaded. In sum, the hydraulic damper features high viscous damping, no air-spring effect, and a higher Coulomb friction compared the custom-designed pneumatic diaphragm damper.

7.3.3 Articulated Leg Design

The characteristics of a viscous damper strongly depend on the speed- and force-loading profile imposed at its piston because of the complex interaction of fluid pressure and compression, viscous friction, and cavitation (Dixon, 2007). We implemented a hardware leg to test our two mechanical dampers at loading

profiles (speed, force) similar to legged hopping and running.

The two-segment hardware leg (Figure 7.3b) is designed with a constant spring and damper lever arm; parameters are provided in Table 7.1. In all experiments with the two-segmented leg, the leg spring provides elastic joint reaction forces. Dampers are swapped in and out in a modular fashion, depending on the experimental settings. The two-segment leg design parameters are identical to those in our simulation model (Table 7.1). A compression spring⑧ is mounted on the upper leg segment⑬. When the leg flexes, the spring is charged by a spring cap⑦ coupled to a cable⑩ attached to the lower leg. Either damper⑮⑯ is fixed on a support⑥ on the upper segment⑬. The support⑥ can be moved within the upper segment⑬, to adjust the cable⑨ pretension. Cables⑨⑩ link the damper piston③ (Figure 7.5) and the spring⑧ to the knee pulley⑪, which is part of the lower segment⑫.

During the leg flexion, the cable under tension transmits forces instantly to the spring and damper. Spring and damper forces counteract the knee flexion. During leg extension, the spring releases energy, while the damper is decoupled due to the slackness of the cable. We included a hard stop into the knee joint to limit the maximum leg extension and achieve a fixed leg length at impact. At maximum leg flexion at high leg loading, segments can potentially collide. We ensured not to hit either hard stops during the drop experiments. The hydraulic damper⑯ requires a reverse mechanism⑭ since its piston requires compression to work. The piston of the diaphragm damper⑮ was directly connected to the knee pulley. The diaphragm damper⑮ included no recovery spring⑤ (Figure 7.5). Hence, we reset the piston position manually after each drop test. In sum, different spring-damper combinations can be tested with the two-segment leg setup. Note that the here shown hardware leg has no actuation. If a motor actuates the knee joint, in parallel mounted to the spring and the damper, the damper will share the external impact load, consequently reducing the impact at the motor.

7.3.4 Experimental setup, data sampling and processing

We implemented an experimental setup for repetitive measurements (Figure 7.3c). A drop bench was used to constrain the leg motion to a single vertical degree of freedom and linear motion. This allowed us to fully instrument the setup (slider position and vertical ground reaction forces, GRF) and ensured repeatable conditions over trials. Adjusting the drop height allowed us to set the touchdown speed. A linear rail (SVR-28, MISUMI) was fixed vertically on a frame. The upper leg segment was hinged to a rail slider. The rail slider was loaded with additional external weights, simulating different robot masses. We set the initial hip angle α_0 to align the hip and foot vertically. A hard stop ensured that the upper leg kept a minimum angle $\alpha > \alpha_0$.

Two sensors measured the leg dynamics: the body position y and the vertical ground reaction force are recorded by a linear encoder (AS5311, AMS) and a force sensor (K3D60a, ME, amplified with 9326, Burster), respectively (Figure 7.3c). The duration from touchdown to mid-stance is very short, typically $t \leq 100\,\text{ms}$, and high-frequency data sampling was required. The encoder data was sampled by Raspberry Pi 3B+ with $\text{f} = 8\,\text{kHz}$ sampling rate. Force data were recorded by an Arduino Uno, with a 10-bit internal ADC at 1 kHz sampling rate. A high-speed camera (Miro Lab 110, Phantom) recorded the drop sequence at $\text{f} = 1\,\text{kHz}$ sampling rate. We performed ten trials for each test condition. Sensor data was processed with MATLAB (the MathWorks, Natick, MA). Data was smoothed with a moving average filter, with a filter span of 35 samples for encoder data and 200 samples for force data. Repeated experiments of the same test condition are summarized as an envelope defined by the average $\pm$ 95%

standard deviation of the filtered signals.

7.4 Hardware experiments and results

In the drop experiments, we characterize both the hydraulic and diaphragm dampers and the two-segment springy leg (Figure 7.6). We chose three orifice settings (labeled as a, b, and c) for each damper and focused on the effects of viscous damping and adjustable dissipation of energy in the hardware setup. Table 7.3 lists an overview of the drop tests and their settings (drop height, weight, orifice setting, damper type). To emphasize the fundamental differences between the damper designs, we compare only one model of the hydraulic damper (1214H) to the diaphragm damper (Section 7.4.1 - Section 7.4.3), and show the potential of the second hydraulic damper (1210M) in Section 7.4.4. Videos of the experiments are downloadable from the supplementary material page of Mo et al. (2020) and online available [1].

Table 7.3: Drop test settings for experiments. Values indicated in bold indicate control parameters for these experiments.

Drop test setup	*Figure*	*Drop height* [cm]	*Drop weight* [g]	*Orifice* [∼]
Damper (1214H)	7.7a	**3, 5, 7**	280	b
	7.7b	5	280	**a, b, c**
	7.7c	3	**280, 620**	b
Damper (1214H, diaphragm) & leg	7.8a, 7.8b	14	408	c
	7.8c	14	408	damper detached
Damper & leg (simulation)	7.9a, 7.9b	14	408	**a, c**
	7.9c	14	408	**viscous, Coulomb**
Damper (1210M) & leg	7.10	14	408	**a, b**

7.4.1 Isolated damper drops, evaluation

In this experiment, we characterized the hydraulic damper by dropping it under changing conditions of the instrumented drop setup, without mounting it to the two-segment leg. The experimental setup allows differentiating effects compared to the two-segment leg setup, emphasizing the viscous damper behavior of the off-the-shelf component. We also applied the results to estimate the range of damping rates available with changing orifice settings. The hydraulic damper was directly fixed to the rail slider into the drop bench (Section 7.3.4). The piston pointed downwards. We measured the vertical ground reaction force to determine the piston force, and we recorded the vertical position of the slider over time to estimate the piston speed after it touches the force sensor.

Figure 7.7 shows the force-speed profiles for drop tests with different drop heights (Figure 7.7a), orifice settings (Figure 7.7b), and drop loads (Figure 7.7c). Data lines in Figure 7.7 should be interpreted from high speed (impact, right side of each plot) to low speed (end of settling phase, 0 m/s, left). The time from impact to peak force (right slope of each plot) is ≈24 ms, while the negative work (shown in legends) was mainly dissipated along the falling slope in the much longer-lasting settling phase after the peak (left slope of each plot, ≈200 ms).

[1] https://youtu.be/F00Sma2BQ4c

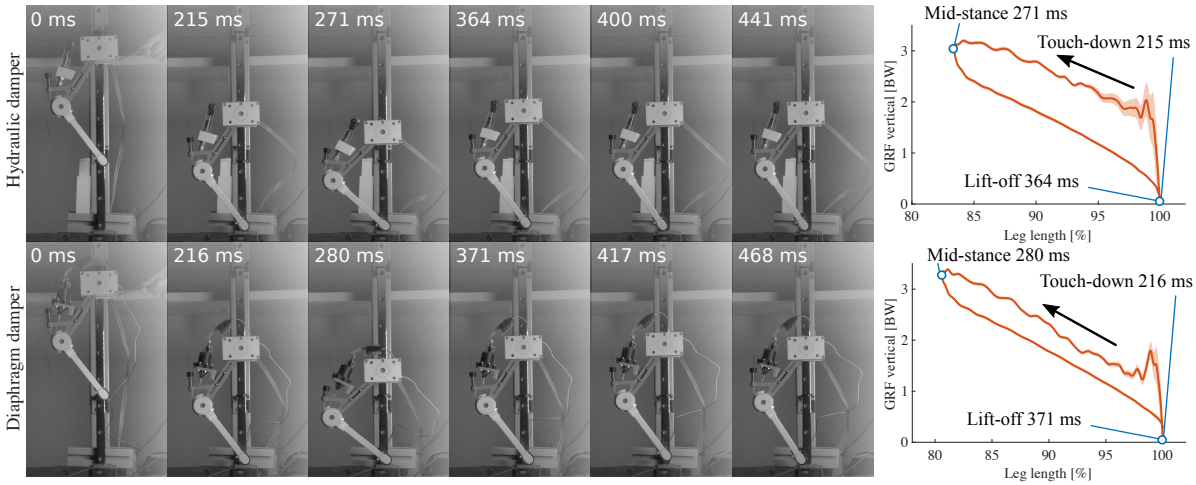

Figure 7.6: High-speed snapshots of drop experiments starting from release to second touchdown. The leg with the hydraulic damper is shown on the top row; the leg with the diaphragm damper is on the bottom row. Depicted are from left to right: release, touchdown, mid-stance, lift-off, apex, second touchdown. The right plots illustrate the timing of the events corresponding to the snapshots.

The results from tests with drop heights from 3 cm to 7 cm show viscous damping behavior in the settling phase after peak force (left slope), with higher reaction forces at higher piston speeds with higher dissipation, ranging from 45 N for maximum speeds of 0.6 m/s with 56 mJ to 65 N at 0.9 m/s with 116 mJ. The piston force almost linearly depends on the piston speed (Figure 7.7a).

Changing the orifice setting at a constant drop height resulted in different settling slopes (Figure 7.7b). Applying a least-squares fit on the left-falling settling slope, we estimate an adjustable damping rate between 91 Ns/m and 192 Ns/m. The dissipated energy changes from 89 mJ to 81 mJ, respectively. Hence, adjusting the orifice setting has an effect on the damping rate and the dissipated energy in the isolated hydraulic damper, but not as we intuitively expected.

We interpret the rising slope in the impact phase (right part of each curve, Figures 7.7a and 7.7b) as a build-up phase; the hydraulic damper takes time (≈24 ms) to build up its internal viscous flow and the related piston movement, after the piston impact. With heavier weights (620 g = heavy, 280 g = light, Figure 7.7c), the impact phase equally lasts ≈24 ms. After the impact phase with heavy weight, the damper shows the same damping rate in the settling phase, in the form of an equal left slope.

Similar drop tests for the evaluation of the isolated diaphragm damper were not possible since the orientation of the internal diaphragm only permits to pull the piston. In the following section, we test the diaphragm (connected by a piston reverse mechanism) and the hydraulic damper directly on the two-segment leg structure.

7.4.2 Composition of dissipated energy

We performed drop tests of two damper configurations: one off-the-shelf hydraulic damper and the custom-made pneumatic damper, each mounted in parallel to a spring at the two-segment leg (Sec-

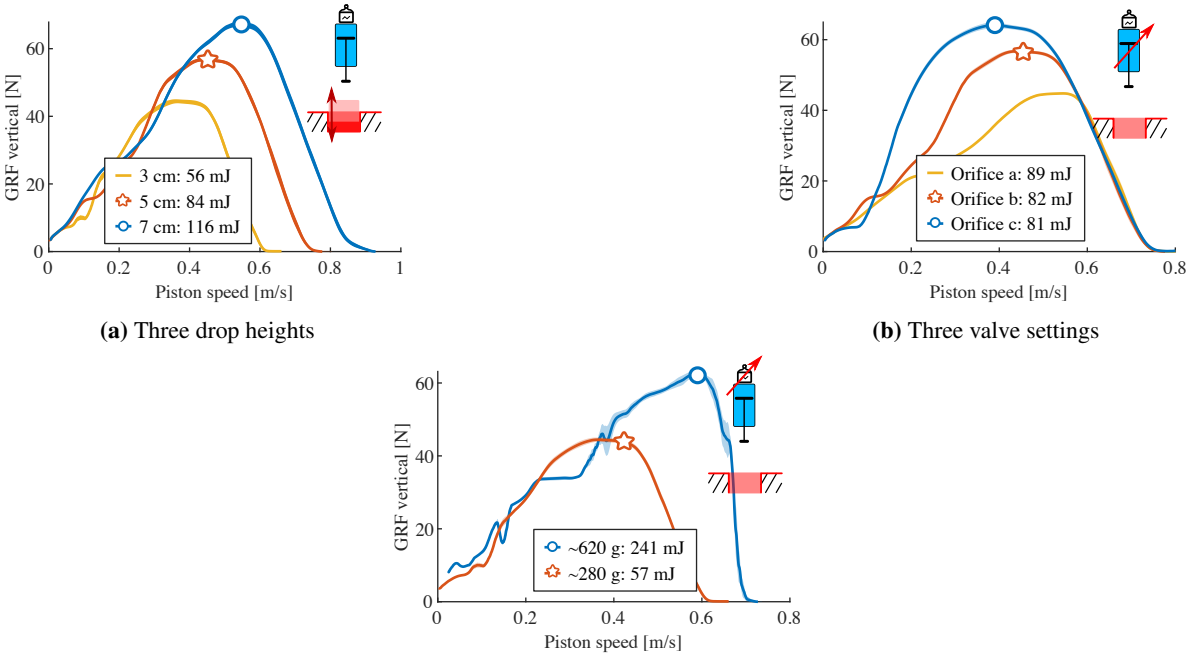

(a) Three drop heights

(b) Three valve settings

(c) Two system weights

Figure 7.7: Characterizing the hydraulic damper A single damper (not leg-mounted) drops onto the force sensor. 10 repeated experiments are plotted as an envelope, defined by the average ±95 % of the standard deviation data. The curves are read from right to left, i.e., from touchdown at maximum speed to zero speed at rest, also corresponding to the maximum damper compression. **(a)** 280 grams drop mass with medium orifice in 3 drop heights. **(b)** 280 grams drop mass with 5 cm drop height in 3 orifice settings. **(c)** 3 cm drop height with medium orifice in 2 drop weights.

tion 7.3.3, Figure 7.3b), to quantify the effect of viscous damping for drop dynamics similar to legged hopping.

For each drop, the effective dissipated energy $E_{\text{effective}}$ was computed by calculating the area enclosed by the vertical GRF-leg length curve from touchdown to lift-off (Josephson, 1985), i.e., the work loop area. These work loops are to be read counter-clockwise, with the rising part being the loading during leg flexion and the falling part being the unloading due to spring recoil. $E_{\text{effective}}$ does not only consist of the viscous loss E_{viscous} due to the damper, but also Coulomb friction loss in the leg ($E_{\text{cfriction}}$) and the impact loss E_{impact} due to unsprung masses:

$$E_{\text{effective}} = E_{\text{cfriction}} + E_{\text{impact}} + E_{\text{viscous}}. \tag{7.12}$$

We propose a method to indirectly calculate the contribution of viscous damping by measuring and eliminating effects from Coulomb friction and unsprung masses.

To quantify the Coulomb friction loss $E_{\text{cfriction}}$, we conducted ‘slow drop’ tests. The mechanical setup is identical to ‘free drops’ test, where the leg is freely dropped from a fixed height. However, in the ‘slow drop’ experiment the two-segment leg is lowered manually onto the force sensor, contacting and pressing the leg-damper-spring system onto the force sensor. At slow speed, only Coulomb friction in joints and damper act, but no viscous damping or impact losses occur. Consequently, the dissipated energy calculated from the size of the work loop is due to Coulomb friction losses $E_{\text{cfriction}}$.

To identify the impact loss E_{impact}, we remove the viscous component first by detaching the damper cable on the setup. A 'free drop' test in this spring-only condition measures the contribution of friction loss $E_{\text{cfriction}}$ and impact loss E_{impact} combined. A 'slow drop' test of the same setup is able to quantify the friction loss $E_{\text{cfriction}}$. The impact loss E_{impact} is therefore estimated as the energy difference between 'free drop' and 'slow drop' in the spring-only condition (Figure 7.8c). Since the effective dissipated energy $E_{\text{effective}}$ is directly measured, and the friction loss $E_{\text{cfriction}}$ and impact loss E_{impact} are obtained separately, the viscous loss E_{viscous} can be computed according to Equation (7.12).

Figures 7.8a and 7.8b show the 'free drop' and 'slow drop' results of the hydraulic damper and diaphragm damper, respectively. Both drop heights are 14 cm at identical orifice setting. We calculated the negative work of each work loop (range indicated by the two vertical dash lines), as shown in Figure 7.8. To provide an objective analysis, the work loop area of each 'slow drop' (manual movement) was cut to the maximum leg compression of the corresponding 'free drop' condition. The dissipated energy of the leg-mounted hydraulic damper is 150 mJ and 60 mJ for 'free drop' and 'slow drop', respectively, and 100 mJ and 67 mJ for the diaphragm damper, respectively. According to Figure 7.8c, the impact loss E_{impact} due to unsprung masses play a large role, accounting for 31 mJ. The viscous loss E_{viscous} of the hydraulic and the diaphragm damper are 59 mJ and 2 mJ, respectively.

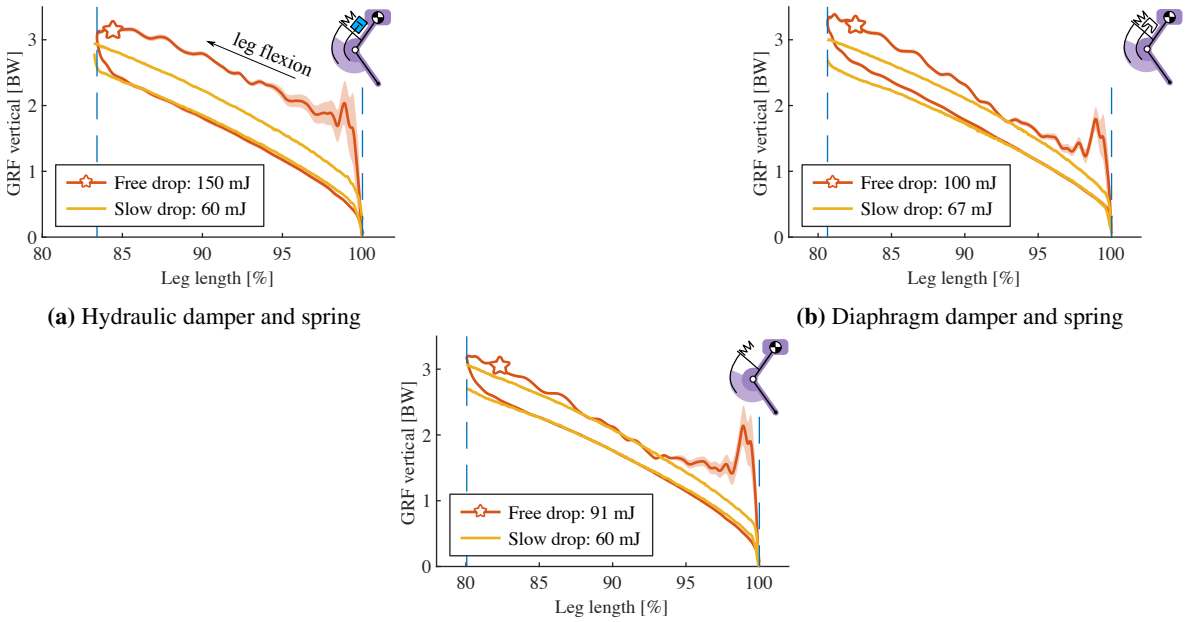

(a) Hydraulic damper and spring

(b) Diaphragm damper and spring

(c) Spring only

Figure 7.8: Characterizing the contribution of velocity-dependent damping: Vertical GRF versus leg length change, a 2-DOF leg with damper/spring drops onto the force sensor. Three different hardware configurations (**a**: hydraulic damper and spring, **b**: diaphragm damper and spring, **c**: spring only) were tested for slow and free drop speeds on the vertical slider. Yellow data lines indicate slow-motion experiments. Experiments 'start' at the bottom right, at normalized leg length 100 %. Reading goes counter-clockwise, i.e., from touchdown to mid-stance is indicated by the upper part of the hysteresis curve, while the lower part indicates elastic spring-rebound without damper contribution.

7.4.3 Adjustability of dissipated energy

For each leg-mounted damper, we tested how changes in the orifice setting adjust the energy dissipation during leg drops, quantified by calculating the size of the resulting work loops. The drop height was fixed to 14 cm, and we used two orifice settings. The identical setup but in the spring-only configuration (damper cables detached) was tested for reference. Work loop and corresponding effective dissipated energies are illustrated in Figures 7.9a and 7.9b. The hydraulic damper-mounted leg dissipated 156 mJ and 150 mJ energy on its two orifice settings, the pneumatic diaphragm damper dissipated 102 mJ and 100 mJ. In Figure 7.9c, we display results from the numerical model introduced in Section 7.2 to estimate the work loop shape that either a pure viscous or pure Coulomb damper would produce, if dissipating the same amount of energy as the hydraulic damper with orifice-a (Figure 7.9a). We set the damping coefficients of our numerical model to $E_{D_0} \approx 156\,\text{mJ}$, so that: $\{d_v, d_c\} = \{51\,\text{Ns/m}, 0\,\text{N}\}$ for pure viscous damping; and $\{d_v, d_c\} = \{0\,\text{Ns/m}, 13.2\,\text{N}\}$ for pure Coulomb damping. Work loops from the numerical simulation differ notably from the experimental data, suggesting that neither the hydraulic or diaphragm damper can easily be approximated as pure viscous or pure Coulomb dampers. Both work loops in Figure 7.9c present about an equal amount of dissipated energy. Yet, both differ greatly due to their underlying damping dynamics, visible in their unique work loop shapes. Their individual characteristics are different enough to uniquely identify pure viscous or pure Coulomb dampers from numerical simulation.

7.4.4 Damper selection choices

In accordance with the simulation results, we aim to use a viscous damper to dissipate energy introduced by a ground disturbance. How much energy could be dissipated by the damper depended mainly on the selected viscous damper and only to a limited degree on the orifice setting. Results from the hydraulic damper 1214H showed significant energy dissipation capabilities: ≈11 % of the system's total energy (59 mJ of 560 mJ) were dissipated (Figure 7.9a at orifice setting 'c' and Table 7.4). At the drop, in sum 150 mJ (27 %) of the leg's system energy were lost, due to Coulomb friction in the joints, impact dynamics, and viscous damping losses. Other dissipation dynamics are feasible by selecting appropriate dampers. We tested a second hydraulic damper (1210M, MISUMI) under equal conditions and compared it to damper-1214H. The two applied orifice settings changed the observed work loop largely by shape and little by area (Figure 7.10). The damper-1210M dissipated ≈60 % system energy, and the leg lost in sum (viscous + Coulomb + impact) 72 % of its system's energy during that single drop. At other orifice settings, we observed over-damping; the 1210M-spring leg came to an early and complete stop and without rebound (data not shown here due to an incomplete work loop). For comparison, time plots of the vertical GRF and the impulse during the stance phase are shown in Figure 7.11. The energy composition (Equation 7.12) is provided in Table 7.4. The 'spring only' data correspond to the curves in Figure 7.8c. The diaphragm + spring data correspond to 'orifice c' in Figure 7.9b. The hydraulic (1214H) + spring data correspond to 'orifice c' in Figure 7.9a. The hydraulic (1210M) + spring data correspond to 'orifice b' in Figure 7.10. Among the tested dampers, the hydraulic 1210M damper showed the largest vertical GRF; peak vertical GRF of 6.3 BW are observed, almost twice as much as the 'spring only' case. The viscous dampers 1214H and 1210M shifted the peak of their legs' vertical GRF to an earlier point in time, compared to the spring-leg and the spring+diaphragm-leg (Figure 7.11).

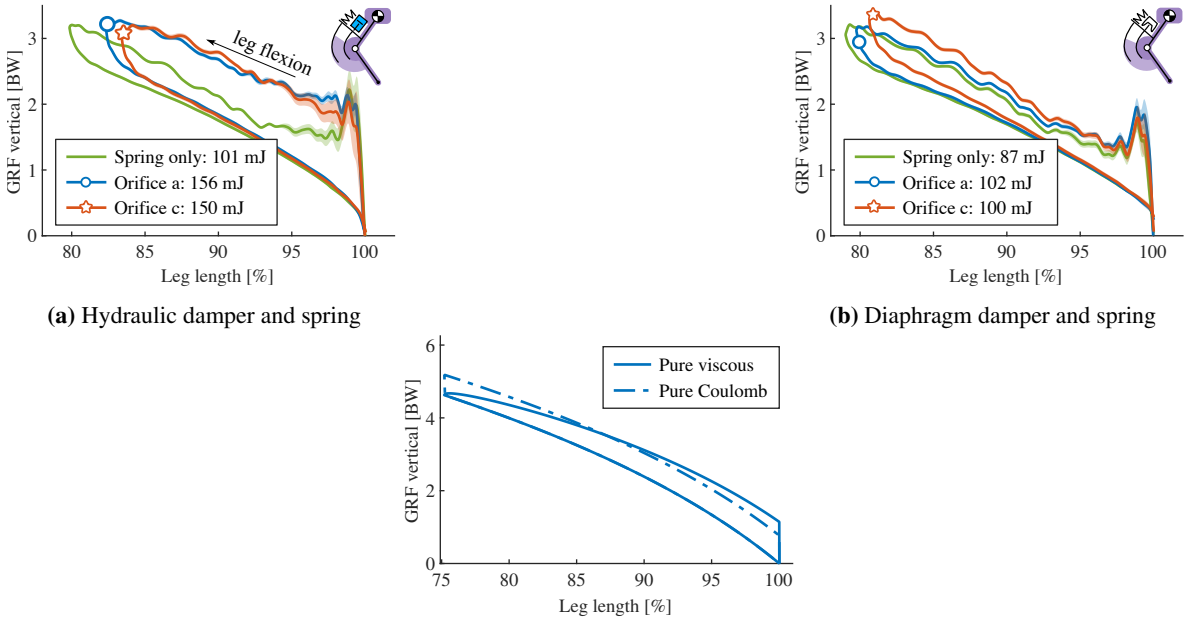

(a) Hydraulic damper and spring

(b) Diaphragm damper and spring

(c) Simulation

Figure 7.9: Adjustability and tunability of damping: Vertical GRF vs. leg length change, a two-segment leg with damper and spring drops onto the force sensor. Two different hardware configurations were tested for different orifice settings. **(a)** and **(b)** show the results from hydraulic damper and diaphragm damper, respectively, where the green data lines indicate the leg drop without damper for comparison. **(c)**: *Simulated* approximation of hydraulic damper orifice 'a' by a pure viscous and a Coulomb damper. Damping coefficients are chosen to allow same dissipated energy, i.e., $E_{D_0} = 156\,\text{mJ}$: respectively — pure viscous damper: $d_c = 0\,\text{N}$ and $d_v = 51\,\text{Ns/m}$; pure Coulomb damper: $d_c = 13.2\,\text{N}$ and $d_v = 0\,\text{Ns/m}$. None of the two curves can fully capture the work loop of the hydraulic damper.

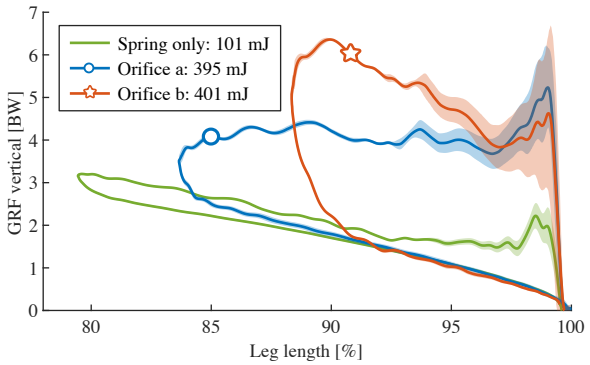

Figure 7.10: Higher energy dissipation with a different model of the hydraulic damper (1210M): Vertical GRF vs. leg length change, a 2-DOF leg with a parallel damper and spring drops onto the force sensor. Two damper orifice settings were tested (blue and red curves). The two resulting curves are compared with the spring-only configuration provided as a reference.

Table 7.4: Leg drop experiments and their individual energetic losses per drop. The system's initial potential energy is 560 mJ. $E_{\text{effective}}$: sum of all energetic losses visible as the area of the hysteresis curve, i.e., in Figure 7.8; $E_{\text{cfriction}}$: negative work dissipated by Coulomb friction; E_{impact}: energetic losses from impact (unsprung mass). The negative work dissipated by viscous damping in the mechanical damper is E_{viscous}. The corresponding work curves are provided in Figures 7.8 to 7.10.

Drop test setup	$E_{\text{effective}}$ [mJ]	$E_{\text{cfriction}}$ [mJ]	E_{impact} [mJ]	E_{viscous} [mJ]
Spring only	91	60	31	0
Diaphragm + spring	100	67	31	2
Hydraulic 1214H + spring	150	60	31	59
Hydraulic 1210M + spring	401	70	31	300

7.5 Discussion

A primary objective of this study was to test how mechanical dampers could be exploited for locomotion tasks by characterizing multiple available technical solutions. Our numerical model predicted three crucial aspects: (1) a pure viscous damper generally performs better than a pure Coulomb damper (Figure 7.4); (2) higher damping rates result in better rejection of ground disturbances (Figure 7.4a), however at the cost of higher dissipation at reference height (Table 7.2); (3) characteristic work loop shapes for pure viscous and Coulomb damper during leg-drop (Figure 7.9c). Our hardware findings show that neither of the tested mechanical dampers approximates pure viscous or pure Coulomb dampers. The experiments also suggest that the mapping between dissipated energy and damping rates is concealed by the dynamics of the impact and the nonlinearity of the force-velocity characteristics of the leg in the stance phase. Therefore, it is vital to test damping in a real leg at impact because the behavior is not merely as expected from the data sheets and the simple model.

Figure 7.7 characterizes how the hydraulic damper dissipates energy during a free drop. The experimental results show that the dissipated energy of the hydraulic damper scales with drop height (Figure 7.7a) and weight (Figure 7.7c), but less intuitively, it reduces with increasing damping rates

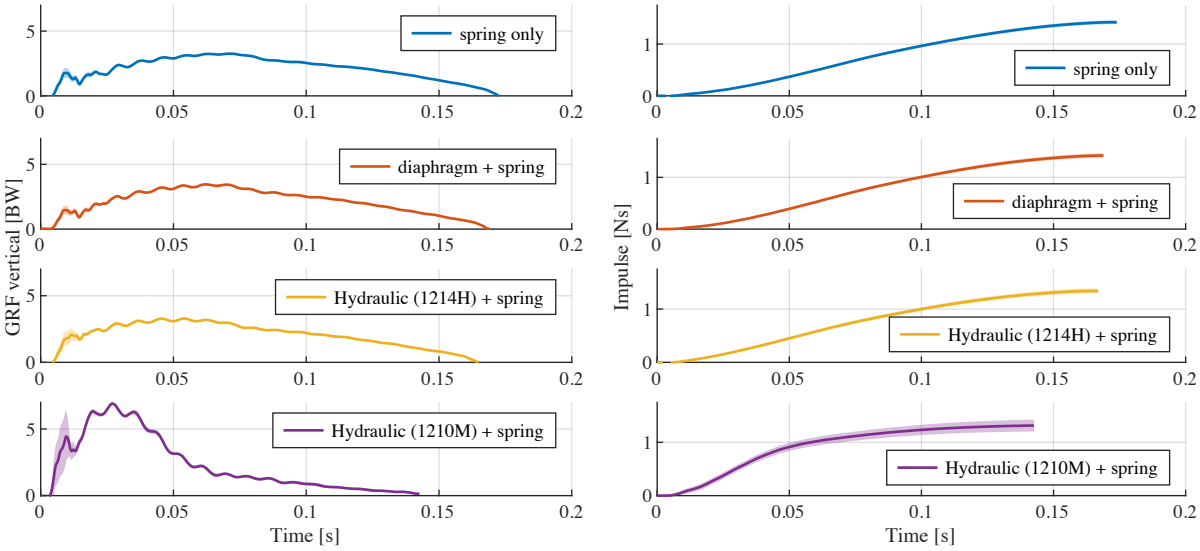

(a) Vertical GRF over time

(b) Vertical Impulse over time

Figure 7.11: Ground reaction forces: (a) shows the vertical GRF and **(b)** the corresponding instantaneous vertical impulse over time, for the leg drop experiments in Figures 7.8 to 7.10.

(Figure 7.7b). This can be partially interpreted in the context of an ideal viscous damper for which the effective dissipated energy $E_{\text{effective}}$ would be calculated as in,

$$E_{\text{effective}} = \int F_p(t) dy_p = \int (d_v \cdot v_p(t))\, dy_p \tag{7.13}$$

where $F_p(t)$ is the damper piston force and y_p is the piston displacement, $v_p(t)$ the corresponding velocity. When increasing the drop height, the velocity at impact is increased, so is $v_p(t)$. With the assumption of Equation (7.13), this results in higher damping forces $F_p(t)$, and thus, dissipated energy $E_{\text{effective}}$, as seen in Figure 7.7a. The heavier drop weight leads to slower deceleration. Therefore the velocity profile $v_p(t)$ is increased, which also leads to higher dissipation $E_{\text{effective}}$ (Figure 7.7b). An orifice setting with a high damping rate will increase the damping coefficient d_v. However, the velocity profile $v_p(t)$ is expected to reduce due to higher resistance. This simple analogy shows that the coupling between damping coefficient d_v and velocity profile $v_p(t)$ makes it difficult to predict the energy dissipation by setting the orifice and serves as an interpretation of why adjusting the orifice generates a relatively small adjustment of 10 % (81 mJ-89 mJ) of the dissipated energy. Also, the impact phase (time for the damper to output its designed damping force under sudden load) introduces additional nonlinearity to the output force profile. Overall, the results in Figure 7.7 indicate that we can approximate the damping force produced by the hydraulic damper to be viscous and tunable— as such dampers are typically designed Dixon (2007)—, but the mapping of energy dissipation to orifice setting is difficult to predict in a dynamic scenario.

The approximation as a linear, velocity-dependent damper allows us to rapidly estimate energy dissipation in simulation over a range of parameters. However, the exact mapping of the hardware leg/spring/damper energy dissipation to the orifice setting is difficult to predict when basing the estimation only on the isolated-damper drop experiments from Figure 7.7. Instead, the leg/spring/damper experiments show that the energetic losses from the impact remove 31 mJ energy, compared to 59 mJ damper losses. The high amount of force oscillations at impact (up to ≈ 1 BW, Figure 7.8a) during

the first 3 % leg length change leads us to believe that these impact oscillations move the damper's dynamic working range, i.e., its resulting instantaneous force and velocity. The oscillations are likely caused by unsprung mass effects of the leg/spring/damper structure and could not be captured in an isolated-damper setup, or—at least not easily—in a simulation.

The work loops of leg drop experiments (Figure 7.8) show the effects of our tested dampers on a legged system. From touchdown to mid-stance (*leg flexion*), the 'free drop' curves show a larger negative work compared to the 'slow drop' curves, illustrating that the damper absorbs extra energy. The returning curves (mid-stance to lift-off) of the hydraulic damper align well with the 'slow drop' curve, indicating the damper is successfully detached due to the slackness cable while the spring recoil. Figure 7.8b shows that the 'free drop' force of the diaphragm damper is slightly higher than 'slow drop' force in the first half of the leg extension phase. This discrepancy is likely caused by the elastic force component of the diaphragm damper due to the sudden expansion of the air chamber volume. The elastic component seems to dominate the damper behavior, which thus acts mostly as an air spring. By separating its energetic components (Equation (7.12)), we found that the hydraulic damper produces a viscous-like resistance higher than the diaphragm damper (59 mJ versus 2 mJ), indicating the hydraulic damper is more effective in dissipating energy under drop impact. Hence, the hydraulic damper shows more viscous behavior, while the diaphragm damper is more elastic.

Mechanical damping in the system comes at the cost of energy loss, and to maintain periodic hopping, it becomes necessary to replenish energy that is dissipated by damping (E_{D_0}). Therefore, there is a trade-off to consider: simulation results show that higher damping results in faster rejection of ground perturbation at the price of more energy consumption at reference drop height (Table 7.2, Figure 7.4). A tunable damper would partly address this problem: on level ground, the damping rate could be minimal, and on rough terrain increased. The adjustability of the two dampers is illustrated in Figures 7.9a and 7.9b. We discuss the adjustability from both energy dissipation and dynamic behavior perspectives.

Compared with the spring-only results, both the hydraulic and the diaphragm damper reduced the maximum leg flexion and dissipated more energy. The orifice setting changes the shape of the work loop differently for the two setups. For the hydraulic damper (Figure 7.9a), orifice setting-c shrinks the work loop from the left edge, indicating more resistance is introduced by the damper to reduce leg flexion. For the diaphragm damper (Figure 7.9b), orifice setting-c not only shrinks the work loop but also increases its slope. We interpret this as the elastic contribution of air compression: relatively fewer air leaves through the smaller orifice, instead acting as an in-parallel spring.

Concerning energy dissipation, changes in orifice settings led to relatively small changes in effective dissipated energy $E_{\text{effective}}$: 150 mJ to 156 mJ for the hydraulic damper, and 100 mJ to 102 mJ for the diaphragm damper. Even for the other damper model (1210M), which dissipates high amounts of energy, changes in orifice setting change the work loop shape drastically, but not the dissipated energy (395 mJ versus 401 mJ).

Similar to the isolated damper drop, the data (Figures 7.9a and 7.9b) shows that specific orifice settings introduce more resistance but do not necessarily lead to higher energy dissipation for both hydraulic and diaphragm damper. However, in our simplified numerical leg model, an increase in viscous damping coefficients leads to a systematic increase of dissipated energy (Table 7.2) and a sharper tip at the left side of the work loop (Figure 7.9c). The discrepancy is likely due to the nonlinear coupling between the damper mechanics and the leg dynamics in the hardware setup: (1) The damping force generated by the fluid dynamics in the orifice only approximates a linear viscosity (Dixon, 2007). (2) The impact loading on both the nonlinear leg structure and the damper. This makes the prediction of the energy dissipation not straightforward based on our simplified numerical leg model and points towards the

need for a combined approach between simulation and hardware testing to fully understand mechanical damping in a legged system.

Viscous, velocity-dependent damping alters the leg's loading characteristics and leads to a peak force at the instance of touchdown. As a result, the vertical GRF is increased in the early stance phase, shifting and increasing the peak vertical GRF before mid-stance (Figure 7.11a). When designing a legged system with a viscous damper, its increasing load on the mechanical structure should be considered.

The selection of viscous dampers depends on the task. High damping can fully reject disturbances in a single cycle, but lower damping could have energetic benefits. Here we looked for a damper that would dissipate significant negative work ($\frac{E_{\text{viscous}}}{E_{T_0}} \approx 10\,\% - 15\,\%$) in the form of viscous damping. The air-filled diaphragm damper lead to insufficient energy losses (2 %), but the hydraulic dampers dissipated 10 % and 60 % of the system's total energy (Table 7.4).

Drawing conclusions about animal locomotion based on the here presented leg-drop experiments is somewhat early. However, observations from (Müller et al., 2014, Table 1, p. 2288) indicate that leg forces can increase at unexpected step-downs during locomotion experiments. Further, Kalveram et al. (2012) suggests in a comparison of experimental human hopping and numerical simulations that damping may be the driving ingredient in passive stabilization against ground-level perturbations. We are consequently excited about the here presented results of viscous dampers mounted in parallel to a leg's spring, producing adaptive forces without the need for sensing.

7.6 Conclusions

We investigated the possibility of exploiting mechanical damping in a simplified leg drop scenario as a template for the early stance phase of legged locomotion. Our results from a) numerical simulation promote the use of tunable and viscous damping over Coulomb damping to deal with a ground perturbation by mechanical damping. As such, we b) tested two technical solutions in hardware: a commercial, off-the-shelf hydraulic damper and a custom-made, rolling diaphragm damper. We dissected the observed dissipated energy from the hardware damper-spring leg drops into its components by experimental design. The resulting data allowed us to characterize dissipation from the early impact (unsprung-mass effects), viscous damping, Coulomb damping, and orifice adjustments *individually and qualitatively*. The rolling diaphragm damper features low-Coulomb friction but dissipates only low amounts of energy through viscous damping. The off-the-shelf, leg-mounted hydraulic damper did exhibit high viscous damping and qualitatively showed the expected relationship between impact speed, output force, and negative work. Changes in orifice setting showed only minor changes in overall energy dissipation but can lead to large changes in leg length dynamics, depending on the chosen technical damper. Hence, switching between different viscous, hydraulic dampers is an interesting future option. Our results show how viscous, hydraulic dampers react velocity-dependent and create an instantaneous, mechanically adaptive response to ground-level perturbations without sensory input.

8 Slack-based tunable damping leads to a trade-off between robustness and efficiency in legged locomotion

The simulation results from the previous chapter (Chapter 7) indicate that viscous damping is desirable for implementing tunable mechanical damping in legged robotics. However, the hardware experiments show that conventional control of the damping rate in viscous dampers that are directly coupled to the knee joint fails to produce effective tunable mechanical damping. The current chapter (Chapter 8) presents our follow-up investigation, where we addressed the limitations in Chapter 7 by proposing a slack-damper mechanism. This device uses a cable with adjustable slackness to connect the mechanical damper to the joint rotation. We evaluated the performance of the slack-damper mechanism through hardware experiments, which involved both vertical and planar hopping across various terrains and perturbations. Our results show that the slack-damper mechanism allows adjustment of damping force, onset timing, effective stroke, and energy dissipation. Thus, it can effectively produce tunable mechanical damping during fast perturbed locomotion. Our experiments also highlight a trade-off: increased mechanical damping improves locomotion robustness at the cost of less energy efficiency. Interestingly, we found that the slack-damper mechanism autoregulates the damper engagement, leading to perturbation-trigger damping. This feature could promote a more favorable trade-off, improving locomotion robustness at a minimum energetic cost.

Note: a large portion of this chapter uses content published in *Scientific Reports* (Mo et al., 2023). For details on this journal article, including the list of authors and my contribution, see Section 2.1.4.

8.1 Introduction

Animals run dynamically over a wide range of terrain (Fig. 8.1). The unevenness and changing compliance of natural terrain demand the capability for fast and dynamic adaptation to unexpected ground conditions. However, animals' neurotransmission delays slow down sensorimotor information propagation (Gordon et al., 2020), rendering a neuronal response impossible for as much as 5 % to 40 % of the stance phase duration, depending on the animal size (More et al., 2010). How animals are able to produce and maintain highly dynamic movements despite delayed sensorimotor information is, therefore, a central question in neuroscience and biorobotics (Ashtiani et al., 2021; Kamska et al., 2020; More et al., 2010; More and Donelan, 2018).

Inherent mechanical properties of muscles facilitate the rejection of unexpected perturbations (Daley et al., 2009; Grillner, 1972; Loeb et al., 1999; Wagner and Blickhan, 1999). Muscular tissue possesses nonlinear elastic and viscous-like mechanical properties, which adapt the muscle force instantly to

changes in the length or contraction velocity of the muscle-tendon fibers. These mechanical properties enable the neuro-musculoskeletal system to react to external perturbations with zero delay, a capacity termed "preflex" (Brown and Loeb, 2000).

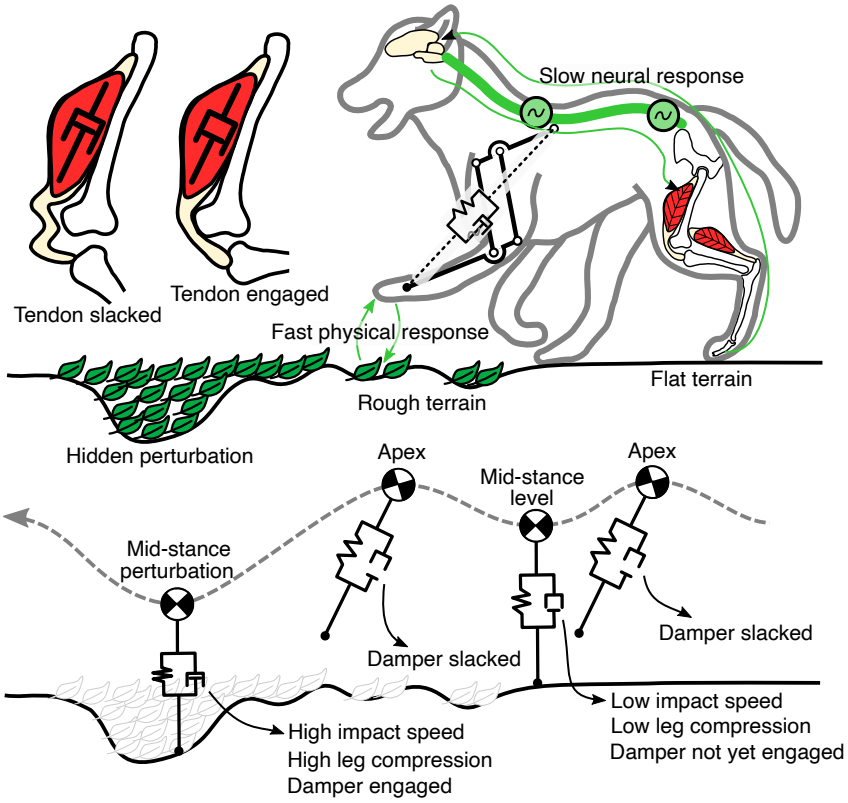

Figure 8.1: Top: Fast running over ground perturbations is challenging. Due to sensorimotor delays up to 50 ms, the central nervous system struggles to perceive and react to sudden ground disturbances (More et al., 2010). In contrast, the intrinsic mechanics of the musculoskeletal system act like a spring damper. They produce a mechanical and, therefore, immediate (< 5 ms) reaction when in contact with the environment. We hypothesize that the leg damping mitigates ground disturbance through adaptive force production and energy dissipation. The tendon's slack, coupled with the joint's motion, auto-engages the damper. This creates a trade-off between locomotion robustness and energetic efficiency. **Bottom**: The damper slack enables perturbation-triggered damping. Sufficiently slacked, the damper does not engage during stance, and only spring-based torque is produced. When encountering a perturbation, the leg's compression increases further, removing all damper slack, and the damper engages in parallel to the spring.

Intrinsic elasticity and its role in legged locomotion have been studied extensively (Alexander et al., 1982; Alexander, 1991; Biewener and Roberts, 2000; Hof, 1990; Robertson and Sawicki, 2014). For instance, tendons, which behave like nonlinear serial springs, store and release mechanical energy during ground contact (Alexander et al., 1982) and improve shock tolerance (Roberts and Azizi, 2010). Inspired by this, parallel and series elastic actuators have successfully been implemented in the design of legged robots (Grizzle et al., 2009; Hubicki et al., 2016; Spröwitz et al., 2013; Zhao et al., 2022), demonstrating improved robustness at low control effort. In contrast, the functional role that damping plays in legged locomotion is less studied and understood.

Damping can produce a force outcome that is adaptive to the impact velocity. This adaptive force

output enhances the effective force output during impacts (Müller et al., 2014), minimize control effort (Haeufle et al., 2014a), stabilize motion (Abraham et al., 2015; Secer and Saranli, 2013; Shen and Seipel, 2012) and reject unexpected disturbances (Haeufle et al., 2010; Kalveram et al., 2012). Nevertheless, damping is usually minimized in the design of (bio)robotic systems, as it can lead to increased energy consumption. Interestingly, vertebrates seem capable of tuning the damping produced by their muscle fibers (Günther and Schmitt, 2010). This suggests that tunable damping can be a solution for regulating damping forces and dissipating energy depending on the terrain conditions.

Tunable damping in biorobotics can be implemented through control (Candan et al., 2020; Monteleone et al., 2022), i.e., virtual damping. Virtual damping poses substantial design constraints. It requires precise velocity estimation, high-frequency control (>1 kHz), strong actuators to produce sufficient peak forces, and means to dissipate the resulting heat effectively (Grimminger et al., 2020; Havoutis et al., 2013; Hutter et al., 2012; Kalouche, 2017; Seok et al., 2015). Alternatively, mechanical dampers can be mounted in parallel to the robot's joints (Vanderborght et al., 2013). A mechanical damper perceives and responds mechanically and instantly, requires no controller or computation, shares peak load of actuators, and thus has the potential for fast adaptation to terrain perturbations (Mo et al., 2020). Tuning damping with a mechanical damper mounted to a legged robot proved challenging. Setting a higher damping rate resulted in the expected higher forces but at reduced leg compression and effective damper stroke (Mo et al., 2020). Consequently, the dissipated energy indicated by the work loop area did not increase. Additionally, fix-mounted mechanical dampers operate continuously and dissipate energy during unperturbed level running. Instead, tunable mechanical damping should ideally be triggered by the perturbation itself. The damper should engage and self-adjust according to the presence and severity of the ground disturbance experienced during running.

The tendon slack observed in muscle-tendon units (Heers et al., 2018; Robi et al., 2013) and animal-inspired robots (Badri-Spröwitz et al., 2022) provided us with a design template for implementing tunable damping in a legged system (Fig. 8.1 Top). Tendon slack length is defined as the "...length beyond which the tendons associated with a muscle begin resisting stretch and producing force" (Heers et al., 2018). In other work, the "tendon is strained up to 2 %, representing the "stretching out" of the crimped tendon fibrils, before starting to transfer considerable force" (Robi et al., 2013). Badri-Spröwitz *et al.* show tendon slack in the flexing motion of the digits of large birds, and implement tendon slack in the related robot (Badri-Spröwitz et al., 2022). By disengaging the damper from its joint via controlled tendon slack, we expect to adjust the onset, timing, and amount of damper engagement. Moreover, the tendon slack allows for a perturbation-trigger strategy (Fig. 8.1Bottom). During steady-state running, for example, on flat terrain, the leg compresses without saturating the tendon slack. Once an unperceived ground perturbation increases leg compression further, the tendon displacement will exceed the tendon's slack and start to auto-engage the damper. This strategy enables adaptive force output triggered by ground perturbations.

We implemented and tested a bio-inspired, tunable mechanical damping strategy based on tendon slack in this work. We aimed at producing perturbation-triggered damping and improving robustness against ground perturbations. We evaluated this design concept on a robotic leg during vertical and forward hopping, both in steady-state and perturbed conditions. Unlike earlier designs (Mo et al., 2020), our slack-damper mechanism enabled straightforward adjustment of the damper engagement and energy dissipation. We observed improved hopping robustness due to the adaptive characteristics of our mechanical damping design, whereas the energetic cost increases. The perturbation-triggered capacity of our slack-damper mechanism allows for a more favorable trade-off between robustness and efficiency.

8.2 Methods

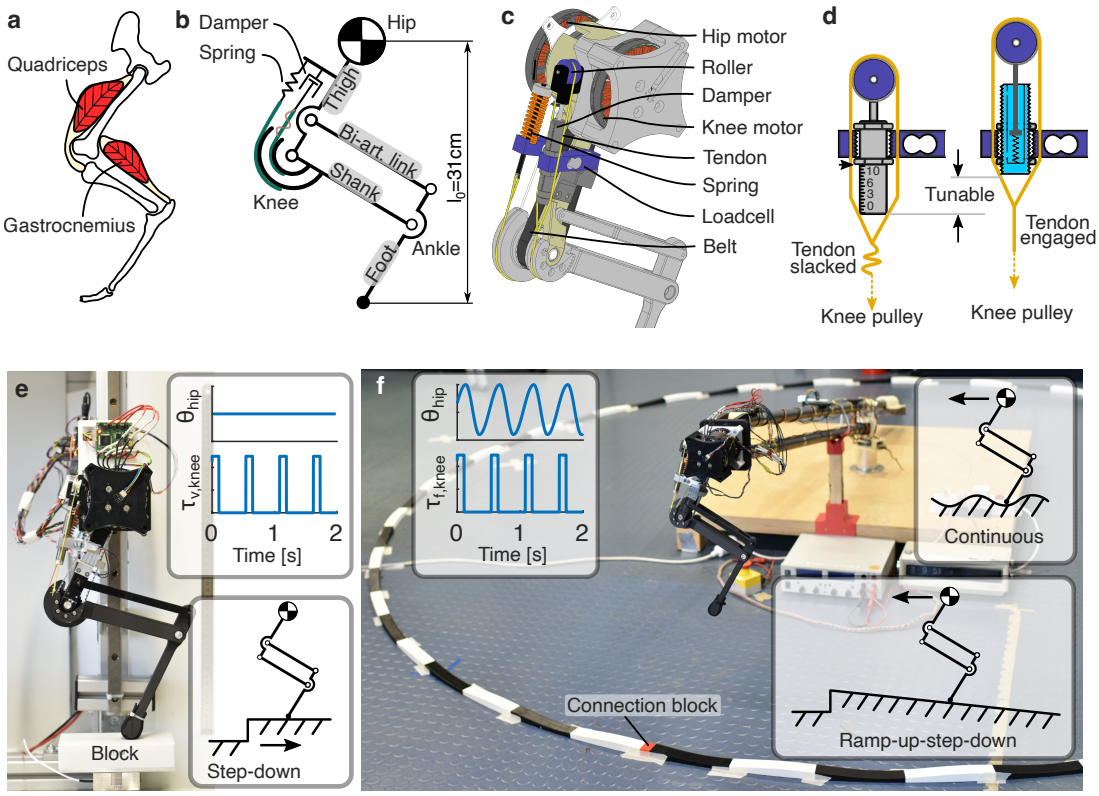

Figure 8.2: Experiment setup overview. (**a**) Our leg design is inspired by the leg anatomy of mammalian quadrupeds. (**b**) We implement a pantograph leg design with spring and damper representing the passive compliance of the quadriceps and a biarticular segment, simplifying the gastrocnemius muscle and the Achilles tendon. (**c**) The rendering of the leg design shows that the knee joint is coupled to the linear spring, the linear damper through tendons, and the knee motor through a timing belt. (**d**) The slack-damper mechanism is realized by the threaded connection between the damper and the loadcell. By rotating the damper, the damper will travel up and down, thus allowing tunable tendon slack. The left schematics illustrate the lowest position of the damper in maximum tendon slack, and the right schematics demonstrate the inner mechanics of the hydraulic damper with minimum tendon slack. (**e**) The vertical hopping setup fixes the robot leg on a vertical slider to test step-down perturbation, which is introduced by removing the perturbation block on top of the force sensor. The top right shows a feedforward control pattern for hip position and knee torque. (**f**) The forward hopping setup fixes the robot leg on a rotary boom to test continuous perturbation (in photo) and ramp-up-step-down perturbation (Supplementary Movie S3, see appendix A3). The top right shows a feedforward CPG control pattern for hip position and knee torque.

Biorobotic leg implementation

The three-segment leg design was inspired and simplified from the leg anatomy of small mammalian quadrupeds (Fig. 8.2a). It consisted of four links forming a pantograph structure (Fig. 8.2b). A spring and a damper coupled to the knee joint mimicked the passive compliance of the quadriceps muscles. The gastrocnemius muscle and Achilles tendon were simplified as a rigid link to reduce parameter space.

The two-degrees-of-freedom leg was fully actuated by two motors (hip and knee). The key design parameters are provided in the supplementary materials (Figure A3.1 and Table A3.1).

The leg was fabricated mostly from off-the-shelf components and 3D-printing (Fig. 8.2c). The main structural components were 3D-printed using polylactic acid (PLA), except for the foot segment, which was 3D-printed using carbon-fiber-reinforced nylon to improve strength and impact resistance. The hip and knee motors (MN7005-KV115, *T-motor*, 1.3 Nm maximum rated torque) were placed co-axially at the hip to reduce leg swing inertia, using a 5:1 planetary gearbox (lgu35-s, *Matex*) to gear them down. The knee torque was transmitted by a timing belt (SYNCHROFLEX 10/T5/390, *Contitech*) with an additional 25:12 gear ratio. We mounted two loadcells (model 3134, *Phidgets*, 20 kg) to the spring and the damper to measure forces. The knee spring (SWS14.5-15, *MISUMI*) was designed to hold the leg in stance. Its stiffness of 10.9 N/mm was empirically determined to generate three times the body weight of the robot at 10% leg length deflection (Bobbert et al., 1992; Walter and Carrier, 2007). The knee damper (1210M, *MISUMI*) was selected as the most effective damper from our previous study (Mo et al., 2020). Both the spring and the damper were coupled to the knee joint through Dyneema tendons (Climax Combat Speed 250/150, *Ockert*), with a cam radius of 30 mm and 20 mm, respectively. A roller (VMRA20-4, *MISUMI*) was attached to the piston of the damper to transform the tendon tension ("muscle lengthening") in knee flexion to a push motion on the damper piston. The whole leg weighs 0.94 kg, with a resting leg length of 31 cm.

Slack-damper mechanism

Tuning an adjustable damper when operating within a legged system is challenging. Higher damping settings make the damper produce larger forces, which in turn can reduce the piston displacement, compromising the projected change in dissipated energy (Mo et al., 2020). Therefore, it is difficult to anticipate how adjusting the orifice of the damper internal valve affects the dissipated energy. Instead of regulating the damper's force by adjusting the orifice size, we propose damping control by adjustment of the damper tendon slack. Tendon slack has been observed in biology, with tendon stretch up to 2 % of the nominal tendon length before starting to produce considerable force (Badri-Spröwitz et al., 2022; Heers et al., 2018; Robi et al., 2013). This is known as the "toe region" in the tendon's stress-strain diagram.

Inspired by this observation, we set a defined tendon slack length when connecting the damper to the knee pulley (Fig. 8.2d). For our mechanism, the damper body and the loadcell are machined with external and internal threading, respectively. By screwing the damper's body into the loadcell, we set the damper's position with a resolution of ± 1 mm per turn. The adjustable threading allows for a precise slack control in the range of 0 mm to 10 mm. Before each experiment, we lock the damper in place with two nuts to prohibit damper body movement.

This slack-damper mechanism permitted tunable damping. The damper energy dissipation E_{damper}, calculated as the integration of damper force F_{damper} and damper piston displacement x, can be controlled by the tendon slack s because of two concomitant effects (equation (8.1)). First, when the ground impact flexes the leg, the parallel spring decelerates leg flexion. At the same time, the tendon slack saturates, thereby softening the engagement conditions for the damper's piston (more slack $s \mathrel{\hat{=}}$ less damper force F_{damper}). Second, the tendon slack reduces the effective damper piston stroke Δx (more slack $s \mathrel{\hat{=}}$ less piston stroke Δx). The combination of these two mechanisms—softened (less F_{damper}) and delayed (less Δx) damper engagement—predicts an inverse relationship between the tendon slack s and the integrated

damper energy dissipation E_{damper}.

$$\left.\begin{aligned} E_{damper} &= \int F_{damper}\, dx \\ F_{damper} &\propto \tfrac{1}{s},\ \Delta x \propto \tfrac{1}{s} \end{aligned}\right\} \Rightarrow E_{damper} \propto \frac{1}{s} \tag{8.1}$$

Experimental setup

We designed two experimental setups and three perturbation types to evaluate the proposed design in four slack settings.

The vertical hopping setup (Fig. 8.2e) investigates only the vertical component of locomotion. Such a reduced-order experiment reduced system complexity, allowing ground reaction force (GRF) measurement in all steps. The forward hopping setup (Fig. 8.2f) fixed the leg on a boom structure, simulating more realistic locomotion dynamics and allowing for more perturbation types.

We focus the investigation on the mechanical response produced by the passive damping embedded in the leg design. Hence, we designed an open-loop locomotion controller such that it could not detect ground perturbation. We tested three types of ground perturbations: step-down perturbation representing a sudden, unexpected disturbance during fast running; continuous perturbation simulating rough terrain conditions, and ramp-up-step-down perturbation combining gradual and sudden disturbance.

We tested damper tendon slack of 10, 6, 3, and 0 mm for each test condition. The damper engaged synchronously with the spring in the 0 mm slack setting. With the 10 mm slack setting, the damper never engaged. Hence, we investigated a wide range of possible slack conditions, from complete to zero tendon slack.

Vertical hopping

In the vertical hopping setup (Fig. 8.2e), the hip of the robot leg was fixed to a vertical rail (SVR-28, *MISUMI*). A force sensor (K3D60a, *ME*) was used to measure the ground reaction force during hopping. The step-down perturbation was realized using a 3D-printed block (PLA) and an automatic block-removal device. The block was placed on top of the force sensor to elevate the ground. Magnets were inserted into the block and the top plate of the force sensor to prevent relative sliding during the leg impact. The block-removal device was a lever arm actuated by a servo motor (1235M, *Power HD*). The arm pushed away the block during the aerial phase of a hopping cycle (Supplementary Movie S1, see appendix A3). This automatic block-removal device was needed to remove the perturbation block within the aerial hopping phase reliably (200 ms in our experiments).

The vertical hopping setup was instrumented as follows. The hip position was measured by a linear encoder (AS5311, *AMS*). The loadcells (spring and damper) and the ground reaction force sensor readings were amplified (9326, *Burster*) and then recorded by a microcontroller (Due, *Arduino*) with internal 12-bit ADC. The motor position was measured by a 12-bit rotary encoder (AEAT8800-Q24, *Broadcom*). We used an open-source motor driver (Micro-Driver (Grimminger et al., 2020)) for motor control, current sensing, and encoder reading, which runs dual motor field-oriented control at 10 kHz. We monitored the motor driver current with a current sensor (ACS723T-AB, *Allegro Microsystems*). A second microcontroller (Uno, *Arduino*) was implemented to control the servo motor for automatic block removal. A single-board computer (Raspberry Pi 4B) was used to centralize and synchronize all sensor readings and motor commands in 1 kHz.

We implemented a Raibert-like (Raibert, 2000) open-loop controller for vertical hopping. The hip was position-controlled with a PD controller to keep a vertical posture. The knee was torque-controlled to produce a defined torque at a given duty cycle, typically during the second half of the stance phase. Motor commands are illustrated in the inserted plots in Fig. 8.2e. Control parameters for a stable hopping gait were found through manual tuning, resulting in a 450 ms cycle time with 100 ms knee motor push-off. The knee torque was tuned for each setting of the damper tendon slack to maintain the same hopping heights across tested conditions (Supplementary Table A3.2).

We tested two perturbation levels: 31 mm and 47 mm, equivalent to 10 % and 15 % of the leg length, respectively. For each hopping trial, the robot hopped for 1 min. We analyzed ten steps before and after the perturbation. Each hopping condition was repeated ten times. We recorded in total 80 trials: two perturbations $\times$ four slack settings $\times$ ten repetitions.

Forward hopping

In the forward hopping setup (Fig. 8.2f), the robot leg was mounted on a boom in a four-bar design. This mount permits only horizontal and vertical motion in the robot's sagittal plane. The length of the boom was 1.613 m, and the travel distance of a complete revolution was around 10 m. The boom design is openly available (Ruppert et al., 2022).

The instrumentation of the forward hopping setup was similar to that of the vertical hopping setup. The force measurement and the automatic block-removal device were incompatible with the boom setup and were removed. All the other sensors remained. Horizontal and vertical motions of the rotating boom were measured by two 11-bit rotary encoders (102-V, *AMS*).

We generated the forward motion of the robot leg using a feedforward central pattern generator (CPG). In most vertebrates, CPGs contribute to controlling rhythmic motion (Ijspeert et al., 2007), such as locomotion. We implemented a CPG controller for the hip angle trajectory θ_{hip}:

$$\theta_{hip} = A_{hip}\cos(\Phi) + O_{hip} \tag{8.2}$$

$$\Phi = \begin{cases} \dfrac{\phi}{2D} & \phi < 2\pi D_{vir} \\ \dfrac{\phi + 2\pi(1-2D_{vir})}{2(1-D_{vir})} & \text{else} \end{cases} \tag{8.3}$$

where A_{hip} is the hip angle amplitude, Φ the hip angle phase, O_{hip} the hip angle offset, D_{vir} the virtual duty factor as the fraction of time when the leg moves forward, and ϕ the oscillator's linearly progressing phase. The knee motor was torque-controlled to generate push-off force in the late stance, following a fixed square-wave pattern as in the vertical hopping with the same frequency as the hip CPG. The motor commands are shown in the overlay plots of Fig. 8.2f. For ease of comparison, the control parameters (Supplementary Table A3.2) remained the same for all forward-hopping experiments.

To replicate rough terrain in a controlled way, we designed 3D-print tracks with a sinusoidal profile (Fig. 8.2f). The circular track was built from 3D-printed blocks. These were serially connected and taped to the floor. Each block is 360 mm long, and 27 blocks fit the circumference of the hopping path. A single, shorter connection block was added (red, Fig. 8.2f). This connection block prevents the hopping cycle from being entrained by the terrain harmonic perturbation pattern, e.g., repeatedly stepping onto the exact position of a cycle length of the track. We tested two rough terrains, with the amplitude of the sinusoidal perturbation being 5 mm and 10 mm. In addition, we also tested hopping on flat terrain. For

each trial, the robot performed a total of six revolutions. We cropped the first and the last revolutions from the recorded data and analyzed the remaining four revolutions (60 steps per condition).

Further, we designed ramp-up-step-down perturbations to disturb stable hopping during forward locomotion. Within a revolution's 10 m hopping path, we built a slope of 3 m length for the robot leg to gradually climb and jump off. We tested two perturbation heights: 47 mm and 93 mm, equivalent to 15% and 30% of leg length, respectively. For each trial, the robot leg performed 12 revolutions. We cropped the first and the last revolution from the recorded data and analyzed the remaining ten revolutions (150 steps per condition).

Data analysis

The ground reaction force and vertical position data were filtered for the vertical hopping experiments with a 4th-order zero-lag Butterworth filter. The loadcells were calibrated to output force reading only at leg flexion. The spring and damper force data were smoothed using a moving average filter with a filter span of 5 samples. The boom encoder data were filtered with a 4th-order zero-lag Butterworth filter for the forward hopping experiments. The cutoff frequencies (9 Hz-19 Hz) of the Butterworth filter were determined by residual analysis (Winter, 2009).

The recovery steps in the vertical hopping experiment were calculated by first computing the average hop height before perturbation as a reference height (dotted lines in Fig. 8.3f) and then finding the post-perturbation hop height that intersected with the $\pm 4\%$ boundary of the reference height (Zhao et al., 2022). The cost of hopping was calculated by normalizing the electric energy consumption E_{elec} of one hopping step to the system's gravitational potential energy at the apex.

$$CoH = \frac{E_{elec}}{m \cdot g \cdot h_{apex}} \tag{8.4}$$

where m is the robot mass, g the gravitational acceleration, h_{apex} the apex height position.

We defined two measurements for evaluating the robustness of forward hopping after the ramp-up-step-down perturbation. The recovery steps were defined as the number of steps needed by the robot leg to recover its stable hopping after the step-down perturbation. This metric quantified how fast the robot system can recover from perturbation, and it was measured by visual inspection of the video recordings and kinematic data. The failure step metric quantified the number of failures after a perturbation was applied. We identified two failure modes from the video recordings: the robot leg could slip or stop after the perturbation (Supplementary Movie S3, see appendix A3). The number of failures was visually counted from the video recordings. The CoT was calculated by the electric energy consumption per distance traveled d, normalized by the robot weight.

$$CoT = \frac{E_{elec}}{m \cdot g \cdot d} \tag{8.5}$$

All data were processed with Matlab (R2021b, *MathWorks*).

8.3 Results

We designed three experiments to study the proposed design with a hydraulic damper mounted to a robotic leg joint (Table 8.1). We tested damper slack values of 10, 6, 3, and 0 mm for all conditions. These

Experiment	Terrain	Perturbation height	No. of perturbation steps	No. of repetitions
Vertical hopping	step-down	10% LL 15% LL	1	10
Forward hopping	flat terrain rough terrain rough terrain	0 mm ±5 mm ±10 mm	15	4
Forward hopping	ramp-up-step-down	15% LL 30% LL	1	10

Table 8.1: Experiment design, all experiments are repeated with damper slack values of 10, 6, 3, and 0 mm, from maximum slack to no slack.

settings span from full slack (10 mm, minimum effective damping) to no slack (0 mm, maximum effective damping). An open-loop controller produced the robot leg's locomotion pattern. Without feedback, ground perturbations were invisible to this high-level control (neural circuits), and perturbations could only be compensated by low-level mechanics in the form of a mechanical response.

We used the vertical hopping setup to investigate the vertical component of locomotion, allowing ground reaction force (GRF) measurement in all steps (Fig. 8.2e). We introduced step-down perturbation to evaluate the robustness of the system. We used the forward hopping setup, which mounts the leg on a boom structure, to simulate more realistic locomotion dynamics (Fig. 8.2f). We analyzed forward hopping performance on rough terrain and robustness against ramp-up-step-down perturbation.

All data can be found in Supplementary Tables A3.3 to A3.5.

Vertical hopping with step-down perturbation

With feedforward control, the leg hopped in the vertical setup for two perturbation levels and four slack values. Figure 8.3a shows an example of a time-series of 10 repetitions. The test condition included a perturbation of 15 % leg length (LL) and tendon slack of 3 mm (Supplementary Movie S1, see appendix A3). At the perturbed step 1, the leg impacted the ground at a higher speed, compressing more. This resulted in higher damper and spring forces than during pre-perturbation levels. We noticed that the damper force did not drop to zero at mid-stance due to the damper's internal recovery spring.

We found that the tunable slack mechanism was effective in tuning damping. Damper slack adjustments of 0 mm to 6 mm resulted in a delayed engagement of the damper: from 0 ms to 50 ms after the onset of the spring force during level hopping (Fig. 8.3b). The damper's force-displacement work loops during level hopping confirmed the controllable onset of the damper force (Fig. 8.3c). The enclosed work loop areas represent the damper's standby dissipated energy. Damper slack values of 0, 3, 6, and 10 mm can be mapped to standby dissipation of 152, 86, 29, and 1 mJ. At the perturbation step, the damper dissipated more energy (65 % to 190 %) compared to level hopping standby dissipation (Fig. 8.3d). The extra dissipated energy is associated with the height of the ground drop, showing an adaptive energy dissipation to terrain disturbance. In all tested conditions, the extra dissipated energy converged to 0 in the following steps, indicating recovery to steady-state hopping.

The robustness of the hopping system can be qualitatively assessed by the phase plot of the hip height (Fig. 8.3e and Supplementary Movie S1, appendix A3). With a 10 mm slack setting, the hopping

behavior was the most variable, as shown by the overlay of gray lines, representing 200 steps in 10 repetitions. With a 6 mm slack setting, the phase plot was clean, and the hopping converged to a new 'limit cycle' in fewer steps than other settings. A quantitative robustness measurement is the number of steps required to bring the system back to its original hopping height after the perturbation (Fig. 8.3f). The system's robustness was highest with the 6 mm slack setting, requiring on average 1.7 and 2.5 steps to recover for 10 % and 15 % LL perturbation, respectively (Fig. 8.3g). At stronger perturbations, the robot needed more steps to recover. We measure the energetics of the hopping system by its cost of hopping (CoH, equation (8.4)). The CoH increased from 6.3 to 7.6 with higher damping or stronger perturbations (Fig. 8.3h). With a damper slack of 6 mm at 10 % LL perturbation, we found 47 % faster perturbation recovery in combination with 5 % higher CoH compared to 10 mm damper slack (Fig. 8.3i).

Forward hopping with continuous perturbation

During forward hopping on the sinusoidal ground, the standard deviation of the step cycle time quantifies the hopping periodicity. In the flat terrain, the standard deviation of the step cycle time decreased from 27 ms to 2 ms with less damper slack, showing improved hopping periodicity with more damping (Fig. 8.4a). This tendency was less apparent in $\pm$5 and $\pm$10 mm rough terrain, as the step cycle time variation increased first for the damper slack value 6 mm, then decreased with less damper slack. The energetic cost of forward hopping was measured as the cost of transport (Tucker, 1975) (CoT, equation (8.5)). The CoT increased from a minimum of 0.75 to 1.35 with increasing damping (Fig. 8.4b). Both hopping periodicity and CoT were affected by the terrain's roughness. In flat terrain, increasing damping was associated with improved periodicity and increased CoT (Fig. 8.4c). At $\pm$5 mm terrain roughness, data for damper slack values of 0, 3, and 6 mm show a similar tendency. The 10 mm damper slack shows the best performance with a CoT of 0.75 and a standard deviation of 2 ms cycle time (Fig. 8.4d). With $\pm$10 mm terrain roughness, the cycle time standard deviation was clustered around 2 mm to 3 mm for all slack settings, while the CoT varied from 0.79 to 1.32. Among these three tested terrains, the strongest damping, i.e., the setting with a slack of 0 mm, showed better periodicity with a cycle time standard deviation of $\approx$2 ms, but with the highest CoT, ranging from 1.24 to 1.35.

Forward hopping with ramp-up-step-down perturbation

We evaluated the system's robustness during forward hopping by testing its response to unexpected, sudden perturbations. Thus, we analyzed the robotic leg's behavior with step-down perturbations in its hopping path. As robustness measurement, we counted the number of steps required for the hopper to recover after the step perturbation. The second measurement of robustness is the number of failures out of ten perturbation attempts. By reducing the damper slack from 10 mm to 0 mm, the average recovery steps needed by the robotic leg decreased from 2.7 to 1.0 for the 15% LL perturbation and from 2.6 to 2.3 for the 30 % LL perturbation (Fig. 8.5a). Similarly, with more damping, the number of failed trials decreased from 7 to 0 for the 15 % LL perturbation and 10 to 3 for the 30 % LL perturbation (Fig. 8.5b). The legged robot was less robust against a stronger perturbation, as it required on average 0.7 more recovery steps or failed, on average, four times more for the two tested perturbation levels. Similar to the other two experiments, the energetic cost of the system increased with more damping, as the CoT increased from 0.95 to 1.44 (Fig. 8.5c). With a damper slack of 0 mm at 15 % LL perturbation, we found 170 % faster perturbation recovery in combination with 27 % higher CoH compared to 10 mm damper slack (Fig. 8.5d). With both measurements of robustness, we observed a tendency of increasing

robustness at the expense of more energetic cost with higher damping settings (Fig. 8.5d and e).

8.4 Discussion

The slack-damper mechanism allows effective tunable damping. This has three consequences. First, depending on the slack setting, the damper produces an immediate or delayed response to ground impacts (Fig. 8.3b). Second, the onset of the damper stroke can be reliably set by the tendon slack (Fig. 8.3c). Third, the mechanical work generated by the damper is tunable, as shown by the change in the size of the enclosed work loops (Fig. 8.3c). Such a level of tunability of the damper response was not possible in our previous, more canonical approach of controlling the damping rate of the same damper model (implemented in a two-segment leg) via orifice adjustment (Mo et al., 2020). In contrast, adjusting the slack of the damper tendon provides an effective strategy for tuning embedded damping in the robotic leg. The slack in the damper tendon system allows the parallel spring to soften the damper impact within tens of milliseconds after the foot touchdown. As a result, the damper produced less force and effective stroke than scenarios with less slack (equation (8.1), Fig. 8.3c).

In the steps following a sudden drop in ground height, the additional gravitational energy results in 20 % to 30 % higher touchdown speeds. The damper force and negative work increase accordingly, providing a beneficial mechanical reaction to compensate for the perturbation (Fig. 8.3d). Therefore, our damper implementation produces mechanical work in an adaptive manner that is consistent with the perturbation level and tunable by just one parameter: the damper tendon slack.

Legged system robustness is required due to the system's inherent sensor- and control-noise and the imprecision of its motor-control (Eliasmith and Anderson, 2003; Faisal et al., 2008; More et al., 2010). Heim *et al.* (Heim et al., 2020) quantified task-level stability in a modified spring-loaded inverted pendulum (SLIP) model that includes perturbation-triggered damping, suggesting that increased damping contributes to improved robustness. Legged locomotion simulation studies (Abraham et al., 2015; Shen and Seipel, 2012) and muscle experiments (Wilson et al., 2001) revealed the stabilizing effect of damping. This theoretical evidence motivated our biorobotic setup to explore and characterize damping and its effect on locomotion robustness.

In general, damping improves system robustness. In the vertical hopping experiments, adding a small amount of damping (6 mm slack) led to the fastest recovery from step perturbations (Fig. 8.3e and g). Above a certain amount of damping, the robotic leg appears to be "over-damped", as shown by the hopping height over steps. For example, with more damping (slack < 6 mm), the convergence to the pre-perturbation behavior is smoother (Fig. 8.3f) but requires more steps (Fig. 8.3g). In forward hopping experiments, more damping improved hopping periodicity (Fig. 8.4a) and robustness (Fig. 8.5a and b) without the emergence of an over-damping threshold. Our system performed well in this perturbed condition. It overcame the perturbation 64 times out of 80 trials despite using the simple feedforward open-loop controller for forward hopping motion. Although no electronic sensors are utilized to perceive the perturbations, the passive compliance embedded in the leg acts as an intrinsic system of mechanical sensors and actuators, which detect and respond immediately to external disturbances. We believe the adaptive force output from damping plays a key role. A reflex-control mammalian quadruped of similar size to our robot has a total sensorimotor delay of 60 ms (More and Donelan, 2018). In comparison, the delay of damping force production in the robotic leg is less than 50 ms (Fig. 8.3b). This confirms that the mechanical damping force effectively acts faster than reflex control in response to a perturbation.

The improved robustness introduced by the damper system comes at an energetic cost. Higher

damping settings (less slack) result in higher energy costs for all the experiments (Fig. 8.3i, Fig. 8.4b, and Fig. 8.5c). This occurs because the actuators need to produce more power to compensate for the lost energy by damping (Fig. 8.3c and d) and achieve a steady-state hopping behavior. Tunable damping leads to a trade-off between the robustness and energy cost of the system (Fig. 8.5d and e). This trade-off implies that hopping can be either robust against perturbations but with a penalty in energy consumption, or be energy efficient but vulnerable to disturbance. Adjusting tendon slack allows for selecting a suitable compromise depending on the terrain.

The benefit of damping for legged systems remains a debate in the field (Cham and Cutkosky, 2006; Heim et al., 2020; Shen and Seipel, 2012). Most research on legged locomotion focuses on optimizing a single aspect, such as robustness, stability, or energy consumption. On the contrary, evolution in biology is likely not a single-objective optimization process. Instead, we argue that a more holistic perspective is required to understand the interaction among the many performance metrics characterizing legged locomotion. Therefore, we argue that the locomotion priority can change. As Fig. 8.1 suggests, less damping is desired to minimize energy consumption during level terrain locomotion. In the case of rough terrain, higher damping is preferred to improve the robustness against ground disturbances. Hence, damping is a key to balance the trade-off between robustness and energy consumption.

The advantage of our slack-damper mechanism concerning energy consumption is that it allows a perturbation-trigger strategy. The damper tendon slack can be tuned to barely engage at level hopping. It will then engage once a ground perturbation induces higher impact velocities. In this way, the absence of a damper minimizes the dissipating energy during level hopping, while the engagement of the damper improves robustness at ground perturbation steps. This automatic on-off control was impossible with previous damper implementations (Arelekatti et al., 2021; Garcia et al., 2011), because damping generated from friction, rheology, eddy currents, and fluid dynamics are hard to switch off completely (Vanderborght et al., 2013). Instead of optimizing the adjustment of the nonlinear damping coefficient, our mechanism features a fixed damping coefficient but exploits a slack tendon to create a tunable on-off damping. The proposed slack tendon could also be applied to selectively engage springs. Hence, the tunable tendon slack mechanism offers a new mechanism for adaptive compliant actuator applications.

Besides the adaptive force output of damping, we expect the tunability of damping to provide better hopping behavior, such as transitioning into new terrain. When expecting a more uneven terrain, the damper slack can be adjusted accordingly to gain more robustness against the stronger perturbation. This requires an online slack tuning mechanism and its feedback control strategy. Possibly, a feedforward controller can be sufficient to produce highly robust running in an uncertain environment (Wu and Geyer, 2013). Limited by the hardware implementation, we did not thoroughly investigate an online tuning design. Nevertheless, the four damper slack settings demonstrate the proof-of-concept of online tunable damping.

We consider extending our system with stiffness control in the future. Tunable spring designs have been studied extensively (Vanderborght et al., 2013), but a combination with tunable damping is rare. Software online tuning of stiffness and damping has been realized (Huerta et al., 2020; Roberts and Koditschek, 2019), but relies on precise sensing, high-frequency control, and strong actuation. Virtual feedback impedance control (Bogdanovic et al., 2020; Xiong and Manoonpong, 2018) combined with mechanical springs and dampers provide software control flexibility and fast mechanical response (Ashtiani et al., 2021). With these improvements, we can readily implement controllers and hardware for versatile and robust locomotion in natural terrains such as gravel.

In summary, this work aims at understanding the tunable damping mechanism in legged locomotion.

We proposed the slack-damper strategy inspired by muscle tendon slack and tested it in robotic legged hopping. The slack-damper mechanism allows effective tunable damping regarding onset timing, engaged stroke, and energy dissipation. This study provides novel insights into the trade-off between energetics and robustness under different damping levels. Additionally, the slack-damper design allows for perturbation-trigger damping, resolving the trade-off during locomotion with unexpected perturbation. Our results could inspire future robotic locomotion hardware and controller design.

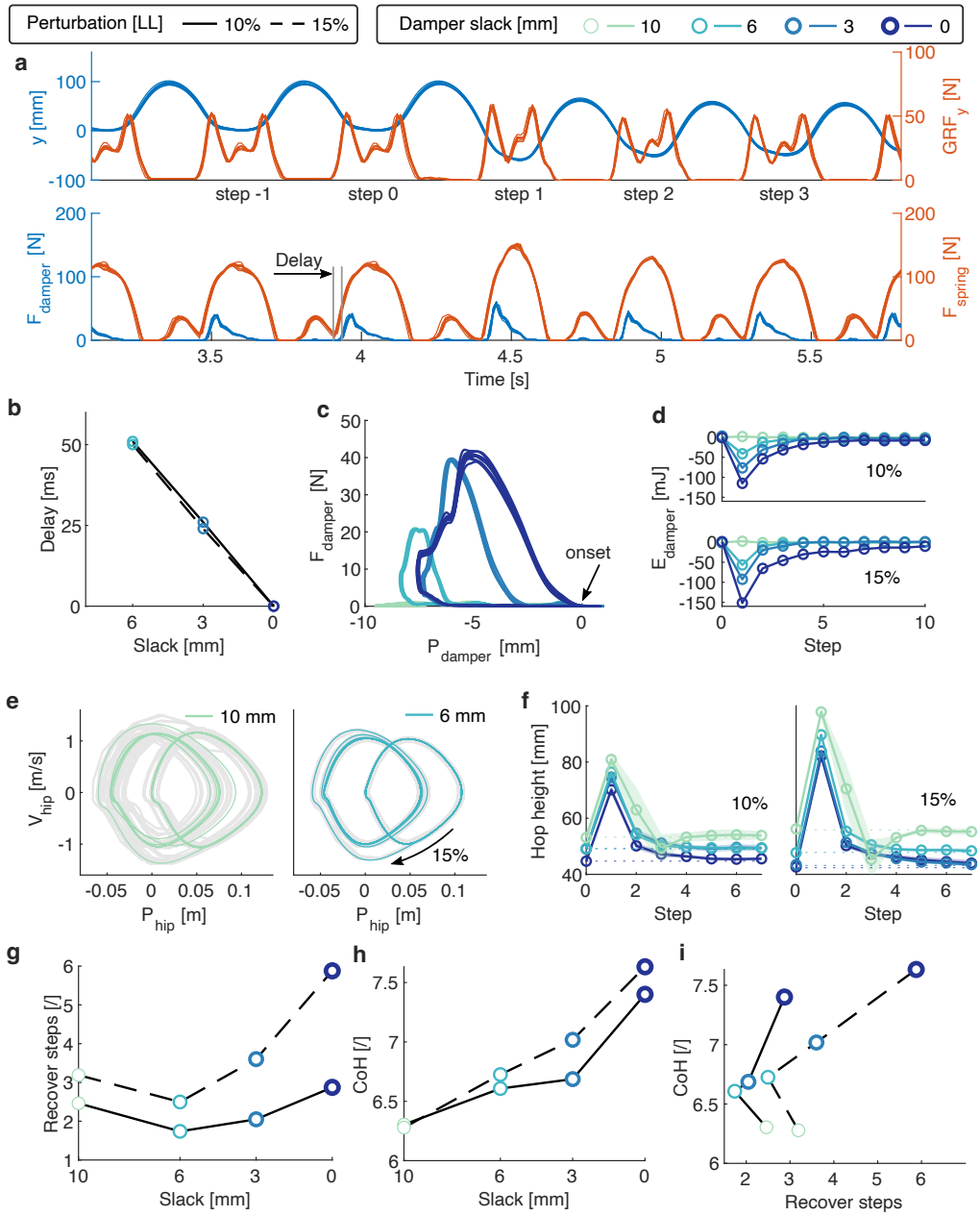

Figure 8.3: Vertical hopping with step-down perturbation: (**a**) 10-repetition-overlay time-series of hip position y, GRF, spring, and damper forces. 15% LL perturbation at step 1 increases the GRF, spring, and damper forces due to higher impact speed. The damper starts to produce force with a delay to touchdown due to the 3 mm slack setting. (**b**) This damper engagement delay is adjustable by the damper slack setting. (**c**) The 10-repetition-overlay damper work loop in unperturbed periodic steps shows that the onset position can be reliably tuned and the standby dissipated energy (enclosed area) adjustable. (**d**) The average extra damper dissipated energy during perturbation steps. (**e**) Phase plot of hip position with 10 mm and 6 mm damper slack under 15% LL perturbation. The grey overlay shows the overlap of 10 repetitions of 20 steps, while the darker line is the averaged trajectory. (**f**) The average hopping apex height during perturbation steps. The transparent overlay represents the 95% confidence boundary. (**g**) The relationship between the number of steps to recovery after perturbation and the damper slack settings. (**h**) The relationship between the cost of hopping and the damper slack settings. (**i**) The relationship between the number of steps to recovery and the cost of hopping under different damper slack settings and perturbation levels.

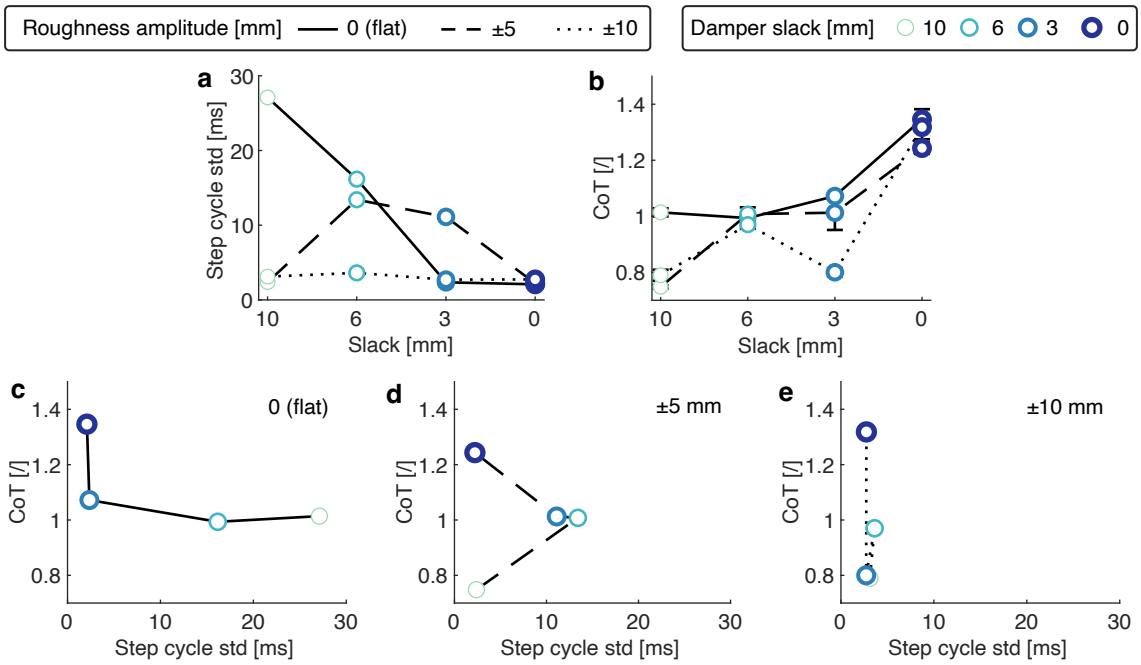

Figure 8.4: Forward hopping with continuous perturbation: (**a**) The standard deviation of the step cycle time shows that the hopping periodicity is improved with higher damping (less slack). (**b**) The relationship between the CoT and the damper slack settings. (**c**) In flat terrain, the robot's ability to maintain periodic hopping is improved by higher damping at the cost of CoT. (**d, e**) In the continuous perturbation terrain, high damping is also associated with high CoT and good periodicity.

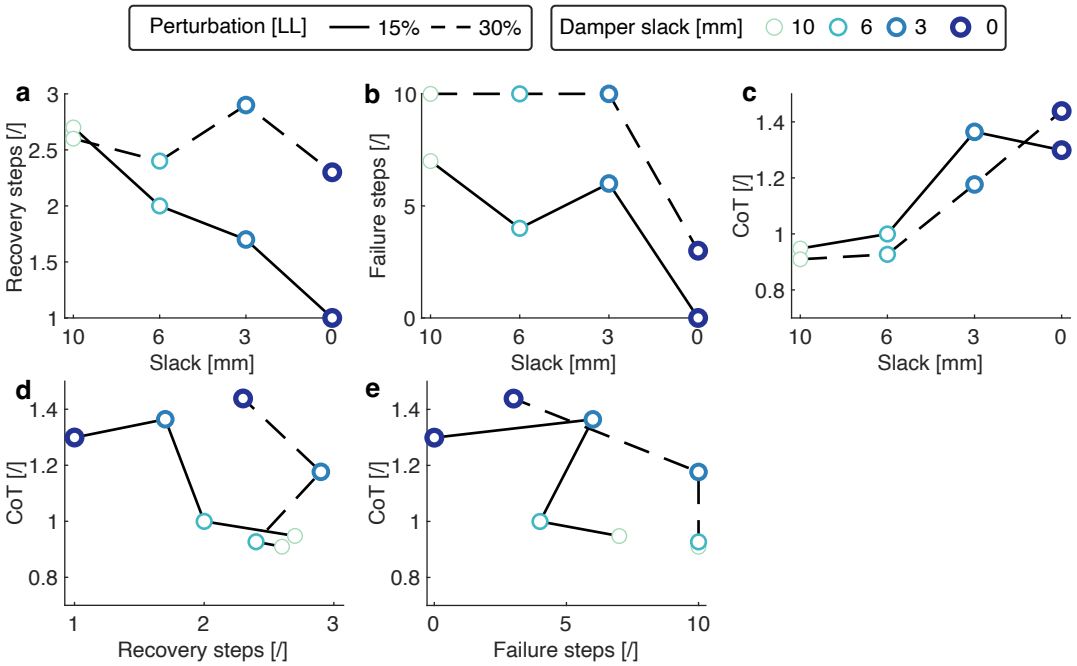

Figure 8.5: Forward hopping with ramp-up and step-down perturbation: The robustness of the robot system is quantified with the number of steps needed to recover stable hopping (**a**) and the number of failed trials in 10 attempts (**b**). (**c**) The relationship between the CoT and the damper slack settings. (**d** and **e**) show the trade-off between robustness and CoT.

9 General discussion

The research objective of this dissertation was to investigate principles of tunable mechanical damping in fast, perturbed legged locomotion. Although less understood than tunable mechanical stiffness, tunable mechanical damping may be crucial in providing a first response to external perturbations. Such instant stabilizing action could benefit locomotion by compensating for delays and noise in the neurotransmission of sensorimotor information. Therefore, this dissertation investigates how tunable mechanical damping occurs in muscle-driven locomotion and how it can be achieved in legged robotics.

My doctoral thesis relies on interdisciplinary research combining computational biomechanical simulations, in vitro experiments on muscle fibers, and hardware testing with robotic prototypes. My main contribution to this research was the computational part, which supported the in vitro and robotic experimentation. A precise description of my contribution to the research presented in this thesis is in Chapter 2.

This final chapter (Chapter 9) starts with a detailed summary of the studies that comprise my dissertation. Afterward, I present my general discussion, separated into two parts. First, I discuss how our findings provide a new quantitative understanding of muscle-produced, tunable mechanical damping. Then, I discuss our implementations of tunable mechanical damping in legged robotics. I conclude the chapter by highlighting the take-home messages from this dissertation.

9.1 Summary of the studies

The research in this dissertation involves five different investigations, corresponding to four journal articles (Araz et al., 2023; Izzi et al., 2023; Mo et al., 2020, 2023) and one pre-print (Izzi et al., 2022).

Chapter 4 presents my core computational study on tunable mechanical damping in muscle-driven locomotion. This study implements a simplified biomechanical model to simulate vertical hopping under different step perturbations. By applying the decomposition algorithm (described in Section 4.2.3) to the knee extensor muscle that drives the model, it was possible to quantify how the force-velocity relation adjusts touchdown force and preflex work to different perturbation intensities. We termed this regulatory capacity "velocity preflex" since it adjusts the preflex response to the change in impact velocity that follows a step perturbation. Although previous studies suggested the force-velocity relation is critical for building a velocity preflex, we found that without neuronal modulation, the force-velocity relation has only a minor effect on the preflex response. When feedforward stimulation is allowed, the damping capacity of the force-velocity relation shapes preflex production far more effectively, indicating the existence and tunability of biological mechanical damping. Thus, our findings support the literature hypothesis that the force-velocity relation produces mechanical damping and plays a role in preflex regulation. However, we conclude that understanding this phenomenon requires considering the interaction between muscle mechanics, feedforward control, and touchdown timing.

The analysis in Chapter 4 shows that, without neuronal modulation, the force-velocity relation

contributes less to preflex regulation primarily because of its flattening side at high eccentric velocities. As a result, the damping capacity of the force-velocity relation may depend on the touchdown velocity of unperturbed locomotion. Chapter 5 tests this hypothesis. Using the same computer model from Chapter 4, we simulated periodic hopping without neuronal modulation at different reference touchdown velocities. We classified these conditions by the operative side of the force-velocity relation at touchdown, separating hopping on the rising-side (rising-cases) from hopping on the flattening side (plateau-cases). We tested the stability of periodic hopping for each condition and analyzed two selected cases in detail, one plateau-case and one rising-case. Our in-depth analysis shows that periodic hopping on the plateau-side reduces the preflex regulation that the force-velocity relation can generate. This finding confirms our hypothesis that the preflex contribution of the force-velocity relation is sensible to the touchdown reference condition. However, we also found that periodic hopping with the force-velocity relation on the plateau-side at touchdown was more stable. Further testing is required, as we limited the in-depth analysis to only two periodic hopping conditions and did not investigate how muscle force influences movement after the preflex duration. Our results also show that the intrinsic coupling between hopping kinematics and perturbation intensity promotes the regulation of dissipated energy. This implies that constant damping of tunable magnitude could be sufficient to implement tunable mechanical damping in legged robotics.

Chapters 4 and 5 base their computational research on a Hill-type muscle model. Hill-type models are approximations of the complex dynamics occurring during biological muscle contraction. To assess the limitations of this modeling choice, Chapter 6 presents a study in which we compared the preflex response predicted by our Hill-type simulations to that from in vitro muscle fiber experiments. Using the computer model in Chapters 4 and 5, we recorded muscle fiber trajectories occurring during periodic and perturbed vertical hopping. Then, we applied the simulated trajectories to in vitro experiments with isolated muscle fibers. We compared the preflex force and work produced by the biological muscle fibers with predictions from the isolated contractile element in our Hill-type model. To highlight the contribution of the force-velocity relation, we compared these results with a quasistatic-scenario, where we applied the same trajectories over a time frame long enough to make the instantaneous velocity close to zero. The in vitro experiments confirm that preflex force modulation by force-velocity dependencies occurs in real muscle fibers, as predicted by our simulations. However, contrary to our model predictions, this viscous modulation did not occur at touchdown. Instead, it followed a phase of short-range stiffness that our Hill-type model does not capture. Regarding mechanical work, we observed little viscous-like modulation of the preflex work. However, muscle activity level could regulate the amount of preflex work produced by the viscous-like properties of the muscle fibers. Therefore, our in vitro analysis supports the hypothesis that muscle fibers can produce some tunable mechanical damping. At the same time, we conclude that better predictions of biological tunable damping require Hill-type models to include short-range stiffness and a more accurate description of the force-velocity relation's eccentric portion.

The remaining chapters present two studies in which we explored technical solutions to achieve tunable mechanical damping in legged robotics during fast perturbed locomotion. Chapter 7 explores the feasibility and benefits of mechanical viscous damping. Given its resemblance with the force-velocity relation of muscle contraction, we hypothesized that viscous damping is effective in rejecting energy perturbation caused by unexpected ground disturbances. To test this hypothesis, we compared its performance with Coulomb friction damping in simulated drop experiments. Coloumb friction damping generates a constant damping force, which can be adjusted in magnitude by setting different friction coefficients. Therefore, comparing viscous damping to Coulomb friction damping highlights the added

benefit of velocity-dependent force modulation. As hypothesized at the end of Chapter 5, some energy regulation was possible with the constant damping force. Nevertheless, viscous damping consistently outperformed Coulomb friction damping. As a result, we conducted hardware experiments with a leg prototype and viscous dampers directly coupled to the knee joint. We investigated whether damping rate adjustment of these devices allowed tuning mechanical damping in perturbed drop experiments. We found that complex nonlinearities conceal the mapping between damping rate and dissipated energy. Consequently, we conclude that damping rate control of a directly-coupled viscous damper is an ineffective design strategy.

Chapter 8 presents a study in which we proposed a slack-damper mechanism to address the hardware limitations identified in Chapter 7. In the slack-damper mechanism, the viscous damper connects to the knee joint through a cable of adjustable slackness. The level of slackness determines when the damper starts breaking the knee rotation. Zero slackness causes the damper to react instantly to the joint motion. High slackness decouples the damper from the joint kinematics, requiring a certain amount of leg compression before the damper can engage. Therefore, more slackness delays the viscous damping response and reduces its magnitude, as leg compression decelerates from touchdown to midstance. We tested the performance of our slack-damper mechanism in producing tunable mechanical damping during various hopping conditions and step perturbations. To accomplish this, we implemented one of the hydraulic dampers tested in Chapter 7 to the knee joint of a pantographic robotic leg. The damping rate of the hydraulic damper remained constant across all tested conditions. Our experimental results reveal that the slack-damper mechanism can adjust the dissipated energy to the perturbation intensity. Unlike controlling the damping rate, slackness adjustments effectively modulated the amount of energy the damper can dissipate. Moreover, the mapping between slackness level and damped energy is intuitive: fewer slackness results in more damped energy due to earlier damper engagement, and vice-versa. With this achieved tunability, we could test and confirm that more mechanical damping increases locomotion robustness at the expense of a higher cost of transport. We conclude that the tunability and perturbation-triggered nature of our slack-damper mechanism could promote a more favorable trade-off.

9.2 Tunable mechanical damping in muscle-driven locomotion

According to previous research (Gerritsen et al., 1998; Geyer et al., 2003; Haeufle et al., 2010), the force-velocity relation grants muscle fibers tunable mechanical damping. This property could facilitate the rejection of external perturbations during fast locomotion. When a step perturbation occurs, touchdown velocity and potential energy change. A damping-like response by the force-velocity relation could adjust the muscle force to the new impact velocity and allow partial rejection of the change in potential energy. Due to its mechanical nature, such a response would be instantaneous and sensor-free. For this reason, we referred to it as a velocity preflex (Chapter 4). However, evidence for such a velocity preflex was only qualitative (Gerritsen et al., 1998; Geyer et al., 2003; Haeufle et al., 2010). As muscle dynamics are highly nonlinear, a qualitative understanding cannot unequivocally characterize the force-velocity relation's role during fast perturbed locomotion. Therefore, a primary research objective of this dissertation was to provide a more quantitative understanding (Chapters 4 to 6).

9.2.1 Constant stimulation during preflexes

Our results support the hypothesis that the force-velocity relation produces tunable mechanical damping during fast perturbed locomotion, which allows preflex regulation in response to step perturbations. However, the interpretation of this phenomenon needs revision. We found that the force-velocity relation can generate only little preflex regulation without neuronal modulation, i.e., when preflex stimulation remains constant. In this scenario, our simulations show that muscle fiber force adjusts to new impact velocities, consistent with the previously hypothesized contribution of the force-velocity relation as mechanical damping (Gerritsen et al., 1998; Geyer et al., 2003; Haeufle et al., 2010). However, such force adjustment remains confined around touchdown and fails to produce meaningful energy regulation by the end of the preflex phase. Furthermore, the degree of force adjustment is sensible to the force-velocity relation's operative side, with large eccentric touchdown velocities compromising it.

We interpret these findings as a consequence of the flattening side of the force-velocity relation for large eccentric velocities. After touchdown, muscle fibers experience an acceleration that rapidly increases their stretching velocity. This makes the force-velocity relation quickly operate along its plateau-side. The constant preflex stimulation cannot alter the shape of the force-velocity relation across different perturbed scenarios. As a result, the force profiles attributed to the force-velocity relation quickly converge to the same trajectory; differences in force profiles remain confined to the touchdown event. Notice that some energy regulation during preflex still occurs without neuronal modulation. However, this is primarily driven by the change in muscle fibers' elongation caused by the perturbed touchdown velocity.

As reviewed in Alcazar et al. (2019), several experimental studies support the existence of a flattening side in the force-velocity relation for the range of moderate-to-high stretching velocities. However, the eccentric side of the force-velocity relation has been studied less than the concentric side. In Chapter 6, our in vitro experiments show that viscous-like regulation of the muscle fiber force occurs in the mid-to-late preflex phase. This finding suggests that flattening of the force-velocity relation did not emerge during our biological experiments. A possible interpretation of this result is that the muscle activation level in our experiments was low enough to restrain the flattening of the force-velocity relation. Evidence indicates that cross-bridge turnover kinetics depends on Ca^{2+} concentration (Brenner, 1988), and thus, low submaximal activation may alter muscle fiber mechanics and the shape of the force-velocity relation's eccentric side. Quick-release or similar experiments to characterize the force-velocity relation's eccentric side at such low submaximal activation are still missing. Thus, further testing is needed to validate a similar explanation of our findings.

Another possible interpretation is the existence of a mechanical delay in the viscous-like response of muscle fibers. Levin et al. (1927) observed that when an isometric muscle is stretched, the muscle fibers' response resembles the mechanical behavior of a pure elastic element in series with a viscous-elastic element. The serial elasticity prevents the direct transmission of the stretching velocity to the viscous-elastic element, causing the damping forces within the muscle fibers to build up gradually in response to suddenly applied muscle fiber velocities. Lännergren (1978) further observed that such build-up dynamics depend on the muscle fiber composition, with slow and twitch fibers characterized by different behaviors. These findings are consistent with our observation of an initial short-range stiffness response, which anticipated the viscous-like regulation of muscle force during our in vitro experiments. Therefore, our results suggest that Hill-type models may wrongly assume that the force-velocity relation acts instantaneously, and some build-up dynamics are likely to occur in reality. Notice, however, that although the force-velocity relation's contribution may not be instantaneous, viscous-like regulation

of muscle force occurred within the preflex duration in our biological experiments. Thus, our results still support the hypothesis that the force-velocity relation generates a faster regulatory response than reflexes and other centrally-driven strategies.

9.2.2 Feedforward stimulation during preflexes

Feedforward control plays an important contribution to motor control. Networks of spinal neurons, referred to as central pattern generators (CPGs), provide rhythmic feedforward signals that support reflex-based control of animal and (likely) human locomotion (for a review, see Duysens and Van de Crommert (1998); Ijspeert (2008); Loeb (1989)). As observed in (Ryu and Kuo, 2021), added feedforward control can serve multiple functions, such as enhancing gait stability (Daley et al., 2007), controlling gait mode transition (Owaki and Ishiguro, 2017), and adjusting walking speed (Dzeladini et al., 2014). The research in this dissertation suggests that feedforward control may also serve to activate preflex regulation in response to unexpected ground disturbances.

Our simulations demonstrate that feedforward stimulation enables the force-velocity relation to effectively generate tunable mechanical damping during preflexes. When disturbing hopping with step-down perturbations, we observed greater adjustment of muscle fiber force at touchdown and up to a fourfold increase in preflex energy regulation if feedforward stimulation was present. We interpret this finding as the scaling capacity of feedforward stimulation on the force-velocity relation's shape and magnitude. In our simulations, the feedforward stimulation was a rising signal with a fixed onset. Consequently, the shift in touchdown timing caused by each step perturbation resulted in a change of muscle fiber excitation upon ground impact. Muscle excitation increased with step-down perturbations, while it decreased with step-up perturbations. More excited muscle fibers exhibit greater viscosity, meaning the force-velocity relation would produce a larger force adjustment for a given change in muscle fiber velocity. Less excited muscle fibers exhibit lower viscosity. This phenomenon amplified muscle fibers' capacity to produce viscous-like adjustments of touchdown force in our simulations. Furthermore, the feedforward stimulation raised muscle fibers' activity level throughout the preflex duration. In scenarios involving step-down perturbations, this helped compensate for the force-saturating effects of the force-velocity relation's flattening side. As a result, the force-velocity relation also became the primary factor in adjusting preflex work to step-down perturbation intensity.

In their study, van der Krogt et al. (2009) observed the same regulatory mechanism when simulating human hopping over variable surface hardness. They found that muscle fiber mechanics alone cannot significantly adjust leg stiffness to an unexpected level of surface hardness. Instead, regulation occurred from the phase shift between feedforward stimulation and the duration of leg compression (van der Krogt et al., 2009). Muscle fiber viscoelasticity also scaled due to this phase shift; however, the authors mainly regarded it as a secondary, beneficial contribution (van der Krogt et al., 2009). Our decomposition algorithm partly contradicts this view by demonstrating that the force-velocity relation is the main factor in regulating preflex work when feedforward stimulation is allowed. In our simulations, the feedforward stimulation could contribute to the adjustment of preflex work by directly altering muscle fiber force. Nevertheless, neuronal direct contribution to preflex regulation was lower than that of the force-velocity relation, indicating that the feedforward stimulation's primary function was activating mechanical damping capacities in the muscle fibers. It should be noted that we limited our analysis to the preflex duration. Thus, we cannot exclude that the phase shift in feedforward control may have a more direct and dominant role in rejecting perturbations when a longer stance duration is examined, as done in van der Krogt et al. (2009).

Our findings align with previous research observing that legged locomotion exploits a close interplay between neuromodulation, inner muscle mechanics, and environmental interaction (Biewener and Daley, 2007; Daley et al., 2009; van der Krogt et al., 2009). Thanks to our decomposition algorithm, we were able to probe such a complex interplay and quantify the distinct mechanisms affecting preflex regulation. We identified phenomena, such as the feedforward adjustment of the force-velocity relation's shape, that promote the rejection of step perturbations by tunable mechanical damping. Interestingly, we also observed mechanisms that hinder muscle fibers from fully exploiting their mechanical damping capacity. For instance, when muscle fibers receive a feedforward stimulation during the initial flight phase, they undergo a shortening contraction at touchdown. This results in a brief injection of mechanical energy following ground impact, rather than dissipation. A step-down perturbation would prolong the initial flight phase, potentially increasing muscle fiber shortening velocity and, consequently, the injected energy. It also allows for more excited muscle fibers at touchdown, which would resist lengthening more. These phenomena would oppose the rise in energy dissipation necessary to reject the step-down perturbation. Notice that the step-down perturbation would also cause the leg to hit the ground at a faster impact velocity, promoting more lengthening acceleration of the muscle fibers after touchdown. Therefore, whether the feedforward stimulation enables the muscle fibers to dissipate more energy and reject the step-down perturbation depends on which dynamics prevail.

In our simulations, the mechanisms that promote tunable mechanical damping consistently emerged as the prevailing factors. However, the associated dynamics are complex, nonlinear, and potentially sensible to multiple conditions. For example, tendon stiffness may affect impact velocity transmission, reference hopping height, and the duration of the initial flight phase. Smoother impact dynamics may reduce the eccentric acceleration of the muscle fibers after touchdown. Even a different feedforward stimulation may influence the interplay between inner muscle mechanics and environmental interaction. Concerning this, the results from Haeufle et al. (2012a) suggest that the stabilizing function of the force-velocity relation may not be so sensitive to the feedforward stimulation profile. However, how the force-velocity relation contributes to locomotion stability may be affected. For instance, we designed our ramp signal inspired by experimental human data from Moritz and Farley (2004); Müller et al. (2015, 2020). Avian experiments in Daley et al. (2009) measured a different feedforward profile, resembling a triangular signal with peak point around expected touchdown. With this stimulation, step-down perturbations resulted in less excited muscle fibers upon ground impact, a trend opposite to our simulations. Despite this, more energy dissipation in response to the step-down perturbations still occurred due to increased muscle stretching.

As Biewener and Daley (2007) observed, the interplay between neuromodulation, inner muscle mechanics, and environmental interaction may be context-dependent and sensitive to the movement's initial conditions. Theoretical studies also suggest that mechanical damping requires proper calibration within the dynamics of a legged system to benefit locomotion (Heim et al., 2020; Shen and Seipel, 2012). Therefore, future research should expand our analysis to more comprehensive neuro-musculoskeletal models, involving multiple muscles and body segments. These models could validate our findings under simulated conditions more representative of muscle fibers' contraction trajectories during biological locomotion. In addition, they would allow the simulation of more complex tasks, such as forward hopping and running. Analysis of such locomotion tasks would permit investigating the benefits of the force-velocity relation and associated preflex regulation for metrics more complex than touchdown force and preflex work adjustment.

9.3 Tunable mechanical damping in legged robotics

The second part of this dissertation (Chapters 7 and 8) investigated solutions to embed tunable mechanical damping in legged robotics. Tunable mechanical damping can benefit legged robotics for two main reasons. First, it delivers a quick mechanical response to external perturbations, enabling sensor-free motion stabilization and less burden on the control architecture. Second, it diminishes unwanted energy losses during steady-state locomotion, which are inevitable with non-tunable mechanical damping.

9.3.1 Physical principle

Multiple physical principles can produce mechanical damping in a robotic system (Laffranchi et al., 2012; Monteleone et al., 2022). The results from Chapters 4 to 6 show that step perturbations alter the kinematics of leg compression, which already provides a certain degree of energy regulation when some damping is present. Therefore, a constant damping force of tunable magnitude may be sufficient to produce a stabilizing response that adapts to variable terrain conditions. We hypothesized, however, that tunable viscous damping could provide better performance. Our hypothesis is supported by the findings in Chapters 4 and 5, which show better preflex regulation when muscle fibers granted more viscous-like mechanical capacities.

Consequently, in Chapter 7, we compared the capacity of a simulated robotic leg to reject step perturbations when embedding either Coulomb friction or viscous damping. The simulated model comprised a two-segment leg with a single degree of freedom, the knee joint, actuated by an ideal spring and damper. In all simulated conditions, we found viscous damping to outperform Coulomb friction damping in adjusting energy dissipation to the step perturbation intensity.

This finding is explained by first noting how the generic knee damper dissipates energy (E_d):

$$E_d = \int_{\theta_k^{TD}}^{\theta_k^{MS}} T_d \, d\theta_k \tag{9.1}$$

where T_d is the torque the damper produces during leg compression, θ_k is the knee angle, and θ_k^{TD} and θ_k^{MS} are the knee angle values at touchdown and midstance, respectively. According to eq. (9.1), the amount of energy the damper dissipates depends on the applied damping torque and the amount of knee compression following ground impact. With a Coulomb friction damper, the damping torque is constant and independent of any step perturbation. Therefore, the Coulomb friction damper adjusts energy dissipation based entirely on the change in knee flexion that follows a step perturbation. In contrast, a viscous damper produces a torque whose intensity depends on the knee's angular velocity, resisting fast rotations more and slow rotations less. As a result, the dissipated energy adjusts to the step perturbation intensity because of simultaneous changes in damper torque and knee flexion. Notice that, in the case of a step-down perturbation, a viscous knee torque would oppose knee flexion more than a constant one. Thus, the maximum knee flexion with Coulomb friction damping is larger than with viscous damping. Our simulations reveal, however, that the combined adjustment of damping torque and knee flexion that occurs with viscous damping is still superior in regulating energy dissipation than any extra knee flexion possible with constant friction damping. This means the viscous damper allowed for better rejection of ground perturbations while also protecting the knee from excessive flexion.

While the viscous damper consistently outperformed the Coulomb friction damper, the performance gap diminished for small and large damping rates. This finding suggests that a Coulomb friction damper could still be suitable for applications requiring either high or low levels of mechanical damping. Friction

dampers are a common strategy for mechanical damping in robotic actuation (Monteleone et al., 2022), as they are cost-effective and easy to manufacture (Arelekatti et al., 2021). However, this technology can be unreliable, as it is sensitive to wear and environmental conditions (Andrysek, 2010). On the other hand, fluid-based dampers provide more precise control of tunable mechanical damping (Guglielmino et al., 2005; Unsal et al., 2004). Arelekatti et al. (2021) even demonstrated that this technology could be compact and cost-effective with an appropriate design. Therefore, we conclude that the advantages of implementing viscous dampers in a legged system significantly outweigh those of Coulomb friction dampers.

9.3.2 Damping in hardware

Based on the considerations in section 9.3.1, we tested two strategies to embed viscous damping into legged robotics and generate tunable mechanical damping. Our first approach was to directly couple the viscous damper to the knee rotation, as described in Chapter 7. We hypothesized that tunable mechanical damping during perturbed drop experiments could be achieved by (offline) damping rate control, which required changing the valve setting of the viscous damper. Our experiments revealed that this strategy is ineffective: the tunability of energy dissipation was small, and the mapping between the damping rate and change in dissipated energy was inconsistent.

We explain this finding by the damping rate's opposite effect on the damper force and piston displacement. A higher damping rate, for instance, increases the damper force and piston's resistance to movement. The first phenomenon promotes more energy dissipation, whereas the second counters it. The complex fluid dynamics of the damper and the nonlinearities of legged locomotion make it challenging to predict which of these two opposing mechanisms will dominate. As a result, there is an unintuitive mapping between damping rate and dissipated energy. Prior studies also argued against the use of hydraulic piston dampers at the knee joint of prosthetic legs due to their intricate nonlinear dynamics (Arelekatti et al., 2018, 2021).

We designed a slack-damper mechanism to overcome our previous design's limitations and achieve more intuitively and effectively tunable mechanical damping. As described in Chapter 8, the slack-damper mechanism implements a cable of adjustable slackness to connect the viscous damper (same model tested in Chapter 7) to the knee joint of a robotic leg. We hypothesized that the degree of slackness would directly control the amount of energy the damper dissipates. With zero slackness, the damper would react immediately to the knee rotation, resulting in large damping forces and energy dissipation. In contrast, high slackness would decouple the damper from the joint rotation, requiring a certain amount of leg compression before the damper can engage. Since leg compression would slow down during this period, we expected high slackness to decrease the damping force and associated energy dissipation. Note that the slack-damper mechanism does not alter the damping rate of the viscous damper, which remained unchanged throughout our tests.

Our experiments validated our assumptions, demonstrating that the slack-damper mechanism can produce effective and intuitive-to-tune mechanical damping across various hopping conditions and ground perturbations. This improved performance can be understood by examining how tendon slackness controls the damper's work loop. In a directly-coupled damper, damping rate control has little impact on the work loop's encircled area, which represents the dissipated energy. As previously explained, this control strategy inversely alters the damping force and piston displacement. In a damper's work loop, the damping force determines the vertical peak, while the piston displacement defines the horizontal width. Thus, damping rate control of a directly-coupled damper cannot significantly regulate energy

dissipation, as the work loop's vertical and horizontal dimensions are affected inversely. In contrast, slackness control concurrently increases (or decreases) the work loop's peak and width. For instance, when slackness is increased, damper engagement is delayed. When the engagement occurs, knee compression is closer to a complete stop, resulting in less piston displacement than reference slackness. Simultaneously, due to the damper's viscous nature and decelerating knee compression, the damping force at damper engagement is reduced. Therefore, increased slackness reduces both the horizontal and vertical dimensions of the damper's work loop, resulting in a smaller encircled area and less energy dissipated during leg compression. The opposite effect occurs when slackness is reduced.

Our slack-damper mechanism makes the nonlinear dynamics of a fluid-based piston damper in a robotic leg more predictable. To achieve similar intuitive dynamics, Arelekatti et al. (2018) proposed an alternative design strategy consisting of a rotary, shear-based architecture. Their damper allows coaxial implementation, which facilitates inserting the device into a robotic joint. Furthermore, it displays a linear dependence between the damping torque and the gait cadence. Despite these advantages, their implementation does not offer means to control the produced damping: the damper size defines the damping rate. Our slack-damper implementation, instead, allowed us to take a viscous damper with a fixed damping coefficient and produce tunable mechanical damping by simply adjusting the slackness level.

Another class of viscous dampers that could provide an alternative strategy to our slack-damper mechanism are magneto-rheological dampers (Agrawal and Amjadian, 2022). These devices exploit a special class of fluids that change rheological behavior when subject to a magnetic field (Monteleone et al., 2022). This technology could successfully adjust the knee damping coefficient of robotic legs throughout the gait cycle, as demonstrated in experiments with unilateral amputees (Herr and Wilkenfeld, 2003) and robotic systems (Garcia et al., 2011). The Össur Rheo leg prosthetic, which implements a magneto-rheological damper, was found to improve gait and metabolic cost relative to prosthetics implementing more conventional hydraulic dampers (Johansson et al., 2005). A magneto-rheological damper was also effectively used by Kostamo et al. (2013) to design a compliant foot and improve foot-ground contact in a robotic leg (HyQ). When we conducted our studies, we had no access to commercially available magneto-rheological dampers that could fit our leg prototypes. Future studies should investigate the potential of these devices in producing tunable mechanical damping in experiments similar to those described in Chapter 8. In particular, it would be interesting to compare their performance and cost-effectiveness with our slack-damper mechanism, as well as evaluate the easiness of implementation relative to our approach.

9.3.3 Trade-off: energy efficiency vs. robustness

Energy efficiency is a vital design objective in legged robotics, as untethered mobile robots suffer limited power autonomy (Kashiri et al., 2018). Elastic actuation has long been explored as a strategy to increase robots' energy efficiency (Beckerle et al., 2017), leading to several successful legged systems (Grizzle et al., 2009; Hubicki et al., 2016; Spröwitz et al., 2013; Zhao et al., 2022). Elastic compliance, however, can produce unwanted oscillations and reduced control bandwidth (Kashiri et al., 2018; Monteleone et al., 2022). Integrated mechanical damping can address this problem (Kashiri et al., 2017), and even enable rejection of energy-based perturbations, such as changes in impact velocity (Shen and Seipel, 2012). Nevertheless, the dissipative nature of mechanical damping may negatively impact energy efficiency. For example, a mechanical damper would dissipate mechanical energy during steady-state locomotion, requiring extra actuation to maintain a periodic gait.

We hypothesized that a trade-off between energy efficiency and locomotion robustness emerges when implementing our slack-damper mechanism in a robotic leg. Experiments in Chapter 8 confirm our hypothesis. For instance, during forward hopping tests, when we reduced the slackness in our slack-damper mechanism, thereby allowing for increased mechanical damping, we observed a faster recovery speed after ground perturbations and a decreased risk of falling. However, the cost of transport increased.

The tunability of our device allows different locomotion strategies, prioritizing robustness or energy efficiency as desired. Based on the considerations in Heim et al. (2020), a robot implementing our slack-damper mechanism could use large slackness over flat terrains, prioritizing energy efficiency; when detecting rougher surfaces, the robot could switch to a reduced slackness, prioritizing locomotion robustness. This would require a mechanism for online adjustment of the tendon slackness, which we did not include in our study.

It is worth noting that our results could partly depend on the leg architecture tested. In our minimalistic robot, a trunk segment is missing. Trunk oscillations and posture greatly influence the energetics of bipedal locomotion (Drama and Badri-Spröwitz, 2020). Our results show that increased mechanical damping smooths locomotion dynamics, potentially reducing the need for active trunk posture control in a bipedal robot. I speculate that in the case of a heavy trunk, this could significantly reduce the external mechanical work required by actuation, leading to a simultaneous increase in locomotion robustness and energy efficiency.

Another key advantage of our slack-damper is its perturbation-triggered nature. The damper engages only after a certain amount of leg compression, meaning it remains inactive over flat terrains or during minor perturbations. Therefore, our design enables a 'damping-as-needed' strategy that is sensor-free and consistent with the principle of morphological computation. As defined in Pfeifer and Bongard (2007), morphological computation refers to the body's capacity to perform operations that would otherwise require the brain to execute them. Morphological computation occurs when a desired behavior, such as resisting external perturbations, develops through the interaction between body morphology (e.g., geometry and compliance) and the environment without direct control. This definition aligns with how our slack-damper mechanism operates: for any slackness level, its activation in response to a ground perturbation uniquely depends on the leg-environment interaction. Conventional implementations of tunable mechanical damping, like those using magneto-rheological fluids, struggle to replicate a similar perturbation-triggered characteristic. Even at their lowest setting, these devices cannot achieve zero damping, which can promote undesired behaviors when they are directly coupled to a joint. For instance, Herr and Wilkenfeld (2003) found that the inability to turn off entirely the viscous damping in their magneto-rheological prosthetic knee could lead to unnatural swing trajectories.

As a final remark, it is worth noting that we focused on the trade-off between energy efficiency and locomotion robustness. However, these are only two of the many task-level demands that legged locomotion can pose, such as high maneuverability (Hubel et al., 2016) and prevention of injuries (Biewener, 1989). Biological legged locomotion often accommodates many, sometimes conflicting, task-level objectives (Birn-Jeffery et al., 2014). Therefore, future research should extend our analysis by testing our slack-damper mechanism over a wider variety of legged locomotion demands, exploring the existence of further trade-offs.

9.4 Take-home messages

- Tunable mechanical damping benefits fast legged locomotion by providing a rapid response to unexpected disturbances;
- We developed a decomposition algorithm to quantify the mechanical damping generated by muscles during simulated perturbed hopping. We also conducted hardware experiments to explore the effective implementation of tunable mechanical damping in legged robotics;
- The force-velocity relation grants muscle fibers tunable mechanical damping. However, this requires feedforward stimulation for effective preflex regulation;
- Tunable mechanical damping in biological actuation emerges from a complex interaction between muscle inner mechanics, neuronal modulation, and environmental conditions. This interplay is highly nonlinear and potentially sensible to simulated conditions. Future work should investigate such sensitivity systematically;
- A more precise estimation of the force-velocity relation's eccentric side is crucial for better understanding biological damping;
- Viscous damping is more effective than Coulomb friction damping in generating tunable mechanical damping in legged robotics;
- Damping rate control of a viscous damper coupled to the knee joint might not be an effective strategy for generating tunable mechanical damping in legged robotics;
- Interposing a cable of controllable slackness between the viscous damper and the joint rotation is a more effective and intuitive method for implementing tunable mechanical damping in a robotic leg;
- Mechanical damping increases locomotion robustness at the cost of less energy efficiency. Tunable mechanical damping can reduce unnecessary energy dissipation by deactivating the damper on even terrains. Perturbation-triggered damping likely increases morphological computation, simplifying the control architecture. Future work should explore the existence of additional trade-offs.

References

Abraham, I., Shen, Z., and Seipel, J. A Nonlinear Leg Damping Model for the Prediction of Running Forces and Stability. *Journal of Computational and Nonlinear Dynamics*, 10(5), 2015. doi:10.1115/1.4028751.

Agrawal, A. and Amjadian, M. 22 - seismic component devices. In Pipinato, A., editor, *Innovative Bridge Design Handbook (Second Edition)*, pages 637–662. Butterworth-Heinemann, 2022. ISBN 978-0-12-823550-8. doi:10.1016/B978-0-12-823550-8.00027-5.

Alcazar, J., Csapo, R., Ara, I., and Alegre, L. M. On the shape of the force-velocity relationship in skeletal muscles: The linear, the hyperbolic, and the double-hyperbolic. *Frontiers in Physiology*, 10: 769, 2019. doi:10.3389/fphys.2019.00769.

Alexander, N., Strutzenberger, G., Ameshofer, L. M., and Schwameder, H. Lower limb joint work and joint work contribution during downhill and uphill walking at different inclinations. *Journal of Biomechanics*, 61:75–80, 2017. doi:10.1016/j.jbiomech.2017.07.001.

Alexander, R., Maloiy, G., Ker, R., Jayes, A., and Warui, C. The role of tendon elasticity in the locomotion of the camel (Camelus dromedarius). *Journal of Zoology*, 198(3):293–313, 1982. doi:10.1111/j.1469-7998.1982.tb02077.x.

Alexander, R. M. Three uses for springs in legged locomotion. *The International Journal of Robotics Research*, 9(2):53–61, 1990. doi:10.1177/027836499000900205.

Alexander, R. M. Energy-saving mechanisms in walking and running. *The Journal of Experimental Biology*, 160(1):55–69, 1991. doi:10.1242/jeb.160.1.55.

Andrysek, J. Lower-limb prosthetic technologies in the developing world: A review of literature from 1994-2010. *Prosthetics and Orthotics International*, 34(4):378–398, 2010. doi:10.3109/03093646.2010.520060.

Araz, M., Weidner, S., Izzi, F., Badri-Spröwitz, A., Siebert, T., and Haeufle, D. F. B. Muscle preflex response to perturbations in locomotion: In vitro experiments and simulations with realistic boundary conditions. *Frontiers in Bioengineering and Biotechnology*, 11, 2023. doi:10.3389/fbioe.2023.1150170.

Arelekatti, V. N. M., Petelina, N. T., Johnson, W. B., Winter, A. G., and Major, M. J. Design of a passive, shear-based rotary hydraulic damper for single-axis prosthetic knees. In *Proceedings of the ASME 2018 International Design Engineering Technical Conferences and Computers and Information in Engineering Conference. Volume 5A: 42nd Mechanisms and Robotics Conference*, page V05AT07A064, Quebec City, Quebec, Canada, 2018. doi:10.1115/DETC2018-85962.

Arelekatti, V. N. M., Petelina, N. T., Johnson, W. B., Major, M. J., and Winter V, A. G. Design of a four-bar latch mechanism and a shear-based rotary viscous damper for single-axis prosthetic knees. *Journal of Mechanisms and Robotics*, 14(3), 2021. doi:10.1115/1.4052804.

Ashtiani, M. S., Aghamaleki Sarvestani, A., and Badri-Spröwitz, A. Hybrid parallel compliance allows robots to operate with sensorimotor delays and low control frequencies. *Frontiers in Robotics and AI*, 8:645748, 2021. doi:10.3389/frobt.2021.645748.

Badri-Spröwitz, A., Aghamaleki Sarvestani, A., Sitti, M., and Daley, M. A. Birdbot achieves energy-efficient gait with minimal control using avian-inspired leg clutching. *Science Robotics*, 7(64): eabg4055, 2022. doi:10.1126/scirobotics.abg4055.

Bayer, A., Schmitt, S., Günther, M., and Haeufle, D. The influence of biophysical muscle properties on simulating fast human arm movements. *Computer methods in biomechanics and biomedical engineering*, 20(8):803–821, 2017. doi:10.1080/10255842.2017.1293663.

Beckerle, P., Verstraten, T., Mathijssen, G., Furnémont, R., Vanderborght, B., and Lefeber, D. Series and parallel elastic actuation: Influence of operating positions on design and control. *IEEE/ASME Transactions on Mechatronics*, 22(1):521–529, 2017. doi:10.1109/TMECH.2016.2621062.

Berkemeier, M. and Desai, K. Design of a robot leg with elastic energy storage, comparison to biology, and preliminary experimental results. In *Proceedings of IEEE International Conference on Robotics and Automation*, volume 1, pages 213–218, Minneapolis, MN, USA, 1996. IEEE. doi:10.1109/ROBOT.1996.503597.

Bhanpuri, N. H., Okamura, A. M., and Bastian, A. J. Predicting and correcting ataxia using a model of cerebellar function. *Brain*, 137(7):1931–1944, 2014. doi:10.1093/brain/awu115.

Biewener, A. A. and Roberts, T. J. Muscle and tendon contributions to force, work, and elastic energy savings: a comparative perspective. *Exercise and sport sciences reviews*, 28(3):99–107, 2000. url: http://www.ncbi.nlm.nih.gov/pubmed/10916700.

Biewener, A. A. Scaling body support in mammals: Limb posture and muscle mechanics. *Science*, 245 (4913):45–48, 1989. doi:10.1126/science.2740914.

Biewener, A. A. Muscle Function in vivo: A Comparison of Muscles used for Elastic Energy Savings versus Muscles Used to Generate Mechanical Power. *American Zoologist*, 38(4):703–717, 1998. doi:10.1093/icb/38.4.703.

Biewener, A. A. and Daley, M. A. Unsteady locomotion: integrating muscle function with whole body dynamics and neuromuscular control. *The Journal of experimental biology*, 210(17):2949–2960, 2007. doi:10.1242/jeb.005801.

Birn-Jeffery, A. V., Hubicki, C. M., Blum, Y., Renjewski, D., Hurst, J. W., and Daley, M. A. Don't break a leg: running birds from quail to ostrich prioritise leg safety and economy on uneven terrain. *Journal of Experimental Biology*, 217(21):3786–3796, 2014. doi:10.1242/jeb.102640.

Bledt, G., Wensing, P. M., Ingersoll, S., and Kim, S. Contact model fusion for event-based locomotion in unstructured terrains. In *2018 IEEE International Conference on Robotics and Automation (ICRA)*, pages 4399–4406, Brisbane, QLD, Australia, 2018. IEEE. doi:10.1109/ICRA.2018.8460904.

Blickhan, R. The spring-mass model for running and hopping. *Journal of Biomechanics*, 22(11): 1217–1227, 1989. doi:10.1016/0021-9290(89)90224-8.

Blickhan, R., Seyfarth, A., Geyer, H., Grimmer, S., Wagner, H., and Günther, M. Intelligence by mechanics. *Philosophical Transactions of the Royal Society A: Mathematical, Physical and Engineering Sciences*, 365(1850):199–220, 2007. doi:10.1098/rsta.2006.1911.

Bobbert, M. F., Yeadon, M. R., and Nigg, B. M. Mechanical analysis of the landing phase in heel-toe running. *Journal of Biomechanics*, 25(3):223–234, 1992. doi:10.1016/0021-9290(92)90022-S.

Bogdanovic, M., Khadiv, M., and Righetti, L. Learning variable impedance control for contact sensitive tasks. *IEEE Robotics and Automation Letters*, 5(4):6129–6136, 2020. doi:10.1109/LRA.2020.3011379.

Brenner, B. Effect of Ca2+ on cross-bridge turnover kinetics in skinned single rabbit psoas fibers: implications for regulation of muscle contraction. *Proceedings of the National Academy of Sciences*, 85(9):3265–3269, 1988. doi:10.1073/pnas.85.9.3265.

Brown, I. E. and Loeb, G. E. A reductionist approach to creating and using neuromusculoskeletal models. In Winters, J. M. and Crago, P. E., editors, *Biomechanics and Neural Control of Posture and Movement*, pages 148–163. Springer, New York, NY, 2000. ISBN 978-1-4612-2104-3. doi:10.1007/978-1-4612-2104-3_10.

Brown, N. A. T., Pandy, M. G., Kawcak, C. E., and McIlwraith, C. W. Force- and moment-generating capacities of muscles in the distal forelimb of the horse. *Journal of Anatomy*, 203(1):101–113, 2003. doi:10.1046/j.1469-7580.2003.00206.x.

Bunz, E. K., Haeufle, D. F. B., Remy, C. D., and Schmitt, S. Bioinspired preactivation reflex increases robustness of walking on rough terrain. *Scientific Reports*, 13(1):13219, 2023.

Campbell, K. S., Jitandrakumar, R., and Moss, R. L. Cycling Cross-Bridges Increase Myocardial Stiffness at Submaximal Levels of Ca+2 Activation. *Biophysical Journal*, 84(6):3807–3815, 2003. doi:10.1016/S0006-3495(03)75108-X.

Candan, S. Ş., Karagöz, O. K., Yazıcıoğlu, Y., and Saranlı, U. Design of a parallel elastic hopper with a wrapping cam mechanism and template based virtually tunable damping control. In *Dynamic Systems and Control Conference*, volume 1, page V001T05A009, Virtual, Online, 2020. doi:10.1115/DSCC2020-3278.

Cham, J. G. and Cutkosky, M. R. Dynamic Stability of Open-Loop Hopping. *Journal of Dynamic Systems, Measurement, and Control*, 129(3):275–284, 2006. doi:10.1115/1.2718237.

Chen, J., Liang, Z., Zhu, Y., Liu, C., Zhang, L., Hao, L., and Zhao, J. Towards the exploitation of physical compliance in segmented and electrically actuated robotic legs: A review focused on elastic mechanisms. *Sensors*, 19(24):5351, 2019. doi:10.3390/s19245351.

Christensen, K. B., Günther, M., Schmitt, S., and Siebert, T. Strain in shock-loaded skeletal muscle and the time scale of muscular wobbling mass dynamics. *Scientific reports*, 7:13266, 2017. doi:10.1038/s41598-017-13630-7.

Claflin, D. R. and Faulkner, J. A. Shortening velocity extrapolated to zero load and unloaded shortening velocity of whole rat skeletal muscle. *The Journal of Physiology*, 359(1):357–363, 1985. doi:10.1113/jphysiol.1985.sp015589.

Cohen, J. *Statistical power analysis for the behavioral sciences (2nd Edition)*. Lawrence Erlbaum Associates, Publishers, Hillsdale, NJ, 1988. ISBN 0-8058-0283-5. doi:10.4324/9780203771587.

Collins, S. H., Wisse, M., and Ruina, A. A three-dimensional passive-dynamic walking robot with two legs and knees. *The International Journal of Robotics Research*, 20(7):607–615, 2001. doi:10.1177/02783640122067561.

Crespi, A., Karakasiliotis, K., Guignard, A., and Ijspeert, A. J. Salamandra robotica ii: An amphibious robot to study salamander-like swimming and walking gaits. *IEEE Transactions on Robotics*, 29(2): 308–320, 2013. doi:10.1109/TRO.2012.2234311.

Cui, L., Perreault, E. J., Maas, H., and Sandercock, T. G. Modeling short-range stiffness of feline lower hindlimb muscles. *Journal of Biomechanics*, 41(9):1945–1952, 2008. doi:10.1016/j.jbiomech.2008.03.024.

Daley, M. A. and Biewener, A. A. Running over rough terrain reveals limb control for intrinsic stability. *Proceedings of the National Academy of Sciences*, 103(42):15681–15686, 2006. doi:10.1073/pnas.0601473103.

Daley, M. A., Felix, G., and Biewener, A. A. Running stability is enhanced by a proximo-distal gradient in joint neuromechanical control. *Journal of Experimental Biology*, 210(3):383–394, 2007. doi:10.1242/jeb.02668.

Daley, M. A., Voloshina, A., and Biewener, A. A. The role of intrinsic muscle mechanics in the neuromuscular control of stable running in the guinea fowl. *The Journal of Physiology*, 587(11): 2693–2707, 2009. doi:10.1113/jphysiol.2009.171017.

Darby, J., Li, B., Costen, N., Loram, I., and Hodson-Tole, E. Estimating skeletal muscle fascicle curvature from b-mode ultrasound image sequences. *IEEE Transactions on Biomedical Engineering*, 60(7):1935–1945, 2013. doi:10.1109/TBME.2013.2245328.

De Groote, F., Allen, J. L., and Ting, L. H. Contribution of muscle short-range stiffness to initial changes in joint kinetics and kinematics during perturbations to standing balance: A simulation study. *Journal of Biomechanics*, 55:71–77, 2017. doi:10.1016/j.jbiomech.2017.02.008.

Dick, T. J. M., Biewener, A. A., and Wakeling, J. M. Comparison of human gastrocnemius forces predicted by Hill-type muscle models and estimated from ultrasound images. *Journal of Experimental Biology*, 220(9):1643–1653, 2017. doi:10.1242/jeb.154807.

Dixon, J. C. *The shock absorber handbook, second edition*. John Wiley & Sons, Chichester, West Sussex, England, 2007. ISBN 978-0-470-51020-9. doi:10.1002/9780470516430.

Drama, Ö. and Badri-Spröwitz, A. Trunk pitch oscillations for energy trade-offs in bipedal running birds and robots. *Bioinspiration & Biomimetics*, 15(3):036013, 2020. doi:10.1088/1748-3190/ab7570.

Duysens, J. and Van de Crommert, H. W. Neural control of locomotion; part 1: The central pattern generator from cats to humans. *Gait & Posture*, 7(2):131–141, 1998. doi:10.1016/S0966-6362(97)00042-8.

Dzeladini, F., van den Kieboom, J., and Ijspeert, A. The contribution of a central pattern generator in a reflex-based neuromuscular model. *Frontiers in Human Neuroscience*, 8:371, 2014. doi:10.3389/fnhum.2014.00371.

Edman, K. A. P. and Hwang, J. C. The force-velocity relationship in vertebrate muscle fibres at varied tonicity of the extracellular medium. *The Journal of Physiology*, 269(2):255–272, 1977. doi:10.1113/jphysiol.1977.sp011901.

Edman, K. A. P., Mulieri, L. A., and Scubon-Mulieri, B. Non-hyperbolic force-velocity relationship in single muscle fibres1. *Acta Physiologica Scandinavica*, 98(2):143–156, 1976. doi:10.1111/j.1748-1716.1976.tb00234.x.

Eliasmith, C. and Anderson, C. H. *Neural engineering: Computation, representation, and dynamics in neurobiological systems*. MIT press, Cambridge, MA, USA, 2003. ISBN 978-0262550604. url: https://mitpress.mit.edu/9780262550604/neural-engineering/.

Faisal, A. A., Selen, L. P., and Wolpert, D. M. Noise in the nervous system. *Nature Reviews Neuroscience*, 9(4):292–303, 2008. doi:10.1038/nrn2258.

Flitney, F. and Hirst, D. Cross-bridge detachment and sarcomere 'give' during stretch of active frog's muscle. *The Journal of Physiology*, 276(1):449–465, 1978. doi:10.1113/jphysiol.1978.sp012246.

Freundt, J. K. and Linke, W. A. Titin as a force-generating muscle protein under regulatory control. *Journal of applied physiology*, 126(5):1474–1482, 2019. doi:10.1152/japplphysiol.00865.2018.

Fukutani, A., Leonard, T., and Herzog, W. Does stretching velocity affect residual force enhancement? *Journal of Biomechanics*, 89:143–147, 2019. doi:10.1016/j.jbiomech.2019.04.033.

Full, R. J. and Koditschek, D. E. Templates and anchors: neuromechanical hypotheses of legged locomotion on land. *Journal of Experimental Biology*, 202(23):3325–3332, 1999. doi:10.1242/jeb.202.23.3325.

Garcia, E., Arevalo, J. C., Munoz, G., and Gonzalez-de Santos, P. Combining series elastic actuation and magneto-rheological damping for the control of agile locomotion. *Robotics and Autonomous Systems*, 59(10):827–839, 2011. doi:10.1016/j.robot.2011.06.006.

Gerritsen, K. G., van den Bogert, A. J., Hulliger, M., and Zernicke, R. F. Intrinsic Muscle Properties Facilitate Locomotor Control—A Computer Simulation Study. *Motor Control*, 2(3):206–220, 1998. doi:10.1123/mcj.2.3.206.

Getz, E. B., Cooke, R., and Lehman, S. L. Phase transition in force during ramp stretches of skeletal muscle. *Biophysical Journal*, 75(6):2971–2983, 1998. doi:10.1016/s0006-3495(98)77738-0.

Geyer, H. and Herr, H. A Muscle-Reflex Model That Encodes Principles of Legged Mechanics Produces Human Walking Dynamics and Muscle Activities. *IEEE Transactions on Neural Systems and Rehabilitation Engineering*, 18(3):263–273, 2010. doi:10.1109/TNSRE.2010.2047592.

Geyer, H., Seyfarth, A., and Blickhan, R. Positive force feedback in bouncing gaits? *Proceedings of the Royal Society of London. Series B: Biological Sciences*, 270(1529):2173–2183, 2003. doi:10.1098/rspb.2003.2454.

Geyer, H., Seyfarth, A., and Blickhan, R. Compliant leg behaviour explains basic dynamics of walking and running. *Proceedings of the Royal Society B: Biological Sciences*, 273(1603):2861–2867, 2006. doi:10.1098/rspb.2006.3637.

Ghazi-Zahedi, K., Haeufle, D. F. B., Montúfar, G., Schmitt, S., and Ay, N. Evaluating morphological computation in muscle and dc-motor driven models of hopping movements. *Frontiers in Robotics and AI*, 3:42, 2016. doi:10.3389/frobt.2016.00042.

Gilliver, S. F., Degens, H., Rittweger, J., and Jones, D. A. Effects of submaximal activation on the determinants of power of chemically skinned rat soleus fibres. *Experimental Physiology*, 96(2): 171–178, 2011. doi:10.1113/expphysiol.2010.054239.

Gordon, J. C., Holt, N. C., Biewener, A., and Daley, M. A. Tuning of feedforward control enables stable muscle force-length dynamics after loss of autogenic proprioceptive feedback. *eLife*, 9:e53908, 2020. doi:10.7554/eLife.53908.

Griffiths, P., Güth, K., Kuhn, H., and Rüegg, J. Cross bridge slippage in skinned frog muscle fibres. *Biophysics of structure and mechanism*, 7(2):107–124, 1980. doi:10.1007/BF00538402.

Grillner, S. The role of muscle stiffness in meeting the changing postural and locomotor requirements for force development by the ankle extensors. *Acta Physiologica Scandinavica*, 86(1):92–108, 1972. doi:10.1111/j.1748-1716.1972.tb00227.x.

Grimminger, F., Meduri, A., Khadiv, M., Viereck, J., Wüthrich, M., Naveau, M., Berenz, V., Heim, S., Widmaier, F., Flayols, T., Fiene, J., Badri-Spröwitz, A., and Righetti, L. An Open Torque-Controlled Modular Robot Architecture for Legged Locomotion Research. *IEEE Robotics and Automation Letters*, 5(2):3650–3657, 2020. doi:10.1109/LRA.2020.2976639.

Grizzle, J., Hurst, J., Morris, B., Park, H.-W., and Sreenath, K. MABEL, a new robotic bipedal walker and runner. In *2009 American Control Conference*, pages 2030–2036, St. Louis, MO, USA, 2009. IEEE. ISBN 978-1-4244-4523-3. doi:10.1109/ACC.2009.5160550.

Guglielmino, E., Staimmers, C. W., Edge, K. A., Sireteanu, T., and Stancioiu, D. Damp-by-wire : Magnetorheological vs. friction dampers. *IFAC Proceedings Volumes*, 38(1):340–345, 2005. doi:10.3182/20050703-6-CZ-1902.01267.

Günther, M. and Schmitt, S. A macroscopic ansatz to deduce the Hill relation. *Journal of theoretical biology*, 263(4):407–418, 2010. doi:10.1016/j.jtbi.2009.12.027.

Günther, M. and Ruder, H. Synthesis of two-dimensional human walking: a test of the lambda-model. *Biological Cybernetics*, 89(2):89–106, 2003. doi:10.1007/s00422-003-0414-x.

Günther, M., Schmitt, S., and Wank, V. High-frequency oscillations as a consequence of neglected serial damping in Hill-type muscle models. *Biological Cybernetics*, 97(1):63–79, 2007. doi:10.1007/s00422-007-0160-6.

Günther, M., Haeufle, D. F., and Schmitt, S. The basic mechanical structure of the skeletal muscle machinery: One model for linking microscopic and macroscopic scales. *Journal of Theoretical Biology*, 456:137–167, 2018. doi:10.1016/j.jtbi.2018.07.023.

Haeufle, D. F. B., Grimmer, S., and Seyfarth, A. The role of intrinsic muscle properties for stable hopping—stability is achieved by the force–velocity relation. *Bioinspiration & Biomimetics*, 5(1): 016004, 2010. doi:10.1088/1748-3182/5/1/016004.

Haeufle, D. F. B., Grimmer, S., Kalveram, K.-T., and Seyfarth, A. Integration of intrinsic muscle properties, feed-forward and feedback signals for generating and stabilizing hopping. *Journal of The Royal Society Interface*, 9(72):1458–1469, 2012a. doi:10.1098/rsif.2011.0694.

Haeufle, D. F. B., Günther, M., Wunner, G., and Schmitt, S. Quantifying control effort of biological and technical movements: an information-entropy-based approach. *Physical Review E*, 89(1):012716, 2014a. doi:10.1103/PhysRevE.89.012716.

Haeufle, D. F. B., Schmortte, B., Geyer, H., Müller, R., and Schmitt, S. The Benefit of Combining Neuronal Feedback and Feed-Forward Control for Robustness in Step Down Perturbations of Simulated Human Walking Depends on the Muscle Function. *Frontiers in Computational Neuroscience*, 12:80, 2018. doi:10.3389/fncom.2018.00080.

Haeufle, D. F. B., Stollenmaier, K., Heinrich, I., Schmitt, S., and Ghazi-Zahedi, K. Morphological Computation Increases From Lower- to Higher-Level of Biological Motor Control Hierarchy. *Frontiers in Robotics and AI*, 7:511265, 2020a. doi:10.3389/frobt.2020.511265.

Haeufle, D. F. B., Wochner, I., Holzmüller, D., Driess, D., Günther, M., and Schmitt, S. Muscles Reduce Neuronal Information Load: Quantification of Control Effort in Biological vs. Robotic Pointing and Walking. *Frontiers in Robotics and AI*, 7:77, 2020b. doi:10.3389/frobt.2020.00077.

Haeufle, D., Günther, M., Blickhan, R., and Schmitt, S. Can quick release experiments reveal the muscle structure? a bionic approach. *Journal of Bionic Engineering*, 9(2):211–223, 2012b. doi:10.1016/S1672-6529(11)60115-7.

Haeufle, D., Günther, M., Bayer, A., and Schmitt, S. Hill-type muscle model with serial damping and eccentric force–velocity relation. *Journal of Biomechanics*, 47(6):1531–1536, 2014b. doi:10.1016/j.jbiomech.2014.02.009.

Hahn, D. Stretching the limits of maximal voluntary eccentric force production in vivo. *Journal of Sport and Health Science*, 7(3):275–281, 2018. doi:10.1016/j.jshs.2018.05.003.

Hatze, H. A myocybernetic control model of skeletal muscle. *Biological Cybernetics*, 25(2):103–119, 1977. doi:10.1007/BF00337268.

Havoutis, I., Semini, C., Buchli, J., and Caldwell, D. G. Quadrupedal trotting with active compliance. In *2013 IEEE International Conference on Mechatronics (ICM)*, pages 610–616, Vicenza, Italy, 2013. IEEE. doi:10.1109/ICMECH.2013.6519112.

Heers, A. M., Rankin, J. W., and Hutchinson, J. R. Building a bird: musculoskeletal modeling and simulation of wing-assisted incline running during avian ontogeny. *Frontiers in Bioengineering and Biotechnology*, 6:140, 2018. doi:10.3389/fbioe.2018.00140.

Heim, S., Millard, M., Le Mouel, C., and Badri-Spröwitz, A. A little damping goes a long way: a simulation study of how damping influences task-level stability in running. *Biology Letters*, 16(9): 20200467, 2020. doi:10.1098/rsbl.2020.0467.

Herr, H. and Wilkenfeld, A. User-adaptive control of a magnetorheological prosthetic knee. *Industrial Robot: An International Journal*, 30(1):42–55, 2003. doi:10.1108/01439910310457706.

Herzog, J. A., Leonard, T. R., Jinha, A., and Herzog, W. Titin (visco-) elasticity in skeletal muscle myofibrils. *Molecular & Cellular Biomechanics*, 11(1):1–17, 2014. doi:10.3970/mcb.2014.011.001.

Herzog, W. Why are muscles strong, and why do they require little energy in eccentric action? *Journal of Sport and Health Science*, 7(3):255–264, 2018. doi:10.1016/j.jshs.2018.05.005.

Hilber, K. and Galler, S. Improvement of the measurements on skinned muscle fibres by fixation of the fibre ends with glutaraldehyde. *Journal of Muscle Research and Cell Motility*, 19(4):365–372, 1998. doi:10.1023/a:1005393519811.

Hill, A. V. The maximum work and mechanical efficiency of human muscles, and their most economical speed. *The Journal of Physiology*, 56(1-2):19–41, 1922. doi:10.1113/jphysiol.1922.sp001989.

Hill, A. V. The heat of shortening and the dynamic constants of muscle. *Proceedings of the Royal Society of London. Series B - Biological Sciences*, 126(843):136–195, 1938. doi:10.1098/rspb.1938.0050.

Hof, A. L. Effects of Muscle Elasticity in Walking and Running. In Winters, J. M. and Woo, S. L.-Y., editors, *Multiple Muscle Systems: Biomechanics and Movement Organization*, pages 591–607. Springer, New York, NY, 1990. ISBN 978-1-4613-9030-5. doi:10.1007/978-1-4613-9030-5_38.

Holt, N. C. and Azizi, E. The effect of activation level on muscle function during locomotion: Are optimal lengths and velocities always used? *Proceedings of the Royal Society B: Biological Sciences*, 283(1823), 2016. doi:10.1098/rspb.2015.2832.

Hu, C.-J., Wang, T.-K., Huang, C.-K., and Lin, P.-C. A torque-actuated dissipative spring loaded inverted pendulum model with rolling contact and its application to hexapod running. *Bioinspiration & biomimetics*, 14(2):026005, 2019. doi:10.1088/1748-3190/aafc4e.

Hu, X., Murray, W. M., and Perreault, E. J. Muscle short-range stiffness can be used to estimate the endpoint stiffness of the human arm. *Journal of Neurophysiology*, 105(4):1633–1641, 2011. doi:10.1152/jn.00537.2010.

Hubel, T. Y., Myatt, J. P., Jordan, N. R., Dewhirst, O. P., McNutt, J. W., and Wilson, A. M. Energy cost and return for hunting in african wild dogs and cheetahs. *Nature Communications*, 7:11034, 2016. doi:10.1038/ncomms11034.

Hubicki, C., Grimes, J., Jones, M., Renjewski, D., Spröwitz, A., Abate, A., and Hurst, J. Atrias: Design and validation of a tether-free 3d-capable spring-mass bipedal robot. *The International Journal of Robotics Research*, 35(12):1497–1521, 2016. doi:10.1177/0278364916648388.

Huerta, C. V., Xiong, X., Billeschou, P., and Manoonpong, P. Adaptive neuromechanical control for robust behaviors of bio-inspired walking robots. In Yang, H., Pasupa, K., Leung, A. C.-S., Kwok,

J. T., Chan, J. H., and King, I., editors, *Neural Information Processing. ICONIP 2020. Lecture Notes in Computer Science()*, volume 12533, pages 775–786, Bangkok, Thailand, 2020. Springer, Cham. doi:10.1007/978-3-030-63833-7_65.

Hutter, M., Gehring, C., Jud, D., Lauber, A., Bellicoso, C. D., Tsounis, V., Hwangbo, J., Bodie, K., Fankhauser, P., Bloesch, M., Diethelm, R., Bachmann, S., Melzer, A., and Hoepflinger, M. Anymal - a highly mobile and dynamic quadrupedal robot. In *2016 IEEE/RSJ International Conference on Intelligent Robots and Systems (IROS)*, pages 38–44, Daejeon, Korea (South), 2016. IEEE. doi:10.1109/IROS.2016.7758092.

Hutter, M., Gehring, C., Bloesch, M., Hoepflinger, M. A., Remy, C. D., and Siegwart, R. Starleth: A compliant quadrupedal robot for fast, efficient, and versatile locomotion. In *Adaptive Mobile Robotics*, pages 483–490. World Scientific, 2012. doi:10.1142/9789814415958_0062.

Huxley, A. 6 - muscle structure and theories of contraction. *Progress in Biophysics and Biophysical Chemistry*, 7:255–318, 1957. doi:10.1016/S0096-4174(18)30128-8.

Iida, F. and Ijspeert, A. J. Biologically inspired robotics. In Siciliano, B. and Khatib, O., editors, *Springer Handbook of Robotics*, pages 2015–2034, Cham, 2016. Springer International Publishing. ISBN 978-3-319-32552-1. doi:10.1007/978-3-319-32552-1_75.

Iida, F., Rummel, J., and Seyfarth, A. Bipedal walking and running with spring-like biarticular muscles. *Journal of Biomechanics*, 41(3):656–667, 2008. doi:10.1016/j.jbiomech.2007.09.033.

Ijspeert, A. J. Central pattern generators for locomotion control in animals and robots: A review. *Neural Networks*, 21(4):642–653, 2008. doi:10.1016/j.neunet.2008.03.014.

Ijspeert, A. J. Biorobotics: Using robots to emulate and investigate agile locomotion. *Science*, 346 (6206):196–203, 2014. doi:10.1126/science.1254486.

Ijspeert, A. J., Crespi, A., Ryczko, D., and Cabelguen, J.-M. From swimming to walking with a salamander robot driven by a spinal cord model. *Science*, 315(5817):1416–1420, 2007. doi:10.1126/science.1138353.

Izzi, F., Mo, A., Schmitt, S., Badri-Spröwitz, A., and Haeufle, D. F. B. Muscle pre-stimulation tunes viscous-like perturbation rejection in legged hopping. *arXiv preprint arXiv:2202.02114*, 2022. doi:10.48550/arXiv.2202.02114.

Izzi, F., Mo, A., Schmitt, S., Badri-Spröwitz, A., and Haeufle, D. F. Muscle prestimulation tunes velocity preflex in simulated perturbed hopping. *Scientific Reports*, 13(1):4559, 2023. doi:10.1038/s41598-023-31179-6.

Johansson, J. L., Sherrill, D. M., Riley, P. O., Bonato, P., and Herr, H. A clinical comparison of variable-damping and mechanically passive prosthetic knee devices. *American Journal of Physical Medicine & Rehabilitation*, 84(8):563–575, 2005. doi:10.1097/01.phm.0000174665.74933.0b.

John, C. T., Anderson, F. C., Higginson, J. S., and Delp, S. L. Stabilisation of walking by intrinsic muscle properties revealed in a three-dimensional muscle-driven simulation. *Computer Methods in Biomechanics and Biomedical Engineering*, 16(4):451–462, 2013. doi:10.1080/10255842.2011.627560.

Josephson, R. K. Mechanical Power Output From Striated Muscle During Cyclic Contraction. *Journal of Experimental Biology*, 114(1):493–512, 1985. doi:10.1242/jeb.114.1.493.

Joyce, G. C., Rack, P. M. H., and Westbury, D. R. The mechanical properties of cat soleus muscle during controlled lengthening and shortening movements. *The Journal of Physiology*, 204(2):461–474, 1969. doi:10.1113/jphysiol.1969.sp008924.

Julian, F. J., Rome, L. C., Stephenson, D. G., and Striz, S. The maximum speed of shortening in living and skinned frog muscle fibres. *The Journal of Physiology*, 370(1):181–199, 1986. doi:10.1113/jphysiol.1986.sp015929.

Kalouche, S. Goat: A legged robot with 3d agility and virtual compliance. In *2017 IEEE/RSJ International Conference on Intelligent Robots and Systems (IROS)*, pages 4110–4117, Vancouver, BC, Canada, 2017. IEEE. doi:10.1109/IROS.2017.8206269.

Kalveram, K. T. and Seyfarth, A. Inverse biomimetics: How robots can help to verify concepts concerning sensorimotor control of human arm and leg movements. *Journal of Physiology-Paris*, 103 (3-5):232–243, 2009. doi:10.1016/j.jphysparis.2009.08.006.

Kalveram, K. T., Haeufle, D. F. B., Seyfarth, A., and Grimmer, S. Energy management that generates terrain following versus apex-preserving hopping in man and machine. *Biological Cybernetics*, 106 (1):1–13, 2012. doi:10.1007/s00422-012-0476-8.

Kamska, V., Daley, M., and Badri-Spröwitz, A. 3D Anatomy of the Quail Lumbosacral Spinal Canal—Implications for Putative Mechanosensory Function. *Integrative Organismal Biology*, 2 (1):obaa037, 2020. doi:10.1093/iob/obaa037.

Kashiri, N., Caldwell, D. G., and Tsagarakis, N. A self-adaptive variable impedance actuator based on intrinsic non-linear compliance and damping principles. In *2017 IEEE International Conference on Robotics and Automation (ICRA)*, pages 1248–1254, Singapore, 2017. IEEE. doi:10.1109/ICRA.2017.7989148.

Kashiri, N., Abate, A., Abram, S. J., Albu-Schaffer, A., Clary, P. J., Daley, M., Faraji, S., Furnemont, R., Garabini, M., Geyer, H., Grabowski, A. M., Hurst, J., Malzahn, J., Mathijssen, G., Remy, D., Roozing, W., Shahbazi, M., Simha, S. N., Song, J.-B., Smit-Anseeuw, N., Stramigioli, S., Vanderborght, B., Yesilevskiy, Y., and Tsagarakis, N. An overview on principles for energy efficient robot locomotion. *Frontiers in Robotics and AI*, 5:129, 2018. doi:10.3389/frobt.2018.00129.

Kim, S. and Wensing, P. M. Design of dynamic legged robots. *Foundations and Trends® in Robotics*, 5 (2):117–190, 2017. doi:10.1561/2300000044.

Kirsch, R., Boskov, D., and Rymer, W. Muscle stiffness during transient and continuous movements of cat muscle: perturbation characteristics and physiological relevance. *IEEE Transactions on Biomedical Engineering*, 41(8):758–770, 1994. doi:10.1109/10.310091.

Kistemaker, D. A., Van Soest, A. J., and Bobbert, M. F. Is equilibrium point control feasible for fast goal-directed single-joint movements? *Journal of Neurophysiology*, 95(5):2898–2912, 2006. doi:10.1152/jn.00983.2005.

Klute, G. K., Czerniecki, J. M., and Hannaford, B. Artificial Muscles: Actuators for Biorobotic Systems. *The International Journal of Robotics Research*, 21(4):295–309, 2002. doi:10.1177/027836402320556331.

Kostamo, E., Focchi, M., Guglielmino, E., Kostamo, J., Semini, C., Buchli, J., Pietola, M., and Caldwell, D. Magnetorheologically Damped Compliant Foot for Legged Robotic Application. *Journal of Mechanical Design*, 136(2):021003, 2013. doi:10.1115/1.4025966.

Krylow, A. M. and Sandercock, T. G. Dynamic force responses of muscle involving eccentric contraction. *Journal of Biomechanics*, 30(1):27–33, 1997. doi:10.1016/S0021-9290(96)00097-8.

Laffranchi, M., Tsagarakis, N. G., and Caldwell, D. G. Variable physical damping actuators (vpdas): Facilitating the control and improving the performance of compliant actuation systems. In *2012 12th IEEE International Workshop on Advanced Motion Control (AMC)*, page 1–6, Sarajevo, Bosnia and Herzegovina, 2012. IEEE. ISBN 978-1-4577-1073-5. doi:10.1109/AMC.2012.6197013.

Lassmann, C., Ilg, W., Rattay, T. W., Schöls, L., Giese, M., and Haeufle, D. F. B. Dysfunctional neuro-muscular mechanisms explain gradual gait changes in prodromal spastic paraplegia. *Journal of NeuroEngineering and Rehabilitation*, 20(1):90, 2023.

Lay, A. N., Hass, C. J., Richard Nichols, T., and Gregor, R. J. The effects of sloped surfaces on locomotion: An electromyographic analysis. *Journal of Biomechanics*, 40(6):1276–1285, 2007. doi:10.1016/j.jbiomech.2006.05.023.

Lee, S. S., Arnold, A. S., Miara, M., Biewener, A. A., and Wakeling, J. M. Accuracy of gastrocnemius muscles forces in walking and running goats predicted by one-element and two-element Hill-type models. *Journal of Biomechanics*, 46(13):2288–2295, 2013. doi:10.1016/j.jbiomech.2013.06.001.

Levin, A., Wyman, J., and Hill, A. V. The viscous elastic properties of muscle. *Proceedings of the Royal Society of London. Series B, Containing Papers of a Biological Character*, 101(709):218–243, 1927. doi:10.1098/rspb.1927.0014.

Linari, M., Caremani, M., Piperio, C., Brandt, P., and Lombardi, V. Stiffness and fraction of myosin motors responsible for active force in permeabilized muscle fibers from rabbit psoas. *Biophysical Journal*, 92(7):2476–2490, 2007. doi:10.1529/biophysj.106.099549.

Loeb, G. E., Brown, I. E., and Cheng, E. J. A hierarchical foundation for models of sensorimotor control. *Experimental Brain Research*, 126(1):1–18, 1999. doi:10.1007/s002210050712.

Loeb, G. Control implications of musculoskeletal mechanics. In *Proceedings of 17th International Conference of the Engineering in Medicine and Biology Society*, volume 2, pages 1393–1394, Montreal, Que., Canada, 1995. IEEE. ISBN 0-7803-2475-7. doi:10.1109/IEMBS.1995.579743.

Loeb, G. E. Neural control of locomotion. *BioScience*, 39(11):800–804, 1989. doi:10.2307/1311186.

Lännergren, J. The force—velocity relation of isolated twitch and slow muscle fibres of xenopus laevis. *The Journal of Physiology*, 283(1):501–521, 1978. doi:10.1113/jphysiol.1978.sp012516.

Manoonpong, P., Geng, T., Kulvicius, T., Porr, B., and Wörgötter, F. Adaptive, fast walking in a biped robot under neuronal control and learning. *PLOS Computational Biology*, 3(7):e134, 2007. doi:10.1371/journal.pcbi.0030134.

McGeer, T. Passive dynamic walking. *The International Journal of Robotics Research*, 9(2):62–82, 1990. doi:10.1177/027836499000900206.

Metzger, J. M. and Moss, R. L. Calcium-sensitive cross-bridge transitions in mammalian fast and slow skeletal muscle fibers. *Science*, 247(4946):1088–1090, 1990. doi:10.1126/science.2309121.

Millard, M., Uchida, T., Seth, A., and Delp, S. L. Flexing Computational Muscle: Modeling and Simulation of Musculotendon Dynamics. *Journal of Biomechanical Engineering*, 135(2):021005, 2013. doi:10.1115/1.4023390.

Millard, M., Franklin, D. W., and Herzog, W. A three filament mechanistic model of musculotendon force and impedance. *bioRxiv preprint 2023.03.27.534347*, 2023. doi:10.1101/2023.03.27.534347.

Mo, A., Izzi, F., Haeufle, D. F. B., and Badri-Spröwitz, A. Effective Viscous Damping Enables Morphological Computation in Legged Locomotion. *Frontiers in Robotics and AI*, 7:110, 2020. doi:10.3389/frobt.2020.00110.

Mo, A., Izzi, F., Gönen, E. C., Haeufle, D., and Badri-Spröwitz, A. Slack-based tunable damping leads to a trade-off between robustness and efficiency in legged locomotion. *Scientific Reports*, 13(1):3290, 2023. doi:10.1038/s41598-023-30318-3.

Mochon, S. and McMahon, T. A. Ballistic walking: An improved model. *Mathematical Biosciences*, 52 (3-4):241–260, 1980. doi:https://doi.org/10.1016/0025-5564(80)90070-X.

Monteleone, S., Negrello, F., Catalano, M. G., Garabini, M., and Grioli, G. Damping in Compliant Actuation: A Review. *IEEE Robotics & Automation Magazine*, 29(3):47–66, 2022. doi:10.1109/MRA.2021.3138388.

Montgomery, J. R. and Grabowski, A. M. The contributions of ankle, knee and hip joint work to individual leg work change during uphill and downhill walking over a range of speeds. *Royal Society Open Science*, 5(8):180550, 2018. doi:10.1098/rsos.180550.

More, H. L., Hutchinson, J. R., Collins, D. F., Weber, D. J., Aung, S. K. H., and Donelan, J. M. Scaling of Sensorimotor Control in Terrestrial Mammals. *Proceedings of the Royal Society B: Biological Sciences*, 277(1700):3563–3568, 2010. doi:10.1098/rspb.2010.0898.

More, H. L. and Donelan, J. M. Scaling of sensorimotor delays in terrestrial mammals. *Proceedings of the Royal Society B: Biological Sciences*, 285(1885):20180613, 2018. doi:10.1098/rspb.2018.0613.

Moritz, C. T. and Farley, C. T. Passive dynamics change leg mechanics for an unexpected surface during human hopping. *Journal of Applied Physiology*, 97(4):1313–1322, 2004. doi:10.1152/japplphysiol.00393.2004.

Mörl, F., Siebert, T., and Häufle, D. Contraction dynamics and function of the muscle-tendon complex depend on the muscle fibre-tendon length ratio: a simulation study. *Biomechanics and Modeling in Mechanobiology*, 15(1):245–258, 2016. doi:10.1007/s10237-015-0688-7.

Mugge, W., Munts, A. G., Schouten, A. C., and van der Helm, F. C. Modeling movement disorders—crps-related dystonia explained by abnormal proprioceptive reflexes. *Journal of Biomechanics*, 45(1): 90–98, 2012. doi:10.1016/j.jbiomech.2011.09.024.

Mörl, F., Siebert, T., Schmitt, S., Blickhan, R., and Guenther, M. Electro-mechanical delay in Hill-type muscle models. *Journal of Mechanics in Medicine and Biology*, 12(05):1250085, 2012. doi:10.1142/s0219519412500856.

Müller, R., Tschiesche, K., and Blickhan, R. Kinetic and kinematic adjustments during perturbed walking across visible and camouflaged drops in ground level. *Journal of Biomechanics*, 47(10): 2286–2291, 2014. doi:10.1016/j.jbiomech.2014.04.041.

Müller, R., Siebert, T., and Blickhan, R. Muscle Preactivation Control: Simulation of Ankle Joint Adjustments at Touchdown During Running on Uneven Ground. *Journal of Applied Biomechanics*, 28(6):718–725, 2012. doi:10.1123/jab.28.6.718.

Müller, R., Häufle, D. F. B., and Blickhan, R. Preparing the leg for ground contact in running: the contribution of feed-forward and visual feedback. *Journal of Experimental Biology*, 218(3):451–457, 2015. doi:10.1242/jeb.113688.

Müller, R., Vielemeyer, J., and Häufle, D. F. Negotiating ground level perturbations in walking: Visual perception and expectation of curb height modulate muscle activity. *Journal of Biomechanics*, 113: 110121, 2020. doi:10.1016/j.jbiomech.2020.110121.

Narwade, P., Deshmukh, R., Nagarkar, M., and Sukhwani, V. Improvement of Ride Comfort in a Passenger Car Using Magneto Rheological (MR) Damper. *Journal of Vibration Engineering & Technologies*, 10(7):2669–2676, 2022. doi:10.1007/s42417-022-00512-0.

Nichols, T. R. and Houk, J. C. Improvement in linearity and regulation of stiffness that results from actions of stretch reflex. *Journal of Neurophysiology*, 39(1):119–142, 1976. doi:10.1152/jn.1976.39.1.119.

Nishikawa, K., Biewener, A. A., Aerts, P., Ahn, A. N., Chiel, H. J., Daley, M. A., Daniel, T. L., Full, R. J., Hale, M. E., Hedrick, T. L., Lappin, A. K., Nichols, T. R., Quinn, R. D., Satterlie, R. A., and Szymik, B. Neuromechanics: An integrative approach for understanding motor control. *Integrative and Comparative Biology*, 47(1):16–54, 2007. doi:10.1093/icb/icm024.

Owaki, D. and Ishiguro, A. A quadruped robot exhibiting spontaneous gait transitions from walking to trotting to galloping. *Scientific Reports*, 7(1):277, 2017. doi:10.1038/s41598-017-00348-9.

Owaki, D., Kano, T., Nagasawa, K., Tero, A., and Ishiguro, A. Simple robot suggests physical interlimb communication is essential for quadruped walking. *Journal of The Royal Society Interface*, 10(78): 20120669, 2013. doi:10.1098/rsif.2012.0669.

Patla, A. Strategies for dynamic stability during adaptive human locomotion. *IEEE Engineering in Medicine and Biology Magazine*, 22(2):48–52, 2003. doi:10.1109/MEMB.2003.1195695.

Petrič, T., Peternel, L., Morimoto, J., and Babič, J. Assistive arm-exoskeleton control based on human muscular manipulability. *Frontiers in Neurorobotics*, 13:30, 2019. doi:10.3389/fnbot.2019.00030.

Pfeifer, R. and Bongard, J. *How the body shapes the way we think: a new view of intelligence*. The MIT Press, Cambridge, MA, 2007. ISBN 9780262537421. url: https://mitpress.mit.edu/9780262537421/how-the-body-shapes-the-way-we-think.

Pfeifer, R., Blumberg, B., Meyer, J.-A., and Wilson, S. W. Bisam: From small mammals to a four-legged walking machine. In *From Animals to Animats 5: Proceedings of the Fifth International Conference on Simulation of Adaptive Behavior*, pages 400–407. MIT Press, 1998. ISBN 9780262291385. doi:10.7551/mitpress/3119.001.0001.

Pinniger, G. J., Ranatunga, K. W., and Offer, G. W. Crossbridge and non-crossbridge contributions to tension in lengthening rat muscle: Force-induced reversal of the power stroke. *Journal of Physiology*, 573(3):627–643, 2006. doi:10.1113/jphysiol.2005.095448.

Qiao, M. and Jindrich, D. L. Leg joint function during walking acceleration and deceleration. *Journal of Biomechanics*, 49(1):66–72, 2016. doi:10.1016/j.jbiomech.2015.11.022.

Rack, P. M. H. and Westbury, D. R. The short range stiffness of active mammalian muscle and its effect on mechanical properties. *The Journal of Physiology*, 240(2):331–350, 1974. doi:10.1113/jphysiol.1974.sp010613.

Raibert, M. *Legged Robots that Balance*. Artificial Intelligence Series. MIT Press, Cambridge, MA, 2000. ISBN 978-0-262-68119-3. url: https://mitpress.mit.edu/9780262681193/legged-robots-that-balance.

Ranatunga, K. W. Temperature-dependence of shortening velocity and rate of isometric tension development in rat skeletal muscle. *The Journal of Physiology*, 329(1):465–483, 1982. doi:10.1113/jphysiol.1982.sp014314.

Ranatunga, K. W. The force-velocity relation of rat fast- and slow-twitch muscles examined at different temperatures. *The Journal of Physiology*, 351(1):517–529, 1984. doi:10.1113/jphysiol.1984.sp015260.

Rijkelijkhuizen, J. M., de Ruiter, C. J., Huijing, P. A., and de Haan, A. Force/velocity curves of fast oxidative and fast glycolytic parts of rat medial gastrocnemius muscle vary for concentric but not eccentric activity. *Pflügers Archiv*, 446(4):497–503, 2003. doi:10.1007/s00424-003-1052-9.

Roberts, S. and Koditschek, D. E. Mitigating energy loss in a robot hopping on a physically emulated dissipative substrate. In *2019 International Conference on Robotics and Automation (ICRA)*, pages 6763–6769, Montreal, QC, Canada, 2019. IEEE. doi:10.1109/ICRA.2019.8793781.

Roberts, T. J. and Azizi, E. The series-elastic shock absorber: tendons attenuate muscle power during eccentric actions. *Journal of Applied Physiology*, 109(2):396–404, 2010. doi:10.1152/japplphysiol.01272.2009.

Roberts, T. J. and Azizi, E. Flexible mechanisms: the diverse roles of biological springs in vertebrate movement. *Journal of Experimental Biology*, 214(3):353–361, 2011. doi:10.1242/jeb.038588.

Robertson, B. D. and Sawicki, G. S. Exploiting elasticity: Modeling the influence of neural control on mechanics and energetics of ankle muscle-tendons during human hopping. *Journal of Theoretical Biology*, 353:121–132, 2014. doi:10.1016/j.jtbi.2014.03.010.

Robi, K., Jakob, N., Matevz, K., and Matjaz, V. The physiology of sports injuries and repair processes. In Hamlin, M., Draper, N., and Kathiravel, Y., editors, *Current Issues in Sports and Exercise Medicine*, pages 43–86, Rijeka, 2013. IntechOpen. ISBN 978-953-51-1031-6. doi:10.5772/54234.

Rockenfeller, R., Günther, M., Schmitt, S., and Götz, T. Comparative Sensitivity Analysis of Muscle Activation Dynamics. *Computational and Mathematical Methods in Medicine*, 2015:1–16, 2015. doi:10.1155/2015/585409.

Rode, C. and Siebert, T. Muscle-like actuation for locomotion. In Maziar, A. S. and Seyfarth, A., editors, *Bioinspired Legged Locomotion*, pages 565–590. Butterworth-Heinemann, 2017. ISBN 978-0-12-803766-9. doi:10.1016/B978-0-12-803766-9.00011-7.

Rosenfeld, E. V. and Günther, M. An enhanced model of cross-bridge operation with internal elasticity. *European Biophysics Journal*, 43(4):131–141, 2014. doi:10.1007/s00249-014-0947-z.

Rummel, J. and Seyfarth, A. Stable Running with Segmented Legs. *The International Journal of Robotics Research*, 27(8):919–934, 2008. doi:10.1177/0278364908095136.

Ruppert, F. and Badri-Spröwitz, A. Series Elastic Behavior of Biarticular Muscle-Tendon Structure in a Robotic Leg. *Frontiers in Neurorobotics*, 13:64, 2019. doi:10.3389/fnbot.2019.00064.

Ruppert, F., Aghamaleki Sarvestani, A., Heim, S., Mo, A., and Badri-Spröwitz, A. Instrumented boom, CAD data, 2022. doi:10.17617/3.RSO2AG, Edmond, V1.

Ryu, H. X. and Kuo, A. D. An optimality principle for locomotor central pattern generators. *Scientific Reports*, 11(1):13140, 2021. doi:10.1038/s41598-021-91714-1.

Schreff, L., Haeufle, D. F. B., Vielemeyer, J., and Müller, R. Evaluating anticipatory control strategies for their capability to cope with step-down perturbations in computer simulations of human walking. *Scientific Reports*, 12(1):10075, 2022.

Secer, G. and Saranli, U. Control of monopedal running through tunable damping. In *2013 21st Signal Processing and Communications Applications Conference (SIU)*, pages 1–4, Haspolat, Turkey, 2013. IEEE. ISBN 978-1-4673-5563-6. doi:10.1109/SIU.2013.6531557.

Seipel, J. and Holmes, P. A simple model for clock-actuated legged locomotion. *Regular and Chaotic Dynamics*, 12(5):502–520, 2007. doi:10.1134/S1560354707050048.

Seok, S., Wang, A., Chuah, M. Y. M., Hyun, D. J., Lee, J., Otten, D. M., Lang, J. H., and Kim, S. Design principles for energy-efficient legged locomotion and implementation on the MIT cheetah robot. *IEEE/ASME Transactions on Mechatronics*, 20(3):1117–1129, 2015. doi:10.1109/TMECH.2014.2339013.

Serafin, S. *The sound of friction: real time models, playability and musical applications*. Thesis (Ph.D.), Stanford University, California, 2004. ISBN 9780496757350. url: `https://ui.adsabs.harvard.edu/abs/2004PhDT.....89S`.

Shen, Z. and Seipel, J. A fundamental mechanism of legged locomotion with hip torque and leg damping. *Bioinspiration & biomimetics*, 7(4):046010, 2012. doi:10.1088/1748-3182/7/4/046010.

Siebert, T. and Rode, C. 6 - computational modeling of muscle biomechanics. In Jin, Z., editor, *Computational Modelling of Biomechanics and Biotribology in the Musculoskeletal System*, pages 173–204. Woodhead Publishing, 2014. ISBN 978-0-85709-661-6. doi:10.1533/9780857096739.2.173.

Siebert, T., Screen, H. R., and Rode, C. 8 - computational modelling of muscle, tendon, and ligaments biomechanics. In Jin, Z., Li, J., and Chen, Z., editors, *Computational Modelling of Biomechanics and Biotribology in the Musculoskeletal System (Second Edition)*, pages 155–186. Woodhead Publishing, 2021. ISBN 978-0-12-819531-4. doi:10.1016/B978-0-12-819531-4.00008-0.

Song, S. and Geyer, H. Evaluation of a Neuromechanical Walking Control Model Using Disturbance Experiments. *Frontiers in Computational Neuroscience*, 11:15, 2017. doi:10.3389/fncom.2017.00015.

Song, S. and Geyer, H. Predictive neuromechanical simulations indicate why walking performance declines with ageing. *The Journal of Physiology*, 596(7):1199–1210, 2018. doi:10.1113/JP275166.

Spröwitz, A., Tuleu, A., Vespignani, M., Ajallooeian, M., Badri, E., and Ijspeert, A. J. Towards dynamic trot gait locomotion: Design, control, and experiments with cheetah-cub, a compliant quadruped robot. *The International Journal of Robotics Research*, 32(8):932–950, 2013. doi:10.1177/0278364913489205.

Stephenson, D. G. Relationship between isometric force and myofibrillar MgATPase at short sarcomere length in skeletal and cardiac muscle and its relevance to the concept of activation heat. *Clinical and Experimental Pharmacology and Physiology*, 30(8):570–575, 2003. doi:10.1046/j.1440-1681.2003.03881.x.

Stephenson, D. G. and Williams, D. A. Effects of sarcomere length on the force-pCa relation in fast- and slow-twitch skinned muscle fibres from the rat. *The Journal of Physiology*, 333(1):637–653, 1982. doi:10.1113/jphysiol.1982.sp014473.

Stephenson, D. and Williams, D. Temperature-dependent calcium sensitivity changes in skinned muscle fibres of rat and toad. *The Journal of physiology*, 360(1):1–12, 1985. doi:https://doi.org/10.1113/jphysiol.1985.sp015600.

Stienen, G. J., Versteeg, P. G., Papp, Z., and Elzinga, G. Mechanical properties of skinned rabbit psoas and soleus muscle fibres during lengthening: effects of phosphate and Ca2+. *The Journal of Physiology*, 451(1):503–523, 1992. doi:10.1113/jphysiol.1992.sp019176.

Stollenmaier, K., Ilg, W., and Haeufle, D. F. B. Predicting perturbed human arm movements in a neuro-musculoskeletal model to investigate the muscular force response. *Frontiers in Bioengineering and Biotechnology*, 8:308, 2020a. doi:10.3389/fbioe.2020.00308.

Stollenmaier, K., Rist, I. S., Izzi, F., and Haeufle, D. F. Simulating the response of a neuro-musculoskeletal model to assistive forces: implications for the design of wearables compensating for motor control deficits. In *2020 8th IEEE RAS/EMBS International Conference for Biomedical Robotics and Biomechatronics (BioRob)*, pages 779–784, New York, NY, USA, 2020b. doi:10.1109/BioRob49111.2020.9224411.

Till, O., Siebert, T., Rode, C., and Blickhan, R. Characterization of isovelocity extension of activated muscle: A Hill-type model for eccentric contractions and a method for parameter determination. *Journal of Theoretical Biology*, 255(2):176–187, 2008. doi:10.1016/j.jtbi.2008.08.009.

Tomalka, A., Rode, C., Schumacher, J., and Siebert, T. The active force–length relationship is invisible during extensive eccentric contractions in skinned skeletal muscle fibres. *Proceedings of the Royal Society B: Biological Sciences*, 284(1854):20162497, 2017. doi:10.1098/rspb.2016.2497.

Tomalka, A., Weidner, S., Hahn, D., Seiberl, W., and Siebert, T. Cross-Bridges and Sarcomeric Non-cross-bridge Structures Contribute to Increased Work in Stretch-Shortening Cycles. *Frontiers in Physiology*, 11:921, 2020. doi:10.3389/fphys.2020.00921.

Tomalka, A., Weidner, S., Hahn, D., Seiberl, W., and Siebert, T. Power Amplification Increases With Contraction Velocity During Stretch-Shortening Cycles of Skinned Muscle Fibers. *Frontiers in physiology*, 12:644981, 2021. doi:10.3389/fphys.2021.644981.

Tsagarakis, N. G., Morfey, S., Dallali, H., Medrano-Cerda, G. A., and Caldwell, D. G. An asymmetric compliant antagonistic joint design for high performance mobility. In *2013 IEEE/RSJ International Conference on Intelligent Robots and Systems*, pages 5512–5517, Tokyo, Japan, 2013. IEEE. doi:10.1109/IROS.2013.6697155.

Tucker, V. A. The energetic cost of moving about: walking and running are extremely inefficient forms of locomotion. much greater efficiency is achieved by birds, fish—and bicyclists. *American Scientist*, 63(4):413–419, 1975. url: http://www.jstor.org/stable/27845576.

Unsal, M., Niezrecki, C., and Crane, C. Two semi-active approaches for vibration isolation: piezoelectric friction damper and magnetorheological damper. *Proceedings of the IEEE International Conference on Mechatronics, 2004. ICM '04.*, page 60–65, 2004. doi:10.1109/ICMECH.2004.1364413.

van der Kooij, H., Koopman, B., and van der Helm, F. C. Human motion control, 2008. Online Reader for TU Delft, accessed 27-Oct-2023. url: http://stiff-project.eu/fileadmin/biomechanics/HMC_Reader.pdf.

van der Krogt, M. M., de Graaf, W. W., Farley, C. T., Moritz, C. T., Richard Casius, L. J., and Bobbert, M. F. Robust passive dynamics of the musculoskeletal system compensate for unexpected surface changes during human hopping. *Journal of Applied Physiology*, 107(3):801–808, 2009. doi:10.1152/japplphysiol.91189.2008.

van Soest, A. J. and Bobbert, M. F. The contribution of muscle properties in the control of explosive movements. *Biological Cybernetics*, 69(3):195–204, 1993. doi:10.1007/BF00198959.

Vanderborght, B., Albu-Schaeffer, A., Bicchi, A., Burdet, E., Caldwell, D., Carloni, R., Catalano, M., Eiberger, O., Friedl, W., Ganesh, G., Garabini, M., Grebenstein, M., Grioli, G., Haddadin, S., Hoppner, H., Jafari, A., Laffranchi, M., Lefeber, D., Petit, F., Stramigioli, S., Tsagarakis, N., Van Damme, M., Van Ham, R., Visser, L., and Wolf, S. Variable impedance actuators: A review. *Robotics and autonomous systems*, 61(12):1601–1614, 2013. doi:10.1016/j.robot.2013.06.009.

Wagner, H. and Blickhan, R. Stabilizing function of skeletal muscles: an analytical investigation. *Journal of Theoretical Biology*, 199(2):163–179, 1999. doi:10.1006/jtbi.1999.0949.

Wahr, P. A. and Rall, J. A. Role of calcium and cross bridges in determining rate of force development in frog muscle fibers. *American Journal of Physiology-Cell Physiology*, 272(5):C1664–C1671, 1997. doi:10.1152/ajpcell.1997.272.5.C1664.

Walter, R. M. and Carrier, D. R. Ground forces applied by galloping dogs. *Journal of Experimental Biology*, 210(2):208–216, 2007. doi:10.1242/jeb.02645.

Webb, B. Can robots make good models of biological behaviour? *Behavioral and Brain Sciences*, 24 (6):1033–1050, 2001. doi:10.1017/S0140525X01000127.

Weidner, S., Tomalka, A., Rode, C., and Siebert, T. How velocity impacts eccentric force generation of fully activated skinned skeletal muscle fibers in long stretches. *Journal of Applied Physiology*, 113(1): 223–233, 2022. doi:10.1152/japplphysiol.00735.2021.

Werner, A., Turlej, W., and Ott, C. Generation of Locomotion Trajectories for Series Elastic and Viscoelastic Bipedal Robots. In *2017 IEEE/RSJ International Conference on Intelligent Robots and Systems (IROS)*, pages 5853–5860, Vancouver, BC, Canada, 2017. IEEE. doi:10.1109/IROS.2017.8206476.

Whitney, J. P., Glisson, M. F., Brockmeyer, E. L., and Hodgins, J. K. A low-friction passive fluid transmission and fluid-tendon soft actuator. In *2014 IEEE/RSJ International Conference on Intelligent Robots and Systems*, pages 2801–2808, Chicago, IL, USA, 2014. IEEE. doi:10.1109/IROS.2014.6942946.

Whitney, J. P., Chen, T., Mars, J., and Hodgins, J. K. A hybrid hydrostatic transmission and human-safe haptic telepresence robot. In *2016 IEEE International Conference on Robotics and Automation (ICRA)*, pages 690–695, Stockholm, Sweden, 2016. IEEE. doi:10.1109/ICRA.2016.7487195.

Wilson, A. M., McGuigan, M. P., Su, A., and Van den Bogert, A. J. Horses damp the spring in their step. *Nature*, 414(6866):895–899, 2001. doi:10.1038/414895a.

Winter, D. *Biomechanics and Motor Control of Human Movement*. John Wiley, Hoboken, N.J., 2009. ISBN 9780470398180. doi:10.1002/9780470549148.

Winters, J. M. and Stark, L. Muscle models: What is gained and what is lost by varying model complexity. *Biological Cybernetics*, 55(6):403–420, 1987. doi:10.1007/BF00318375.

Wu, A. and Geyer, H. The 3-D spring–mass model reveals a time-based deadbeat control for highly robust running and steering in uncertain environments. *IEEE Transactions on Robotics*, 29(5): 1114–1124, 2013. doi:10.1109/TRO.2013.2263718.

Xiong, X. and Manoonpong, P. Adaptive motor control for human-like spatial-temporal adaptation. In *2018 IEEE International Conference on Robotics and Biomimetics (ROBIO)*, pages 2107–2112, Kuala Lumpur, Malaysia, 2018. IEEE. doi:10.1109/ROBIO.2018.8665222.

Zahedi, K. and Ay, N. Quantifying morphological computation. *Entropy*, 15(5):1887–1915, 2013. doi:10.3390/e15051887.

Zhang, L., Liu, Y., Wang, R., Smith, C., and Gutierrez-Farewik, E. M. Modeling and simulation of a human knee exoskeleton's assistive strategies and interaction. *Frontiers in Neurorobotics*, 15:620928, 2021. doi:10.3389/fnbot.2021.620928.

Zhang, S., Bates, B., and Dufek, J. Contributions of lower extremity joints to energy dissipation during landings. *Medicine & Science in Sports & Exercise*, 32(4):812–819, 2000. doi:10.1097/00005768-200004000-00014.

Zhao, G., Mohseni, O., Murcia, M., Seyfarth, A., and Sharbafi, M. A. Exploring the effects of serial and parallel elasticity on a hopping robot. *Frontiers in Neurorobotics*, 16:919830, 2022. doi:10.3389/fnbot.2022.919830.

Zhao, Y. and Kawai, M. Kinetic and thermodynamic studies of the cross-bridge cycle in rabbit psoas muscle fibers. *Biophysical journal*, 67(4):1655–1668, 1994. doi:10.1016/S0006-3495(94)80638-1.

Zhou, X. and Bi, S. A survey of bio-inspired compliant legged robot designs. *Bioinspiration & Biomimetics*, 7(4):041001, 2012. doi:10.1088/1748-3182/7/4/041001.

Appendix

A1 Supplementary Material - Chapters 4 and 5

This is the supplementary material for Chapters 4 and 5, with Chapter 4's material being previously published in (Izzi et al., 2023). Figures A1.1 to A1.5 belong to Chapter 4's study. Table A1.1 contains model parameters used for the computer simulations in both Chapters 4 and 5.

A1.1 Supplementary figures and tables

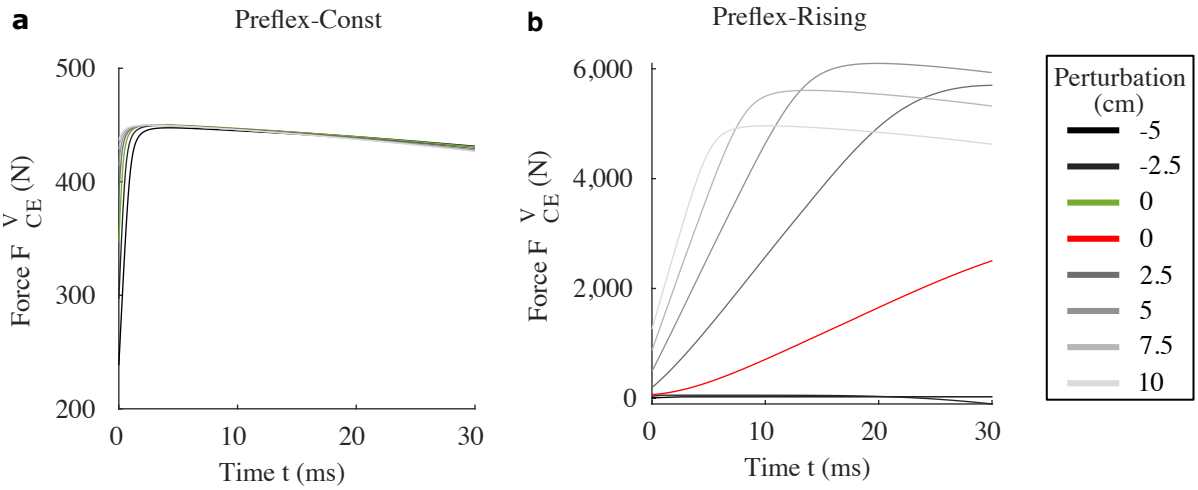

Figure A1.1: Time trajectories of the force component produced by the force-velocity relation (F^V_{CE}). Data plotted from touchdown ($t = 0ms$) to the end of the preflex duration ($t = 30ms$). (a) Preflex-Const, with reference hopping case in green; (b) Preflex-Rising, with reference hopping case in red. Figure from Izzi et al. (2023).

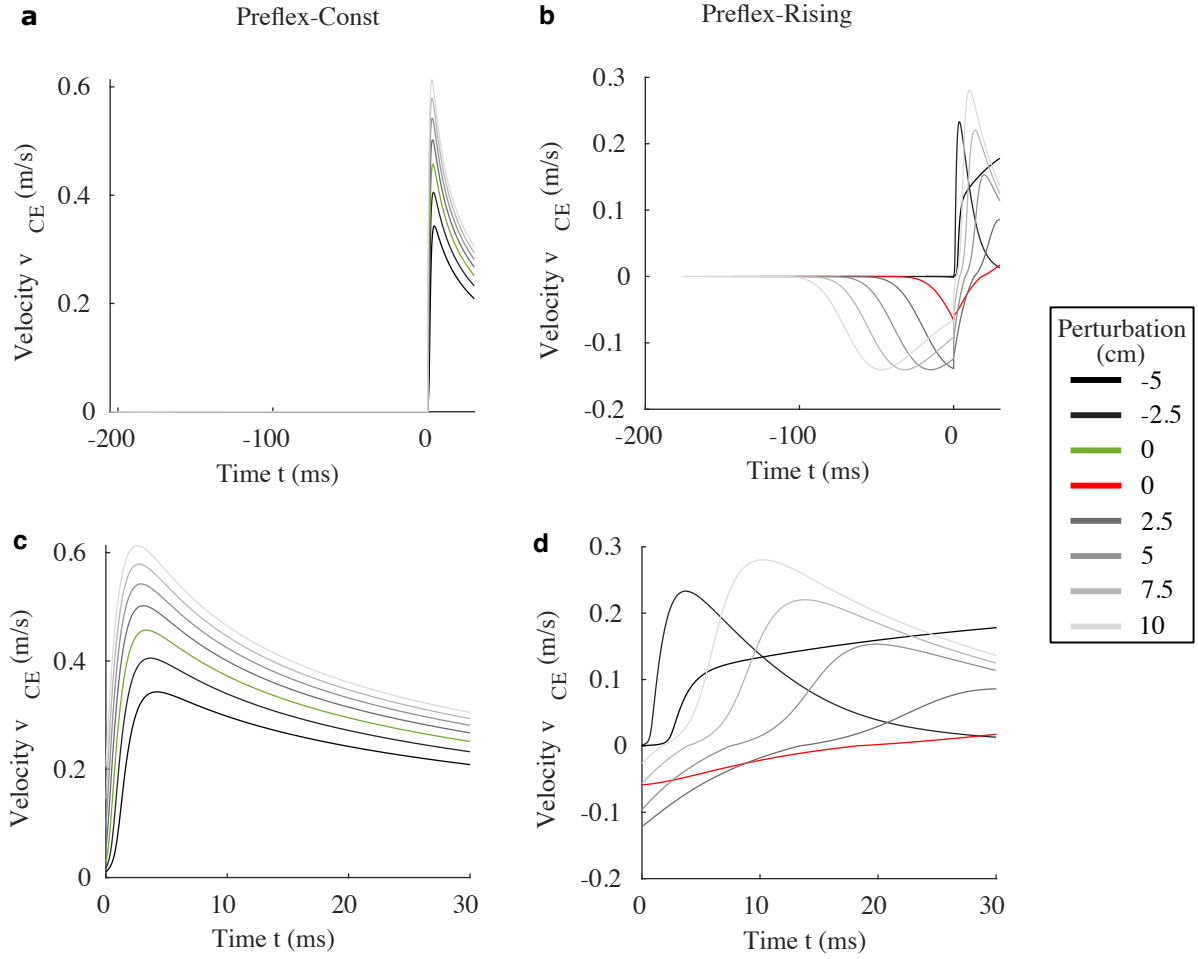

Figure A1.2: (a,b) Time trajectories of the muscle fiber velocity (v_{CE}). Data plotted from the start of the leg's vertical fall to the end of the preflex duration ($t = 30ms$). All dataset are centered to the touchdown event ($t = 0ms$). (c,d) Close up (touchdown to preflex end) of the time trajectories of the muscle fiber velocity (v_{CE}). (a,c) Preflex-Const, with reference hopping case in green; (b,d) Preflex-Rising, with reference hopping case in red. Figure from Izzi et al. (2023).

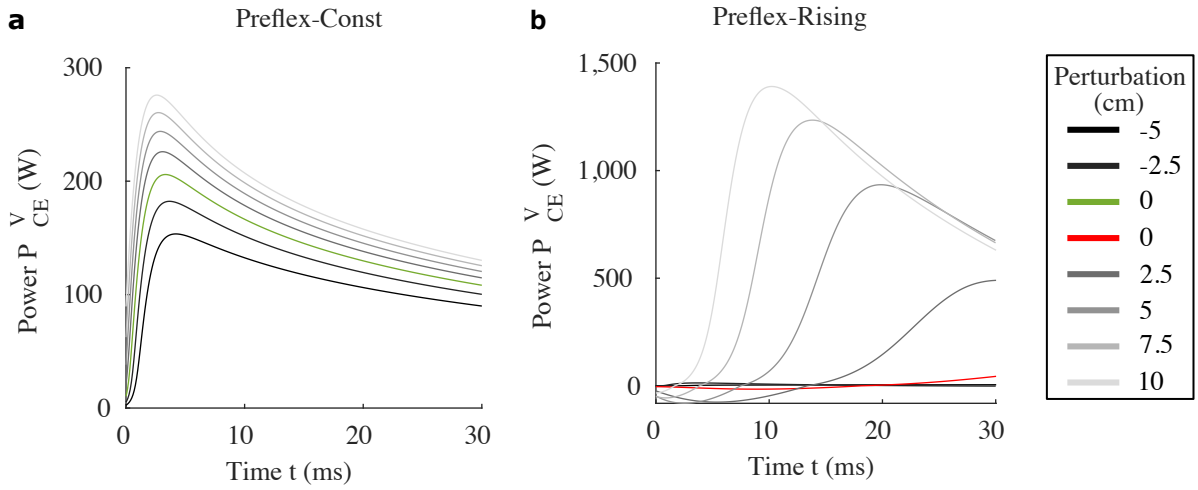

Figure A1.3: Time trajectories of the muscle fiber power component produced by the force-velocity relation ($P^V_{CE} = F^V_{CE} \cdot v_{CE}$). Data plotted from touchdown ($t = 0ms$) to the end of the preflex duration ($t = 30ms$). (a) Preflex-Const, with reference hopping case in green; (b) Preflex-Rising, with reference hopping case in red. Figure from Izzi et al. (2023).

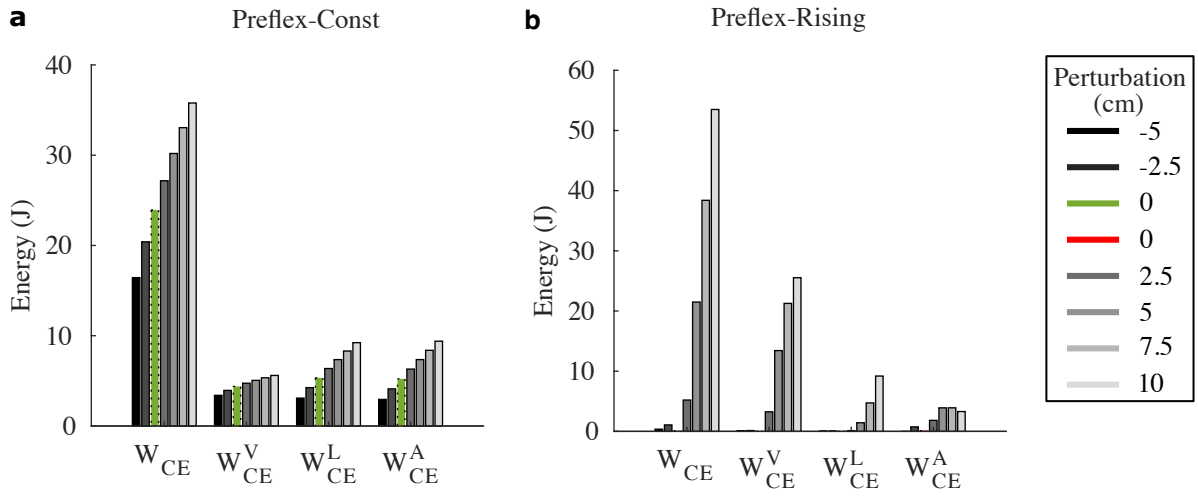

Figure A1.4: Work dissipated by the muscle fibers during the preflex phase. W_{CE} is the net dissipated work; W^V_{CE} is the work component dissipated by the force-velocity relation, W^L_{CE} by the force-length relation, and W^A_{CE} by the muscle activity. (a) Preflex-Const, with reference hopping case in green; (b) Preflex-Rising, with reference hopping case in red. Figure from Izzi et al. (2023).

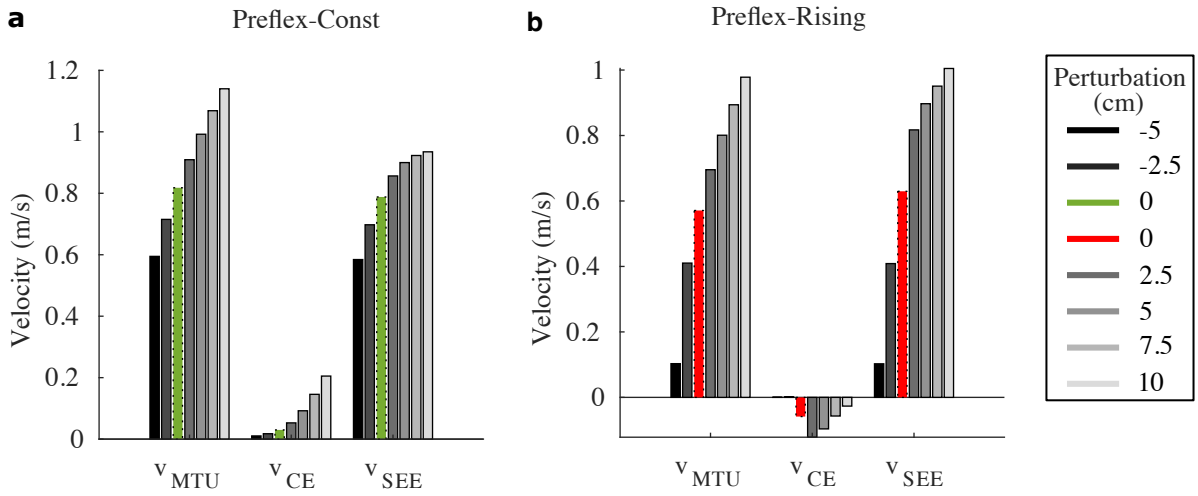

Figure A1.5: Touchdown values of muscle-tendon unit velocity (v_{MTU}), muscle fiber velocity (v_{CE}) and tendon fiber velocity (v_{SEE}). (a) Preflex-Const, with reference hopping case in green; (b) Preflex-Rising, with reference hopping case in red. Figure from Izzi et al. (2023).

Table A1.1: Table of supplementary parameters used in the muscle model and activation dynamics (Hatze). These parameters were used for computer simulations in both Chapters 4 and 5. Table from Izzi et al. (2023).

	Parameter	Unit	Value	Source	Description
MTU	$l_{MTU,ref}$	m	0.5	(Geyer et al., 2003)	muscle-tendon unit's reference length, alias l_{ref} in (Geyer et al., 2003)
CE	ΔW^{des}	[ ]	0.45	similar to (Bayer et al., 2017); (Kistemaker et al., 2006)	width of normalized bell curve in descending branch, adapted to match observed force-length curves
	ΔW^{asc}	[ ]	0.45	similar to (Bayer et al., 2017); (Kistemaker et al., 2006)	width of normalized bell curve in ascending branch, adapted to match observed force-length curves
	$\nu_{CE,des}$	[ ]	1.5	(Mörl et al., 2012)	exponent for descending branch of force-length relation
	$\nu_{CE,asc}$	[ ]	3.0	(Mörl et al., 2012)	exponent for ascending branch of force-length relation
	$A_{rel,0}$	[ ]	0.2	(Bayer et al., 2017)	parameter for contraction dynamics: maximum value of A_{rel}
	$B_{rel,0}$	1/s	2.0	(Bayer et al., 2017)	parameter for contraction dynamics: maximum value of B_{rel}
	$\mathscr{S}_{ecc}$	[ ]	2.0	(van Soest and Bobbert, 1993)	ratio of the derivatives of the force-velocity relation at the transition point ($v_{CE} = 0$ m/s)
	$\mathscr{F}_{ecc}$	[ ]	1.5	(van Soest and Bobbert, 1993)	factor by which the force can exceed F_{isom} for large eccentric velocities
PEE	$\mathscr{L}_{PEE,0}$	[ ]	0.95	(Bayer et al., 2017)	rest length of PEE normalized to optimal length of CE
	ν_{PEE}	[ ]	2.5	(Mörl et al., 2012)	exponent of F_{PEE}
	$\mathscr{F}_{PEE}$	[ ]	2.0	(Mörl et al., 2012)	force of PEE if l_{CE} is stretched to ΔW_{des}
SDE	D_{SDE}	[ ]	0.3	(Mörl et al., 2012)	dimensionless factor to scale $d_{SDE,max}$
	R_{SDE}	[ ]	0.01	(Mörl et al., 2012)	minimum value of d_{SDE} (at $F_{MTU} =$ 0N), normalized to $d_{SDE,max}$
SEE	$l_{SEE,0}$	m	0.4	(Geyer et al., 2003)	tendon's rest length, alias l_{rest} in (Geyer et al., 2003)
	$\Delta U_{SEE,nll}$	[ ]	0.0425	(Mörl et al., 2012)	relative stretch at nonlinear linear transition
	$\Delta U_{SEE,l}$	[ ]	0.017	(Mörl et al., 2012)	relative additional stretch in the linear part providing a force increase of $\Delta F_{SEE,0}$
	$\Delta F_{SEE,0}$	N	0.4 F_{max}	(Bayer et al., 2017)	both force at the transition and force increase in the linear part

Hatze	m	1/s	11.3	(Kistemaker et al., 2006)	inverse of time constant for the activation dynamics ($1/\tau$, τ defined in Table 4.1)
	c	mol/l	1.37e-4	(Kistemaker et al., 2006)	constant for the activation dynamics
	μ	l/mol	5.27e4	(Kistemaker et al., 2006)	constant for the activation dynamics
	k	[ ]	2.9	(Kistemaker et al., 2006)	constant for the activation dynamics
	a_0	[ ]	0.005	(Kistemaker et al., 2006)	resting active state for all activated muscle fibers
	ν	[ ]	3	(Kistemaker et al., 2006)	constant for the activation dynamics

A2 Supplementary Material - Chapter 6

This is Chapter 6's supplementary material, which is published in Araz et al. (2023).

A2.1 Supplementary figures and tables

Table A2.1. Parameters used in the leg-muscle model and activation dynamics (Hatze). Table from Araz et al. (2023).

	Parameter	Unit	Value	Source	Description
General	g	m/s^2	9.81	(Geyer et al., 2003)	gravitational constant
	ℓ_{f}	m	0.99	(Geyer et al., 2003)	assumed flight leg length
	ℓ_{s}	m	0.5	(Geyer et al., 2003)	segment length
	m	kg	80	(Geyer et al., 2003)	body weight
	r_a	m	0.04	(Geyer et al., 2003)	knee joint lever arm
	h_{ref}	cm	9.27		reference hopping height producing periodic hopping
MTU	$l_{MTU,ref}$	m	0.5	(Geyer et al., 2003)	muscle-tendon unit's reference length, alias l_{ref} in (Geyer et al., 2003)
	$F_{\max}$	kN	22	(Geyer et al., 2003)	maximum isometric force
CE	ℓ_{opt}	m	0.1	(Geyer et al., 2003)	optimum length contractile element
	ΔW^{des}	[ ]	0.45	similar to (Bayer et al., 2017); (Kistemaker et al., 2006)	width of the normalized bell curve in the descending branch, adapted to match observed force-length curves
	ΔW^{asc}	[ ]	0.4		width of the normalized bell curve in the ascending branch, adapted to match experimented isometric force-length curves
	$\nu_{CE,des}$	[ ]	1.5	(Mörl et al., 2012)	exponent for descending branch of force-length relation
	$\nu_{CE,asc}$	[ ]	3.8		exponent for ascending branch of force-length relation adapted to match experimented isometric force-length curves
	$A_{rel,0}$	[ ]	0.2	(Bayer et al., 2017)	parameter for contraction dynamics: maximum value of A_{rel}
	$B_{rel,0}$	1/s	2.0	(Bayer et al., 2017)	parameter for contraction dynamics: maximum value of B_{rel}
	$\mathscr{S}_{ecc}$	[ ]	2.0	(van Soest and Bobbert, 1993)	ratio of the derivatives of the force-velocity relation at the transition point ($v_{CE} = 0\,$m/s)

...

Continued on next page

Table A2.1 – *Continued from previous page*

	Parameter	Unit	Value	Source	Description
	$\mathscr{F}_{ecc}$	[ ]	1.5	(van Soest and Bobbert, 1993)	factor by which the force can exceed F_{isom} for large eccentric velocities
PEE	$\mathscr{L}_{PEE,0}$	[ ]	0.95	(Bayer et al., 2017)	rest length of PEE normalized to optimal length of CE
	ν_{PEE}	[ ]	2.5	(Mörl et al., 2012)	exponent of F_{PEE}
	$\mathscr{F}_{PEE}$	[ ]	2.0	(Mörl et al., 2012)	force of PEE if l_{CE} is stretched to ΔW_{des}
SDE	D_{SDE}	[ ]	0.3	(Mörl et al., 2012)	dimensionless factor to scale $d_{SDE,max}$
	R_{SDE}	[ ]	0.01	(Mörl et al., 2012)	minimum value of d_{SDE} (at $F_{MTU} = 0$N), normalized to $d_{SDE,max}$
SEE	$l_{SEE,0}$	m	0.4	(Geyer et al., 2003)	tendon's rest length, alias l_{rest} in (Geyer et al., 2003)
	$\Delta U_{SEE,nll}$	[ ]	0.0425	(Mörl et al., 2012)	relative stretch at nonlinear linear transition
	$\Delta U_{SEE,l}$	[ ]	0.017	(Mörl et al., 2012)	relative additional stretch in the linear part providing a force increase of $\Delta F_{SEE,0}$
	$\Delta F_{SEE,0}$	N	0.4 F_{max}	(Bayer et al., 2017)	both force at the transition and force increase in the linear part
Hatze	m	1/s	11.3	(Kistemaker et al., 2006)	inverse of time constant for the activation dynamics
	c	mol/l	1.37e-4	(Kistemaker et al., 2006)	constant for the activation dynamics
	μ	l/mol	5.27e4	(Kistemaker et al., 2006)	constant for the activation dynamics
	k	[ ]	2.9	(Kistemaker et al., 2006)	constant for the activation dynamics
	a_0	[ ]	0.005	(Kistemaker et al., 2006)	resting active state for all activated muscle fibers
	ν	[ ]	3	(Kistemaker et al., 2006)	constant for the activation dynamics

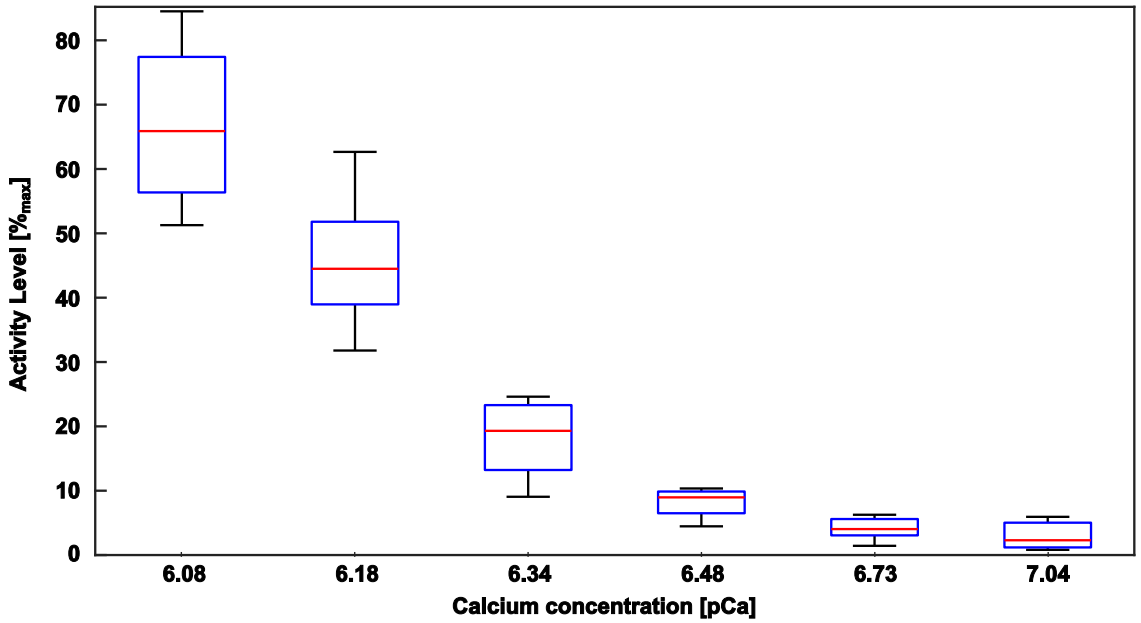

Figure A2.1: Measured activity level of skinned fibers (n=7) from the muscle used in the current study depending on the pCa of the experimental solution. Temperature while testing was 12 °C as in the perturbation experiment. Figure from Araz et al. (2023).

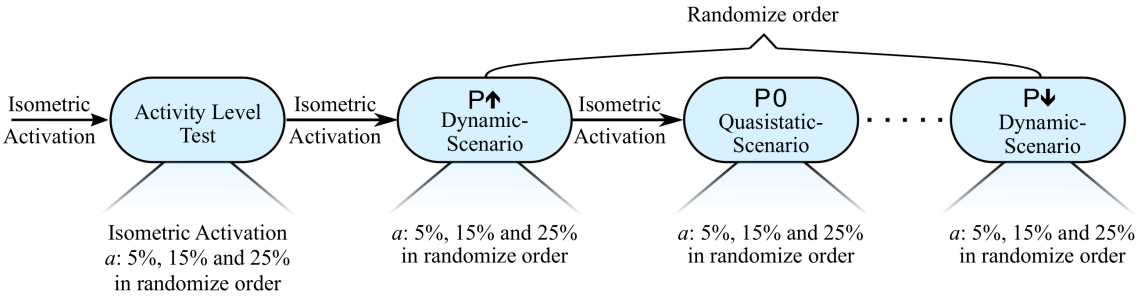

Figure A2.2: The Flow chart of an experimental day is shown here. First the activity level for every fiber was checked using the 6.73 , 6.34 and 6.3 pCa concentration solution to ensure that the experiment is matching the simulation condition. Afterwards the experimental blocks were conducted. One block contained all contractions (n=3) of a perturbation for one velocity-scenario. The order of the blocks were randomized on the day of the experiment. Between two blocks a reference contraction at optimal length and full activity was conducted to check for the degradation of the skinned fiber. Figure from Araz et al. (2023).

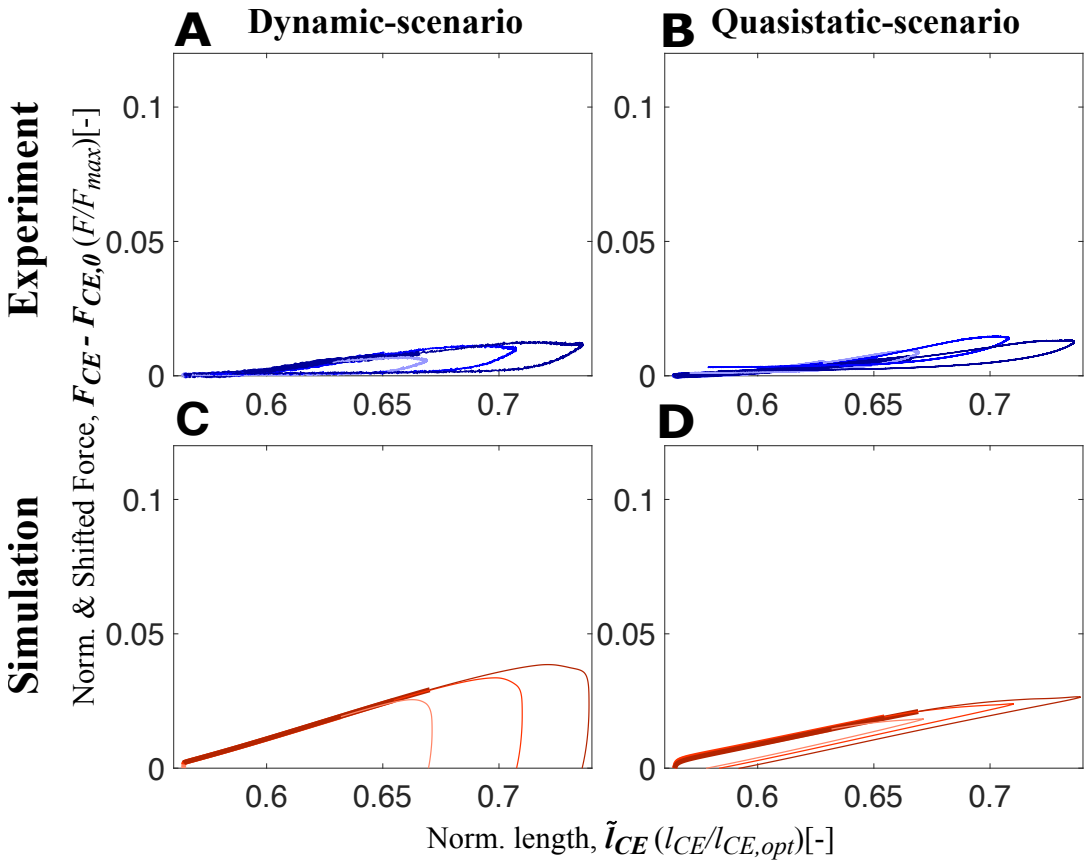

Figure A2.3: Shifted work loops for dynamic-scenario and quasistatic-scenario analysis step-up(P↑), no (P0) and step-down (P↓) perturbations for both experiments (**A-B**) and simulations (**C-D**) at 5 % activity level. The experimental data presented on **A** and **B** show the mean of all experimental trials. From touchdown to toe-off, all stretch-shortening cycle loops are plotted in the clockwise direction, and the thick and thin sections of the loops represent the preflex and remaining part of the stretch-shortening cycle, respectively. Figure from Araz et al. (2023).

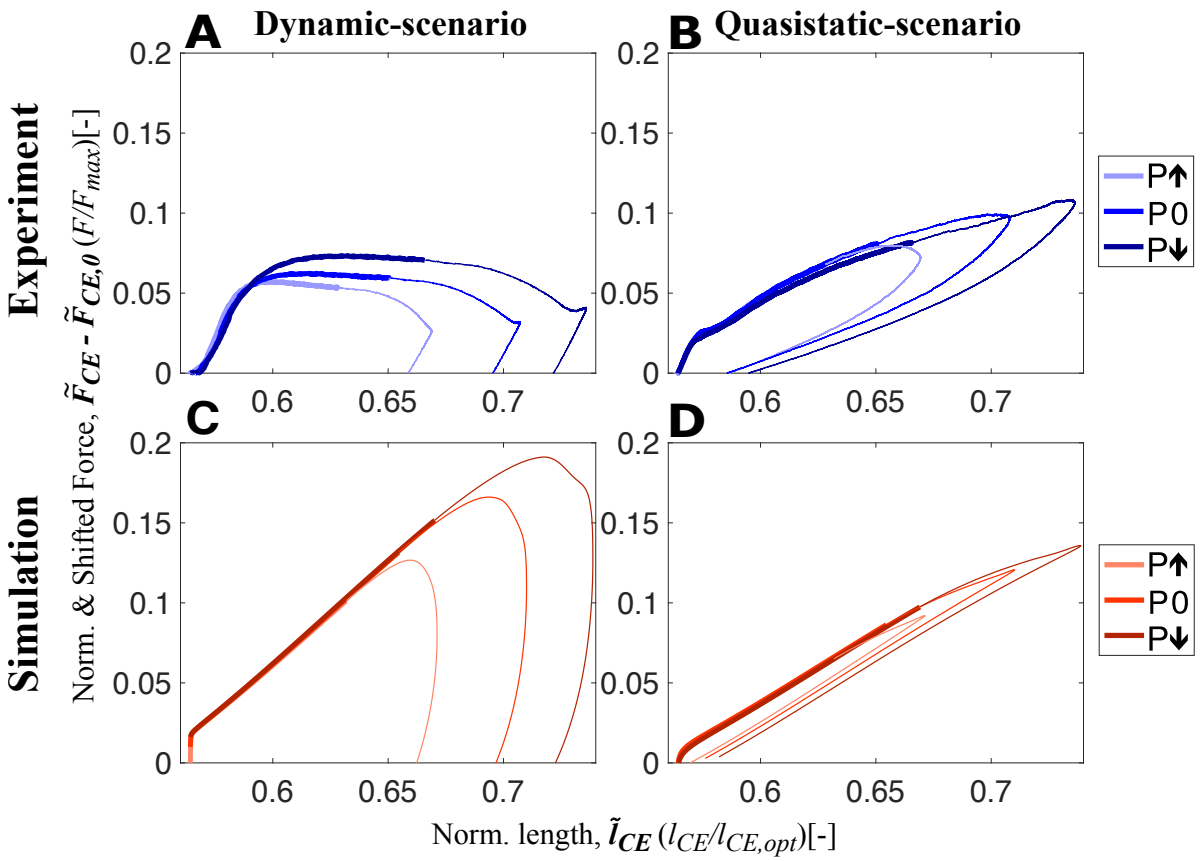

Figure A2.4: Shifted work loops for dynamic-scenario and quasistatic-scenario analysis step-up(P↑), no (P0) and step-down (P↓) perturbations for both experiments (**A-B**) and simulations (**C-D**) at 25 % activity level. The experimental data presented on **A** and **B** show the mean of all experimental trials. From touchdown to toe-off, all stretch-shortening cycle loops are plotted in the clockwise direction, and the thick and thin sections of the loops represent the preflex and remaining part of the stretch-shortening cycle, respectively. Figure from Araz et al. (2023).

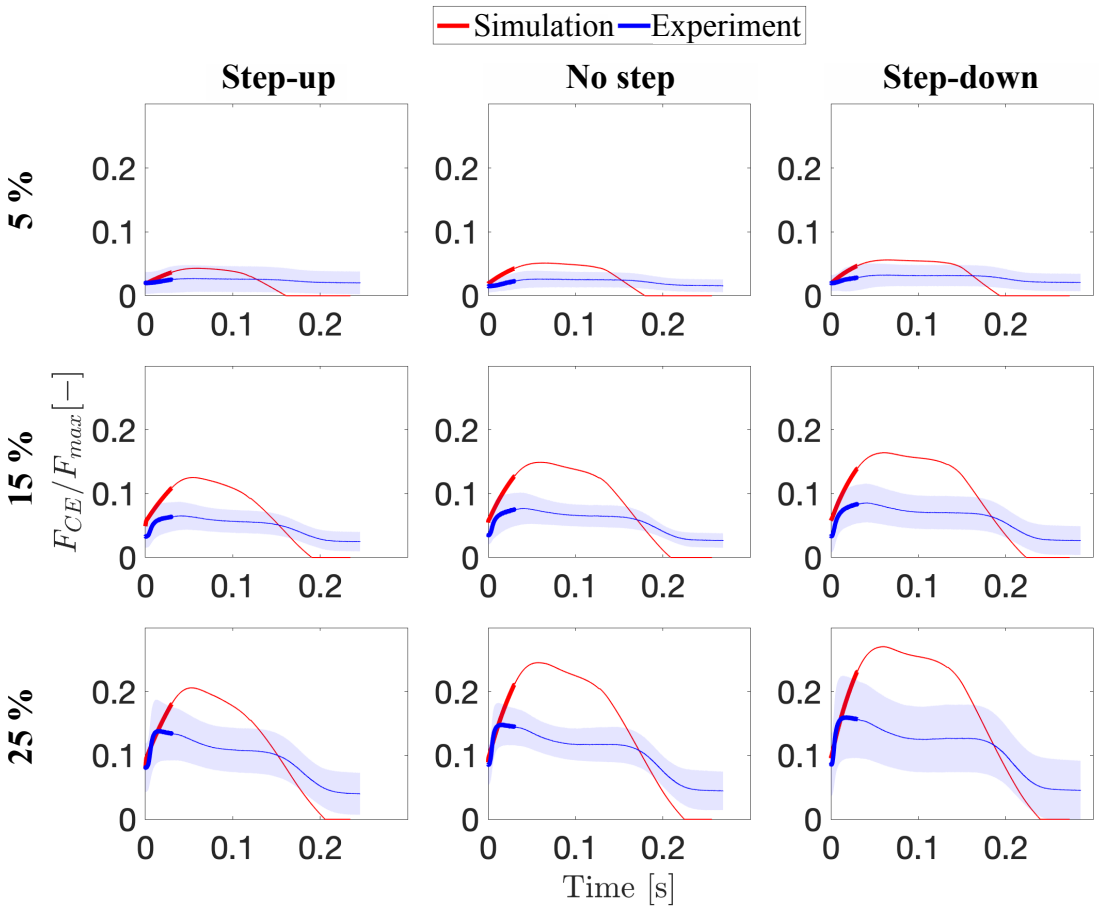

Figure A2.5: Force generated in dynamic-scenario by both muscle fibers and the Hill-type muscle model during one hopping cycle — from touchdown to toe-off — are presented for all perturbation and activity levels. The thick and thin sections of the loops represent the preflex and remaining part of the stretch-shortening cycle, respectively. The blue line and shaded area represent the mean of all experimental trials and the standard deviation, respectively. Figure from Araz et al. (2023).

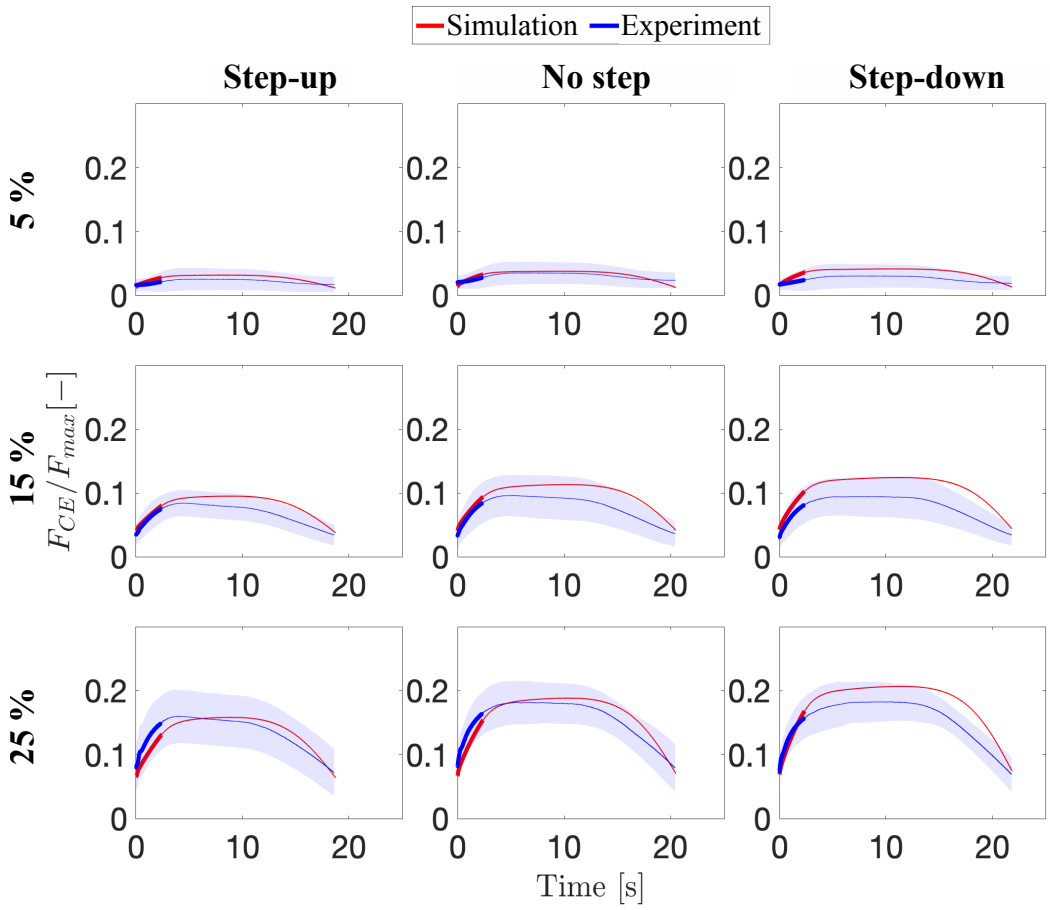

Figure A2.6: Force generated in quasistatic-scenario by both muscle fibers and the Hill-type muscle model during one hopping cycle — from touchdown to toe-off — are presented for all perturbation and activity levels. The thick and thin sections of the loops represent the preflex and remaining part of the stretch-shortening cycle, respectively. The blue line and shaded area represent the mean of all experimental trials and the standard deviation, respectively. Figure from Araz et al. (2023).

Table A2.2: Statistical comparison of muscle fibers' perturbation response for each activity level. Significantly different results are indicated by *; a: activity level; SRS: short range stiffness; χ^2: test value of Friedmantest; p: significance value; r: effect size; P0: no-perturbation; P↑: step-up perturbation; P↓: step-down perturbation. Table from Araz et al. (2023).

Condition	a	Parameter	χ^2	p	P0 vs. P↑(r)	P0 vs. P↓(r)	P↓ vs. P↑ (r)
Dynamic-Scenario	5 %	Preflex work	8.222	0.016*	0.029(.41)*	1	0.055
		SRS	0.889	0.641	-	-	-
		Work Figure 6.5A	1.556	0.459	-	-	-
	15 %	Preflex work	16.222	0.001*	0.055	0.297	0.001(0.63)*
		SRS	0	1	-	-	-
		Work Figure 6.5A	4.667	0.097	-	-	-
	25 %	Preflex work	14.889	0.001*	0.029(0.41)*	0.716	0.001(0.59)*
		SRS	1.556	0.459	-	-	-
		Work Figure 6.5A	3.556	0.169	-	-	-
Quasistatic-Scenario	5 %	Preflex work	4.222	0.121	-	-	-
		Stiffness	4.222	0.121	-	-	-
	15 %	Preflex work	16.222	0.001*	0.055	0.297	0.001(0.63)*
		Stiffness	0.667	0.717	-	-	-
	25 %	Preflex work	16.222	0.001*	0.055	0.297	0.001(0.63)*
		Stiffness	0.667	0.717	-	-	-
Dynamic vs. Quasistatic-Scenario Figure 6.5B	5 %	Preflex work	2.667	0.264	-	-	-
	15 %	Preflex work	4.222	0.121	-	-	-
	25 %	Preflex Work	1.556	0.459	-	-	-

Table A2.3: Statistical comparison of activity differences for each perturbation case. Significantly different results are indicated by *; effect size is shown for significant differences in (); SRS: short range stiffness; χ^2: test value of Friedmantest; p: significance value; P0: no-perturbation; P↑: step-up perturbation; P↓: step-down perturbation. Table from Araz et al. (2023).

Condition	P	Parameter	χ^2	p	5 % vs. 15 %	5 % vs. 25 %	15 % vs. 25 %
Dynamic-Scenario	P0	Preflex work	18	0.001*	0.102	0.001(0,67)*	0.102
		SRS	18	0.001*	0.102	0.001(0.67)*	0.102
		Work Figure 6.5A	12.667	0.002*	0.472	0.001(0.56)*	0.102
	P↑	Preflex work	18	0.001*	0.102	0.001(0.67)*	0.102
		SRS	18	0.001*	0.102	0.001(0.67)*	0.102
		Work Figure 6.5A	18	0.001*	0.102	0.001(0.67)*	0.102
	P↓	Preflex work	18	0.001*	0.102	0.001(0.67)*	0.102
		SRS	18	0.001*	0.102	0.001(0.67)*	0.102
		Work Figure 6.5A	18	0.001*	0.102	0.001(0.67)*	0.102
Quasistatic-Scenario	P0	Preflex work	16.22	0.001*	0.055	0.001(0.63)*	0.297
		Stiffness	12.667	0.002*	0.102	0.001(0.56)*	0.472
	P↑	Preflex work	16.22	0.001*	0.055	0.001(0.63)*	0.297
		Stiffness	11.556	0.003*	0.055	0.003(0.52)*	1
	P↓	Preflex work	18	0.001*	0.102	0.001(0.67)*	0.102
		Stiffness	11.556	0.003*	0.055	0.003(0.52)*	1
Dynamics vs. Quasistatic-Scenario Figure 6.5B	P0	Preflex work	2	0.368	-	-	-
	P↑	Preflex work	0.222	0.895	-	-	-
	P↓	Preflex work	0.222	0.895	-	-	-

Table A2.4: Statistical comparison between Dynamic- and Quasistatic-Scenario. Significantly different results are indicated by *; SRS: short range stiffness; *z*: test value of t-test; *p*: significance value; *r*: effect size; P0: no-perturbation; P↑: step-up perturbation; P↓: step-down perturbation. Table from Araz et al. (2023).

Activity Level	Parameter	P	*z*	*p*	*r*
5 %	Preflex work	P0	0.533	0.594	-
		P↑	0.296	0.767	-
		P↓	1.333	0.182	-
	SRS	P0	0	1	-
		P↑	0	1	-
		P↓	0	1	-
15 %	Preflex work	P0	0.667	0.505	-
		P↑	0.533	0.594	-
		P↓	0.667	0.505	-
	SRS	P0	1.333	0.182	-
		P↑	2	0.046*	0.67
		P↓	2.666	0.008*	0.89
25 %	Preflex work	P0	0.667	0.505	-
		P↑	0.652	0.515	
		P↓	0.667	0.505	-
	SRS	P0	2.666	0.008*	0.89
		P↑	2.666	0.008*	0.89
		P↓	2	0.046*	0.67

A3 Supplementary material - Chapter 8

This is Chapter 8's supplementary material, which is published in (Mo et al., 2023).

The PDF file includes:

Figure A3.1
Tables A3.1 to A3.5
Legends for movies S1 to S3

Other Supplementary Material for this manuscript includes the following:

Movies S1 to S3: https://youtu.be/Sa-q-5NucGY
CAD model of the robot leg and data analysis: https://doi.org/10.17617/3.THJWG8

A3.1 Supplementary Videos

Movie-S1: Vertical hopping with step-down perturbation. The leg is hopping on a block whose height is 15% of the leg length. The slack of the damper is set to 3 mm. The first part of the video shows the experiment in real-time. In the second part, slow motion of the same experiment is repeated. In both cases, hip position y, GRF, spring and damper forces are plotted synchronized to the video. In the last part, the phase plots of the all experiments show the relation between hopping speed and the hopping position.

Movie-S2: Forward hopping with continuous perturbation. The leg moves forward by hopping on the sinusoidal terrain with ± 10 mm amplitude. The damper is fully engaged, i.e., the slackness is 0 mm. After the leg completes one full rotation on the terrain, the video shows frames taken by the high-speed video camera.

Movie-S3: Failure modes of forward hopping with ramp-up-step-down perturbation. The leg moves on the flat surface, and it gradually climbs on the ramp to jump off. The perturbation height is 30% of the leg length, and the damper slack is set to 3 mm. The bottom-right plot shows the synchronized hip position in planer motion. The video shows three cases: slipping, stopping, and the good response after the step-down perturbations. The slipping case can be identified by audio irregularity.

A3.2 Leg design parameters

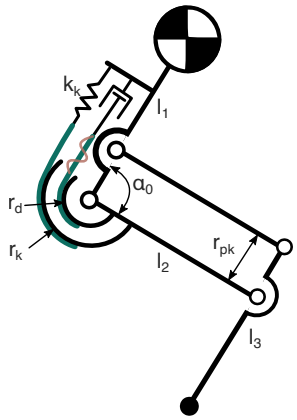

Figure A3.1: Schematics of the leg with the key design parameters. Figure from Mo et al. (2023).

Parameters		**Value**
Robot mass - vertical hopping	m_v	1.94 kg
Robot mass - forward hopping	m_f	0.94 kg
Leg resting length	l_0	310 mm
Segment 1 length	l_1	150 mm
Segment 2 length	l_2	150 mm
Segment 3 length	l_3	150 mm
Knee spring pulley radius	r_k	30 mm
Knee damper pulley radius	r_d	20 mm
Knee spring stiffness	k_k	10.9 N/mm
Bi-articular insertion radius	r_{pk}	32 mm
Knee resting angle	α_0	100°

Table A3.1: Robot design parameters. Table from Mo et al. (2023).

A3.3 Robot control parameters

Parameters		Value
Vertical hopping		
Hopping frequency	f_v	2.2 Hz
Knee torque amplitude	τ_v	4.0 - 4.3Nm
Knee duty cycle	–	0.22
Forward hopping		
Hip amplitude	θ_{hip}	18°
Hip offset	O_{hip}	2°
Hopping frequency	f_f	1.85 Hz
Hip virtual duty factor	D_{vir}	0.4
Knee torque amplitude	τ_f	1.3 Nm
Knee phase shift	–	0.75
Knee duty cycle	–	0.2

Table A3.2: Robot control parameters. Table from Mo et al. (2023).

A3.4 Experimental results

Perturbation [LL]	Damper slack [mm]	Hop height [mm]	CoH [/]	Recovery steps [/]	Delay [ms]	E_d [mJ]
10%	10	53.3	6.3	2.5	-	1
10%	6	49.3	6.6	1.7	51	26
10%	3	49.1	6.7	2.0	26	117
10%	0	44.7	7.4	2.9	0	186
15%	10	55.8	6.3	3.2	-	1
15%	6	47.8	6.7	2.5	50	29
15%	3	43.2	7.0	3.6	24	86
15%	0	42.4	7.6	5.9	0	152

Table A3.3: Experimental results of vertical hopping with step-down perturbation. The energy dissipated by the damper (E_d) is calculated by integrating the damping force with respect to the damper compression (Figure 8.3c). Table from Mo et al. (2023).

Roughness amplitude [mm]	Damper slack [mm]	Speed [m/s]	CoT [/]	Step cycle std [ms]
0	10	0.80	1.01	27.1
0	6	0.79	0.99	16.2
0	3	0.71	1.07	2.4
0	0	0.67	1.35	2.1
±5	10	0.76	0.75	2.4
±5	6	0.76	1.01	13.4
±5	3	0.74	1.01	11.1
±5	0	0.68	1.24	2.2
±10	10	0.76	0.79	3.1
±10	6	0.71	0.97	3.6
±10	3	0.72	0.80	2.7
±10	0	0.66	1.32	2.7

Table A3.4: Experimental results of forward hopping with continuous perturbation. Table from Mo et al. (2023).

Perturbation [LL]	Damper slack [mm]	Speed [m/s]	CoT [/]	Recovery steps [/]	Failure steps [/]
15%	10	0.81	0.95	2.7	7
15%	6	0.78	1.00	2.0	4
15%	3	0.72	1.36	1.7	6
15%	0	0.68	1.30	1.0	0
30%	10	0.80	0.91	2.6	10
30%	6	0.75	0.93	2.4	10
30%	3	0.73	1.18	2.9	10
30%	0	0.64	1.44	2.3	3

Table A3.5: Experimental results of forward hopping with ramp-up-step-down perturbation. Table from Mo et al. (2023).